Skulls of Neandertal ancestors *pp. 1338 & 1358*

African scientists and the genomic revolution *p. 1346*

Ultralightweight materials that don't bend *p. 1373*

Science

$10
20 JUNE 2024
sciencemag.org

AAAS

The song of the bat

Decoding a mammal's startling vocal skills

p. 1334

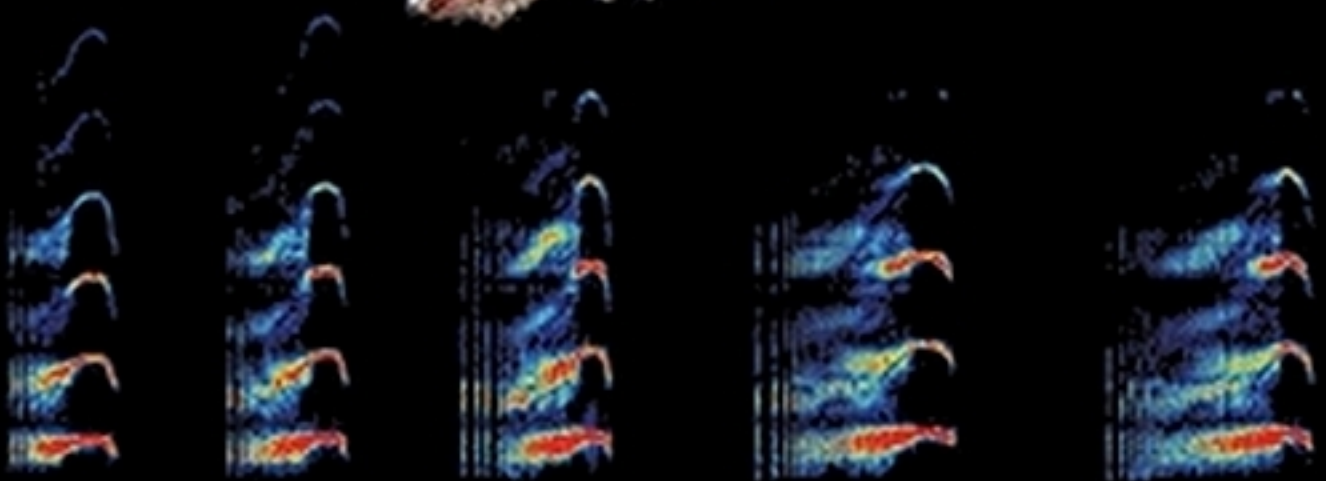

CONTENTS

20 JUNE 2014 • VOLUME 344 • ISSUE 6190

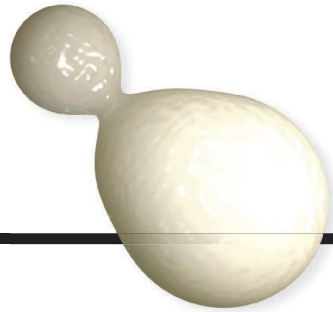

1341 & 1389

Extending the replicative life span of yeast

NEWS

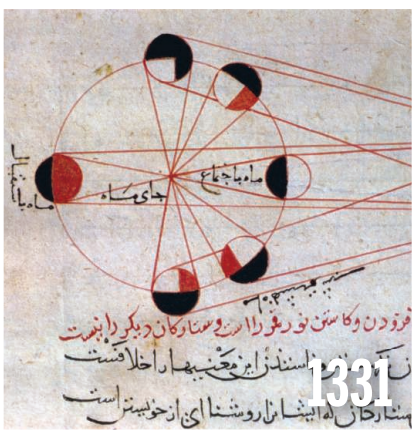

IN BRIEF

1324 Roundup of the week's news

IN DEPTH

1327 NIH PUTS MASSIVE U.S. CHILDREN'S STUDY ON HOLD
National Academies report calls for overhaul *By J. Kaiser*

1328 JUST ONE PROPOSAL PER YEAR, PLEASE, NSF TELLS ASTRONOMERS
As success rates drop, agency seeks to limit applications *By J. Mervis*

1329 'RIGHT TO TRY' LAWS BYPASS FDA FOR LAST-DITCH TREATMENTS
But companies may be reluctant to supply unapproved drugs *By K. Servick*

1330 QUANTUM OR NOT, CONTROVERSIAL COMPUTER YIELDS NO SPEEDUP
Conventional computer ties D-Wave machine *By A. Cho*
▸ *SCIENCE* EXPRESS REPORT BY T. F. RØNNOW *ET AL.*

1331 WAS AMERICA 'DISCOVERED' IN MEDIEVAL CENTRAL ASIA?
Ancient texts suggest Silk Road polymath inferred the existence of unknown continents *By R. Stone*

1332 SECRET BUNDLES OF PROFIT
Study lifts veil on journal price negotiations *By J. Bohannon*

FEATURE

1334 WHEN THE BAT SINGS
The trills and chirps of bats can be as complex and meaningful as bird song—and may be a closer analog for human speech *By V. Morell*

INSIGHTS

PERSPECTIVES

1338 HOW TO BUILD A NEANDERTAL
Fossils from Sima de los Huesos show a mixture of Neandertal and more ancient features
By J.-J. Hublin
▸ RESEARCH ARTICLE P. 1358

1340 CONNECTING THE DOTS
Understanding nanocrystal surfaces helps to direct their assembly into novel material architectures
By M. A. Boles and D. V. Talapin
▸ REPORTS PP. 1377 & 1380

1341 A CELL DEATH AVENUE EVOLVED FROM A LIFE-SAVING PATH
Altruistic cell suicide model is challenged
By H. H. Kampinga
▸ REPORT P. 1389

1343 TEACHING THE IMMUNE SYSTEM "SELF" RESPECT AND TOLERANCE
An anti-inflammatory milieu promotes immune tolerance
By L. Chatenoud

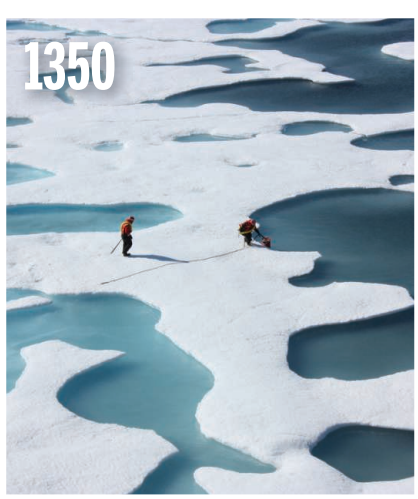

1344 ELECTRONICALLY ERASED
Erasing knowledge of a quantum system changes its state
By D. E. Feldman
▸ REPORT P. 1363

1345 HOW CARRION AND HOODED CROWS DEFEAT LINNAEUS'S CURSE
How two crow species maintain their identity raises questions about species concepts
By P. de Knijff
▸ REPORT P. 1410

1346 ENABLING THE GENOMIC REVOLUTION IN AFRICA
H3Africa is developing capacity for health-related genomics research in Africa
By The H3Africa Consortium

BOOKS *ET AL.*

1349 SECOND GROWTH
By R. L. Chazdon, reviewed by V. Kapos

1350 COMING TO OUR SENSES
By V. McCabe, reviewed by A. Walker-Andrews

LETTERS

1351 BIOLOGY'S DRONES: UNDERMINED BY FEAR
By T. Humle et al.

1351 BIOLOGY'S DRONES: NEW AND IMPROVED
By C. Luo et al.

1351 INVESTIGATIVE BIOETHICS
By K. L. Galbraith

1352 DEEP-SEA PROTECTION: COORDINATE EFFORTS
By C. Gobin and G. A. B. da Fonseca

DEPARTMENTS

1323 EDITORIAL
Warming U.S.-Russia relations
By Cathleen A. Campbell

1422 WORKING LIFE
What it takes
By Jim Austin

Science Staff 1322
New Products 1415
Science Careers 1416

Published by AAAS

CONTENTS

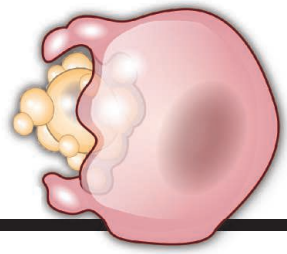

1343
Reprogramming the immune system for tolerance

20 JUNE 2014 • VOLUME 344 • ISSUE 6190

RESEARCH

IN BRIEF

1354 From *Science* and other journals

REVIEW

1357 **SOCIAL COGNITION**
The cultural evolution of mind reading
C. M. Heyes and C. D. Frith
REVIEW SUMMARY; FOR FULL TEXT:
HTTP://DX.DOI.ORG/10.1126/SCIENCE.1243091
▸ PODCAST

RESEARCH ARTICLE

1358 **HUMAN EVOLUTION**
Neandertal roots: Cranial and chronological evidence from Sima de los Huesos
J. L. Arsuaga et al.
▸ PERSPECTIVE P. 1338

REPORTS

1363 **QUANTUM MECHANICS**
An electronic quantum eraser
E. Weisz et al.
▸ PERSPECTIVE P. 1344

1366 **NANOMAGNETISM**
Nanoscale imaging and control of domain-wall hopping with a nitrogen-vacancy center microscope
J.-P. Tetienne et al.

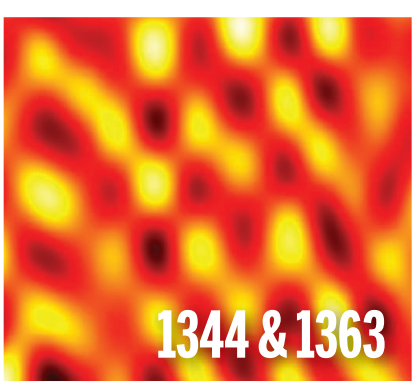

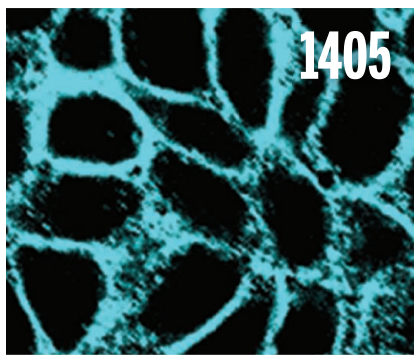

1369 **NANOPHOTONICS**
Controlling graphene plasmons with resonant metal antennas and spatial conductivity patterns
P. Alonso-González et al.

1373 **LOW-DENSITY MATERIALS**
Ultralight, ultrastiff mechanical metamaterials *X. Zheng* et al.

1377 **NANOMATERIALS**
Long-range orientation and atomic attachment of nanocrystals in 2D honeycomb superlattices
M. P. Boneschanscher et al.

1380 **NANOMATERIALS**
Hydroxylation of the surface of PbS nanocrystals passivated with oleic acid *D. Zherebetskyy* et al.
▸ PERSPECTIVE P. 1340

1384 **COMPUTATIONAL BIOLOGY**
Controlling low rates of cell differentiation through noise and ultrahigh feedback
R. Ahrends et al.

1389 **AGING CELL BIOLOGY**
Life-span extension by a metacaspase in the yeast *Saccharomyces cerevisiae*
S. Malmgren Hill et al.
▸ PERSPECTIVE P. 1341

1392 **HIV LATENCY**
Screening for noise in gene expression identifies drug synergies *R. D. Dar* et al.

1396 **CANCER GENOMICS**
Single-cell RNA-seq highlights intratumoral heterogeneity in primary glioblastoma
A. P. Patel et al.

1401 **HIV PATHOGENESIS**
HIV-1–induced AIDS in monkeys
T. Hatziioannou et al.

1405 **TOXIN MECHANISM**
Molecular basis for disruption of E-cadherin adhesion by botulinum neurotoxin A complex
K. Lee et al.

1410 **ECOLOGICAL GENOMICS**
The genomic landscape underlying phenotypic integrity in the face of gene flow in crows
J. W. Poelstra et al.
▸ PERSPECTIVE P. 1345

ON THE COVER

A greater sac-winged bat (*Saccopteryx bilineata*) in flight, with sonograms of a male's territorial song below. *S. bilineata* is one of 20 bat species known to sing, producing calls that are as varied and structurally complex as bird song. See page 1334. *Images: (bat) © Bruce D. Taubert/Bat Conservation International; (sound waves) Mirjam Knörnschild/University of Ulm*

SCIENCE (ISSN 0036-8075) is published weekly on Friday, except the last week in December, by the American Association for the Advancement of Science, 1200 New York Avenue, NW, Washington, DC 20005. Periodicals mail postage (publication No. 484460) paid at Washington, DC, and additional mailing offices. Copyright © 2014 by the American Association for the Advancement of Science. The title SCIENCE is a registered trademark of the AAAS. Domestic individual membership and subscription (51 issues): $153 ($74 allocated to subscription). Domestic institutional subscription (51 issues): $1282; Foreign postage extra: Mexico, Caribbean (surface mail) $55; other countries (air assist delivery) $85. First class, airmail, student, and emeritus rates on request. Canadian rates with GST available upon request, GST #1254 88122. Publications Mail Agreement Number 1069624. **Printed in the U.S.A.**
Change of address: Allow 4 weeks, giving old and new addresses and 8-digit account number. **Postmaster:** Send change of address to AAAS, P.O. Box 96178, Washington, DC 20090–6178. **Single-copy sales:** $10.00 current issue, $15.00 back issue prepaid includes surface postage; bulk rates on request. **Authorization to photocopy** material for internal or personal use under circumstances not falling within the fair use provisions of the Copyright Act is granted by AAAS to libraries and other users registered with the Copyright Clearance Center (CCC) Transactional Reporting Service, provided that $30.00 per article is paid directly to CCC, 222 Rosewood Drive, Danvers, MA 01923. The identification code for *Science* is 0036-8075. *Science* is indexed in the *Reader's Guide to Periodical Literature* and in several specialized indexes.

Published by AAAS

Science
AAAS
1200 New York Avenue, NW, Washington, DC 20005
Bateman House, 82-88 Hills Road, Cambridge, UK CB2 1LQ

Editor-in-Chief Marcia McNutt
Executive Editor Monica M. Bradford **News Editor** Tim Appenzeller
Managing Editor, Research Journals Katrina L. Kelner
Deputy Editors Barbara R. Jasny, Andrew M. Sugden(UK), Valda J. Vinson, Jake S. Yeston

Research and Insights

SR. EDITORS Caroline Ash(UK), Gilbert J. Chin, Lisa D. Chong, Maria Cruz(UK), Julia Fahrenkamp-Uppenbrink(UK), Pamela J. Hines, Stella M. Hurtley(UK), Paula A. Kiberstis, Marc S. Lavine(Canada), Kristen L. Mueller, Ian S. Osborne(UK), Beverly A. Purnell, L. Bryan Ray, Guy Riddihough, H. Jesse Smith, Peter Stern(UK), Phillip D. Szuromi, Brad Wible, Nicholas S. Wigginton, Laura M. Zahn **ASSOCIATE EDITORS** Brent Grocholski, Melissa R. McCartney, Margaret M. Moerchen, Jelena Stajic, Sacha Vignieri **BOOK REVIEW EDITOR** Sherman J. Suter **ASSOCIATE LETTERS EDITOR** Jennifer Sills **EDITORIAL MANAGER** Cara Tate **SR. COPY EDITORS** Jeffrey E. Cook, Chris Filiatreau, Cynthia Howe, Harry Jach, Lauren Kmec, Barbara P. Ordway, Trista Wagoner **SR. EDITORIAL COORDINATORS** Carolyn Kyle, Beverly Shields **EDITORIAL COORDINATORS** Ramatoulaye Diop, Joi S. Granger, Lisa Johnson, Anita Wynn **PUBLICATIONS ASSISTANTS** Aneera Dobbins, Jeffrey Hearn, Dona Mathieu, Le-Toya Mayne Flood, Shannon McMahon, Scott Miller, Jerry Richardson, Rachel Roberts(UK), Alice Whaley(UK), Brian White **ADMINISTRATIVE SUPPORT** Janet Clements(UK), Joan Cuthbert(UK), Maryrose Madrid, John Wood(UK)

News

NEWS MANAGING EDITOR John Travis **INTERNATIONAL EDITOR** Richard Stone **DEPUTY NEWS EDITORS** Daniel Clery(UK), Robert Coontz, Elizabeth Culotta, David Grimm, David Malakoff, Leslie Roberts **CONTRIBUING EDITORS** Martin Enserink(Europe), Mara Hvistendahl (Asia) **SR. CORRESPONDENTS** Jeffrey Mervis, Elizabeth Pennisi **NEWS WRITERS** Yudhijit Bhattacharjee, Adrian Cho, Jennifer Couzin-Frankel, Carolyn Gramling, Eric Hand, Jocelyn Kaiser, Kelly Servick, Robert F. Service, Erik Stokstad, Emily Underwood **CONTRIBUTING CORRESPONDENTS** Pallava Bagla(South Asia), Michael Balter(Paris), John Bohannon, Jon Cohen, Ann Gibbons, Sam Kean, Richard A. Kerr, Eli Kintisch, Kai Kupferschmidt(Berlin), Andrew Lawler, Christina Larson(Beijing), Mitch Leslie, Charles C. Mann, Eliot Marshall, Virginia Morell, Dennis Normile(Tokyo),Heather Pringle, Tania Rabesandratana(Brussels), Gretchen Vogel(Berlin), Lizzie Wade(Mexico City) **CAREERS** Jim Austin(Editor), Donisha Adams **COPY EDITORS** Kara Estelle, Nora Kelly, Jennifer Levin **ADMINISTRATIVE SUPPORT** Scherraine Mack

Executive Publisher Alan I. Leshner
Publisher Beth Rosner **Chief Digital Media Officer** Rob Covey

BUSINESS OPERATIONS AND ADMINISTRATION DIRECTOR Deborah Rivera-Wienhold **BUSINESS SYSTEMS AND FINANCIAL ANALYSIS DIRECTOR** Randy Yi **MANAGER OF FULFILLMENT SYSTEMS** Neal Hawkins **SYSTEMS ANALYST** Nicole Mehmedovich **ASSISTANT DIRECTOR, BUSINESS OPERATIONS** Eric Knott **MANAGER, BUSINESS OPERATIONS** Jessica Tierney **BUSINESS ANALYSTS** Cory Lipman, Cooper Tilton, Celeste Troxler **FINANCIAL ANALYST** Jeremy Clay **RIGHTS AND PERMISSIONS: ASSISTANT DIRECTOR** Emilie David **PERMISSIONS ASSOCIATE** Elizabeth Sandler **RIGHTS, CONTRACTS, AND LICENSING ASSOCIATE** Lili Kiser

MARKETING DIRECTOR Ian King **MARKETING MANAGER** Julianne Wielga **MARKETING ASSOCIATE** Elizabeth Sattler **SR. MARKETING EXECUTIVE** Jennifer Reeves **SR. ART ASSOCIATE, PROJECT MANAGER** Tzeitel Sorrosa **ART ASSOCIATE** Seil Lee **ASSISTANT COMMERCIAL EDITOR** Selby Frame **MARKETING PROJECT MANAGER** Angelissa McArthur **SR. WRITER** Bill Zimmer **PROGRAM DIRECTOR, AAAS MEMBER CENTRAL** Peggy Mihelich **FULFILLMENT SYSTEMS AND OPERATIONS** membership@aaas.org **MANAGER, MEMBER SERVICES** Pat Butler **SPECIALISTS** LaToya Casteel, Javia Flemmings, Latasha Russell **MANAGER, DATA ENTRY** Mickie Napoleoni **DATA ENTRY SPECIALISTS** JJ Regan, Jaimee Wise, Fiona Giblin

DIRECTOR, SITE LICENSING Tom Ryan **DIRECTOR, CORPORATE RELATIONS** Eileen Bernadette Moran **SR. PUBLISHER RELATIONS SPECIALIST** Kiki Forsythe **PUBLISHER RELATIONS MANAGER** Catherine Holland **PUBLISHER RELATIONS, EASTERN REGION** Keith Layson **PUBLISHER RELATIONS, WESTERN REGION** Ryan Rexroth **MANAGER, SITE LICENSE OPERATIONS** Iquo Edim **FULFILLMENT ANALYST** Lana Guz **ASSOCIATE DIRECTOR, MARKETING** Christina Schlecht **MARKETING ASSOCIATES** Thomas Landreth, Minah Kim

DIRECTOR OF WEB TECHNOLOGIES Ahmed Khadr **SR. DEVELOPERS** Jumoke Adekanmi, Chris Coleman **DEVELOPER** Dan Berger **SR. PROJECT MANAGER** Trista Smith **SYSTEMS ENGINEER** Luke Johnson **PRODUCT MANAGER** Walter Jones

CREATIVE DIRECTOR, MULTIMEDIA Martyn Green **DIRECTOR OF ANALYTICS** Enrique Gonzales **SR. WEB PRODUCER** Sarah Crespi **WEB PRODUCER** Alison Crawford **VIDEO PRODUCER** Nguyen Nguyen **SOCIAL MEDIA PRODUCER** Meghna Sachdev

DIRECTOR OF OPERATIONS PRINT AND ONLINE Lizabeth Harman **ASSISTANT MANAGER** Lisa Stanford **PRODUCTION SPECIALISTS** Amy Hardcastle, Antoinette Hodal, Nichele Johnston, Yuse Lajiminmuhip, Lori Murphy, Kimberley Oster **PRODUCTION DIRECTOR** Wendy K. Shank **ASSISTANT MANAGER** Rebecca Doshi **SR. SPECIALISTS** Steve Forrester, Anthony Rosen **SPECIALIST** Jacob Hedrick **PREFLIGHT MANAGER** Marcus Spiegler **SR. SPECIALISTS** Jason Hillman, Tara Kelly

DESIGN DIRECTOR Beth Rakouskas **ASSOCIATE ART DIRECTOR** Laura Creveling **SR. ILLUSTRATORS** Chris Bickel, Katharine Sutliff **ILLUSTRATOR** Valerie Altounian **SR. ART ASSOCIATES** Holly Bishop, Preston Huey **ART ASSOCIATES** Kay Engman, Garvin Grullón, Chrystal Smith **SR. PHOTO EDITOR** William Douthitt **PHOTO EDITOR** Leslie Blizard

DIRECTOR, GLOBAL COLLABORATION, CUSTOM PUBLICATIONS, ADVERTISING Bill Moran **EDITOR, CUSTOM PUBLISHING** Sean Sanders: 202-326-6430 **ASSISTANT EDITOR, CUSTOM PUBLISHING** Tianna Hicklin: 202-326-6463 **ADVERTISING MARKETING MANAGER** Justin Sawyers: 202-326-7061 science_advertising@aaas.org **ADVERTISING SUPPORT MANAGER** Karen Foote: 202-326-6740 **ADVERTISING PRODUCTION OPERATIONS MANAGER** Deborah Tompkins **SR. TRAFFIC ASSOCIATE** Christine Hall **SALES COORDINATOR** Shirley Young **ASSOCIATE DIRECTOR, COLLABORATION, CUSTOM PUBLICATIONS/CHINA/TAIWAN/KOREA/SINGAPORE** Ruolei Wu: +86-186 0822 9345, rwu@aaas.org **EAST COAST/E. CANADA** Laurie Faraday: 508-747-9395, FAX 617-507-8189 **WEST COAST/W. CANADA** Lynne Stickrod: 415-931-9782, FAX 415-520-6940 **MIDWEST** Jeffrey Dembksi: 847-498-4520 x3005, Steven Loerch: 847-498-4520 x3006 **UK EUROPE/ASIA** Roger Goncalves: TEL/FAX +41 43 243 1358 **JAPAN** Makiko Hara: +81 (0) 3 6802 4616, FAX +81 (0) 3 6802 4615, ads@sciencemag.jp **CHINA/TAIWAN** Ruolei Wu: +86-186 0822 9345

WORLDWIDE ASSOCIATE DIRECTOR OF SCIENCE CAREERS Tracy Holmes: +44 (0) 1223 326525, FAX +44 (0) 1223 326532 tholmes@science-int. co.uk **CLASSIFIED** advertise@sciencecareers.org **U.S. SALES** Tina Burks: 202-326-6577, Nancy Toema: 202-326-6578 **SALES ADMINISTRATOR** Marci Gallun **EUROPE/ROW SALES** Axel Gesatzki, Sarah Lelarge **SALES ASSISTANT** Kelly Grace **JAPAN** Yuri Kobayashi: +81 (0)90-9110-1719, careerads@sciencemag.jp **CHINA/TAIWAN** Ruolei Wu: +86-186 0822 9345 rwu@aaas.org **MARKETING MANAGER** Allison Pritchard **MARKETING ASSOCIATE** Aimee Aponte

AAAS BOARD OF DIRECTORS RETIRING PRESIDENT, CHAIR Phillip A. Sharp **PRESIDENT** Gerald R. Fink **PRESIDENT-ELECT** Geraldine (Geri) Richmond **TREASURER** David Evans Shaw **CHIEF EXECUTIVE OFFICER** Alan I. Leshner **BOARD** Bonnie L. Bassler, May R. Berenbaum, Carlos J. Bustamante, Claire M. Fraser, Laura H. Greene, Elizabeth Loftus, Raymond Orbach, Inder M. Verma

SUBSCRIPTION SERVICES For change of address, missing issues, new orders and renewals, and payment questions: 866-434-AAAS (2227) or 202-326-6417, FAX 202-842-1065. Mailing addresses: AAAS, P.O. Box 96178, Washington, DC 20090-6178 or AAAS Member Services, 1200 New York Avenue, NW, Washington, DC 20005

INSTITUTIONAL SITE LICENSES 202-326-6755 **REPRINTS:** Author Inquiries 800-635-7181 **COMMERCIAL INQUIRIES** 803-359-4578 **PERMISSIONS** 202-326-6765, permissions@aaas.org **AAAS Member Services** 202-326-6417 or http://membercentral.aaas.org/discounts

Science serves as a forum for discussion of important issues related to the advancement of science by publishing material on which a consensus has been reached as well as including the presentation of minority of conflicting points of view. Accordingly, all articles published in *Science*—including editorials, news and comment, and books reviews—are signed and reflect the individual views of the authors and not official points of view adopted by AAAS or the institutions with which the authors are affiliated.

INFORMATION FOR AUTHORS See pages 680 and 681 of the 7 February 2014 issue or access www.sciencemag.org/about/authors

SENIOR EDITORIAL BOARD
A. Paul Alivisatos, *Lawrence Berkeley Nat'l. Laboratory,* **Ernst Fehr,** *U. of Zürich*
Susan M. Rosenberg, *Baylor College of Medicine,* **Michael S. Turner,** *U. of Chicago*

BOARD OF REVIEWING EDITORS
Adriano Aguzzi, *U. Hospital Zürich*
Takuzo Aida, *U. of Tokyo*
Leslie Aiello, *Wenner-Gren Foundation*
Judith Allen, *U. of Edinburgh*
Sonia Altizer, *U. of Georgia*
Virginia Armbrust, *U. of Washington*
Sebastian Amigorena, *Institut Curie*
Kathryn Anderson, *Memorial Sloan-Kettering Cancer Center*
Peter Andolfatto, *Princeton U.*
Meinrat O. Andreae, *Max-Planck Inst. Mainz*
Paola Arlotta, *Harvard U.*
Johan Auwerx, *EPFL*
David Awschalom, *U. of Chicago*
Jordi Bascompte, *Estación Biológica de Doñana CSIC*
Facundo Batista, *London Research Inst.*
Ray H. Baughman, *U. of Texas, Dallas*
David Baum, *U. of Wisconsin*
Mark Bear, *Massachusetts Inst. of Technology*
Kamran Behnia, *ESPCI-ParisTech*
Yasmine Belkaid, *NIAID, NIH*
Philip Benfey, *Duke U.*
Stephen J. Benkovic, *Penn State U.*
Gabriele Bergers, *U. of California, San Francisco*
Christophe Bernard, *Aix-Marseille U.*
Bradley Bernstein, *Massachusettes General Hospital*
Gregory C. Beroza, *Stanford U.*
Peer Bork, *EMBL*
Bernard Bourdon, *Ecole Normale Supérieure de Lyon*
Chris Bowler, *École Normale Supérieure*
Ian Boyd, *U. of St. Andrews*
Emily Brodsky, *U. of California, Santa Cruz*
Christian Büchel, *U. Hamburg-Eppendorf*
Joseph A. Burns, *Cornell U.*
William P. Butz, *Population Reference Bureau*
Gyorgy Buzsaki, *New York U. School of Medicine*
Blanche Capel, *Duke U.*
Mats Carlsson, *U. of Oslo*
David Clapham, *Children's Hospital Boston*
David Clary, *U. of Oxford*
Joel Cohen, *Rockefeller U., Columbia U.*
Jonathan D. Cohen, *Princeton U.*
James Collins, *Boston U.*
Robert Cook-Deegan, *Duke U.*
Alan Cowman, *Walter & Eliza Hall Inst.*
Robert H. Crabtree, *Yale U.*
Janet Currie, *Princeton U.*
Jeff L. Dangl, *U. of North Carolina*
Tom Daniel, *U. of Washington*
Frans de Waal, *Emory U.*
Stanislas Dehaene, *Collège de France*
Robert Desimone, *MIT*
Claude Desplan, *New York U.*
Ap Dijksterhuis, *Radboud U. of Nijmegen*
Dennis Discher, *U. of Pennsylvania*
Gerald W. Dorn II, *Washington U. School of Medicine*
Jennifer A. Doudna, *U. of California, Berkeley*
Bruce Dunn, *U. of California, Los Angeles*
Christopher Dye, *WHO*
Todd Ehlers, *U. of Tuebingen*
David Ehrhardt, *Carnegie Inst. of Washington*
Tim Elston, *U. of North Carolina at Chapel Hill*
Gerhard Ertl, *Fritz-Haber-Institut, Berlin*
Barry Everitt, *U. of Cambridge*
Ernst Fehr, *U. of Zurich*
Anne C. Ferguson-Smith, *U. of Cambridge*
Michael Feuer, *The George Washington U.*
Peter Fratzl, *Max-Planck Inst.*
Elaine Fuchs, *Rockefeller U.*
Daniel Geschwind, *UCLA*
Andrew Gewirth, *U. of Illinois*
Karl-Heinz Glassmeier, *TU Braunschweig*
Julia R. Greer, *Caltech*
Elizabeth Grove, *U. of Chicago*
Kip Guy, *St. Jude's Children's Research Hospital*
Taekjip Ha, *U. of Illinois at Urbana-Champaign*
Christian Haass, *Ludwig Maximilians U.*
Steven Hahn, *Fred Hutchinson Cancer Research Center*
Michael Hasselmo, *Boston U.*
Martin Heimann, *Max-Planck Inst. Jena*
Yka Helariutta, *U. of Finland*
James A. Hendler, *Rensselaer Polytechnic Inst.*
Janet G. Hering, *Swiss Fed. Inst. of Aquatic Science & Technology*
Michael E. Himmel, *National Renewable Energy Lab.*
Kai-Uwe Hinrichs, *U. of Bremen*
Kei Hirose, *Tokyo Inst. of Technology*
David Hodell, *U. of Cambridge*
David Holden, *Imperial College*
Lora Hooper, *UT Southwestern Medical Ctr. at Dallas*
Thomas Hudson, *Ontario Inst. for Cancer Research*
Raymond Huey, *U. of Washington*
Steven Jacobsen, *U. of California, Los Angeles*
Kai Johnsson, *EPFL Lausanne*
Peter Jonas, *Inst. of Science & Technology (IST) Austria*
Matt Kaeberlein, *U. of Washington*
William Kaelin Jr., *Dana-Farber Cancer Inst.*
Daniel Kahne, *Harvard U.*
Daniel Kammen, *U. of California, Berkeley*
Masashi Kawasaki, *U. of Tokyo*
Joel Kingsolver, *U. of North Carolina at Chapel Hill*
Robert Kingston, *Harvard Medical School*
Alexander Kolodkin, *Johns Hopkins U.*
Roberto Kolter, *Harvard Medical School*
Alberto R. Kornblihtt, *U. of Buenos Aires*
Leonid Kruglyak, *UCLA*
Thomas Langer, *U. of Cologne*
Mitchell A. Lazar, *U. of Pennsylvania*
David Lazer, *Harvard U.*
Thomas Lecuit, *IBDM*
Virginia Lee, *U. of Pennsylvania*
Stanley Lemon, *U. of North Carolina at Chapel Hill*
Ottoline Leyser, *Cambridge U.*
Marcia C. Linn, *U. of California, Berkeley*
Jianguo Liu, *Michigan State U.*
Luis Liz-Marzan, *CIC biomaGUNE*
Jonathan Losos, *Harvard U.*
Ke Lu, *Chinese Acad. of Sciences*
Christian Lüscher, *U. of Geneva*
Laura Machesky, *CRUK Beatson Inst. for Cancer Research*
Anne Magurran, *U. of St. Andrews*
Oscar Marin, *CSIC & U. Miguel Hernández*
Charles Marshall, *U. of California, Berkeley*
C. Robertson McClung, *Dartmouth College*
Graham Medley, *U. of Warwick*
Yasushi Miyashita, *U. of Tokyo*
Richard Morris, *U. of Edinburgh*
Sean Munro, *MRC Lab. of Molecular Biology*
Thomas Murray, *The Hastings Center*
James Nelson, *Stanford U. School of Med.*
Karen Nelson, *J. Craig Venter Institute*
Daniel Neumark, *U. of California, Berkeley*
Timothy W. Nilsen, *Case Western Reserve U.*
Pär Nordlund, *Karolinska Inst.*
Helga Nowotny, *European Research Advisory Board*
Ben Olken, *MIT*
Luke O'Neill, *Trinity College, Dublin*
Joe Orenstein, *U. of California Berkeley & Lawrence Berkeley National Lab*
Harry Orr, *U. of Minnesota*
Andrew Oswald, *U. of Warwick*
Steve Palumbi, *Stanford U.*
Jane Parker, *Max-Planck Inst. of Plant Breeding Research*
Donald R. Paul, *U. of Texas, Austin*
John H. J. Petrini, *Memorial Sloan-Kettering Cancer Center*
Joshua Plotkin, *U. of Pennsylvania*
Philippe Poulin, *CNRS*
David Randall, *Colorado State U.*
Colin Renfrew, *U. of Cambridge*
Trevor Robbins, *U. of Cambridge*
Jim Roberts, *Fred Hutchinson Cancer Research Ctr.*
Barbara A. Romanowicz, *U. of California, Berkeley*
Jens Rostrup-Nielsen, *Haldor Topsoe*
Mike Ryan, *U. of Texas, Austin*
Mitinori Saitou, *Kyoto U.*
Shimon Sakaguchi, *Kyoto U.*
Miquel Salmeron, *Lawrence Berkeley National Lab*
Jürgen Sandkühler, *Medical U. of Vienna*
Alexander Schier, *Harvard U.*
Randy Seeley, *U. of Cincinnati*
Vladimir Shalaev, *Purdue U.*
Robert Siliciano, *Johns Hopkins School of Medicine*
Joseph Silk, *Institut d'Astrophysique de Paris*
Denis Simon, *Arizona State U.*
Alison Smith, *John Innes Centre*
John Speakman, *U. of Aberdeen*
Allan C. Spradling, *Carnegie Institution of Washington*
Jonathan Sprent, *Garvan Inst. of Medical Research*
Eric Steig, *U. of Washington*
Paula Stephan, *Georgia State U. and National Bureau of Economic Research*
Molly Stevens, *Imperial College London*
V. S. Subrahmanian, *U. of Maryland*
Ira Tabas, *Columbia U.*
Sarah Teichmann, *Cambridge U.*
John Thomas, *North Carolina State U.*
Christopher Tyler-Smith, *The Wellcome Trust Sanger Inst.*
Herbert Virgin, *Washington U.*
Bert Vogelstein, *Johns Hopkins U.*
Cynthia Volkert, *U. of Göttingen*
Douglas Wallace, *Dalhousie U.*
David Wallach, *Weizmann Inst. of Science*
Ian Walmsley, *U. of Oxford*
David A. Wardle, *Swedish U. of Agric. Sciences*
David Waxman, *Fudan U.*
Jonathan Weissman, *U. of California, San Francisco*
Ian A. Wilson, *The Scripps Res. Inst.*
Timothy D. Wilson, *U. of Virginia*
Rosemary Wyse, *Johns Hopkins U.*
Jan Zaanen, *Leiden U.*
Kenneth Zaret, *U. of Pennsylvania School of Medicine*
Jonathan Zehr, *U. of California, Santa Cruz*
Len Zon, *Children's Hospital Boston*
Maria Zuber, *MIT*

BOOK REVIEW BOARD
David Bloom, *Harvard U.,* **Samuel Bowring,** *MIT,* **Angela Creager,** *Princeton U.,* **Richard Shweder,** *U. of Chicago,* **Ed Wasserman,** *DuPont*

Published by AAAS

EDITORIAL

Warming U.S.-Russia relations

The ups and downs in the political relationship between the United States and Russia are clearly deteriorating scientific cooperation between the two nations. However, it is scientists who can and should lead a reversal in this situation.

Last month saw another setback. In response to U.S. economic sanctions over Russia's annexation of Crimea, the Russian government announced that it will stop cooperating with the United States on the International Space Station by 2020. Russia is also threatening to shut down 11 Global Positioning System stations that scientists use for geophysical research. Furthermore, the U.S. Department of Energy is imposing a ban on Russian scientists working in its laboratories, raising concerns about collaborative work by U.S. and Russian scientists on Earth's climate.

These events are reminiscent of the early 1980s, when science and technology engagement with the USSR was stopped in the wake of the Soviet invasion of Afghanistan and concern about Soviet treatment of Nobel laureate Andrei Sakharov. Cooperation in science did not actively resume until later that decade, formalized by the 1989 signing of the U.S.-USSR agreement in basic sciences and, 4 years later, the U.S.-Russia Science and Technology Agreement. The latter (which I helped negotiate in 1993) is up for renewal in 2015. It should be allowed to lapse. Such agreements are useful when initiating cooperation between countries but are less valuable when there is a robust level of scientific cooperation driven by mutual interest and capabilities. The latter principles, and not political factors, should dictate U.S.-Russia science collaboration.

Scientists are most effective when they can work directly with their counterparts rather than through cooperation that is driven by high-level government initiatives such as the U.S.-Russia Science and Technology Agreement, the U.S.-Russia Bilateral Presidential Commission, and the Gore-Chernomyrdin Commission. Indeed, during the Cold War period, U.S. and Soviet scientists maintained contact despite deep political differences. This early example of science diplomacy established lasting connections that helped avert nuclear war and laid a foundation for collaboration in the post-Soviet years.

Today, two conditions are necessary for a bottom-up investigator-initiated approach to collaboration across all categories of research. After decades of cooperation, U.S. and Russian scientists understand that there must be opportunities to work together. Russian scientists could do more, for example, to cultivate interaction with industries that would benefit from advancements arising from U.S.-Russian science cooperation. And because Russia is doing well economically, its scientists should support efforts for Russia to cover its own costs and provide financial support for U.S. partners, given the past decades of U.S. funding for Russian science. This could open the doors for collaborative projects. Another condition is that the quality of science in both nations must remain high. The United States is a leader in world science, but there is perennial concern about this status as other countries strengthen, and the U.S. fails to maintain, robust investments in basic and applied research. The situation in Russia is more problematic, with limited resources, a decline in the number of scientists, and low publication and citation rates as compared with its European counterparts. Scientists in both nations must exercise thought leadership in finding ways to incentivize the funding of high-quality research that produces mutually beneficial innovation and inspires the next generation of creative scientists.

"...mutual interest and capabilities...and not political factors, should dictate U.S.-Russia science cooperation."

Let us not forget Ukraine. U.S. and European cooperation with Ukraine must increase to help scientists there and address the country's challenges, support reforms in its higher education system, and build sustainable science institutions that function on the basis of openness, competition, and transparency.

At this critical juncture, the power of science is greater than ever. As both the United States and Russia face challenges to their overall standing in the global science community, each is poised to gain from continued cooperation. This potential will only fully be realized, however, if we allow scientists to take the lead.

– Cathleen A. Campbell

Cathleen A. Campbell is president and chief executive officer of CRDF Global, Washington, DC. E-mail: ccampbell@crdfglobal.org

Downloaded from www.sciencemag.org on June 28, 2014

PHOTOS: (RIGHT) CRDF GLOBAL; (INSET) TOMOH/ISTOCKPHOTO.COM

10.1126/science.1257373

Published by AAAS

NEWS

> "When President Kennedy set us on a course for the moon, ... nobody ignored the science. ... I don't remember anybody saying that the moon wasn't there or that it was made of cheese."
>
> **President Barack Obama**, in a commencement speech on 14 June at the University of California, Irvine, disparaging climate change deniers.

IN BRIEF

Big boost for Pacific reserves

Kiribati pledged to ban all fishing in the Phoenix Islands Protected Area.

Two nations moved this week to strengthen massive marine reserves in the Pacific. The United States on 17 June announced plans to expand and strengthen wildlife protections within the Pacific Remote Islands Marine National Monument in the south-central Pacific. The protected area now covers 212,000 square kilometers, but could expand to some 2 million under the initiative. The island nation of Kiribati, meanwhile, announced on 16 June that it will end commercial fishing in the Phoenix Islands Protected Area (PIPA), a biologically-rich, California-sized swath of the Central Pacific, by the end of the year. Kiribati created PIPA in 2008 but banned fishing in only 3% of the 408,250-square-kilometer reserve. Its waters are heavily fished by tuna fleets, and the closure will give notable refuge to bigeye tuna, a species prized for sushi that has been heavily overfished. Both announcements came during the Our Ocean conference, organized by U.S. Secretary of State John Kerry in Washington, D.C. http://scim.ag/_PIPA

AROUND THE WORLD

Europe relents on data sharing

LONDON | Academics breathed a cautious sigh of relief when the European Medicines Agency announced on 12 June that it would expand controversial draft rules to open clinical trial data to scrutiny. The agency's previous draft policy for data sharing would have allowed researchers only to view data on their computer screens, which researchers and the European ombudsman slammed as too restrictive and impractical (*Science*, 23 May, p. 784). The agency now says it will let researchers "download, save and print the trial data for academic and non-commercial research purposes." The final text should be adopted in mid-July, before the new rules are rolled out in October. http://scim.ag/EMArules

Bringing up baby's DNA

DAVIS, CALIFORNIA | A baby boy born earlier this month in California may mark a first in the world of genetics—the first healthy child whose genome was sequenced while still in utero. The baby's father, a biology graduate student at the University of California, Davis, and genetics blogger named Razib Khan, told *MIT Technology Review* that his son's DNA is "mostly pretty boring. So that is good." Khan reportedly obtained his baby's DNA from placental cells, which share a fetus's DNA, garnered during chorionic villus sampling, a relatively common prenatal test typically used to help diagnose significant chromosomal problems. He believes he's not the only parent to parse his child's DNA before birth—just the only one to have gone public. "Hopefully this story will prompt these individuals to come out of the shadows," he writes on his blog, www.razib.com. "There's nothing to hide."

PHOTOS: (TOP TO BOTTOM) KEITH ELLENBOGEN/NEW ENGLAND AQUARIUM; GETTY IMAGES/ISTOCKPHOTO

Downloaded from www.sciencemag.org on June 28, 2014

Published by AAAS

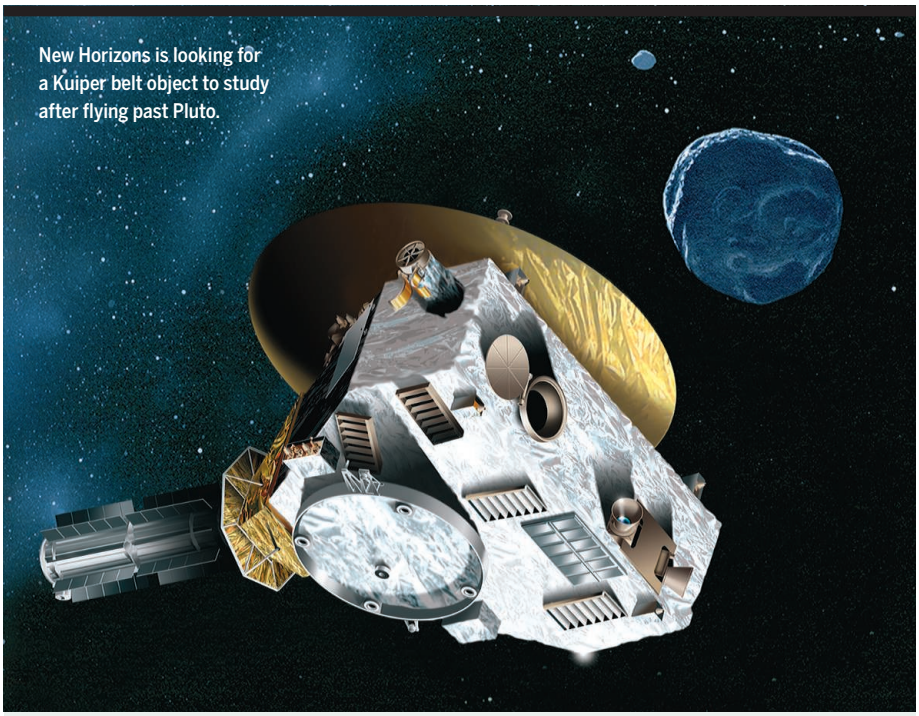

New Horizons is looking for a Kuiper belt object to study after flying past Pluto.

New Horizons borrows Hubble

New Horizons, NASA's mission to the outer solar system, has been given a large chunk of time on the Hubble Space Telescope to assist an increasingly desperate search for an icy object the spacecraft can study after it hurtles past Pluto in July 2015, NASA headquarters announced on 16 June. The mission team has been unable to find a suitable Kuiper belt object for follow-up study, despite dozens of nights of time on some of Earth's largest ground-based telescopes. It needs to identify one as soon as possible to plan orbital adjustments with the spacecraft's limited supply of fuel. The team hopes that Hubble's sharper vision—and the darker background sky, as seen from space—will improve their chances. Beginning this week, the mission team will get 40 orbits, or about 40 hours, of Hubble time from the discretionary budget of the director of the Space Telescope Science Institute in Baltimore, Maryland, which operates the telescope. **http://scim.ag/HorizonsHubble**

STAP scandal threatens center

TOKYO | Shutting down the research center at the heart of an unfolding scientific scandal may be necessary to prevent further research misconduct, found a report released at a press conference on 13 June. In April, an investigative committee found that two papers in *Nature* by scientists at the RIKEN Center for Developmental Biology (CDB) in Kobe, Japan, were riddled with image and data manipulation and plagiarism. The papers outlined a surprisingly simple way of reprogramming mature cells into stem cells—called stimulus-triggered acquisition of pluripotency, or STAP. Last week, another committee surmised that a drive at CDB to produce groundbreaking results led to publishing results prematurely. The committee blamed lead author Haruko Obokata of CDB and her senior co-authors for a lack of proper oversight—and even CDB, which it recommends undergo a complete overhaul. **http://scim.ag/RIKENSTAP**

Europe still snubs GM crops

LUXEMBOURG | Angering both sides of a fractious debate, the European Union's member states agreed last week on a plan allowing individual countries to refuse to plant E.U.-sanctioned genetically modified (GM) crops. In 2010, the European Commission proposed letting individual member states ban a given crop, while the commission would still grant pan-European marketing approvals based on the European Food Safety Authority's scientific opinion. On 12 June, 26 of 28 member states agreed to this "cultivation proposal" as a compromise. Under the proposal, member states can opt out before or after cultivation approval is granted; after approval, they can ban a GM crop for national planning or socioeconomic reasons, for example. Europe's Council of Ministers must next agree on a joint version of the plan with the European Parliament before adopting the final text, possibly next year. **http://scim.ag/EUcultprop**

The E.U. Environment Council met on 12 June.

BY THE NUMBERS

14

Percent of sites that had levels of organic chemicals high enough to kill laboratory test organisms, in the first large-scale risk assessment of European rivers and lakes, published online on 16 June in the *Proceedings of the National Academy of Sciences*.

$25 million

Funding, derived from the 2014 Farm Bill, offered by the U.S. Department of Agriculture for research to combat huanglongbing, also known as citrus greening disease.

$150 million

Cost for a trip to the moon with Space Adventures, a space tourism company offering rides aboard a Russian spacecraft to within 100 kilometers of the lunar surface.

PHOTOS: (TOP TO BOTTOM) JOHNS HOPKINS UNIVERSITY APPLIED PHYSICS LABORATORY/SOUTHWEST RESEARCH INSTITUTE (JHUAPL/SWRI); NICOLAS BOUVY/EPA/CORBIS

Published by AAAS

White sharks in the North Atlantic Ocean are making a comeback.

Jaws returns

Atlantic white sharks may be at the top of the food chain, but trophy fishing and by-catch decimated their numbers in the western North Atlantic Ocean by as much as 73% in the 1970s and 1980s. That led to major international protections, restricting, in some waters, finning or commercial harvesting—and a new database on shark sightings in the western North Atlantic Ocean suggests the measures are working. The study, which included 649 confirmed records of shark captures or sightings between 1800 and 2010, combined new records gathered by the National Oceanic and Atmospheric Administration with previously published data. Since 1990, scientists found, the sharks' abundance is now "comparable to what it was in the 1930s and 1940s," wrote authors in *PLOS ONE* last week, noting that this is "a more optimistic outlook for the recovery of this iconic predator." While rebounds are also apparent in the southern Atlantic and Pacific oceans, preventing by-catch worldwide can help protect "the long-term sustainability of their populations," the authors add. Some celebratory chum for shark fans: The biggest animal documented in the study was more than 5 meters long.

NEWSMAKERS

Three Q's

Earlier this month, scientists reported finding "plastiglomerates," rocks made of plastic, on a Hawaiian beach. Some researchers speculate that humanmade objects could become part of the fossil record, defining a human-dominated period of Earth's history called the Anthropocene. *Science* chatted with paleontologist **Jan Zalasiewicz** of the University of Leicester in the United Kingdom about what humans are leaving behind. http://scim.ag/techfossil

Q: What is a "technofossil"?
A: Technofossils are basically all the things we manufacture. They can survive for thousands, millions, perhaps billions of years in rock strata.

Q: What kinds of things could we expect to survive?
A: Looking around, I'm struggling to see anything that is not fossilizable. Let's take my desk—it's been seasoned, dried out, and varnished. [My] computer, I see plastic, titanium, bits of rubber—if buried in the stratum—it will at least leave a nice oblong detail and impression.

Q: What could future beings infer about us from these fossils?
A: One thing will strike them: [All of these artifacts] will be crammed into a very small physical space. The stratum itself may not be much more than a few meters thick. It will probably appear instantaneous, and it will be very hard work to figure out … this hyperevolution of the technofossils within the human stratum.

PHOTOS: (TOP TO BOTTOM) ALEXIUS SUTANDIO/SHUTTERSTOCK; UNIVERSITY OF LEICESTER

Published by AAAS

IN DEPTH

A plan to track the health of 100,000 U.S. babies is in jeopardy.

PUBLIC HEALTH

NIH puts massive U.S. children's study on hold

National Academies report calls for overhaul

By **Jocelyn Kaiser**

After more than a decade of costly delays, a controversial plan to study the health of 100,000 U.S. babies to age 21 is in limbo again, in the wake of a critical outside review released on 16 June. At best, researchers will need to rethink their plans yet again. At worst, the National Institutes of Health (NIH) may cancel the study.

The National Children's Study (NCS) "offers enormous potential, but it also presents a large number of … challenges," says the critique from a National Academies panel. To overcome them, the academies recommend that the study's leader, the National Institute of Child Health and Human Development (NICHD), refine the study's guiding hypotheses, bolster scientific input and oversight, and modify how it recruits children.

"It's not like [NICHD needs] to start at square zero again," because much of the groundwork for NCS has already been laid, says the panel's chair, Greg Duncan, an economist at the University of California, Irvine. But the needed changes would likely delay initial recruitment, now planned for 2015. And the price tag that the National Academies puts on the revamped study—upward of $1.5 billion—could erode support for the ambitious effort. In a statement, NIH Director Francis Collins said that in response to the "significant concerns" raised by the report, he is putting NCS on hold.

NCS grew out of a request from Congress, made 14 years ago, that NIH follow a large group of children from birth to adulthood in a bid to understand how environmental factors, including social settings and chemical pollutants, influence health. Planners decided to recruit 100,000 women and their unborn babies by knocking on household doors in a random sample of about 100 U.S. counties. But this approach proved too expensive, so NICHD turned to other designs. Members of Congress expressed concern in 2012, after NICHD, having spent $1 billion, decided to pull the plug on 40 NCS sites run by academic investigators and turn over to large contractors the job of tracking the 4000 families it had already enrolled in a pilot study (*Science*, 11 January 2013, p. 133). In March 2013, Congress called for the National Academies' National Research Council and Institute of Medicine to review the study and suggest improvements.

In general, the panel endorses the NCS concept. Similar studies are under way in Europe and Japan, it notes, but the U.S. version would be more comprehensive, in part because researchers would collect extensive data on environmental exposures. The panel also agreed with NICHD's decision to design the study as a "data collection platform" guided by just a few hypotheses—such as that exposure to kitchen dust exacerbates respiratory problems—and add more later. But these "exemplar hypotheses" need to be more scientifically robust, the National Academies found.

The panel also found fault with how NCS planned to recruit subjects: by enrolling 45,000 babies during the mother's pregnancy and the same number at birth. Because this would miss prenatal exposures during pregnancy, the panel urged NCS to enroll 95,000 pregnant women—which it could do for the same cost if it dropped plans for separate studies of 10,000 women. Those smaller studies were to focus on questions such as preconception exposures and the effects of natural disasters. Enrolling siblings, as is planned, could provide similar data on preconception exposures, the panel noted.

Such changes would enable NICHD to enroll participants for about $1.5 billion over 7 years, the panel estimates, with annual costs peaking at just over $300 million. (NIH is now allocating $165 million per year for the study.) Earlier NIH estimates predicted the study could cost $3 billion. But the National Academies estimate does not include costs such as archiving data and storing biological samples, the report notes.

Scientific leadership of NCS is a major deficiency, the report finds. Although the study has various advisory committees, "the processes by which study decisions are made and vetted are opaque," it says. NCS needs more expertise within its program office, the panel concludes, as well as a new scientific management group that has the authority to approve the study's design.

The report is seen as vindication by some NCS critics, including academic scientists who were pushed out of the study 2 years ago. "Its conclusions are essentially the same as mine. They're just putting it more nicely," says epidemiologist Nigel Paneth of Michigan State University in East Lansing, who led a former NCS site in Detroit and has been a vocal critic of study leadership.

Now that the National Academies has had its say, the question is whether NIH will embrace its recommendations—and whether Congress will keep funding the study. Collins said he will assemble a team of experts to advise him in the coming weeks on whether the study is "actually feasible" given current budget constraints and to help him decide "the right thing to do with the study." ■

PHOTO: ERPRODUCTIONS LTD./GETTY IMAGES

Downloaded from www.sciencemag.org on June 28, 2014

Published by AAAS

FUNDING

Just one proposal per year, please, NSF tells astronomers

As success rates drop, agency seeks to limit applications

By **Jeffrey Mervis**

Gary Ferland, a theoretical astrophysicist at the University of Kentucky in Lexington, is old enough to remember when he and his colleagues had a 50-50 chance of winning a research grant from the astronomy division of the National Science Foundation (NSF). Now, success rates are at 15% (see graph), creating a situation he compares to playing the lottery.

"If you're trying to support your family on lottery winnings," says the 63-year-old Ferland, "you need to buy a lot of tickets." For many astronomers, that means submitting multiple proposals to NSF every year. The strategy has paid off for Ferland: In 2011, he submitted three proposals and snared two awards; this year, he won another grant by submitting the same proposal to two different NSF programs (with the agency's permission).

Now, Ferland will need to come up with a new approach: Later this summer, NSF's astronomy division intends to announce a new policy that will "strongly encourage" scientists to submit just a single proposal for each annual funding cycle. The voluntary cap is designed to boost success rates, which would please applicants. It's also meant to ease the workload and frustration levels of peer reviewers poring over proposals that they know have little chance of getting funded.

"It's a first step," says James Ulvestad, director of NSF's astronomy division. If it doesn't achieve the desired effect, he adds, "we may have to make it mandatory in 2016 for the sake of reviewers' sanity."

Biomedical researchers and the National Institutes of Health have long wrestled with similar problems. But a plummeting success rate is a relatively new phenomenon for U.S. astronomers, a much smaller group. "For the astronomy community to be at 15% or below is just now becoming a big deal," notes Joel Parriott, director of public policy at the American Astronomical Society in Washington, D.C.

The numbers behind the crisis are stark. Applications for NSF's bread-and-butter grants to investigators and small teams have doubled in the past decade, to more than 700; in contrast, the agency's astronomy budget has grown by just 40% over the same period. In addition, the average size of an NSF astronomy grant, roughly $325,000 a year over 3 years, is almost 30% larger than it was a decade ago.

Last fall, in a report to the community, Ulvestad noted that there were just two ways to boost success rates: limit submissions or reduce grant size. But few scientists want awards to shrink, so that leaves finding ways to reduce the applicant pool.

Ulvestad discussed the voluntary cap strategy last week at a meeting of the federal Astronomy and Astrophysics Advisory Committee (AAAC), which reports to the fields' main funders: NSF, NASA, and the Department of Energy. Starting with the 2015 funding cycle, he said, NSF will ask scientists to list themselves as either the principal investigator (PI) or co–principal investigator (co-PI) on just a single application.

A strict limit could be "a disaster," worries Jason Wright, an assistant professor of astronomy and astrophysics at Pennsylvania State University, University Park, who studies stars and exoplanets. Having only one shot a year as a PI or co-PI will make scientists more reluctant to collaborate, he says, and "having a ton of co-PIs with different skills is what makes an application so strong." Wright, who submitted two proposals to NSF in 2011 and was "stunned" when both were funded, says a ceiling would also change his approach to grant writing: "If you only get one shot, I'd put in more sprawling proposals, and ask for more money."

AAAC members believe federal officials need better data on the nature of the problem before they announce any additional steps. To that end, AAAC agreed last week to carry out a survey of how scientists view the current grantsmaking process. "The solutions ought to be data-driven, but they can't be until we have more data," says Priscilla Cushman, incoming chair of AAAC and a physics professor at the University of Minnesota, Twin Cities.

NSF's data on multiple submissions, for example, show that almost 100 of the 732 proposals it received this year came from scientists who submitted more than one application; a few sent in five proposals. Are those repeat submitters mostly senior scientists heading large teams, Cushman wonders, or younger scientists desperate to obtain a coveted NSF grant before coming up for tenure? The surge in proposals is another mystery, because the community hasn't grown over the past decade.

Nobody expects the submission cap to solve the entire problem. And it does not touch the underlying mismatch between astronomers' ambitions and the amount of funding available. "It's going to be hard to sustain a long-term research program with success rates this low," says Ferland, who began submitting multiple proposals to NSF in 2010 after getting his first rejection in 3 decades. "I'm just glad I'm closer to retirement than to the start of my career." ■

The no's have it

More astronomy proposals contribute to plunging success rates at NSF

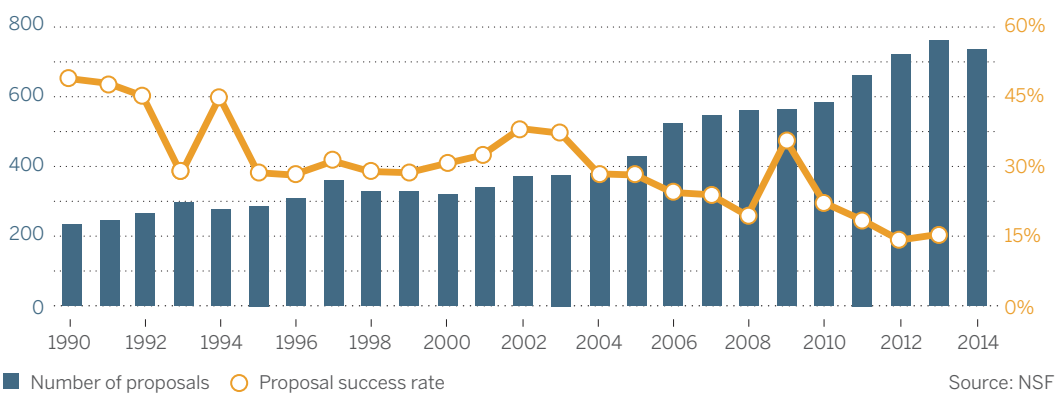

Source: NSF

Downloaded from www.sciencemag.org on June 28, 2014

Published by AAAS

Colorado Governor John Hickenlooper signed the first Right to Try law in May.

PHOTO: ALEX WONG/GETTY IMAGES

PATIENT ADVOCACY

'Right to Try' laws bypass FDA for last-ditch treatments

But companies may be reluctant to supply unapproved drugs

By **Kelly Servick**

Several state legislatures, prodded by desperately ill patients and a libertarian think tank, are defying federal regulators to make experimental drugs available outside of clinical trials. The new laws, called Right to Try, allow terminally ill patients to request unapproved drugs after early-stage testing. Last month, Right to Try went on the books in Colorado and Louisiana; a similar law awaits the governor's signature in Missouri, and Arizona will put the issue to a vote in November.

The movement taps into long-standing frustration over what some view as the sluggish pace of clinical trials. Although the laws are framed as a boon for dying patients, critics raise a long list of caveats. Companies, they say, will often be reluctant to offer a drug outside of its clinical trials—and the untested therapies will rarely work. Only about one in 10 drugs in phase I clinical trials ever demonstrate efficacy to win Food and Drug Administration (FDA) approval. "It sounds like, 'We're throwing you a life preserver, and you'll have your shot at being cured,' " says Arthur Caplan, a medical ethicist at New York University's Langone Medical Center in New York City. "I can't tell you how rare that scenario is."

Rare it may be, supporters say, but not impossible. "Any patients alive today with ALS will most likely be dead by the time we're finished with our trials," says I. Richard Garr, president of Neuralstem Inc. in Germantown, Maryland, whose stem cell treatment for the fatal neurodegenerative disease is in phase II clinical trials. His company plans to take advantage of Colorado's Right to Try law to make its unapproved treatment available to ALS patients, well ahead of any FDA decision.

Right to Try laws are being spearheaded by the Goldwater Institute, a libertarian group based in Phoenix. The laws require that patients be terminally ill, have considered other available treatment options, and be unable to participate in a clinical trial. The institute describes the laws as a "complement" to an existing expanded access program at FDA, which allows patients with serious or life-threatening diseases to try experimental drugs if they've exhausted their other options. But with expanded access, an institutional review board must also approve each request, and the patient's doctor must report follow-up data to FDA.

According to FDA's submission receipts report for fiscal year 2013, the agency granted all but three of nearly 1000 expanded access requests it received. When patients can't access experimental treatments, the holdup is often the drug developer, not FDA, Caplan says. Companies cannot be forced to supply an experimental treatment outside a clinical trial, and often they don't wish to do so. Manufacturing more of a drug can strain a company's resources, says Emil Kakkis, CEO of the biotech company Ultragenyx Pharmaceutical Inc. in Novato, California, and president of the EveryLife Foundation for Rare Diseases, which promotes innovation for rare disease treatments.

Companies also worry that a bad outcome from FDA's expanded access will torpedo a therapy, even though the agency maintains that this has never happened.

The fervor over Right to Try has some patient advocates worried that existing options for dying patients will be overlooked. A one-person expanded access request through FDA is an uphill battle, but the system can accommodate larger groups, says Jess Rabourn, director of the ALS Emergency Treatment Fund in San Jose, California, which helps biotech companies apply for and fund expanded access programs.

Legally, Right to Try raises major questions. Federal law limits moving drugs or their components across state lines without first applying to FDA, notes Meredith Manning, a lawyer specializing in the FDA approval process at Hogan Lovells in Washington, D.C. "If FDA were to assert" that the federal law takes precedence, "it would have a good argument," she believes. So far, FDA has not taken a public position on Right to Try, and agency officials declined to comment on the laws for this story.

"I don't think that patient populations and foundations and advocates should be duped into thinking that this is something that it's not," Rabourn says. "It's not something that changes the federal law, and that's the law of the land that governs drug development. It's what any shareholder-owned drug company has to abide by."

Garr says that if FDA forbids the company from offering its unapproved treatment, an injection of neural stem cells into a patient's spinal cord, he'll follow the rules. Still, Garr, who accepted an invitation to join the Goldwater Institute's Right to Try National Advisory Council, says he believes in offering the treatment to patients who want it. The inclusion criteria will be almost identical to those of the ongoing trial: Patients must be in the early stages of ALS. So far, no other company has said it will follow Neuralstem's lead.

Meanwhile, Garr says, "we're already getting tremendous numbers of people writing, saying they're ready to move to Colorado tomorrow." ■

Downloaded from www.sciencemag.org on June 28, 2014

Published by AAAS

COMPUTER SCIENCE

Quantum or not, controversial computer yields no speedup

Conventional computer ties D-Wave machine

By **Adrian Cho**

The D-Wave computer, marketed as a groundbreaking quantum machine that runs circles around conventional computers, solves problems no faster than an ordinary rival, a new test shows. Some researchers call the test of the controversial device, described online this week in *Science* (http://scim.ag/quantspeedup), the fairest comparison yet. But D-Wave argues that the computations used in the study were too easy to show what its novel chips can do.

"This is likely the most thorough and precise study that has been done on the performance of the D-Wave machine," says Helmut Katzgraber, a computational physicist at Texas A&M University, College Station, who was not involved in the work. However, Colin Williams, a quantum-computer scientist and D-Wave's director of business development, says the problems used as benchmarks were "not at all the right choice for probing a quantum speedup."

> ***"We don't see quantum speedup, but that doesn't mean you won't see one eventually."***
>
> **Matthias Troyer**, Swiss Federal Institute of Technology in Zurich

D-Wave Systems, a startup in Burnaby, Canada, started selling the supposed quantum computer in 2011. Although skeptics have questioned the company's claims, D-Wave has sold machines to Lockheed Martin Corp. and Google and has been written up in myriad news reports. The company claimed an earlier version of its $10 million machine was 35,500 times faster than an ordinary computer—in a test at which skeptics scoff.

To test D-Wave's machine, Matthias Troyer, a physicist at the Swiss Federal Institute of Technology in Zurich, and colleagues didn't just race it against an ordinary computer. Instead, they measured how the time needed to solve a problem increases with the problem's size. That's key because the whole idea behind quantum computing is that the time will grow much more slowly for a quantum computer than for an ordinary one.

For example, for a conventional computer running today's best algorithm, the time needed to factor a number explodes almost exponentially: according to an exponent that increases with the number of digits. For a full-fledged quantum computer, that time should grow at a far milder rate, as the number of digits cubed (see figure, top right). Thanks to that "quantum speedup," problems that would overwhelm a classical computer would merely slow a quantum one.

Factoring numbers, however, requires a "universal" quantum computer. The D-Wave machine is a more limited device called a quantum annealer. Its processor consists of a 2D array of quantum bits, or qubits, made of superconducting loops that carry electric currents. The qubits act like tiny magnets that can point up, down, or—thanks to quantum weirdness—both up and down at the same time. Each qubit can interact with certain others through linkers that can be programmed so that the qubits can lower their energy by pointing either in the same direction or in opposite directions (see figure, bottom right). The idea is to encode a problem by specifying the hundreds of interactions within the chip and solve it by finding the qubits' lowest energy "ground state."

To find the ground state, the machine starts with each qubit in an up-and-down state and slowly turns on the interactions. The system then seeks the lowest energy state, like a marble rolling across an evolving energy landscape to find the deepest valley. In a nonquantum device, the jiggling of thermal energy would drive the marble over the terrain to the low spot through a process called thermal annealing. In the D-Wave machine, however, the marble supposedly also "tunnels" quantum mechanically between the low spots to find the lowest one faster. For problems such as pattern recognition or machine learning, that might give the quantum machine an edge.

But is the D-Wave chip really quicker than a conventional computer? To find out, Troyer and Daniel Lidar, a physicist at the University of Southern California in Los Angeles, tested the Lockheed Martin machine against a conventional computer programmed to simulate thermal annealing. To keep things simple for the D-Wave chip, they didn't ask it to do practical calculations. Instead, they merely set the interactions between qubits randomly and timed how long it took the machine to find its ground state.

In spite of that home-field advantage,

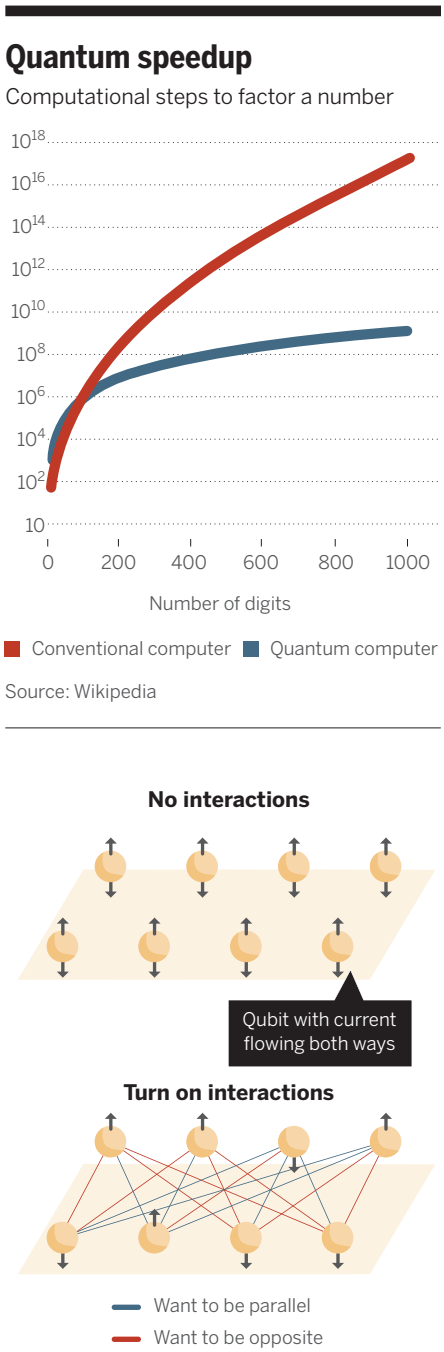

A universal quantum computer would factor numbers far faster than an ordinary computer (*top*). Nobody knows whether D-Wave's quantum annealing technique (*bottom*) provides a similar speedup.

DIAGRAM: G. GRULLÓN/*SCIENCE*

Downloaded from www.sciencemag.org on June 28, 2014

Published by AAAS

the D-Wave chip produced no quantum speedup. The researchers ran problems for different-sized groups of qubits, ranging from the chip's basic unit of eight to its total of 512. The computing time for the conventional computer increased exponentially with the number of qubits. But so did the time for the D-Wave machine. Troyer takes care not to overstate the finding: "We don't see quantum speedup, but that doesn't mean you won't see one eventually" for some other problem.

Indeed, the test problems may have been easy for the ordinary computer, too, says Texas A&M's Katzgraber. Choosing interactions at random, he explains, typically creates test problems in which qubits lock into a low-energy configuration only exactly at zero temperature. So at any higher temperature, thermal annealing can readily coax the system to the solution. Given the easiness of the problems for both machines, Katzgraber says, the study is like "two world-class skiers racing on the bunny slope." Hartmut Neven, director of engineering at Google, says his team has already found patterns of interactions for which the D-Wave machine beats simulated annealing.

However, some researchers doubt that a quantum annealer will ever produce a useful quantum speedup. Although computer scientists have proved that a dreamed-of universal quantum computer should excel at factoring, theory strongly suggests that in actuality a quantum annealer will produce no similar speedup for any problem, says Umesh Vazirani, a computer scientist at the University of California, Berkeley. "I would bet that there's not a speedup," he says. Neven counters that he is "convinced that we will be able to find problem classes for which a next-generation quantum annealer will outperform any classical algorithm."

Meanwhile, the sniping between D-Wave and its critics continues. D-Wave co-founder Geordie Rose recently told *Wired* magazine that Troyer's work was "total bullshit."

Such rhetoric rankles some researchers. By making claims that may not pan out, D-Wave could jeopardize the whole field of quantum computing, says Scott Aaronson, a computer scientist at the Massachusetts Institute of Technology in Cambridge. "If it becomes common knowledge that they're not seeing a speedup, then the same people who are backing them may turn and say, 'Well, I guess quantum computing is a failed idea,' " he says. In response to accusations of hype, D-Wave's Williams says, "We're a commercial company, and all commercial companies have to market their products and services." ■

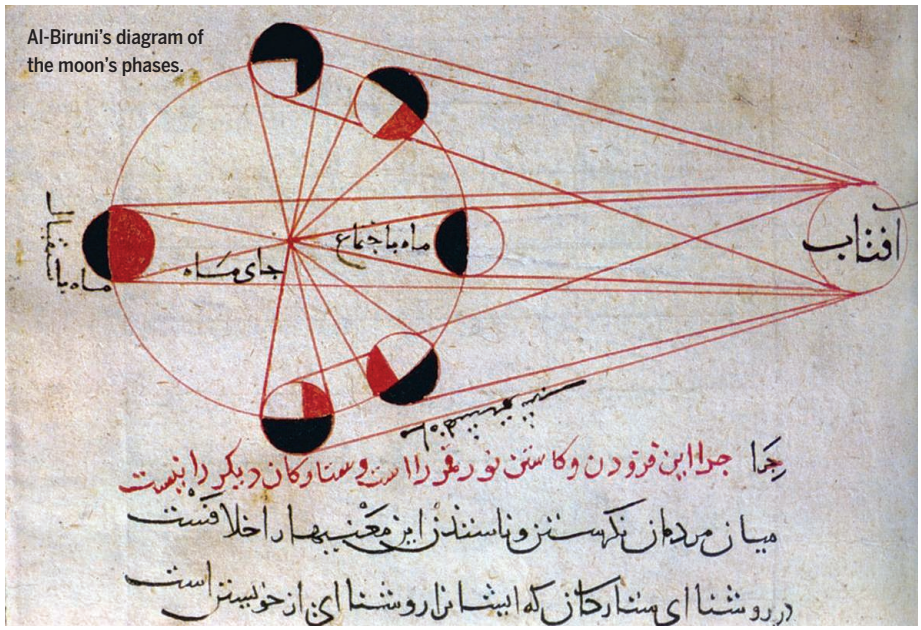

Al-Biruni's diagram of the moon's phases.

PHOTO: REPRODUCTION FROM SEYYED HOSSEIN NASR, *ISLAMIC SOCIAL SCIENCE: AN ILLUSTRATED STUDY* (WORLD OF ISLAM FESTIVAL PUBL. CO., 1976)

HISTORY OF SCIENCE

Was America 'discovered' in medieval Central Asia?

Ancient texts suggest Silk Road polymath inferred the existence of unknown continents

By **Richard Stone**
in Samarkand, Uzbekistan

He was a Renaissance man long before the Renaissance. Abu Rayhan al-Biruni, born a thousand years ago in this region of Central Asia, calculated Earth's circumference with astounding accuracy and invented specific gravity, the measure of a substance's density compared to that of water. He rejected creationism, accepted that time has neither a beginning nor an end, and—5 centuries before Copernicus—argued that the sun might be the center of the solar system. Now, an influential scholar has proposed adding another laurel to that list: inferring the existence of America.

The discovery of America is bitterly contested, with vying claims on behalf of prehistoric peoples who crossed over Beringia or the Pacific Ocean, Norse seafarers who landed in Newfoundland around 1000 C.E., and the 15th century explorers Christopher Columbus and John Cabot. Biruni, who never laid eyes on any ocean, also deserves "to wear the crown of discovery," averred S. Frederick Starr, chair of the Central Asia-Caucasus Institute of the Johns Hopkins School of Advanced International Studies in Washington, D.C., at a conference on medieval Central Asia held here last month. "His tools were not wooden boats powered by sail and muscular oarsmen but an adroit combination of carefully controlled observation, meticulously assembled quantitative data, and rigorous logic."

Some experts are not persuaded. "There is a tendency these days to read too many modern discoveries into the works of the medieval scientists," says Jan Hogendijk, an authority on Biruni at Utrecht University in the Netherlands. "We don't say that Copernicus 'discovered' that the Earth moves around the sun simply based on the fact that he hypothesized that it does," adds Nathan Sidoli, a science historian at Waseda University in Tokyo, "so I don't see why we should say that al-Biruni 'discovered' the American continent."

But others think Biruni deserves credit for his prediction. "Assuming that the key passages in Biruni's texts have been correctly read, I see no reason to exclude al-Biruni from the list of early 'discoverers' of America," says Robert van Gent, a specialist on the history of astronomy at Utrecht University who attended Starr's talk here.

Biruni was one of a constellation of Cen-

Published by AAAS

Corrected 26 June 2014; see full text.

tral Asian scholars who led an "Eastern Renaissance" spanning 7 centuries, from about 800 to 1500 C.E. These scholars include some of the greatest minds you've never heard of, and their achievements include the principles of algebra and trigonometry, the invention of the algorithm and the astrolabe, and the foundations of modern medicine. "These were tremendous figures," Starr says. Yet, he says, "This incredible effervescence in science has largely escaped our attention in the West."

Starr, an archaeologist by training who has made dozens of trips to Central Asia, is at the vanguard of a scholarly movement to document the Eastern Renaissance and the factors that nurtured it. At the crossroads of the vibrant cultures of China, India, the Middle East, and Europe, Central Asians became traders nonpareil, and for that they had to know how to calculate. "The Chinese were amazed that young boys in Samarkand were learning mathematics when they were 8 years old," Starr says.

Biruni boldly sorted scientific fact from fantasy.

The brightest star in the Central Asian firmament may have been Biruni. "He was really a universal genius," versed not only in the hard sciences and anthropology, but in pharmacology and philosophy as well, says Jules Janssens, a specialist on medieval Central Asia at the Catholic University of Leuven in Belgium. Biruni authored at least 150 texts, although only 31 have survived—and these are virtually unknown outside a small circle of scholars.

Born in 973 C.E. near the Aral Sea in present-day Khiva, Uzbekistan, Biruni used the height of the midday sun to calculate the latitude of his hometown when he was just 16. He traveled widely as an adult, and at a hilltop fortress near present-day Islamabad he devised a technique for measuring Earth's circumference using an astrolabe, spherical trigonometry, and the law of sines. (Like the ancient Greeks, Biruni was aware that Earth is round.) His calculation was a mere 16.8 kilometers off the modern value, Starr says. "I don't know where he became a data freak, but he's the real thing. His was an original kind of mind."

In a massive tome called the *Masudic Canon* completed in 1037 C.E., Biruni analyzed classical Greek, Indian, and Islamic astronomy and used "bold hypothesizing" to sort out credible claims from fantasy, Starr says. In another treatise, Biruni introduced the concept of specific gravity and applied it to scores of minerals and metals, making measurements accurate to three decimal points that Starr says Europeans could not match until the 18th century.

Most sensational of all may be Biruni's "discovery" of America. For the purpose of precisely determining the qiblah—the direction of Mecca during Islamic prayers—Biruni meticulously recorded coordinates of the places he visited, and compiled data on thousands of other Eurasian settlements from other sources. After plotting out the known world—possibly on a 5-meter-tall globe he is said to have constructed—he found that three-fifths of Earth's surface was unaccounted for.

"The most obvious way to account for this enormous gap was to invoke the explanation that all geographers from antiquity down to Biruni's day had accepted, namely, that the Eurasian land mass was surrounded by a 'world ocean,' " Starr relates in *Lost Enlightenment: Central Asia's Golden Age from the Arab Conquest to Tamerlane,* a book published last October. Biruni rejected that notion in a passage flagged by the Indian scholar Sayyid Hasan Barani in the mid-1950s but overlooked in the decades since, Starr says. Biruni argued that the same forces that gave rise to land on two-fifths of our planet must have been at work in the other three-fifths. He concluded that one or more landmasses must lie between Europe and Asia, writing, "There is nothing to prohibit the existence of inhabited lands."

In the December 2013 issue of *History Today,* Starr wrote that Biruni's "*modus operandi* strikes one as astonishingly modern, a voice of calm and dispassionate scientific enquiry sounding forth from the depths of the irrational and superstitious medieval world." The Eastern Renaissance wound down, Starr says, when "a pall of suspicion fell on science" in Central Asia. For centuries, Biruni and other scholars of that era—like America—awaited rediscovery. ■

SCIENTIFIC PUBLISHING

Secret bundles of profit

Study lifts veil on journal price negotiations

By **John Bohannon**

For many purchases, price comparisons are a few mouse clicks away. Not for academic journals. Universities buy access to most of their subscription journals through large bundled packages, much like home cable subscriptions that include hundreds of TV stations. But whereas cable TV providers largely stick to advertised prices, universities negotiate with academic publishing companies behind closed doors, and those deals usually come with agreements that keep the bundled prices secret. After years of digging, and even legal action, a team of economists has pried out some of those numbers.

The results of their investigation, published on 16 June in the *Proceedings of the National Academy of Sciences* (*PNAS*), reveal that some universities are paying nearly twice what universities of seemingly similar size and research output pay for access to the very same journals. For example, the University of Wisconsin, Madison, paid Elsevier $1.22 million in 2009 for a bundle of journals, while the University of Michigan, Ann Arbor—a university with similar enrollment and number of Ph.D. students—paid $2.16 million for the same bundle. At *Science*'s request, the authors even calculated a potential measure of how good or bad a deal U.S. universities are getting, providing a graphic view of the price spread (see p. 1333).

The price of journals has become a source of friction between academics and publishers. Publishers pay nothing for most of the labor that goes into academic articles—the writing and revision by authors, the quality control by volunteer peer reviewers—yet the largest of these companies reap annual profits upward of 35% on billions of dollars of revenue. According to the industry leader, Amsterdam-based Elsevier, the high profits are the result of innovation and efficiency, while the subscription bundling gives universities access to journals "at a substantially discounted rate." But according to Peter Suber, director of the Office for Scholarly Communication at Harvard University, publishing companies "use bundling to protect second-rate or little-used journals from can-

PHOTO: COURTESY OF THE ACADEMY OF SCIENCES OF UZBEKISTAN

Downloaded from www.sciencemag.org on June 28, 2014

Published by AAAS

cellation," and they enforce secrecy "partly to limit the bargaining power of buyers and partly to hide the results of this unequal bargaining power."

The journal pricing investigation began in 2009 when Theodore Bergstrom, an economist at the University of California, Santa Barbara, faced a time crunch. "I decided that I didn't have time to referee all the papers that I was asked to," he says. "On a whim, I decided to give priority to journals with relatively low subscription prices. … I was amazed at what the commercial [publishers] were charging and much annoyed that they thought I should work for them for free." Since then, Bergstrom has become a data activist, contributing to projects that measure cost and value in academic publishing, such as the Eigenfactor project and journalprices.com. He has gotten pushback. "Some librarians defended the commercial publishers by suggesting that the prices we quoted were misleading because they didn't account for bundle discounts," Bergstrom says. "So we set out to find out bundle prices."

That was easier said than done. Bergstrom teamed up with two other economists—Preston McAfee, chief economist at Microsoft in Redmond, Washington, and Paul Courant, at the University of Michigan, Ann Arbor—and reached out directly to librarians at nearly 100 universities and university consortia across the United States. Only half shared the terms of their bundled journal subscriptions. For the rest, the team requested the subscription contracts through the various Freedom of Information Act laws covering each state-funded institution. Some publishers fought back. In 2009, Elsevier even sued one university, Washington State University in Pullman, to set a precedent for blocking the release of bundled subscription terms, claiming that the deals are a trade secret. A state judge ruled against Elsevier.

The team's analysis, which looked at the prices charged by publishers in 2009, indicates that the secret haggling between university librarians and academic publishers produces some startling disparities. The University of Texas, Austin, paid $481,932 for Springer journals, while an institution with far fewer Ph.D.s, the University of Miami in Florida, paid $553,923. For access to Wiley's journals, the University of Missouri, Columbia, paid $233,659, while the smaller University of Oklahoma paid $500,744.

Publishers and some academic librarians caution that the numbers can be misleading. The price that any university pays a publisher "doesn't tell you the whole story," says Doug Way, a librarian at the University of Wisconsin, Madison. A university's prior history with a publisher can play into the negotiation and strongly influence the final price, he says. For example, Way says that his university had been "canceling large numbers of subscriptions for a number of years before it entered into [the bundled] 'Big Deal' " with Elsevier, a history that helped the university negotiate a better rate.

Also missing are data about how many journal articles are actually downloaded over the course of a year. "Our use-analysis of the Springer packages shows we got a good deal," says Elizabeth Fish, a librarian at the University of Miami. "A recent internal study showed our cost for a Springer article download at about $2.00."

In his analysis for *Science*, Bergstrom compared deals at universities by using a statistical model based on the number of full-time students enrolled and the number of Ph.D. degrees granted. (A spreadsheet with that data can be found at http://scim.ag/JournalBundles.) "We realize that a simple linear equation involving enrollment and Ph.D.s does not fully explain the value of journals to universities," he says. "On the other hand, we think that it may be helpful for librarians to compare the price they are paying with prices paid by their peers."

Elsevier declined to comment on the study, and Springer could not be reached. "Wiley offers a range of flexible pricing and licensing options that include the full collection as well as a number of other collection options," the company told *Science* in an e-mail. "We recognize that there is no one size or type of deal that suits all of our customers."

Will the pricing disclosure make a difference? "I think it's possible that publishers could try to level or adjust the pricing to make it seem more fair to subscribing libraries from a comparative standpoint, but the total revenue going to the publishers won't get smaller," predicts Scott Stangroom, who coordinates journal acquisitions for the University of Massachusetts, Amherst.

"We have a collective-action problem," says Tim Gowers, a mathematician at the University of Cambridge in the United Kingdom who launched a petition calling for a boycott of Elsevier. "If all libraries were simultaneously to refuse to sign any more Big Deals and switched instead to paying for journal subscriptions individually, then the market rate for the journals would be at a level where they reflected the actual value of the subscriptions to the universities, which is much lower than the current list prices." ■

Journal prices: good deal or not?

Payment premium (% > 0) or discount, based on expected price from modeling; circle size reflects university's 2009 payment

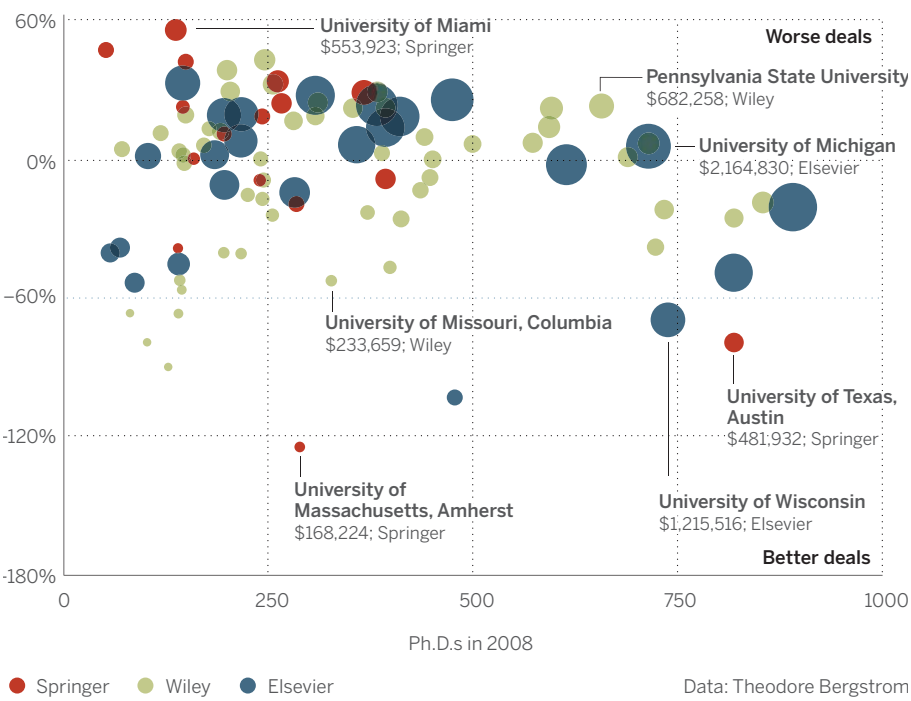

Published by AAAS

Brazilian free-tailed bats, like these in Texas, use song to court mates and defend territory.

Downloaded from www.sciencemag.org on June 28, 2014

When the bat sings

The trills and chirps of bats can be as complex and meaningful as bird song—and may be a closer analog for human speech

By **Virginia Morell**

Archaeologists aren't sure how the Governor's Palace, a cream-and-white limestone structure at Uxmal, Mexico, figured in Maya religious ceremonies. Its walls of carefully chiseled blocks are now crumbling; the chants of priests no longer echo in its halls. Yet if you're quiet and observant, you'll hear the songs of the current residents of the palace: bats.

"Do you hear them?" asks Kirsten Bohn, a behavioral ecologist and bat expert at Florida International University in Miami. "It's like the walls are singing."

It takes a moment to tune my ear to the right pitch, but once I do, I realize the air is filled with the bats' soft, birdlike twitters, chirps, and trills. And this is not during the deep of the night, but in the middle of the day. So if you know where to look, you can see the bats, too.

"Well, hello there, boo-boo," Bohn says, peering into a long, narrow fissure that time and erosion have opened up between the wall's stones. She presses her face close to the crack, squinting to get a better look at the mouse-sized bats sandwiched inside. I do the same, and once my eyes adjust to the dark of the crevice, I'm eye to eye with a brown-eyed *Nyctinomops laticaudatus*, the broad-eared bat. He scuttles back into his rocky lair, but I can still see his chattering jaws: "Zzzzzzzzz."

"That's an aggressive warning call," Bohn explains. "He's telling us to back off. He doesn't want to bother with us; he wants to do what's important—[which is] to sing."

Bohn has traveled to Uxmal to capture the songs of this and dozens of other broad-eared bats scrunched inside the ruin's walls in order to study the evolution and function of bat song. Biologists commonly use the word "song" to describe any acoustic displays by males, including the simple calls of frogs, insects, and many other creatures. Bohn, however, reserves "song" for something as complex as bird song—calls "composed of multiple syllables combined in a specific way, and which have repeatable patterns and rhythm." By this reckoning, many birds, some cetaceans, and humans sing. So, it turns out, do some bats.

That bats emit any kind of song comes as a surprise to most people, partly because we tend to think chiefly of their echolocation calls, ultrasonic sounds beyond

PHOTO: © MERLIN D. TUTTLE, BAT CONSERVATION INTERNATIONAL. WWW.BATCON.ORG

Published by AAAS

our hearing, or their short, sharp social calls. It's also a surprise because it is so rare for a mammal to sing like a songbird. "So why do bats?" Bohn asks. "What are the social and environmental pressures that have led them to evolve this ability, which is so mentally demanding?"

To find out, researchers are seeking out bat troubadours from New Zealand to Africa. Already, studies by Bohn, her collaborator Michael Smotherman, a neurophysiologist at Texas A&M University, College Station, and others have shown that like many songbirds, most bat songsters are male, live in polygynous societies where males mate with more than one female, and tend to sing during the mating season to court females and defend territories. Their complex songs are probably not innate, and so require vocal learning, as bird song and human speech do. At least one species of bat appears to have a specialized neural loop in its forebrain, analogous to the circuit in songbirds that underlies vocal learning. Geneticists have added another parallel: The *FOXP2* gene, which is tied to vocal learning in humans and birds, has also been under intense selection in bats.

"There's much left to discover," says Mirjam Knörnschild, a behavioral ecologist and bat song expert at the University of Ulm in Germany. But already, the bat song enthusiasts are wondering if these winged mammals can help explain the evolution of complex vocal abilities overall—including that of their fellow mammals, human speech.

Three songsters. Top to bottom: The parti-colored bat (*Vespertilio murinus*), the broad-eared bat (*Nyctinomops laticaudatus*), and the heart-nosed bat (*Cardioderma cor*).

SCIENTISTS HAVE KNOWN that bats sing since at least 1974, when Jack Bradbury, a behavioral ecologist and now a professor emeritus at Cornell University, and zoologist Louise Emmons of the Smithsonian Institution reported recordings of greater sac-winged bats, *Saccopteryx bilineata*, from Trinidad. "I used a shotgun mic and reel-to-reel recording gear," Bradbury recalls. "The bats would land on their roosts at dawn and sing like birds, and in a low enough register that I could hear them."

The study of bat song didn't take off until this century, however, when recording equipment became more portable, making it easier to work in the wild. By now, song has been documented in 20 of the 1116 known species of bats, although scientists suspect that many more are talented songsters. Some, such as New Zealand's *Mystacina tuberculata*, hunker down in a cleft of a tree or similar grotto to belt out their tunes. Others, such as the European *Vespertilio murinus*, sing both from roosts and on the wing, erupting into song at the end of autumn when females may be seeking a male to spend the winter with. Male Brazilian (also known as Mexican) free-tailed bats, *Tadarida brasiliensis*, the species that Bohn and Smotherman have studied the most, sing year-round, but especially during mating season.

To study the details of bat song, Smotherman and others have started captive colonies—captive bats won't sing alone, underscoring the social nature of bat song. But researchers also venture to caves, trees, parking garages, and ruins, studying known songster species and searching for new ones. "You have to know which ones sing and which ones don't to fully understand song in bats," Bradbury says.

Answering that question is one reason why Bohn traveled to Uxmal. "Do all the Molossidae species—there are at least 100—and their related genera sing?" she asks. "If they don't, why not? I'm trying to figure out how and why this complex form of communication came about."

In spite of our presence, the broad-eared bats are still twittering to each other. Close to the wall, I catch a whiff of a strong, pungent odor. "They sure smell like males," Bohn says, taking another peek at the bats. "Yuck. It's got to be a bachelors' pad."

In the related Brazilian free-tailed bat that Bohn studies back home in the United States, each male stakes out a territory within the larger mixed roost and sings both to lure females in for mating and to keep other males out. The broad-eared bat may have similar arrangements, but no one knows; Bohn is only now exploring its habits. "They're peeing on everything, marking every bit of their territories," she observes. "And just singing their hearts out."

So far, scientists have found few similarities in the notes or syllables used by the various species of bats, or in the structure of their tunes. But in three major papers, one published just last year in *Animal Behaviour*, Smotherman and Bohn traced striking similarities between the tunes of the Brazilian free-tailed bats and those of songbirds. The bat song is as complex and structured—as "songlike"—as that of songbirds, they reported. Both are hierarchically structured, composed of multiple syllables and phrases; among the bats they include chirps, trills, and buzzes.

Bat song even has syntax, or rules for constructing a tune. For instance, in the songs of the free-tailed bat only chirp syllables can be included in chirp phrases, and buzz syllables belong in buzz phrases. Yet there is also room for flexibility, so that each male's song is unique—rather like a jazz player riffing on a tune. "Their songs aren't just honk-honk-honk or eee-eee-eee," Bohn says. "They're polysyllabic; they

PHOTOS: (TOP TO BOTTOM) JENS RYDELL; KIRSTEN BOHN; GRACE SMARSH/TEXAS A&M UNIVERSITY

Published by AAAS

Scientists collect songs of *Nyctinomops laticaudatus* bats roosting in the walls of a ruin at Uxmal, Mexico.

have sequences, temporal structures, and a timed rhythm."

Perhaps most surprising, Bohn and her colleagues discovered that these bats can also quickly vary the syntax of their songs in response to social circumstances, again as songbirds do. This type of audio-vocal plasticity is rare in mammals, aside from humans. For instance, Brazilian free-tailed bats can instantly (in less than 100 milliseconds) switch from belting out a courtship song to singing a territorial tune, if another male echolocates nearby. "It means they can adjust their output—their songs—based on what they hear," says Cynthia Moss, a neuroethologist and bat echolocation expert at the University of Maryland, College Park. "It's a very exciting discovery, as is all the work on bat acoustic communication, because it shows that bats have the same degree of vocal flexibility as songbirds, and it gets at bats' social behaviors," which are as yet not well understood.

Bohn is full of unanswered questions about bats' social life and songs. But after enumerating them she pauses, her blue eyes twinkling. "Actually, there's an even bigger question. Why don't we use bats to study the evolution of human speech?"

IT'S A QUESTION that many bat researchers raise. For more than 50 years, songbirds have been the animal model of choice for investigating the roots of human speech. That's because of the many parallels—developmental, behavioral, neural, and genetic—between how human children learn to speak and how young songbirds, such as zebra finches, learn to sing, explains Richard Mooney, a neuroscientist who studies bird song at Duke University in Durham, North Carolina.

But songbirds are not mammals. "They don't have a mammal's neural architecture," Smotherman says. "So working out how bats use song and how bats' brains produce song may give us a better idea of the changes and adaptations that had to occur for human speech to evolve." Mice that sing ultrasonic tunes have been suggested as a model, but questions remain about their abilities, whereas "bats' vocal production is fertile ground," Mooney says.

The bat researchers have already found that certain bats use songs in a slightly more complicated way than do some songbirds. Many songbirds use a single "dual-function" song to both attract mates and defend territories. But both greater sac-winged and Brazilian free-tailed bats have distinct songs for courtship and territorial defense. And male free-tailed bats sing even when it's not the mating season, a time when they're in an all-male roost with a million other guys. "They may be using their songs for other social purposes," depending on the situation, Smotherman says.

Bat expert Kirsten Bohn with bat song recording gear at Uxmal.

Bird song researchers are miles ahead, Smotherman concedes. They know the regions in a bird's brain that produce song, and the selective pressures, such as female choice and male-male competition, that caused song to evolve. More than 100 labs worldwide, many with steady

PHOTOS: VIRGINIA MORELL/*SCIENCE* (2)

Published by AAAS

funding, explore bird song from all angles; there are dedicated conferences and a supportive website, http://songbirdscience.com.

Although bird song researchers would welcome a comparative mammalian model, the nascent study of bat song has nothing to compare with this. Bat song researchers are still identifying which species sing and in what social situations. "There's such variation in the songs and their functions," Knörnschild says. Some sound deceptively simple. The male Seba's short-tailed bat (*Carollia perspicillata*) from Central and South America rhythmically repeats one variable note over and over, much like a frog calling, Knörnschild says. Within that simple tune, however, there is an "individual vocal signature," a sound that identifies the caller and may help a female find her chosen mate, Knörnschild and her colleagues reported in April in *Behaviour*.

The crooning of other bats is more baroque. A team of researchers from the Czech Republic has decoded much of the courtship song of male European *Pipistrellus nathusii*, a migratory species that sings both on the wing and from a roost. The scientists analyzed nearly 3000 recordings they had gathered at 33 roosts in southern Bohemia, and reported in *Acta Chiropterologica* in 2008 that these songs are semantically structured. The rhythmic tunes begin with a phrase (which the scientists designated as motif A) announcing the bat's species, include an individual vocal signature (motifs B and C), information about the bat's population (motif D), and a signal about where to land (motif E). "Hence, translated into human words, the message ABCED could be approximately: (A) 'Pay attention: I am a *P. nathusii*, (B, C) specifically male 17b, (E) land here, (D) we share a common social identity and common communication pool,' " the researchers wrote in their paper.

Even more complicated are the courtship songs of the greater sac-winged bats, Knörnschild says. "When you look at their sonograms, they are as complex as [those depicting] the melodies of nightingales. They have motifs within motifs." A male sac-winged bat roosts during the day in a tree hollow or grotto with a harem of females. He uses a song with soft tones to lure the ladies, and a harsher tune to compete with other males in countersinging bouts. They air these latter territorial tunes at dawn and early in the evening when females are most likely to be away. The song lasts a mere 1.6 seconds, yet contains some 20 syllables and ends with loud, low-frequency buzzes that are individually distinct and advertise the male's strength. And there's a big payoff for a song well sung: Male sac-winged bats that sing the most territorial songs at the lowest frequency father more offspring. Knörnschild is investigating the possibility that this species has culturally transmitted dialects, as humans and some birds do.

Young sac-winged bats (and likely those of other species) must learn these complex songs from their parents. Knörnschild and her colleagues found that male and female sac-winged bat pups learn songs by babbling and imitating, as do human infants and the chicks of many bird species. (Although the females don't sing as adults, they need to know the songs in order to choose a mate.) Some bat species may even be able to imitate new songs throughout their lives, Knörnschild, Bohn, and Smotherman think. Only some songbirds possess such "vocal plasticity"; most songbird chicks have only a short developmental period during which they're able to learn songs. To clinch the case for bats, these scientists say, someone needs to show an adult bat imitating another adult bat's song. "That would be the ultimate proof," Smotherman says, and could help push bats up to the level of birds in studies about the origin of speech.

That's why Bohn carted both recording and broadcasting equipment to the palace's wall at Uxmal. She and her graduate student assistant Fernando Montiel run cables from their laptops over the ancient stones to a pair of microphones and a single speaker on a long bar atop a tripod. Montiel raises the array and points the speaker and microphones at the wall's fissures, where the small bats lurk and sing. By now, my ears are tuned to their tiny melodies, and I, too, can tell the difference between an aggressive call and a rhythmic ditty.

Earlier, Bohn and Montiel had recorded some of the bats' songs, and, using specialized software, altered them so that they sound like the tunes of different, unknown individuals. As soon as Bohn broadcasts the remixed bat songs, the palace residents burst into twitters and trills, which the scientists capture both in audio files and sonograms. These pulse across the screen of Bohn's laptop like miniature lightning strikes as she watches transfixed.

"We're getting territorial buzzes, and some contact calls, I think. They know there's an intruder. And, yes! That's what I want. One of the guys is trying to match the intruder's song." That's just the kind of hard evidence for long-term vocal learning and plasticity that she and Smotherman were hoping for. ■

Singing for love and territory

At least 20 bat species produce songs, which can be as flexible and complex as bird song

SPECIES	LOCATION	SONG TYPE	SONG DESCRIPTION	
Tadarida brasiliensis	North and South America	Courtship	Rhythmic, multisyllabic trills, chirps, and buzzes	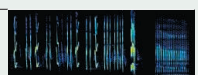
Saccopteryx bilineata	Central and South America	Courtship	Complicated multisyllabic phrases, with various trills	
Saccopteryx bilineata	Central and South America	Territorial	Low-frequency buzzes; males with the most and lowest calls sire the most chicks	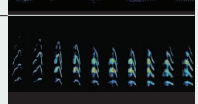
Carollia perspicillata	Central and South America	Courtship	Repeated monosyllabic trills	
Nyctinomops laticaudatus	Central and South America	Possibly courtship	Multisyllabic with chirps, trills, and buzzes	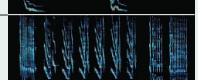
Mystacina tuberculata	New Zealand	Courtship; possibly lekking competition	Trills, sweeps, and tones, with ultrasonic components	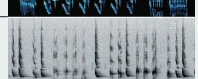
Pipistrellus nathusii	Europe	Courtship at roost and while flying	Multisyllabic phrases and location information	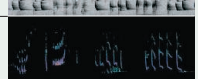
Cardioderma cor	East Africa	Territorial, but outside of roost	Low-frequency twitters and trills that carry long distance	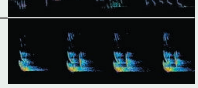

ONLINE

Listen to bat songsters at http://scim.ag/6190_media.

PHOTOS: (TOP TO BOTTOM) KIRSTEN BOHN; MIRJAM KNÖRNSCHILD/ULM UNIVERSITY (3); KIRSTEN BOHN; STUART PARSONS; JON RUSS; GRACE SMARSH

Published by AAAS

INSIGHTS

Understanding nanocrystal surfaces *p. 1340*

Crows challenge species concepts *p. 1345*

PERSPECTIVES

Morphological divergence. The skulls of a modern human (Cro-Magnon 1, far left) and a Neandertal (La Ferrassie 1, center left) show the morphological divergence between the two hominin species 500,000 to 600,000 years after their ancestral populations split. In contrast, after about 2 million years of separation, common chimpanzees (center right) and bonobos (far right) still display very similar morphologies, likely owing to strong stabilizing selection.

FIGURE CREDIT: FOSSIL SKULLS AND CHIMPANZEE/J.-J. HUBLIN; BONOBO/ROYAL MUSEUM FOR CENTRAL AFRICA, TERVUREN, BELGIUM

ANTHROPOLOGY

How to build a Neandertal

Fossils from Sima de los Huesos show a mixture of Neandertal and more ancient features

By **Jean-Jacques Hublin**

Under a desolate sierra of northern Spain, in the darkness of a deep shaft, lies the largest accumulation of hominin fossils ever found. On page 1358 of this issue, Arsuaga *et al.* (*1*) date this paleontological treasure at the Sima de los Huesos (see the photo) and shed new light on one of the most impassioned issues in the field of human evolution: How did Neandertals evolve?

Four to five hundred thousand years ago, archaic humans in western Eurasia diverged from other groups of that period in Africa and eastern Asia. Their skull, jaw, and teeth began to display features that characterize later Neandertals. When modern humans—which had evolved in Africa—finally colonized Eurasia 50,000 years ago, they occasionally interbred with local Neandertals, but the two groups already showed some signs of reproductive incompatibility (*2*). The extent of their morphological divergence over such a short period of time is striking (see the figure). Polar bears and brown bears provide another example of rapid divergence over a few hundred thousand years (*3*). However, other sister species have stayed quite similar for much longer periods of time (see the figure), and among mid-sized mammals, complete reproductive isolation generally takes at least 1.4 million years to develop (*4*).

Why did the Neandertals differentiate so quickly? Isolation and genetic drift likely played a key role (*5*, *6*). Archaic Europeans already dwelled, at least sporadically, at the edge of the boreal zone 850,000 years ago (*7*), but 200,000 years later, a major glaciation dramatically reduced their habitable domain. Since this time, extreme climatic conditions prevailed roughly every 100,000 years within the European cul-de-sac. The time period of the Sima de los Huesos population (~430,000 years ago) coincides with the onset of a long interglacial period that followed a severe glacial episode. Hominin groups dispersed again into higher latitudes. However, in areas like modern-day Germany and the British Isles, human occupations remained scarce and discontinuous, with periodic demographic crashes during subsequent climatic cycles. Paleogenetic data (*8*) confirm that Neandertal populations were small and

Published by AAAS

generally isolated from one another, with very low genetic diversity. These conditions are the most favorable to the rapid and random fixation of features by genetic drift

Obtaining an accurate picture of the European populations around 400,000 years ago remains challenging. The Sima de los Huesos stands alone with its 28 very complete individuals. At most other sites, isolated fragments make it impossible to assess local variability; accurate dating is also often difficult. Still, the existing evidence suggests that at this early stage of the Neandertal lineage, European populations differed in their combinations of Neandertal and primitive traits. As Arsuaga *et al.* show, the Sima de los Huesos series displays an almost full set of Neandertal dental features. These features are less frequent at other sites of comparable age (*9*) and became ubiquitous in western Eurasia only after further pruning of the western European archaic populations.

Repeated local extinctions may also explain the occurrence at the Sima de los Huesos of mitochondrial DNA similar to that sequenced in the Denisovans (*10*), an archaic group that diverged from the Neandertal lineage after its separation from the African groups and that peopled most of Asia. The Sima de los Huesos population is close in age to the split of the two Eurasian lineages. Because mitochondrial DNA does not recombine at each generation, an ancient lineage could have survived in the Denisovans but got lost in the Neandertals along successive genetic bottlenecks.

Arsuaga *et al.* confirm that Neandertal features did not evolve as a block but rather were fixed at different rates and paces in different parts of the anatomy (*5*). In the Sima de los Huesos fossils, Neandertal conditions are mostly evident in the face and teeth, whereas the braincase still retains primitive conditions. The fact is that one does not find Neandertal braincase shapes in Europe before ~200,000 years ago. Comparing brain sizes in late Neandertals and in the Sima de los Huesos hominins, Arsuaga *et al.* also document a substantial increase of the encephalic volume along this evolutionary branch.

An independent increase in brain volume also took place along the African branch leading to modern humans, as well as in the late *Homo erectus* of East Asia. Hominins rely on technology and social complexity, and it is therefore not surprising to observe such parallel evolutions, because similar pressures of selection were at work in all of these lineages. However, their separation for several hundred thousand years resulted in different evolutionary pathways to achieve bigger brains. Neandertal and modern brains are anatomically different. The former display a smaller cerebellum, less projecting parietal areas, smaller olfactory bulbs and temporal lobe poles, and a narrower orbitofrontal cortex (*11*). Furthermore, there is clear evidence that the growth pattern of modern human brains deviates from that of the Neandertals. In modern humans, parietal areas and cerebellum expand in early infancy, at a crucial stage for the establishment of cognitive skills (*12*).

The different pathways for brain evolution are also perceptible in the DNA of both groups. Among the 87 genes that distinguish modern humans from Neandertals, a whole series are involved in brain function or development, particularly in its connectivity (*13*). Some of these genes belong to the most conservative part of the primate genome. They remained protected by stabilizing selection through millions of years of evolution before mutating along the modern human lineage.

Although genes involved in behavior seem to have changed more in the modern human lineage than along the Neandertal line (*8*), it is difficult to say what this means for their phenotypic expression. The paleolithic archaeological record can yield a wealth of information regarding stone technologies or food procurement, but remains mute on key aspects of human behaviors, such as mating strategies, aggression, or large-scale cooperation. There is, however, no doubt that after more than half a million years of separate evolution, idiosyncratic features that developed in modern human groups played a key role in the almost complete replacement not only of the Neandertals but of all other archaic humans whom they met during their expansion out of Africa. ■

PHOTO: JAVIER TRUEBA/MADRID SCIENTIFIC FILMS

A treasure trove of hominin fossils. At the Sima de los Huesos (bone pit) in the Atapuerca Mountains in northern Spain, the remains of 28 hominins have been recovered. Arsuaga *et al*. date these fossils to around 430,000 years ago and show that they have Neandertal facial and dental features together with more primitive braincases.

Department of Human Evolution, Max Planck Institute for Evolutionary Anthropology, Deutscher Platz 6, Leipzig, 04103 Germany. E-mail: hublin@eva.mpg.de

REFERENCES AND NOTES

1. J. L. Arsuaga *et al.*, *Science* **344**, 1358 (2014).
2. S. Sankararaman *et al.*, *Nature* **507**, 354 (2014).
3. S. Liu *et al.*, *Cell* **157**, 785 (2014).
4. T. W. Holliday, in *Neanderthals Revisited: New Approaches and Perspectives*, K. Harvati, T. Harrison, Eds. (Springer, New York, 2006), pp. 281–298.
5. J.-J. Hublin, *Proc. Natl. Acad. Sci. U.S.A.* **106**, 16022 (2009).
6. T. D. Weaver, C. C. Roseman, C. B. Stringer, *J. Hum. Evol.* **53**, 135 (2007).
7. S. A. Parfitt *et al.*, *Nature* **466**, 229 (2010).
8. S. Castellano *et al.*, *Proc. Natl. Acad. Sci. U.S.A.* **111**, 6666 (2014).
9. M. Martinón-Torres, J. M. Bermúdez de Castro, A. Gómez-Robles, L. Prado-Simón, J. L. Arsuaga, *J. Hum. Evol.* **62**, 7 (2012).
10. M. Meyer *et al.*, *Nature* **505**, 403 (2014).
11. M. Bastir *et al.*, *Nat. Commun.* **2**, 588 (2011).
12. P. Gunz *et al.*, *J. Hum. Evol.* **62**, 300 (2012).
13. K. Prüfer *et al.*, *Nature* **505**, 43 (2014).

ACKNOWLEDGMENTS

I thank the Museum National d'Histoire Naturelle, Paris, for allowing the computed-tomography of the fossil skulls used here as an illustration.

10.1126/science.1255554

Published by AAAS

CHEMISTRY

Connecting the dots

Understanding nanocrystal surfaces helps to direct their assembly into novel material architectures

By **Michael A. Boles** *and* **Dmitri V. Talapin**

Nanocrystals—nanometer-sized inorganic crystals containing hundreds to thousands of atoms—offer exciting opportunities in areas as varied as photonics, catalysis, biotechnology, and medicine. For example, nanocrystals enrich the display color palette in tablet computers and advanced TVs. Two reports in this issue, by Zherebetskyy *et al.* on page 1380 (*1*) and Boneschanscher *et al.* on page 1377 (*2*), investigate nanocrystal surfaces and show how these surfaces can be merged in a controllable fashion, allowing the assembly of novel material architectures.

The ability to control matter at the nanometer scale was spurred by the discovery of advanced solution-based synthesis techniques in the 1990s (*3*). For example, lead sulfide (PbS) nanocrystals may be synthesized by reacting simple molecular species, such as lead acetate and hydrogen sulfide, in the presence of surfactant molecules such as oleic acid. The surfactant molecules bind to the nanocrystal surface, decorating the nanocrystals with a corona of organic chains (see the figure, panel A). It remains unclear, however, how the surfactant molecules bind to different nanocrystal facets.

Zherebetskyy *et al.* use ab initio density functional theory (DFT) to study the facets of PbS nanocrystals, which have an inorganic core structure identical to that of common table salt. These nanocrystals, used as building blocks for solar cells, photodetectors, and transistors, mainly display two types of surfaces. The (001) surface has a checkerboard arrangement of alternating Pb^{2+} cations and S^{2-} anions, whereas the (111) surface presents a dense hexagonal arrangement of Pb^{2+} or S^{2-}. Each nanocrystal has six (001) and eight (111) facets. How does oleic acid interact with these distinct surface patterns? And how does the nanocrystal preserve overall charge neutrality? Investigation of ligands on nanocrystal surfaces is conceptually related to the more established field of self-assembled monolayers on planar crystal surfaces (*4*). Nanocrystals add another element of complexity: They expose different types of crystallographic facets and have a high concentration of corner and edge sites.

Zherebetskyy *et al.*'s calculations suggest that (001) surfaces are most stable when oleic acid binds as a neutral molecule. It is rather surprising that oleic acid does not lose a proton to form a covalent bond with lead ions, as it does in lead oleate and other salts.

The results for the (111) surfaces are even more intriguing. Elemental analysis of PbS nanocrystals gives a cation-to-anion ratio of 1.2 to 1.4, with smaller particles having higher lead content (*5*); this suggests that all (111) surfaces are completely covered with Pb^{2+} (see the figure, panel A). However, oleic acid molecules are too bulky to bind all atoms on lead-terminated (111) surfaces. Zherebetskyy *et al.* propose a solution: Small OH^- anions sneak to the nanocrystal surface and bind to sites not accessible to large surfactant molecules. The hydroxide anion, they suggest, is small enough to be interspersed in equal abundance with oleate (deprotonated oleic acid) ligands, providing charge compensation and eliminating broken bonds. Such small surface-bound anions tucked beneath large fatty acid ligands may be a general feature of most nanocrystal surfaces.

Ligand molecules bound to the nanocrystal surface reduce surface energy. To fully eliminate energetically expensive surfaces, nanocrystals may align their atomic lattices and fuse into a single crystal through merging of identical facets. This "oriented attachment" (*6*) process allows nanocrystals to be used as building blocks to construct nanowires (*7*), crystalline rings (*8*), or two-dimensional sheets (*9*). Boneschanscher *et al.* use this process to assemble lead selenide (PbSe) nanocrystals into a honeycomb structure similar to silicene (*10*), silicon's graphene analog.

By evaporating a solution of PbSe nanocrystals capped with oleic acid over a liquid ethylene glycol surface, the authors coaxed the particles to arrange themselves into an ordered superlattice. Upon gentle heating, the PbSe cores fused into a honeycomb architecture (see the figure, panel B). Electron

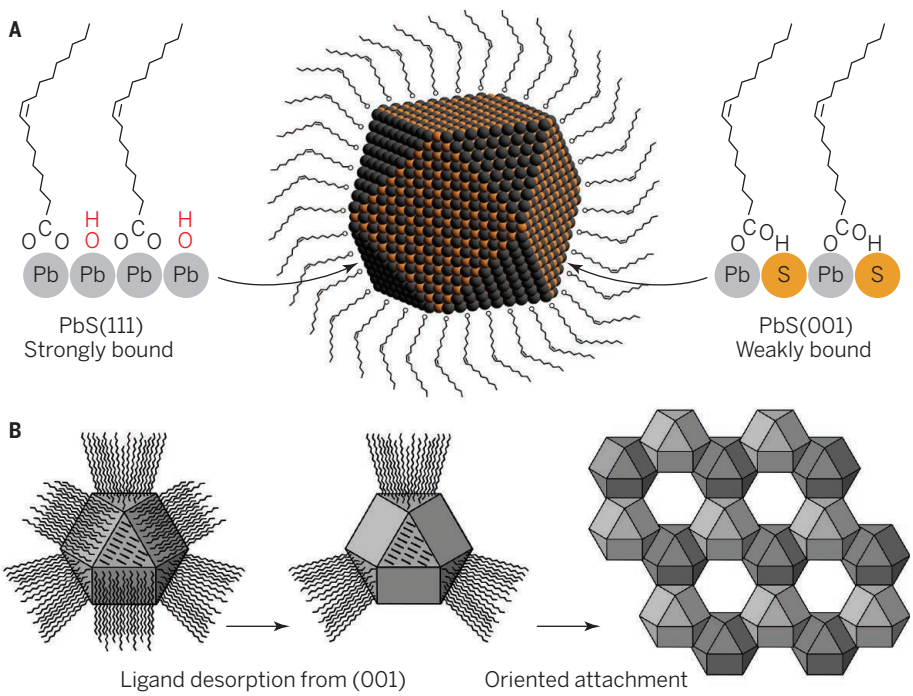

Directed assembly. (**A**) The theoretical and experimental investigation by Zherebetskyy *et al*. expands on the basic picture of ligand binding (center) by showing that lead sulfide nanocrystals coated with oleic acid have cation-terminated (111) facets stabilized by strongly bound surface hydroxide groups and deprotonated oleate ligands (left). PbS (001) surfaces, on the other hand, are passivated by weakly bound oleic acid chains and may be left unprotected after ligand desorption (right). (**B**) Boneschanscher *et al*. show that selective removal of (001)-bound ligands and fusing of nanocrystal cores yields two-dimensional nanostructures through oriented attachment of nanocrystal facets.

Department of Chemistry and James Franck Institute, University of Chicago, Chicago, IL 60637, USA. E-mail: dvtalapin@uchicago.edu

Published by AAAS

microscopy and modeling revealed oriented attachment through (001) facets. The honeycomb superlattices resemble atomic two-dimensional crystals such as graphene or molybdenum disulfide and are remarkably robust: Lead ions may be exchanged for cadmium without disrupting the selenium anion lattice.

How can such a complex structure form through attachment of nanocrystals that were originally separated by surface ligands? Given the similarity between PbSe and PbS, we can draw inspiration from the theoretical work of Zherebetskyy *et al.* For PbS nanocrystals, the binding energy of oleic acid to the (001) facet is too low to keep surfactant molecules in place for a long period of time. Binding of oleate/hydroxyl pairs to the (111) surface is much stronger. A simple calculation based on reported binding energies suggests that surfactants are less likely to desorb from a (111) surface than from a (001) surface by a factor of ~10^6. Furthermore, the ethylene glycol surface used by Boneschanscher *et al.* may not only act as the stage on which self-assembly takes place, but may also gently remove loosely bound (001) ligands from PbSe nanocrystals. In contrast, (111) surfaces remain protected by the oleate and hydroxyl ligands. Bare (001) facets become "sticky patches," guiding the attachment of PbSe nanocrystals into buckled silicene-like two-dimensional sheets that may have exotic electronic properties (*11*).

The work of Zherebetskyy *et al.* offers a new understanding of the nanocrystal surface and lays the foundation for targeted design of unusual nanocrystal architectures like that presented by Boneschanscher *et al.* Thoughtful use of surface ligands that bind strongly to some crystal facets and weakly to others may enable the construction of novel materials by merging crystalline particles through engineered surface patches (*12*). The first chapter of colloidal nanocrystal research was written by those who managed to tame the surface; the next challenge is to put it to work. ■

REFERENCES

1. D. Zherebetskyy *et al.*, *Science* **344**, 1380 (2014).
2. M. P. Boneschanscher *et al*, *Science* **344**, 1377 (2014).
3. C. B. Murray, D. J. Norris, M. G. Bawendi, *J. Am. Chem. Soc.* **115**, 8706 (1993).
4. J. C. Love, L. A. Estroff, J. K. Kriebel, R. G. Nuzzo, G. M. Whitesides, *Chem. Rev.* **105**, 1103 (2005).
5. I. Moreels *et al.*, *ACS Nano* **3**, 3023 (2009).
6. R. L. Penn, J. F. Banfield, *Science* **281**, 969 (1998).
7. Z. Tang, N. A. Kotov, M. Giersig, *Science* **297**, 237 (2002).
8. K. S. Cho, D. V. Talapin, W. Gaschler, C. B. Murray, *J. Am. Chem. Soc.* **127**, 7140 (2005).
9. C. Schliehe *et al.*, *Science* **329**, 550 (2010).
10. P. Vogt *et al.*, *Phys. Rev. Lett.* **108**, 155501 (2012).
11. E. Kalesaki *et al.*, *Phys. Rev. X* **4**, 011010 (2014).
12. Z. Zhang, S. C. Glotzer, *Nano Lett.* **4**, 1407 (2004).

10.1126/science.1256197

ILLUSTRATION: V. ALTOUNIAN/*SCIENCE*

CELL BIOLOGY

A cell death avenue evolved from a life-saving path

Altruistic cell suicide model is challenged

By **Harm H. Kampinga**

Yeast metacaspases are the ancestral enzymes of caspases that execute cellular suicide ("programmed cell death") in multicellular organisms. Studies on metacaspase 1 (Mca1) have suggested that single-cell eukaryotes can also commit programmed cell death (*1*, *2*). However, on page 1389 of this issue, Malmgren Hill *et al.* (*3*) show that Mca1 has positive rather than negative effects on the life span of the budding yeast *Saccharomyces cerevisiae*, especially when protein homeostasis is impaired. Mca1 helps to degrade misfolded proteins that accumulate during aging or that are generated by acute stress, and thereby ensures the continuous and healthy generation of daughter cells that are free of insoluble aggregates that otherwise would limit life span.

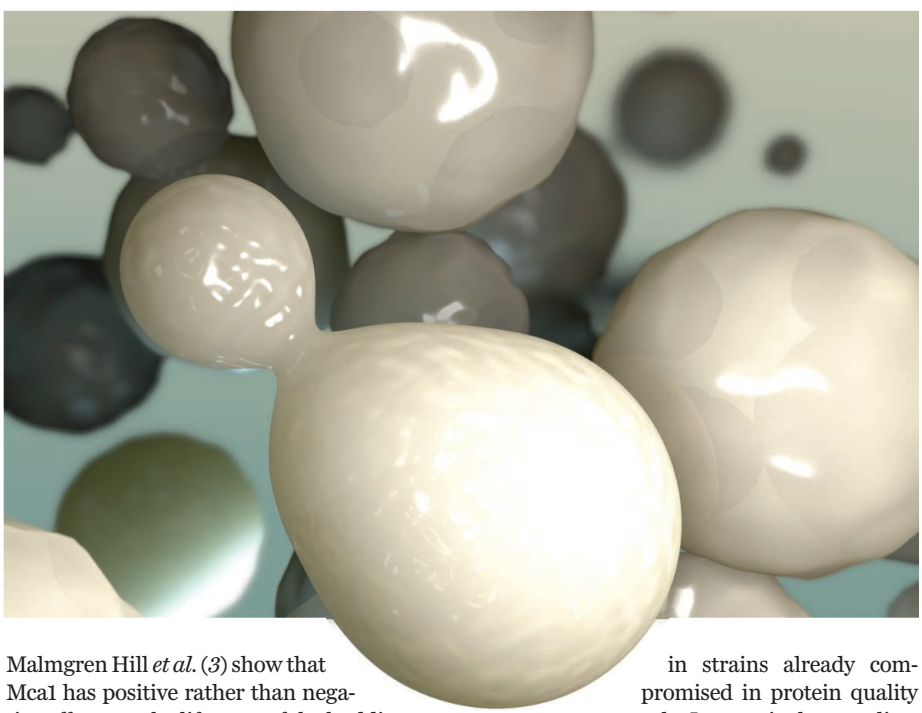

Loss of Mca1 activity has been associated with a reduced appearance of programmed cell death markers (*1*, *4*), implying that its overexpression should decrease the replicative life span of yeast (the number of daughter cells a mother cell can produce throughout its life). Cells lacking Mca1 have increased amounts of protein aggregates and oxidized proteins (*4*, *5*). Malmgren Hill *et al.* not only show that this is related to decreased survival, but also provide mechanistic insights into the mode of action of Mca1. Its pro-life action depends on the chaperone heat shock protein 104 (Hsp104), a protein that can disentangle protein aggregates and is crucial for the asymmetric segregation of protein aggregates in dividing cells. Mca1 deficiency does not affect life span of wild-type strains, but further decreases life span in strains already compromised in protein quality control. In particular, replicative aging is accelerated in strains lacking the Hsp70 co-chaperone Ydj1. Mca1 does not improve protein folding but supports degradation of terminally misfolded proteins. Malmgren Hill *et al.* show that Mca1 requires proteasomes (protein structures that break down proteins) for all its effects.

The study by Malmgren Hill *et al.* challenges the idea that caspases are activated as an altruistic suicide mechanism in single-cell eukaryotes as a means to provide nutrients for younger and fitter cells in the population (*2*). Rather, the data sug-

Department of Cell Biology, University Medical Center Groningen, University of Groningen, Groningen, Netherlands. E-mail: h.h.kampinga@umcg.nl

Published by AAAS

gest that from an evolutionary perspective, caspase activation is an integrated part of a protective response to help cells survive toxic stress caused by the accumulation of misfolded proteins. When, however, activated incorrectly (e.g., in the absence of proteotoxic stress) or too strongly (e.g., in the case of excessive damage to the cell), the caspase activity may become nonselective and thus lead to the typical Mca1-dependent hallmarks of programmed cell death (*1*, *2*, *4*). Also, caspase activation in metazoa may function primarily in cell-autonomous protection and cellular remodeling or pruning. Its role in programmed cell death may also simply reflect overactivation upon severe cellular damage or hijacking of the caspases in the absence of stress to serve in non–cell-autonomous regulated tissue homeostasis.

The results of Malmgren Hill *et al.* also highlight the importance of protein quality control for cellular aging. A collapse of protein homeostasis has been implicated mostly in chronological aging of differentiated cells and, for example, as a cause of neurodegenerative diseases (*6*). The authors show that it also plays a prominent role in replicative aging. This supports early findings in yeast (*7*) and may also be relevant to metazoa, in which stem cells have extremely efficient protein degradation mechanisms (*8*) and also use asymmetric segregation of protein damage for rejuvenation (*9*).

The data of Malmgren Hill *et al.* also suggest the existence of an additional layer of control of protein homeostasis. Beyond the activation and induction of chaperones that assist in protein sorting, refolding, and protein degradation via proteasomes and autophagosomes (membrane structures that deliver proteins to lysosomes for enzymatic destruction) (*10*), Malmgren Hill *et al.* show that activation of caspases also belongs to the cell's repertoire of defense mechanisms against protein damage. Mca1 might act in parallel to the Ssa-Ydj1 machinery. Although Ssa-Ydj1 collaborates with Hsp104 to refold proteins after their aggregation (*11*), Mca1 primarily supports protein degradation, as its actions require not only Hsp104 but also proteasomal activity (*3*).

Precisely how Mca1 exerts its effect is yet unclear. It can associate with aggregates independent of other chaperones (*3*, *5*) and independent of its catalytic activity (*5*), suggesting that it binds directly to misfolded proteins [likely through its amino-terminal "pro-domain" that is rich in glutamine and asparagine repeats]. This interaction may exert chaperone-like activity by keeping unfolded proteins in a proteasome-competent form, which explains why part of Mca1's protective actions in wild-type strains is independent of its protease activity. However, the caspase activity of Mca1 is required for protein homeostasis and control of life span in Ydj1-deficient strains. It could be that for more terminally misfolded proteins that accumulate in the absence of Ydj1, protease cleavage may help to dismantle such aggregates in concert with Ssa and Hsp104 (see the figure). This would also explain why the strongest phenotypes of Mca1 are seen under conditions in which Ydj1 is absent. More biochemical data with purified proteins will be needed to test these ideas.

The study of Malmgren Hill *et al.* suggests that altruism may not exist among cells. However, life and death seem to be close neighbors, and the things that are life saving may also become lethal. It will therefore be a challenge to make use of these insights into caspase function in order to treat diseases by selectively tipping the balance toward life (e.g., in neurodegenerative diseases) or death (e.g., in cancer). ■

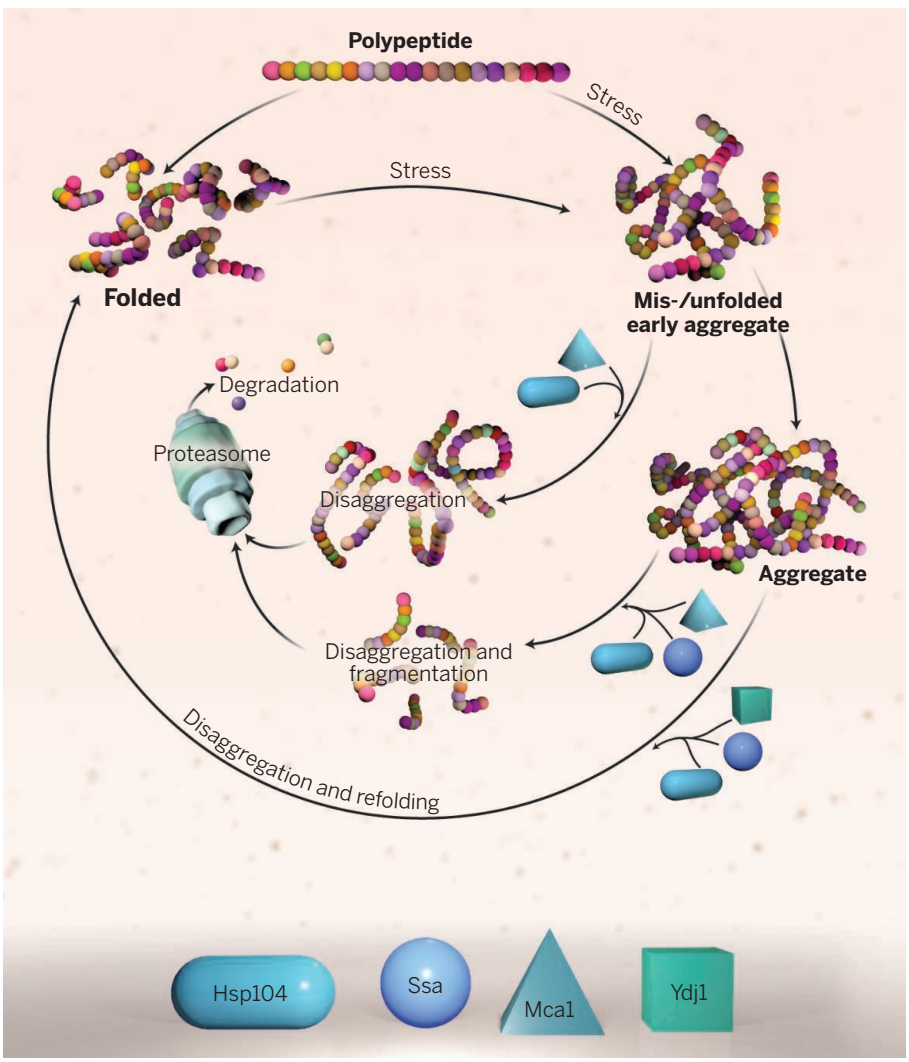

Defense against protein damage. Stress-damaged proteins that form aggregates in cells can be reactivated with the Hsp104-Ssa-Ydj1 chaperone machinery. Mca1 may act in parallel by binding to misfolded proteins during early stages of aggregation for proteasomal degradation (this is independent of Mca1's enzymatic activity). Alternatively, Mca1 may associate with misfolded proteins formed at late stages of aggregation (together with Hsp104 and Ssa), helping to disentangle the aggregates by its protease cleavage activity before shunting them to the proteasome for degradation.

ILLUSTRATION: V. ALTOUNIAN/*SCIENCE*

REFERENCES

1. F. Madeo *et al.*, *Mol. Cell* **9**, 911 (2002).
2. E. Herker *et al.*, *J. Cell Biol.* **164**, 501 (2004).
3. S. Malmgren Hill *et al.*, *Science* **344**, 1389 (2014).
4. M. A. Khan, P. B. Chock, E. R. Stadtman, *Proc. Natl. Acad. Sci. U.S.A.* **102**, 17326 (2005).
5. R. E. Lee, S. Brunette, L. G. Puente, L. A. Megeney, *Proc. Natl. Acad. Sci. U.S.A.* **107**, 13348 (2010).
6. W. E. Balch, R. I. Morimoto, A. Dillin, J. W. Kelly, *Science* **319**, 916 (2008).
7. H. Aguilaniu, L. Gustafsson, M. Rigoulet, T. Nyström, *Science* **299**, 1751 (2003).
8. D. Vilchez *et al.*, *Nature* **489**, 304 (2012).
9. M. A. Rujano *et al.*, *PLOS Biol.* **4**, e417 (2006).
10. H. H. Kampinga, E. A. Craig, *Nat. Rev. Mol. Cell Biol.* **11**, 579 (2010).
11. J. R. Glover, S. Lindquist, *Cell* **94**, 73 (1998).

10.1126/science.1256084

Published by AAAS

IMMUNOLOGY

Teaching the immune system "self" respect and tolerance

An anti-inflammatory milieu promotes immune tolerance

By **Lucienne Chatenoud**

The immune system protects the individual from infectious agents and the emergence of tumors while preserving the host's integrity (*1*). The latter implies that the immune system will not attack the individual's own tissues ("self"). This peaceful coexistence, or immune tolerance, is broken when an autoimmune disease develops, such as multiple sclerosis or insulin-dependent diabetes. Tolerance is what we would like to restore to cure such disabling diseases. Kasagi *et al.* (*2*) indicate that it may be possible to teach the immune system to tolerate "self" again.

The pathogenesis of several diseases involves a primary or secondary autoimmune reaction, and their incidence now constitutes the third leading cause of morbidity and mortality after cardiovascular disease and cancer (*3*). There is yet no cure for autoimmune diseases. For those causing serious disabling organ damage such as multiple sclerosis, lupus erythematosus, or rheumatoid arthritis, the usual recourse is chronic treatment with immunosuppressive drugs that globally depress the immune system. This can render patients vulnerable to infections and tumors.

Immune tolerance is not innate. It is established during fetal and postnatal development and relies on mechanisms that operate in lymphoid organs where lymphocytes differentiate (i.e., bone marrow and thymus) as well as in peripheral secondary lymphoid organs (i.e., spleen, lymph nodes, intestinal lymphoid tissue) and in tissues that become inflammatory targets. Recently, the central role of regulatory T cells (T_{regs}) (*4*–*7*) in maintaining immune tolerance has spurred cell therapy strategies in which T_{regs} are isolated from an autoimmune patient, expanded in vitro, and then reinjected into the individual (*8*, *9*). However, such studies use polyclonal T_{regs} that are not antigen specific, and the in vitro expansion of substantial numbers of antigen-specific T_{reg} cells is a challenge. An alternative approach is to promote the differentiation and expansion of autoantigen-specific T_{reg} cells in vivo, without compromising other immune system functions.

Massive production of the immunoregulatory cytokine transforming growth factor–β (TGF-β) by phagocytic cells, blocks the vicious cycle of self-perpetuating inflammation that is the hallmark of all autoimmune responses (*10*). This burst of TGF-β occurs when phagocytes engulf cells that are dying by programmed cell death (apoptosis). In a host suffering from autoimmunity, a key question is how apoptosis of a sufficient number of cells can be induced in vivo to stimulate the release of TGF-β from phagocytes, all in the context of an immune environment that supports the generation of T_{reg} cells to restore self-tolerance?

Kasagi *et al.* demonstrate how this can be accomplished in two mouse models: induced experimental autoimmune encephalitis (a model of multiple sclerosis) and spontaneous insulin-dependent diabetes in nonobese diabetic (NOD) mice. The authors first established that phagocytes are essential to the approach. After destroying 60 to 80% of the animal's immune cells (including phagocytes) by whole body γ irradiation, the mouse was replenished with normal phagocytes and was also injected with the antigen that elicited the autoimmune response (autoantigen) in the first place. Remarkably, the autoimmune disease was abolished (see the figure). The authors demonstrate that phagocytes, their production of TGF-β, and the generation of T_{reg} cells specific for the autoantigen are all necessary components of the therapeutic approach.

Moreover, Kasagi *et al.* could replace the whole-body radiation protocol with the administration of two monoclonal antibodies directed to B cells (to the CD20 B cell antigen) and T cells (to the CD8 T cell antigen). Antibody-bound immune cells were destroyed by apoptosis in the animal. Thus, by removing these two "innocent bystander" subsets of immune cells, phagocytes were

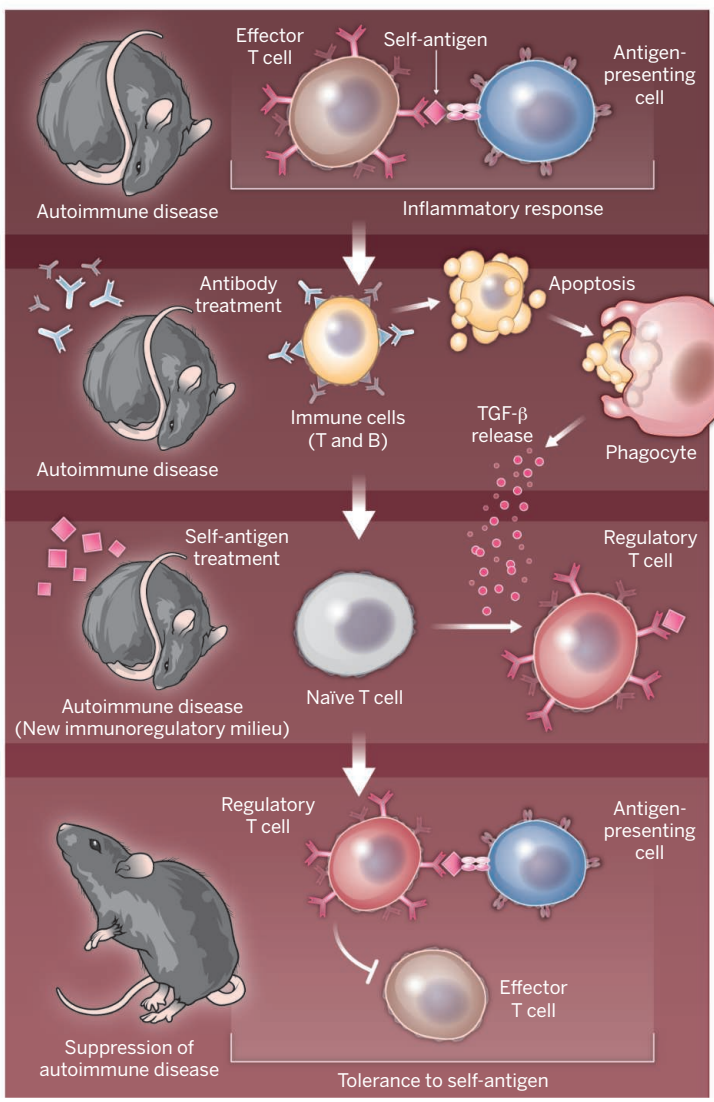

Breakdown and reprogram. Immune tolerance is achieved an animal models of autoimmune disease in a two-step approach. Immune cell apoptosis is induced by administering antibodies that recognize immune cells. This is followed by treatment with the specific autoantigen, which stimulates the production of specific regulatory T cells. These cells suppress effector T cells (that also respond to the autoantigen) and therefore promote tolerance.

ILLUSTRATION: C. BICKEL/*SCIENCE*

Université Paris Descartes, Sorbonne Paris Cité, F-75475 Paris, France, and INSERM U1151, Hôpital Necker-Enfants Malades, 75015 Paris, France. E-mail: lucienne.chatenoud@inserm.fr

Published by AAAS

spared. This preserved the essential TGF-β burst and the generation of an environment in vivo conducive to the development of autoantigen-specific T_{reg} cells (in response to injection with autoantigen). This "reprogrammed" immune system could still respond to bacterial antigen, so overall immunity in the animal appears not to have been compromised.

What is the true origin of the autoantigen-specific T_{reg} cells that are responsible for the therapeutic effect? It is not known whether they derive from the distinct lineage of CD4 T cells from the thymus ($FoxP3^+T_{reg}$ cells) (*4*–*6*, *11*). Alternatively, they may derive from conventional peripheral CD4 T cells under the influence of TGF-β and the autoantigen (*12*). It is also not clear whether autoantigen-specific T_{reg} cells can be sustained over time at sufficient amounts to ensure that the needed balance between "effectors" and "regulators" underlying immune tolerance is maintained.

From a more practical point of view, therapeutic autoantigens for major autoimmune diseases (such as multiple sclerosis and autoimmune insulin–dependent diabetes) are available as therapeutic products and are safe (*13*). Also, monoclonal antibodies that recognize CD20 are likewise available and are safe (*14*, *15*); CD8 monoclonal antibodies are still in development after many years. Aside from the scientific questions that must be addressed, there is the question of forging a strong academic-industry relationship if we want the strategy described by Kasagi *et al.* to become a clinical reality. It may be that the approach has implications far beyond autoimmune diseases, extending to the arenas of tolerance induction in transplantation, gene therapy, and regenerative medicine. ■

REFERENCES

1. R. H. Schwartz, *Cold Spring Harb. Perspect. Biol.* **4**, a006908 (2012).
2. S. Kasagi *et al.*, *Sci. Transl. Med.* **6**, 241ra78 (2014).
3. J. F. Bach, *N. Engl. J. Med.* **347**, 911 (2002).
4. J. D. Fontenot, M. A. Gavin, A. Y. Rudensky, *Nat. Immunol.* **4**, 330 (2003).
5. J. D. Fontenot *et al.*, *Immunity* **22**, 329 (2005).
6. S. Sakaguchi *et al.*, *Immunol. Rev.* **212**, 8 (2006).
7. S. Sakaguchi, N. Sakaguchi, M. Asano, M. Itoh, M. Toda, *J. Immunol.* **155**, 1151 (1995).
8. N. Marek-Trzonkowska, M. Myśliwiec, J. Siebert, P. Trzonkowski, *Pediatr. Diabetes* **14**, 322 (2013).
9. Q. Tang, J. A. Bluestone, *Cold Spring Harb. Perspect. Med.* **3**, a015552 (2013).
10. S. Perruche *et al.*, *Nat. Med.* **14**, 528 (2008).
11. J. A. Bluestone, A. K. Abbas, *Nat. Rev. Immunol.* **3**, 253 (2003).
12. W. Chen *et al.*, *J. Exp. Med.* **198**, 1875 (2003).
13. J. Ludvigsson *et al.*, *N. Engl. J. Med.* **359**, 1909 (2008).
14. S. L. Hauser *et al.*, *N. Engl. J. Med.* **358**, 676 (2008).
15. M. D. Pescovitz *et al.*, *N. Engl. J. Med.* **361**, 2143 (2009).

10.1126/science.1256864

PHYSICS

Electronically erased

Erasing knowledge of a quantum system changes its state

By **D. E. Feldman**

The fate of Schrödinger's cat depends on the particular path of a single electron. If the electron hits the trigger, which opens a bottle of poisonous gas, then the cat dies. If the path misses the trigger, the cat lives. According to quantum mechanics, electrons do not normally follow a definite trajectory. Instead, an electron can trace both paths at the same time. As a result, Schrödinger's cat is both dead and alive. Quantum mechanics also teaches us that a "which-path" detector—that is, any measurement device that can show where the electron travels—forces the electron to choose just one path, thus sealing the cat's destiny. But what will happen after the information collected by the detector has been erased? The results of a semiconductor version of such an experiment, reported by Weisz *et al.* on page 1363 of this issue (*1*), suggest that the cat will come back to the middle ground between life and death.

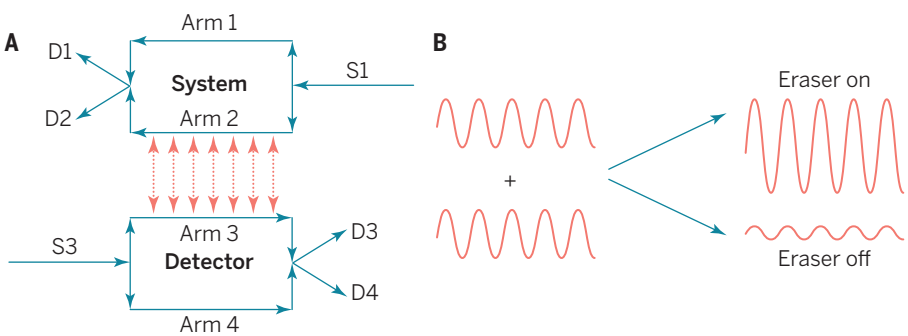

Electronic quantum eraser. (**A**) A schematic of the device. Electrons follow arms 1 to 4 in the directions of the arrows. Electrons in arm 2 repel electrons in arm 3. (**B**) The eraser effect on the quantum interference of matter waves.

In contrast to classical physics, any measurement on a quantum system affects its behavior. Hence, the properties of the system depend on what questions one asks. For example, according to the uncertainty principle, it is meaningful to ask about a position or velocity of a quantum particle, but it cannot have a definite position and velocity at the same time. Weisz *et al.* add another twist: What happens if a question is asked but the answer (that is, the measurement result) is erased?

To address this problem, Weisz *et al.* have realized an electronic quantum eraser in a semiconductor nanostructure as proposed by Kang (*2*). Electrons exhibit rich behavior when confined to two dimensions in a very pure semiconductor in a strong magnetic field. This is known as the quantum Hall effect. In particular, transport is one-dimensional, with electrons following just a small set of paths determined by metallic gates on top of the sample. This property was used by Weisz *et al.* to define the allowed trajectories for electrons in the experiment (see the figure, panel A).

The experimental setup consists of two identical devices, known as electronic Mach-Zehnder interferometers (*3*). One of them plays the role of a quantum system under investigation; the other is a detector (see the figure, panel A). To understand the experiment, we first need to address how a single interferometer works. Electrons depart from terminal S1 along the upper and lower arms 1 and 2 and are detected in terminals D1 and D2. If electrons were classical particles, the number of arrivals to D2 would simply be determined by the incoming current at S1. The wave-particle duality of quantum mechanics implies more complexity: Electrons propagate along paths 1 and 2 in the form of waves. The waves interfere where the two arms meet (essentially, the oscillations in the two waves add up). Hence, the output signal at D2 depends on the phase difference between the waves. The latter is controlled by the area between the device arms. Thus, the number of electron arrivals to D2 oscillates as a function of the area.

In the two-interferometer system, electric forces result in repulsion between the electrons in the lower arm of the quantum system and those in the upper arm of the de-

Department of Physics, Brown University, Providence, RI 02912, USA. E-mail: dmitri_feldman@brown.edu

Published by AAAS

tector. Also, the upper arm of the quantum system is too far to have much effect on the lower interferometer. Thus, the electric current in the detector depends on the paths of the electrons in the upper interferometer. In other words, the detector reads the which-path information. Such a measurement disturbs the quantum system and suppresses interference between arms 1 and 2. As a result, the current oscillations in D2 are reduced. The experimentally measured correlation between the currents in D2 and D4 also shows reduced oscillations (see the figure, panel B).

The last important piece of the physics is interference between arms 3 and 4 in the detector. By tuning the magnetic field, Weisz *et al.* reach the regime where the interference effect makes the electric current in D4 almost independent of the which-path information about the upper interferometer. Thus, they erase the data, detected by arm 3, before it can be read out. What is the effect on the quantum system? The oscillations in the current correlation between D2 and D4 return in full force: Schrödinger's cat is brought back to the middle ground between life and death.

Quantum eraser experiments were previously performed in an optical setting with photons (*4*–*6*). The electronic setting of Weisz *et al.* brings in an additional advantage due to Coulomb interaction. In contrast to photons, electrons strongly interact, and this opens ways to manipulate and entangle them. In a striking difference from optical experiments, the quantum system and the detector used by Weisz *et al.* are identical. Essentially, two Schrödinger's cats are staring at each other. A possible extension of the experiment would be a delayed-choice experiment (*7*–*10*). Weisz *et al.* erase the which-path information immediately after it is obtained. But what if the information is stored for some time before being deleted? Would this revive a cat that has long been dead? ■

REFERENCES AND NOTES

1. E. Weisz *et al.*, *Science* **344**, 1363 (2014).
2. K. Kang, *Phys. Rev. B* **75**, 125326 (2007).
3. Y. Ji *et al.*, *Nature* **422**, 415 (2003).
4. M. O. Scully, K. Drühl, *Phys. Rev. A* **25**, 2208 (1982).
5. P. G. Kwiat, A. M. Steinberg, R. Y. Chiao, *Phys. Rev. A* **45**, 7729 (1992).
6. T. J. Herzog, P. G. Kwiat, H. Weinfurter, A. Zeilinger, *Phys. Rev. Lett.* **75**, 3034 (1995).
7. Y.-H. Kim, R. Yu, S. P. Kulik, Y. Shih, M. O. Scully, *Phys. Rev. Lett.* **84**, 1 (2000).
8. X. S. Ma *et al.*, *Proc. Natl. Acad. Sci. U.S.A.* **110**, 1221 (2013).
9. A. Peruzzo, P. Shadbolt, N. Brunner, S. Popescu, J. L. O'Brien, *Science* **338**, 634 (2012).
10. F. Kaiser, T. Coudreau, P. Milman, D. B. Ostrowsky, S. Tanzilli, *Science* **338**, 637 (2012).

ACKNOWLEDGMENTS

Supported by NSF grant DMR-1205715.

10.1126/science.1255501

PHOTO: PETER DE KNIJFF

GENETICS

How carrion and hooded crows defeat Linnaeus's curse

How two crow species maintain their identity raises questions about species concepts

By **Peter de Knijff**

Ever since the carrion crow (*Corvus corone*) and the hooded crow (*Corvus cornix*) were described by Linnaeus as two species in 1758 (*1*), their taxonomic status has been debated. These two phenotypically distinct crow taxa have a Palearctic breeding distribution with two stable zones of hybridization, one of which runs roughly north to south through central Europe (*2*) (see the figure). Primarily based on lack of complete reproductive isolation and because of genome-wide genetic homogeneity, they are often considered to represent two subspecies of the carrion crow (*3*, *4*). Some researchers, however, elevated these two taxa to full species in 2003 (*5*), a proposal supported by apparent nonrandom mating and reduced hybrid fitness. Earlier work (*4*) suggested that differences in gene expression, despite the lack of genomic nucleotide divergence, could serve as a sensitive indicator of speciation, although the exact mechanisms driving this process remained unknown. On page 1410 of this issue, Poelstra *et al.* (*6*) show, using a speciation genomics approach (*7*), how differential gene expression of only a small proportion (<0.28%) of the crow genome helps the carrion crow and hooded crow to remain phenotypically distinct.

Carrion crow

Reconstructing exactly how these two crow taxa maintain phenotypic divergence despite substantial gene flow was made possible by combining high-coverage whole-genome sequencing, RNA (transcriptome) sequencing, and a unique set of biostatistical tools. This deceptively simple approach sets a standard for resolving similar speciation issues among other problematic taxa. The near-complete genomes of crows from four distinct populations (two each of the two taxa) were screened for the presence of "speciation islands" (*8*). One particular 1.95-Mb segment, on the avian chromosome 18, showed clear genetic differentiation between carrion crow and hooded crow individuals. This region encompassed 81 of all 83 fixed differences [of 8.4 million single-nucleotide polymorphisms (SNPs) in total] between the two taxa. In this region, a complex pattern of inversions was discovered among carrion crows when compared to hooded crows. RNA-sequencing and gene expression analyses revealed underexpression, among hooded crows, of several genes in this region that are involved in the regulation of pigmentation, visual perception, and hormonal balance. Elsewhere in the crow genome, a number of smaller speciation islands were also found to harbor genes underlying these traits, which were also underexpressed in hooded crows. In this way, Poelstra *et al.* present a unique case of speciation whereby, despite substantial gene flow (especially from hooded crows into German carrion crows), phenotypic divergence likely caused by assortative mating and sexual selection is maintained by genetic variation in less than 1% of the genome.

Ever since Linnaeus (*1*) invoked his taxonomic "curse," by requiring all biologists to use a stringent hierarchical species classification, researchers have been unable to define a single all-inclusive species concept. In this context, it is fascinating to read how 100 years later, Charles Darwin (*9*) dealt with this problem. He simply preferred not to address the issue of species concepts, stating: "But to discuss whether they are rightly called species or varieties, before any definition of these terms has been generally accepted, is vainly to beat the air" [see also (*10*)]. Obviously, forcing complex patterns of biological variation into a single hierarchically structured archive is a purely anthropogenic project. No matter how hard we try, there cannot be a robust, all-inclusive, objective species concept.

Department of Human Genetics, Leiden University Medical Center, Post Office Box 9600, 2300 RC Leiden, Netherlands. E-mail: knijff@lumc.nl

Published by AAAS

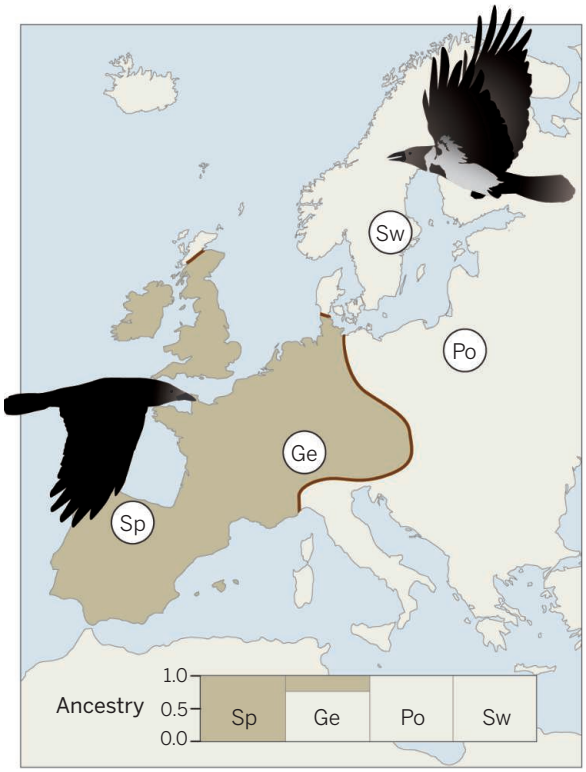

Speciation battleground. On either side of the narrow hybridization zone (dark brown), the carrion crow (*Corvus corone*) (dark area) and hooded crow (*Corvus cornix*) (pale area) (*2*) maintain their marked phenotypic differentiation, despite apparent lack of genetic differentiation. Genome-wide admixture analyses (inset at bottom) show that German carrion crows most closely resemble (80%) hooded crows, and are quite distinct from Spanish carrion crows. Sampling sites for the present study (*6*) are shown as circles. Sp, Spain; Ge, Germany; Po, Poland; Sw, Sweden.

Yet, roughly a decade ago, newly proposed DNA-based taxonomy (*11*) promised to solve the species debate. A Barcode of Life Data Systems (BOLD) (*12*) quickly emerged, seeking to provide a reliable, cost-effective solution to the problem of species identification (*12*) and a standard screening threshold of sequence difference (10× average intraspecific difference) to speed the discovery of new animal species (*13*). Sometimes considered a "caricature of real taxonomy" (*14*), this approach failed to identify, perhaps not surprisingly, two American crow species and a number of members of the herring gull *Larus argentatus* species assemblage above the set threshold (*13*). Furthermore, despite past (*3*) and present (*6*) sequencing projects, carrion crows and hooded crows can also not be differentiated from one another by means of DNA-barcode approaches. By contrast, Poelstra *et al.* show that much more DNA sequencing data are needed, combined with RNA expression data, to reconstruct the evolution of a reproductive barrier that culminated in the speciation of these two crow taxa. Armed with this new very detailed genetic information, it is clear that none of the currently formulated species concepts fully apply to these two crow taxa (unless one is willing relax some stringency in the various definitions). Indeed, the genomes of German carrion crows are much more similar to those of hooded crows than to Spanish carrion crows. Put simply, apart from the few carrion crow type "speciation islands," German carrion crows could be considered to represent hooded crows with a black (carrion crow) phenotype.

There is a clear need for additional population genomic studies using a more dense sampling, especially among the fully black carrion crows, before the complexity of reproductive isolation and speciation among these two taxa can be fully understood. The speciation genomics strategy already proved itself in unraveling the complexities of mimicry among many *Heliconius* butterfly taxa (*7*) and, as in the study of Poelstra *et al.*, stresses the importance of using RNA-based information in addition to DNA. Only time will tell if, and when, German carrion crows will adopt the "hooded phenotype," a fate that seems unavoidable. Until then, we can only applaud these crows for defeating Linnaeus's curse. ■

REFERENCES

1. C. Linnaeus, *Systema Naturae* (Tomus I, Holmiae, Impensis Laurentii Salvii, Stockholm, 1758).
2. S. Cramp, C. M. Perrins, Eds., *The Birds of the Western Palearctic* (Oxford Univ. Press, Oxford, 1994), vol. 8.
3. E. Haring, B. Däubl, W. Pinsker, A. Kryukov, A. Gamauf, *J. Zoological Syst. Evol. Res.* **50**, 230 (2012).
4. J. B. W. Wolf *et al.*, *Mol. Ecol.* **19** (suppl. 1), 162 (2010).
5. D. T. Parkin *et al.*, *Br. Birds* **96**, 274 (2003).
6. J. W. Poelstra *et al.*, *Science* **344**, 1410 (2014).
7. O. Seehausen *et al.*, *Nat. Rev. Genet.* **15**, 176 (2014).
8. J. L. Feder, S. P. Egan, P. Nosil, *Trends Genet.* **28**, 342 (2012).
9. C. Darwin, *On the Origin of Species by Means of Natural Selection* (Murray, London, 1859).
10. K. Winkler *et al.*, *Ornithol. Monogr.* **63**, 30 (2007).
11. D. Tautz, P. Arctander, A. Minelli, R. H. Thomas, A. P. Vogler, *Trends Ecol. Evol.* **18**, 70 (2003).
12. P. D. N. Hebert, A. Cywinska, S. L. Ball, J. R. deWaard, *Proc. R. Soc. London Ser. B* **270**, 313 (2003).
13. P. D. N. Hebert, M. Y. Stoeckle, T. S. Zemlak, C. M. Francis, *PLOS Biol.* **2**, e312 (2004).
14. O. Seberg *et al.*, *Trends Ecol. Evol.* **18**, 63 (2003).

10.1126/science.1255744

RESEARCH CAPACITY

Enabling the genomic revolution in Africa

H3Africa is developing capacity for health-related genomics research in Africa

By **The H3Africa Consortium*†**

Our understanding of genome biology, genomics, and disease, and even human history, has advanced tremendously with the completion of the Human Genome Project. Technological advances coupled with significant cost reductions in genomic research have yielded novel insights into disease etiology, diagnosis, and therapy for some of the world's most intractable and devastating diseases—including malaria, HIV/AIDS, tuberculosis, cancer, and diabetes. Yet, despite the burden of infectious diseases and, more recently, noncommunicable diseases (NCDs) in Africa, Africans have only participated minimally in genomics research. Of the thousands of genome-wide association studies (GWASs) that have been conducted globally, only seven (for HIV susceptibility, malaria, tuberculosis, and podoconiosis) have been conducted exclusively on African participants; four others (for prostate cancer, obsessive compulsive disorder, and anthropometry) included some African participants (www.genome.gov/gwastudies/). As discussed in 2011 (www.h3africa.org), if the dearth of genomics research involving Africans persists, the potential health and economic benefits emanating from genomic science may elude an entire continent.

POLICY

The lack of large-scale genomics studies in Africa is the result of many deep-seated issues, including a shortage of African scientists with genomic research expertise, lack of biomedical research infrastructure, limited computational expertise and resources, lack of adequate support for biomedical research by African governments, and the participation of many African scientists in collaborative research at no more than the level of sample collection. Overcoming these limitations will, in part, depend on African

ILLUSTRATION: P. HUEY/*SCIENCE*. ADAPTED FROM JELMER POELSTRA

Published by AAAS

scientists acquiring the expertise and facilities necessary to lead high-quality genomics research aimed at understanding health problems relevant to African populations and to become internationally competitive in genomic science and its applications.

In June 2010, the U.S. National Institutes of Health (NIH) and UK-based Wellcome Trust, in partnership with the African Society of Human Genetics, announced a plan to enhance the ability of African scientists to apply genomic and epidemiological approaches to shed light on the determinants of chronic and infectious diseases in Africa (*1*). The Human Heredity and Health in Africa (H3Africa) initiative, now funded at $76 million over 5 years, is focused on capacity building, as well as specific scientific goals. H3Africa research grants are awarded directly to African institutions where principal investigators are based (table S1), which allows African scientists to develop and direct their independent research agendas. The program encourages formation of intra-continental collaborations and development of specific infrastructural elements, i.e., African-based biorepositories and a pan-African bioinformatics network (H3ABioNet). H3Africa also includes training programs aimed at retaining African scientists on the continent to help build a sustainable critical mass of researchers. Open calls for research proposals have emphasized collaborations within Africa, plus accessible biorepositories and a bioinformatics network with nodes across the continent (table S2). The footprint of H3Africa extends across Africa (see the map), comprising 21 grants (table S1). It is anticipated that, together, H3Africa projects will analyze samples from 50,000 to 75,000 participants.

H3Africa is predicated on the belief that diseases and nonmedical issues relevant to Africans can be best explored in partnership with inhabitants of Africa (both researchers and research participants) who can provide a rich context and deep knowledge of the continent's past and present environment. African genomes and the unique genetic structure of African populations harbor many clues to understanding human evolutionary history which, in turn, can help shed light on disease etiology. For example, recent genomic studies showed that African Americans (AA) with chronic kidney disease (CKD) who harbor risk variants of the apolipoprotein L1 gene (*APOL1*) have a risk for accelerated CKD progression and the development of end-stage renal disease, that is two to five times normal, respectively (*2*, *3*). These variants also confer 29 times the risk of HIV-associated nephropathy (HIVAN) (*4*). Despite these renal outcomes, the prevalence of the risk genotype is 13% among AA and virtually absent among those of non-African ancestry. The prevailing hypothesis is that APOL1 renal risk variants evolved in sub-Saharan Africa about 10,000 years ago to confer protection against the regionally endemic trypanosome parasite, the cause of African sleeping sickness. Recent studies led by African scientists showed that the frequency of the risk variants, as well as the prevalence of CKD and HIVAN in carriers of the risk variant, are much higher in West Africa (Yoruba, 28%; Igbo, 23%; the major ancestral populations of AA) where the trypanosome parasite is endemic as compared with the non-endemic region of Ethiopia (~1%) (*5*–*7*). The association between CKD and *APOL1* [a component of high-density lipoprotein (HDL) cholesterol] is shedding light on the complicated protective relation between HDL cholesterol and CKD in global populations (*8*). In another example, African scientists participating in H3Africa have used genomic tools to understand how genes interact with life style (barefoot farming practices) to increase susceptibility to podoconiosis, a neglected tropical disease in Ethiopia and Cameroon (*9*).

A key challenge to building critical mass for genomic research in Africa is the retention of scientific leadership capable of developing and maintaining sustainable research programs. The dearth of research-intensive institutions on the continent, coupled with a shortage of funded positions, continues to drive Africa's talented scientists to countries where they have better opportunities to develop their potential and pursue their interests. Furthermore, the African continent lacks a strong history of collaborative scientific endeavor (*10*), as African researchers have turned to their well-resourced counterparts from Europe, North America, and Asia, rather than to their neighbors, to achieve scientific excellence and strong publication records. Consequently, African scientists have not adequately developed the necessary infrastructure and large-scale biomedical research culture required to promote research in Africa. H3Africa has begun building a strong foundation for genomic research based on collaboration among African scientists. Perhaps more important, H3Africa is facilitating

National Institutes of Health Wellcome Trust H3Africa Research Network

*H3Africa Consortium research investigators, funding agencies, and institutions appear in the supplementary materials. †Corresponding author. Charles Rotimi, Center for Research on Genomics and Global Health, National Human Genome Research Institute, NIH, Bethesda, MD 20892–5635, USA. E-mail: rotimic@mail.nih.gov

Published by AAAS

the implementation of the norms and standards for project oversight, goal orientation, and timely dissemination of discoveries and training of the next generation of biomedical researchers across Africa. The consortium is also addressing the use of standardized protocols with detailed attention to community engagement and ethics approval (see below), protocols and policies for sharing biospecimens and data, and publication policies for large collaborative groups.

Approaches to these issues are facilitated by frequent interactions among consortium members to share experiences in developing genomic research programs, to support and promote interactions among the collaborative projects, and to jointly tackle ethical and policy concerns. An important example is data harmonization. By standardizing phenotype measurement and how collected responses are coded to facilitate data merging, statistical power for discovery of genetic variants and for modeling gene-by-environment interactions can be greatly increased.

Implementation of multinational and multiinstitutional genomics research projects in Africa faces additional challenges. Many local ethics review committees have little experience in genomic studies that require broad consent for long-term storage and sharing of biospecimens and data, and some have balked at the concept of global sharing of biospecimens and data with no immediate local benefit, viewing it as another form of exploitation. Several African countries have restrictive legislative policies that hamper sharing across national boundaries. Cultural beliefs and practices regarding donating any body part, including blood, need to be addressed. The growing international debate about return of individual genomic results is also an issue in Africa (*11*). Finally, there are huge disparities across Africa that span rural communities adhering to long-established cultural beliefs and practices on the one hand to sophisticated "citizens of the world" residing in major cities on the other. These communities share genetic heritage, but require different approaches to engagement and informed consent. Thus, H3Africa includes a grant program that supports empirical research on innovative approaches to informed consent; community engagement; and the ethical, legal, social, and cultural factors unique to the African research environment.

The H3Africa Consortium has developed an approach that attempts to balance (i) protection of the ability of African scientists to be the first to analyze and publish findings about their main research questions, given their limited resources and capacity to deal with data as quickly as scientists in developed countries with (ii) the benefit of global access to H3Africa data and biospecimens. To reach these not completely compatible ends, the H3Africa Consortium has agreed that data will be made initially available to the consortium members via H3ABioNet until submission to the European Genome-phenome Archive, from which they will be publicly accessible (through an independent Data and Biospecimen Access Committee). As is common in genomics, there will be a short lag (12 months) between data submission and publication; this is somewhat longer than the norm (6 to 9 months) to provide resource-challenged African investigators a bit more time to analyze and submit their manuscripts for peer review.

Similar considerations went into development of the policy for the release of biospecimens collected in H3Africa. The biospecimens will be stored in an African biorepository (with backup elsewhere on the continent), and from there shared globally for further research. Data and biospecimen sharing does, however, raise the often contentious issues of ownership and commercialization rights. The H3Africa Consortium is addressing this issue while embracing an ethos that promotes research for the global common good. Resources generated by H3Africa are expected to be useful in future genomic research not only in Africa but also globally.

H3ABioNet has also embarked on a program of training and accreditation of its bioinformatics nodes to carry out specific data analysis techniques, i.e., of GWAS or next-generation sequencing data. Part of the training involves a series of workshops, often held at the nodes, to prepare for an accreditation exercise. The accreditation involves giving the nodes raw data sets to analyze, with their results being assessed by an international accreditation committee. One of the major challenges in holding training courses or even just joining working-group Skype calls, is poor Internet connectivity. H3ABioNet is using creative approaches to overcome these issues by seeking low latency alternatives and using portable devices that host data and tools and run independently of the network.

There are several criteria for success that have been defined to assess the accomplishments of the H3Africa initiative (see the table). Each of the component grants has a set of specific, yearly milestones, progress toward which is assessed on an annual basis by the funders (with input from an Independent Experts Committee of outside scientists. Both Wellcome Trust and the NIH will also critically evaluate the progress of H3Africa through peer review toward the end of the initial funding period. Accomplishments of both individual grants and the overall program will be considered in each funder decision process to determine whether continued support is justified.

The efforts of the African scientific community and their international colleagues will not in themselves be sufficient. It is essential that national governments and regional political and economic organizations support sustained funding of all research fields, including genomics and research infrastructure development. In fact, H3Africa has been useful in leveraging additional funding from local sources, as demonstrated by support from the South African Department of Science and Technology to enhance data collection in an H3Africa project of cardiometabolic disease genomics, an early promise of potential long-term success. ■

Measures of success for the 5-year H3Africa program

Publication in high-impact journals with African lead and senior authors
Increased availability of funding for biomedical and genomics research in Africa
Effective operation of a pan-African bioinformatics network
Regular data release
Establishment of one or more full-scale biorepositories
Effective release of samples within and outside of the African continent
Contribution to the ongoing efforts to reverse African "brain drain"
Extension of funding for a second 5 years

REFERENCES AND NOTES

1. *Nature* **465**, 990 (2010).
2. G. Genovese *et al.*, *Science* **329**, 841 (2010).
3. A. Parsa *et al.*, *N. Engl. J. Med.* **369**, 2183 (2013).
4. J. B. Kopp *et al.*, *J. Am. Soc. Nephrol.* **22**, 2129 (2011).
5. D. M. Behar *et al.*, *Am. J. Nephrol.* **34**, 452 (2011).
6. I. I. Ulasi *et al.*, *Nephron Clin. Pract.* **123**, 123 (2013).
7. B. O. Tayo *et al.*, *Int. Urol. Nephrol.* **45**, 485 (2013).
8. A. R. Bentley *et al.*, *Int. J. Nephrol.* **2012**, 748984 (2012).
9. F. Tekola Ayele *et al.*, *N. Engl. J. Med.* **366**, 1200 (2012).
10. R. De Vré *et al.*, Closing the R&D gap in African health care. *McKinsey Quarterly Report* (McKinsey & Co., Washington, DC, June 2010).
11. C. N. Rotimi, P. A. Marshall, *Genome Med.* **2**, 20 (2010).

SUPPLEMENTARY MATERIALS

www.sciencemag.org/content/344/6190/1346/suppl/DC1

10.1126/science.1251546

Published by AAAS

TROPICAL ECOLOGY

But will it grow back?

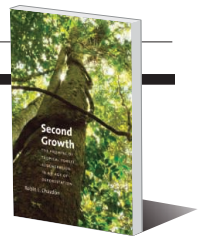

Second Growth
The Promise of Tropical Forest Regeneration in an Age of Deforestation
Robin L. Chazdon
University of Chicago Press, 2014. 469 pp.

By **Valerie Kapos**

Ever since the early 1990s, people I talk to on planes and at parties about what I do (tropical forest ecology and conservation) have invariably said something along the lines of "oh yes, deforestation, it's dreadful … but won't the forest grow back?" The answer is, of course, a combination of "to a degree," "slowly," and "it depends." In *Second Growth,* Robin Chazdon expands comprehensively on the question and the answers for a scientific audience and presents a well-argued case for why they matter.

While deforestation has slowed in many parts of the tropics, land-use change continues to contribute substantially to greenhouse gas emissions and biodiversity loss. Much of the remaining forest has been disturbed and is regenerating; soon, the only forest in some areas will be secondary. Overall, Chazdon suggests, remaining tropical old-growth forests will be insufficient to retain forest biodiversity. This makes it critical to understand how secondary forests compare with, and do or do not fulfill the ecological roles of, old-growth forests. As demographics, economies, and patterns of land use change, cultivation is no longer the sole fate of previously cleared areas. Thus, opportunities are increasing both to study the resulting natural regeneration and to facilitate it or actively alter its course. Forest restoration is rapidly becoming a critical part of the climate change mitigation and biodiversity conservation agendas. Chazdon (an ecologist at the University of Connecticut) summarizes the science that underpins our understanding of the status and importance of secondary forests, the factors that influence regeneration trajectories, and strategies for effective forest restoration efforts.

The book reflects Chazdon's impressive record of research on, and encyclopedic knowledge of, regenerating tropical forests. It pulls together a huge literature (the references occupy more than 110 pages) on topics ranging from the history of human impacts, through pathways of primary and secondary succession and the factors that influence them, to the drivers of reforestation and the importance of landscape in affecting the course of regeneration. For each of these, the author summarizes current knowledge, identifies common themes, and highlights knowledge gaps.

With its range of topics, the table of contents reads more like one from a volume of contributed papers; a thorough review of this breadth is impressive indeed. Everyone will find something new and interesting. For me, the sections on ancient human legacies and forest transformation through prehistory were especially fascinating. They forcefully make the point about the importance of humans in shaping the tropical forests we see today and those of the future.

Perhaps because of the breadth of topics covered, there is a certain amount of repetition among sections, and not all sections contain much in the way of synthesis. Chazdon does an excellent job of reviewing the existing work, but the flow is not always smooth and she doesn't always find a thread to pull together divergent (or even parallel) views of a topic into a clear conclusion. While this accurately reflects the state of the science, readers looking for "answers" will find some sections frustrating. They may be mollified to some degree by the clear explanations of how study designs (and the spatial and temporal realities of regenerating forest landscapes that influence them) often constrain our ability to draw clear conclusions.

Although the book contains some clear and practical guidance on factors that will increase likelihood of successful regeneration or restoration, the scientific review format means that it will appeal more to academics than to decision-makers and practitioners. It will be an especially important resource for students of tropical forest ecology. I set out to dip into particular sections, but found myself reading the book carefully cover to cover while making notes as I would from a textbook. The liberal sprinkling of references to specific current knowledge gaps is especially useful—and might have been even more so if there was a unified summary of them. These cover topics as diverse as landscape-scale effects of logging on species, soil carbon dynamics at depth, effects of spatial variation in species composition on carbon and nutrient cycling during regeneration, and socioeconomic impacts of restoration.

The final two chapters begin to put the academic review of forest regeneration into the wider context of societal needs and concerns. But they only scratch the surface of the challenges and the political, economic, and social complexity entailed in making and taking advantage of opportunities for forest regeneration and restoration, which in many cases boil down to a question of land allocation. Although incentives for climate change mitigation may provide added impetus, the challenges go far beyond gaps in scientific knowledge to fostering cross-sectoral collaboration and integrated land use and landscape planning.

Second Growth combines an in-depth review with an eloquent case for the importance of understanding, promoting, and managing forest regeneration in contexts ranging from climate change to provision of ecosystem services and biodiversity conservation. In doing so, it may help to meet those challenges by providing evidence to ensure that the value of secondary forests is recognized. It will certainly stimulate the science needed to support practical action.

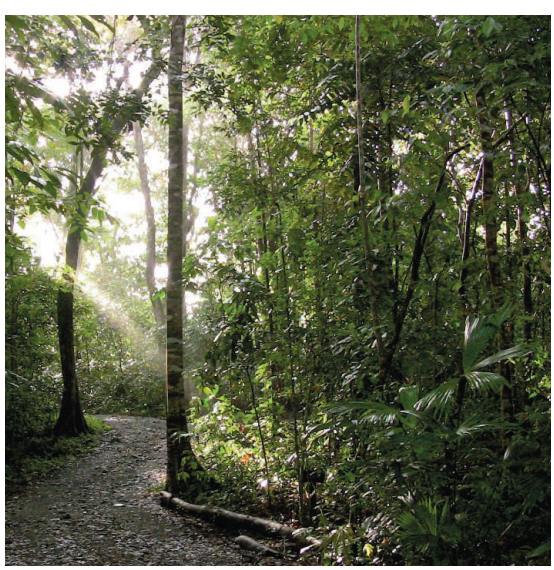

30-year-old second growth forest, Osa peninsula, Costa Rica.

CREDIT: ROBIN CHAZDON

The reviewer is at the United Nations Environmental Programme World Conservation Monitoring Centre, 219 Huntingdon Road, Cambridge CB3 0DL, UK. E-mail: val.kapos@unep-wcmc.org

10.1126/science.1252468

Downloaded from www.sciencemag.org on June 28, 2014

Published by AAAS

PSYCHOLOGY

Ecologically scaled perception

By **Arlene Walker-Andrews**

Coming to Our Senses
Perceiving Complexity to Avoid Catastrophes
Viki McCabe
Oxford University Press, 2014. 285 pp.

Throughout their respective, allied careers, James J. and Eleanor J. Gibson maintained that the received view of perception was incorrect. The traditional view holds that the human perceiver requires a cognitive apparatus to infer reality by making meaning out of ambiguous elementary sensations. Instead, the Gibsons argued that perception was direct and that events in the world lead to changes in perceptible patterns that uniquely specify the event that caused them. This perspective emphasizes that perceivers actively engage the world to learn more about its properties and to contribute to its changing structural character (*1*).

In *Coming to Our Senses: Perceiving Complexity to Avoid Catastrophes*, psychologist Viki McCabe contends that recent disasters stem in great part from three related errors: rejection of the Gibsons' hypothesis; scant attention to the complex, dynamic structure of the environment; and setting aside perceptual evidence in favor of preconceived theories about how the world works. McCabe's argument rests on the Gibsonian view: Humans evolved in a complex, dynamic world and come prepared to detect higher-order structure, yet we often choose to focus on disembodied features from which to infer the truth. Somehow we have conflated perception-based observation and theoretical conceptions that are frequently based on mistaken premises. This can lead to disaster. Far-ranging examples abound. "At 9:54 a.m. on July 3, 1988, the U.S. Navy cruiser *Vincennes* mistakenly shot down Iran Air's Flight 655, killing all 290 people on board." Apparently the radar on each of two vessels (*Vincennes* and *USS Sides*) showed an ascending plane larger than a fighter jet, but the *Vincennes* commander heeded his own beliefs and fired.

To demonstrate the value of relying on perception, McCabe offers the rich observations that a skilled physical therapist uses to diagnose injured patients by watching them as they walk, get out of a car, open doors, or sit. The therapist attends to dynamic structural information that specifies the interaction of a system, in this case the human body with its joints, muscles, and tissues all working together to produce movement.

A harder task for McCabe is to describe how preconceived theories lead to blunders in response to complex circumstances such as climate change or vacillations in economic markets, but she provides chilling illustrations. She argues that scientific theories are closer to direct perception: "Scientists confirm their theories through systematic observation, experimentation, and peer review, and … their results can, on occasion, come close to gaining the status of accepted fact." Nonetheless, sometimes "our culture provides us with theories that distract us and obscure … information." For example, Nobel laureate Barbara McClintock's genetic discoveries were initially discounted. Evidence that genes jump and make new connections flew in the face of conclusions about the immutability of DNA. Furthermore, and crucial to McCabe's thesis, McClintock's "direct perceptual methodology defied the widespread assumption that our senses and the data they access are suspect." Denials of climate change reveal analogous behavior. McCabe's economic examples emphasize that the real world is a dynamic, nonlinear complex system, but attempts at simplification have led to catastrophes. For example, introduction of monoculture crops coupled with adoption of flat field farming is implicated in the Irish famine. McCabe claims that the sale of over-the-counter derivatives divorced from actual products and complex systems of trading goods and services led inexorably to economic collapse in 2008.

Researchers atop sea ice and melt ponds in the Chukchi Sea (July 2011).

Consistent with the Gibsonian approach is that we coevolved with and adapted to this world and that "our perceptions of the physical world carve out receptive pathways that create the interconnected neural structures in our brain. Each new perception amends these patterned channels and in doing so increases their range of responsiveness." Consequently, if not led astray by convictions that we must interpret our sensations, perception becomes more veridical with time, with development, and, especially, with the information sentient beings provide. Our imitative, empathic responses to others' expressions yield comprehension of feelings and a highly tuned ability to understand others' intentions. One aspect missing from McCabe's book is discussion of the development during infancy of the ability to read the world, but she would agree with Eleanor Gibson: "man evolved as a seeker of information, not an intellectual pauper who must build something to believe in, because there would be no truth otherwise" (*2*).

The major thesis of *Coming to Our Senses* is that, indeed, we are building something to believe in rather than perceiving the truth. By failing to trust our senses and reducing the complexity of dynamic systems, we overlook that we live in an "intact complex system that require[s] all of its components working together to sustain the whole." In the Epilogue, McCabe returns to "the example set by the ice." Media and politicians may debate whether climate change exists, but as glaciers disappear, the West Antarctic ice sheet disintegrates, and the effect of ice melt upends ecosystems, we must again attend to sensory data and the evidence provided by technological sensors to respond effectively.

The reviewer at the Department of Psychology and the Office of the Provost, University of Montana, 32 Campus Drive, Missoula, MT 59812, USA. E-mail: arlene.walker-andrews@umontana.edu

REFERENCES AND NOTES

1. M. J. Braund, *Kritike* **2**, 123 (2008).
2. E. J. Gibson, *An Odyssey in Learning and Perception* (MIT Press, Cambridge, MA, 1991).

10.1126/science.1255226

CREDIT: ICESCAPE MISSION/COURTESY NASA EARTH OBSERVATORY

Downloaded from www.sciencemag.org on June 28, 2014

Published by AAAS

LETTERS

Edited by **Jennifer Sills**

Biology's drones: Undermined by fear

IN HIS NEWS & ANALYSIS STORY "Drones flying high as new tool for field biologists" (2 May, p. 459), R. Schiffman reports the use of drone technology for conservation law enforcement to combat the surge in elephant and rhino poaching. This rush to deploy such technologies is based on compelling ideas, partly influenced by narratives that describe the current situation in terms of a war between poachers and conservation staff.

The reality of conservation is much more complicated, as many people live in or around protected areas and depend on them for fuel wood, medicines, and food (*1*). Seen from the ground and through their eyes, drones may be perceived as sinister technologies of surveillance or be associated with warfare and civilian casualties. Such negative perceptions could be seen as a return to fortress conservation, reducing support for protected areas and undermining the relationships on which successful research and conservation projects are built.

Given the rise in poaching activities, one could argue these negative risks are part of a necessary trade-off. However, there are two reasons for doubting the value of such a compromise. First, the long-term cost-effectiveness of drones in deterring poaching remains untested. Second, drone data will only be effective if fed into well-functioning management and legal systems, which are lacking in many countries. Thus, funding for enforcement may be better spent on increasing park staff numbers, resources, and training; developing intelligence networks to catch poachers in the act and identify corrupt officials; and strengthening the judicial system (*2*).

T. Humle,[1]* R. Duffy,[2] D. L. Roberts,[1,3] C. Sandbrook,[4,5] F. A. V St John,[1] R. J. Smith[1]

[1]Durrell Institute of Conservation and Ecology, School of Anthropology and Conservation, University of Kent, Canterbury CT2 7NR, UK. [2]Department of Development Studies, SOAS, University of London, London WC1H 0XG, UK. [3]Interdisciplinary Centre for Cyber Security Research, University of Kent, Canterbury, Kent, CT2 7NF, UK. [4]United Nations Environment Programme World Conservation Monitoring Centre, 219 Huntingdon Road, Cambridge, CB3 0DL, UK. [5]Department of Geography, University of Cambridge, Cambridge CB2 3EN, UK.

*Corresponding author. E-mail: t.humle@kent.ac.uk

REFERENCES

1. W. M. Adams, J. Hutton, *Conserv. Soc.* **5**, 147 (2007).
2. R. Hilborn *et al.*, *Science* **314**, 1266 (2006).

Biology's drones: New and improved

IN THE NEWS & ANALYSIS STORY "Drones flying high as new tool for field biologists" (2 May, p. 459), R. Schiffman presents a new useful application of unmanned aerial vehicles (UAVs) in the field of monitoring wildlife, but the drones still have some limitations. The quadrotor UAVs that they use to drive elephants out of the woods or monitor tigers can only work for a maximum of 20 minutes and have to fly back to the ground station to recharge. In this case, the supervision time that biologists could get from the UAVs will be quite little.

To provide longer working time and finish tasks in different flight conditions, scientists and engineers are working to improve the design of UAVs. At the University of Pennsylvania, researchers have added a mechanical claw at the bottom of a quadricopter (*1*) to allow the UAV to catch a target. At the University of Utah (*2*) and Tsinghua University, UAVs can land in hazardous terrain or even tree branches thanks to their biomimetic design.

Such improvements that merge bionics and robotics together will let UAVs fly inside caves, claw into tunnels, or perch on tress. Biologists or scientists in other fields will then be able to track their targets more effectively.

Cai Luo,* Xiu Li, Qionghai Dai

Department of Automation, Tsinghua University, Beijing, 100084, China.

*Corresponding author. E-mail: luo_cai@tsinghua.edu.cn

REFERENCES

1. J. Thomas, J. Polin, K. Sreenath, V. Kumar, "Avian-inspired grasping for quadrotor micro UAVs" (IDETC/CIE, Portland, OR, 2013).
2. C. Doyle *et al.*, *IEEE/ASME Trans. Mechatronics* **18**, 506 (2013).

Investigative bioethics

IN HIS PLENARY ADDRESS at the 2009 annual meeting of the American Society for Bioethics and Humanities, Carl Elliott challenged attendees to take up the role of the investigative reporter. Many past research scandals, he noted, were not brought to light by traditional scholarship of professional bioethicists. Rather, they were discovered through the diligent efforts of investigative journalists who followed evidence wherever it led and then shared their findings in a way that grabbed the attention of the American public. As newspapers continue to downsize or go bankrupt, Elliott argued, it should be the goal of the bioethics community to fill that role in the realms of clinical research and medicine. J. Couzin-Frankel's Feature "A lonely crusade" (23 May, p. 793) details Elliott's efforts to live by his own words.

I commend Couzin-Frankel for helping to shine a light into those "odd, interesting corners" of psychiatric drug trials of the kind Elliott is investigating. Serious questions remain unsettled about such research, not just the CAFE study in which Dan Markingson, who committed suicide 10 years ago, was a participant: questions of conflicts of interest, the distinctions between research and therapy, standards for assessing competency to provide informed consent, and the adequacy of the

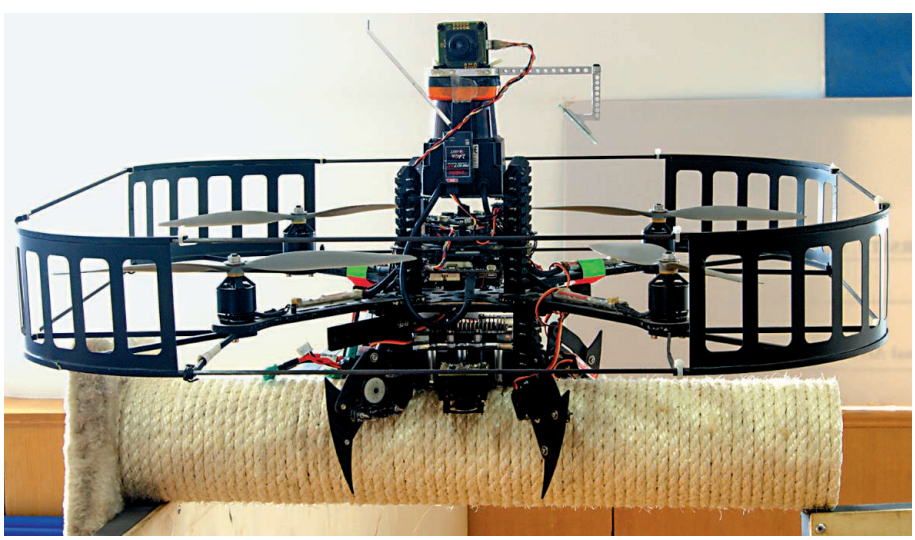

PHOTO: CAI LUO, XIU LI, AND QIONGHAI DAI/DEPARTMENT OF AUTOMATION, TSINGHUA UNIVERSITY

A new, biomimetic design for flying robots allows them to land on a convex cylindrical structure.

Downloaded from www.sciencemag.org on June 28, 2014

Published by AAAS

regulatory framework under which this research takes place. As bioethics is still trying to sort out its features as a discipline, I hope it heeds the example of Elliott and his allies. Otherwise, these issues will not receive the critical examination they warrant and Markingson's story will be, sadly, one of many.

Kyle L. Galbraith

Human Subject Protection, Carle Foundation Hospital, Urbana, IL 61801, USA. E-mail: kyle.galbraith@carle.com

Deep-sea protection: Coordinate efforts

THE PLIGHT OF deep-sea ecosystems in areas beyond national jurisdiction (ABNJ) has been persistently overlooked. As a consequence, they remain very poorly protected despite calls for action dating back more than a decade. In 2002, the United Nations General Assembly called upon intergovernmental organizations including the Food and Agriculture Organization, the Convention on Biological Diversity, and the UN Secretariat itself to urgently consider means to reduce risks to the biodiversity of seamounts and other vulnerable deep-sea habitats within the framework of the United Nations Convention on the Law of the Sea (UNCLOS) (*1*). Since then, various international and regional bodies such as the International Maritime Organization (IMO), the International Seabed Authority (ISA), and Regional Fisheries Management Organizations (RFMOs) began exploring measures and regulations pertaining to shipment; oil, gas, and mineral extraction; and fishing and trawling (*2*). However, these efforts have been slow to materialize, in addition to lacking effective coordination. Therefore, we praise the call by K. J. Mengerink *et al.* ("A call for deep-ocean stewardship," Policy Forum, 16 May, p. 696) for the UN General Assembly to consider the resolution of governance issues of the ABNJ as a priority in its 2015 deliberations.

States agreed during the Rio+20 Conference to address the issue of conservation and sustainable use of marine biological diversity of ABNJ (*3*). This includes a call for the UN General Assembly to consider the wisdom of establishing an international instrument under the UNCLOS to overcome the lack of coordination between different intergovernmental organizations and their respective mandates. Such an instrument could become more effective in promoting comprehensive oceans governance reform within the framework of an already established convention, together with fostering complementarity among relevant organizations.

We also recognize the paucity of funding to generate baseline, protection, and mitigation actions. At the same time, we question whether the multiplication of funding mechanisms would be practical or even desirable. We believe that the finance question should complement the resolution of the key governance issues, while building on existing platforms.

Charlotte Gobin* *and* ***Gustavo A. B. da Fonseca***

Global Environment Facility, Washington, DC 20433, USA.

*Corresponding author. E-mail: cgobin@thegef.org

REFERENCES

1. United Nations, A/RES/57/141 (www.un.org/en/ga/search/view_doc.asp?symbol=A/RES/57/141&Lang=E).
2. E. B. Barbier *et al.*, *Nature* **505**, 475 (2014).
3. United Nations, The Future We Want (www.uncsd2012.org/thefuturewewant.html).

RESEARCH

High-resolution view of lead selenide nanocrystals reveals "necking"
Boneschanscher et al. *p. 1377*

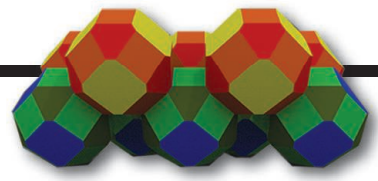

IN *SCIENCE* JOURNALS

Edited by **Stella Hurtley**

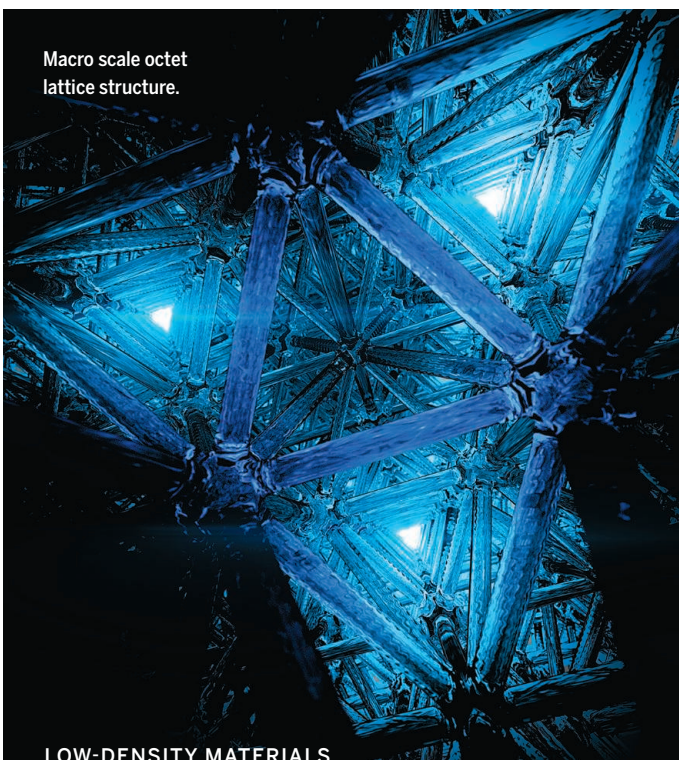

Macro scale octet lattice structure.

LOW-DENSITY MATERIALS

Microlattices make marvelous materials

Framework or lattice structures can be remarkably strong despite their very low density. Using a very precise technique known as projection microstereolithography, Zheng *et al*. fabricated octet microlattices from polymers, metals, and ceramics. The design of the lattices meant that the individual struts making up the materials did not bend under pressure. The materials were therefore exceptionally stiff, strong, and lightweight. — MSL

Science, this issue p. 1373

HUMAN EVOLUTION

Neandertal ancestors from Pleistocene Spain

The Sima de los Huesos site in Atapuerca, northern Spain, is a rich source of fossil hominin specimens. The site has now yielded further skull specimens that illuminate patterns of human evolution in Europe nearly half a million years ago. Arsuaga *et al.* studied 17 crania, including 7 that are new specimens and 6 that are more complete than before (see the Perspective by Hublin). This assemblage of specimens reveals the cranial, facial, and dental features of the Atapuerca hominins, which allows more precise evolutionary positioning of these Neandertal ancestors. — AMS

Science, this issue p. 1358; see also p. 1339

ECOLOGICAL GENOMICS

Crows of a feather flock together

Closely related species with overlapping ranges typically evolve genetic barriers to prevent crossbreeding. Poelstra *et al.* sequenced genes from two species of central European crows: gray-bodied hooded crows and black carrion crows (see the Perspective by de Knijff). Although most of the genomes shared genes between the two species, one region that affected coat color and color vision differed. The authors suggest that black and gray-coated crows prefer to mate with birds like themselves. — LMZ

Science, this issue p. 1410; see also p. 1345

HIV LATENCY

Noisy genes flush HIV out of hiding

HIV can hide in the body, making it hard to kill with drugs. Increasing variation or "noise" in the virus's gene expression turns out to be an effective strategy for reactivating latent HIV. Once reawakened, the virus is more sensitive to antiviral drugs. Dar *et al*. screened for agents that increased variation in the expression of HIV genes. In a model system with HIV-infected human cells, the noise enhancers worked with existing compounds used to reactivate latent HIV and helped eradicate the virus. — LBR

Science, this issue p. 1392

QUANTUM MECHANICS

Creating and erasing quantum knowledge

Particles in the quantum world can also assume wavelike properties. Researchers often use photons to illustrate this particle/wave duality, but electrons interact with each other, which might make them a better choice. Weisz *et al.* used electrons to create a "quantum eraser" (see the Perspective by Feldman). By taking advantage of the electrons' interaction, the researchers first acquired information about the electrons' path—a process that destroys their wavelike properties. Next, they deliberately erased this information in order to recover the electrons' wave nature. — JS

Science, this issue p. 1363; see also p. 1344

NANOPHOTONICS

A controlled launch for plasmons

To create nanophotonic devices, engineers must combine large-scale optics with tiny nanoelectronics. Plasmons, the collective light-induced excitations of electrons at a metal's surface, can bridge that difference in size scales. Alonso-Gonzalez *et al.* placed structured gold "antennas" on top of a graphene layer to launch and propagate plasmonic excitations into the graphene. By carefully

PHOTOS: (TOP TO BOTTOM) BONESCHANSCHER *ET AL.*; RYAN CHEN/LAWRENCE LIVERMORE NATIONAL LABORATORY

Downloaded from www.sciencemag.org on June 28, 2014

Published by AAAS

designing the antennas, the researchers could engineer the wavefronts of the plasmons and control the direction of propagation. This approach illustrates a versatile approach for the development of nanophotonics. — ISO

Science, this issue p. 1369

TOXIN MECHANISM

Breaking through the epithelial barrier

Botulinum neurotoxin (BoNT) poisons its host when it crosses the intestinal epithelial barrier. To help it cross this barrier, the toxin forms a large complex with three bacterial proteins called hemagglutinins (HAs). To find out what happens when this complex binds to a cell-adhesion protein called E-cadherin, Lee *et al.* crystallized the bound complex and protein. Toxin binding disrupted the way E-cadherin maintains the epithelial barrier. When the researchers prevented the toxin complex from binding to E-cadherin, mice were protected from the toxin's deadly effects. — VV

Science, this issue p. 1405

CELL BIOLOGY

Cell proliferation in hard environments

The extracellular matrix that surrounds cells in tissues and organs can be harder or softer. In damaged blood vessels, the extracellular matrix becomes stiffer around the site of damage. Smooth muscle cells that surround blood vessels then proliferate to repair the damage. Bae *et al.* found that stiff surfaces stimulated cell proliferation through a signaling pathway that included the enzyme Rac. Mice that lacked Rac in their smooth muscle cells were unable to repair damaged blood vessels efficiently. — WW

Sci. Signal. **7**, ra57 (2014).

MULTIPLE SCLEROSIS

A surprising culprit attacks the brain

The brain deterioration in mice with a multiple sclerosis (MS)–like disease is exacerbated by a signaling molecule called interleukin-17 (IL-17), raising hopes that MS patients could be treated with drugs that target this cytokine. In an unexpected twist, however, Noster *et al.* find that in humans the culprit is a different cytokine, GM-CSF, a small molecule that promotes inflammation in many autoimmune diseases. What's more, in human patients IL-17 blocked GM-CSF production, a striking contrast to its effect in mice. These data suggest a new rationale for a therapeutic approach in MS patients: decreasing GM-CSF. — AC

Sci. Transl. Med. **6**, 241ra80 (2014).

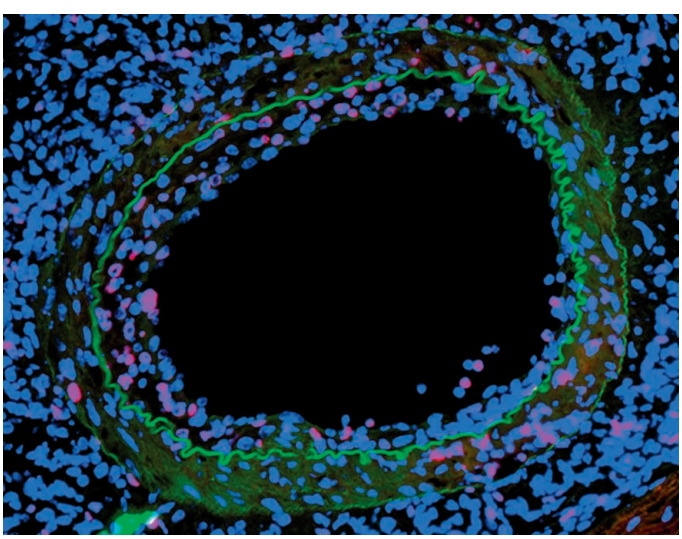

PHOTO: BAE *ET AL.*; ILLUSTRATION: V. ALTOUNIAN/*SCIENCE*

Cross-section of a mouse femoral artery undergoing repair.

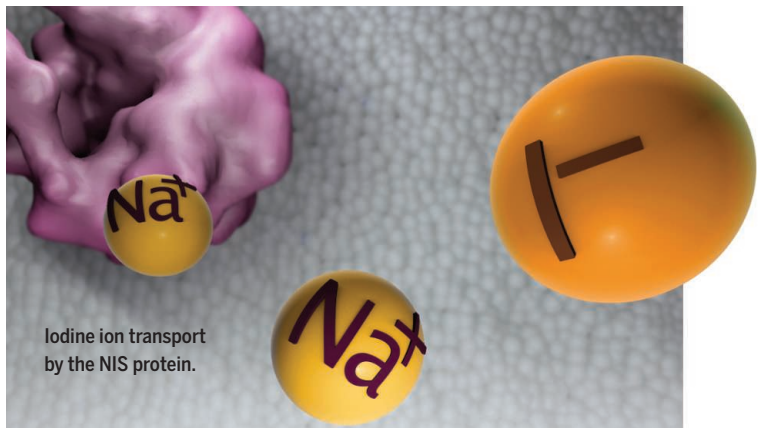

Iodine ion transport by the NIS protein.

ION TRANSPORT

Solving the mystery of iodine uptake

The thyroid gland produces iodine-containing hormones that regulate metabolism. The cell membrane protein NIS (sodium/iodine symporter) transports iodine into thyroid cells, but because iodine concentrations outside of the cell are so low, how it does so is a mystery. The key? Moving two sodium ions along with the iodine ion, Nicola *et al* found. NIS also does not bind sodium very tightly, but the high concentrations of sodium outside the cell allow one sodium ion to bind. This binding increases the affinity of NIS for a second sodium ion and also for iodine. With the three ions bound, NIS changes its conformation so that it opens to the inside of the cell, where the sodium concentration is low enough for NIS to release its sodium ions. When the sodium goes away, so does NIS's affinity for iodine, leading NIS to release it. — VV

Nat. Commun. 10.1038/ncomms4948 (2014).

DISEASE MECHANISMS

An airborne agent of heart disease?

Kawasaki disease is the most common cause of acquired heart disease in children, but even now—40 years after its discovery—doctors still don't know its cause. Infectious and environmental agents are both possibilities. Rodó *et al*. compared daily Kawasaki disease case records in Japan with models of regional air trajectories. Spikes in disease incidence, they found, occurred when the wind blew from an agricultural region in northeastern China. Aerosol samples identified a high abundance of *Candida*, a fungus. Although the results are only a correlation, they support an existing model suggesting that genetically susceptible children may develop the disease when a windborne toxin or environmental agent triggers an aberrant immune response. — BJ

Proc. Natl. Acad. Sci. U.S.A. 10.1073/pnas.1400380111 (2014).
Nat. Genet. 10.1038/ng.2982 (2014)

METABOLIC GENETICS

Genetic variation affects blood metabolites

Genetic variation influences human metabolism dramatically. Understanding the process could help researchers identify drugs and develop better treatments for complex diseases. In a study of over 7000 adults, Shin *et al*. reconstructed metabolic

Published by AAAS

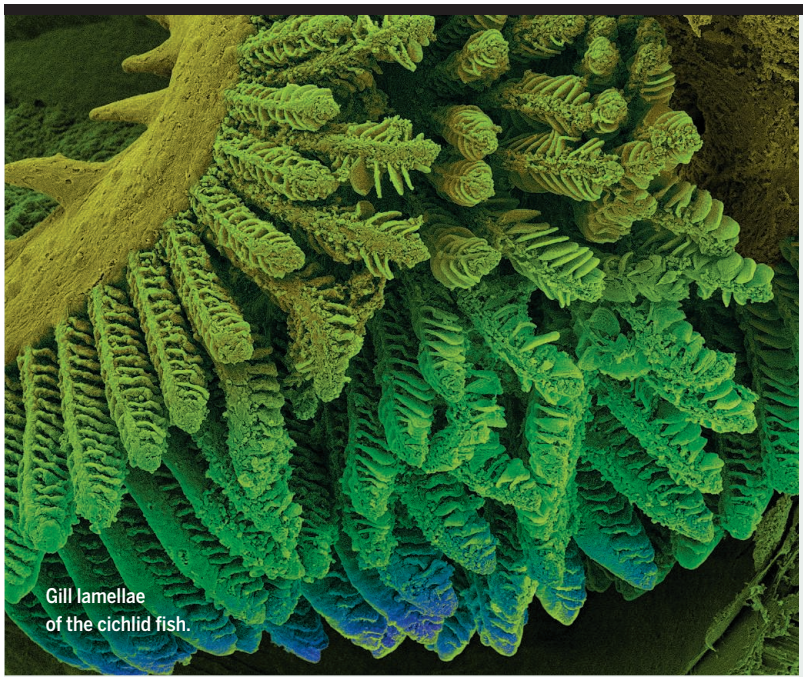
Gill lamellae of the cichlid fish.

PHYSIOLOGY

Gill-on-a-chip illuminates evolution

Fish gills are natural microfluidic devices that evolution has optimized to extract oxygen from water. The spacing between the lamellae, the tiny protrusions that cover gill filaments, varies little between fish of wildly different sizes, which suggests that this spacing is important for gill function. To test this, Park *et al*. developed a mathematical model for oxygen transfer across lamellae. Indeed, they found, lamellae spacing is critical for gill function, as is the way fish pump water through their gills. The researchers then tested their model against an artificial gill—a microfluidic chip where oxygen diffuses across synthetic membranes. When they varied the distance between the membranes, the artificial gill extracted the most oxygen with membrane spacing similar to that of lamellae in fish gills. — GR

Proc. Natl. Acad. Sci. U.S.A. 10.1073/pnas.1403621111 (2014).

pathways by combining genetics with metabolomics, the study of small molecules (aka metabolites) in biological systems. They identified 145 genetic loci, 84 previously unidentified, that they predicted would affect a wide range of biological functions. These 145 genetic loci were connected in a network to 400 biochemically relevant blood metabolites, forming an atlas of metabolites in the blood. Identifying these genetic variants that affect blood metabolites helps us gain a better understanding of human biology and potential treatments for disease. — LMZ

Nat. Genet. 10.1038/ng.2982 (2014).

PALEOCLIMATE

Seasonal rainfall and Indonesian vegetation

Both gradual and abrupt changes in rainfall—similar in many ways to those happening today—had dramatic effects on the vegetation of Indonesia over the past 25,000 years. Dubois *et al.* report that variations in the seasonality of rainfall there, and the resulting water stress during the dry season, caused large swings in the balance between grasslands and forests. Vegetation type depended more on the depth of seasonal dry cycles than on the amount of annual rainfall, they found. These results, obtained by analyzing the stable isotopic composition of fatty acids produced by vascular plants and preserved in marine sediments, reflect the importance of the monsoonal precipitation that's so vital to Indonesian agriculture and human well-being. — HJS

Nat. Geosci. 10.1038/ngeo2182 (2014).

GREEN CHEMISTRY

Making plastic bottles more renewable

All of the components of the plastic used to make clear soda bottles now can be supplied by renewable materials. The polymer polyethylene terphthalate is made from two monomers, ethylene and terphthalic acid (PTA). Chemists already can make ethylene from ethanol produced from plants, but PTA is made by oxidizing *p*-xylene, a petroleum derivative. Pachero and Davis show that a chemical derived on a commercial scale from biomass, 5-hydroxymethylfurfural (HMF), can be converted to PTA with the help of a catalyst called tin-beta. This process opens a route to more environmentally friendly plastic bottle manufacture. — PDS

Plastic bottle made from all-green stock.

Proc. Natl. Acad. Sci U.S.A. 10.1073/pnas.1408345111 (2014).

PHYSICS

A second hump in a superconducting dome

Pure strontium titanate ($SrTiO_3$) does not conduct electricity, but adding tiny amounts of impurities can turn it into a perfect conductor: a superconductor. Lin *et al.* found that, for a particular concentration of extra electrons introduced by adding Nb to the samples, the temperature at which $SrTiO_3$ becomes superconducting (T_c) has a maximum. This concentration coincides with the state when the electrons have filled up one energy band of the material and are just starting to fill up another. By measuring the electrical resistivity of the samples, they found that the overall shape of the T_c dependence on the electron concentration was a two-humped dome. Unlike superconducting domes in other materials, the base of the dome was quite broad and spanned a range of over three orders of magnitude of carrier concentration. — JS

Phys. Rev. Let. **112,** 207002 (2014).

POLAR ECOLOGY

Iceberg scours alter seafloor diversity

The ocean seabed is a patchwork quilt of colors and species. But along the West Antarctic Peninsula, increased iceberg activity—due to climate change and fewer days of frozen seas—is reducing sea floor biodiversity. Icebergs scouring the sea floor temporarily destroy habitat; different species recover at different rates. Barnes *et al.* examined spatial distribution, diversity, interactions between and within species, and ice scour hits near Rothera Research Station from 1997 to 2013. One species, *Fenestrulina rugula*, was quickest to recover; it now dominates, and is involved in, 96% of all interactions. Such reduced diversity could mean more vulnerability to invasive species. — CG

Curr.Biol. 10.1016/j.cub.2014.04.040(2014).

PHOTOS: (TOP TO BOTTOM) DENNIS KUNKEL MICROSCOPY, INC./VISUALS UNLIMITED, INC.; © MAXAL TAMOR/ALAMY

Published by AAAS

ALSO IN *SCIENCE*

Edited by **Stella Hurtley**

NANOMATERIALS

Nanoparticle lattices and surfaces

The challenge of resolving the details of the surfaces or assemblies of colloidal semiconductor nanoparticles can be overcome if several characterization methods are used (see the Perspective by Boles and Talapin). Boneschanscher *et al.* examined honeycomb superlattices of lead selenide nanocrystals formed by the bonding of crystal faces using several methods, including high-resolution electron microscopy and tomography. The structure had octahedral symmetry with the nanocrystals distorted through "necking": the expansion of the contact points between the nanocrystals. Zherebetskyy *et al.* used a combination of theoretical calculations and spectroscopic methods to study the surface layer of lead sulfide nanocrystals synthesized in water. In addition to the oleic acid groups that capped the nanocrystals, hydroxyl groups were present as well. — PDS

Science, this issue p. 1377, p. 1380; see also p. 1340

SOCIAL COGNITION

Learning to read minds starts early

No parent needs reminding that children are born with a surprising set of abilities. But children still need many hours of guidance and instruction. Heyes and Frith review one particular social cognitive skill: reading the minds of others (or at least working out what other people are thinking and feeling). An unrefined capacity for "mind reading" is present in infants, but teaching is necessary to develop the full-blown capacity seen in adults. The authors draw parallels between learning to read and learning to read minds. — GJC

Science, this issue p. 1357

NANOMAGNETISM

Observing jumping domain walls

Domain walls, which separate regions of opposite magnetization in a ferromagnet, have rich dynamics that are difficult to characterize in small samples. Tetienne *et al.* imaged the magnetization of a thin ferromagnetic wire and observed the jumping of a domain wall between different positions along the wire. They used a scanning magnetic microscope based on a defect in diamond. The laser light needed to operate the microscope also enabled the control of the domain wall motion by causing local heating, which made the illuminated position more likely to contain a domain wall. — JS

Science, this issue p. 1366

AGING CELL BIOLOGY

Yeast metacaspase: Grim Reaper or savior?

Yeast metacaspases are structural and possibly functional homologs of caspases that execute apoptosis—programmed cell death—in higher organisms. Malmgren Hill *et al.* tested whether yeast metacaspase Mca1 acts as an executioner or beneficial protein during replicative aging of yeast (see the Perspective by Kampinga). Boosting metacaspase levels caused a substantial and robust extension of life span. This lifespan extension was only partly dependent on the caspase activity of Mca1 but required the presence of the protein disaggregase Hsp104. Consistent with a role in proteostasis, Mca1 was recruited to chaperone-enriched aggregates during aging. Mca1 increased aggregate asymmetry during yeast cytokinesis and counteracted the age-associated accumulation of inclusions. — SMH

Science, this issue p. 1389; see also p. 1341

CANCER GENOMICS

Cancer at single-cell resolution

Single-cell sequencing can illuminate the genetic properties of brain cancers and reveal heterogeneity within a tumor. Patel *et al.* examined the genome sequence of single cells isolated from brain glioblastomas. The findings revealed shared chromosomal changes but also extensive transcription variation, including genes related to signaling, which represent potential therapeutic targets. The authors suggest that the variation in tumor cells reflects neural development and that such variation among cancer cells may prove to have clinical significance. — LMZ

Science, this issue p. 1396

HIV PATHOGENESIS

Adapting HIV-1 to infect monkeys, too

HIV-1 replicates well in humans but not in monkeys or mice. On the up side, this reduces the risk of cross-species transmissions, but it makes the study of HIV-1 and AIDS more difficult. Hatziioannou *et al*. overcame this hurdle by serially passaging HIV-1 in pigtailed macaques. Over time, the HIV-1 acquired mutations that allowed it to adapt to the monkeys. Depleting $CD8^+$ T cells during acute infection resulted in a subset of animals developing an AIDS-like disease by the fourth passage. HIV-1 envelope protein gene selection and the acquisition of mutations in the HIV protein Vpu, which allowed HIV-1 to overcome host restriction by the macaque protein tetherin, accompanied the viral adaptation to the monkeys. — KLM

Science, this issue p. 1401

COMPUTATIONAL BIOLOGY

Cell fate control—a numbers game

Precursor cells in adult mammalian tissues differentiate at very low rates; for example, only 10% of fat cells are replaced per year. If all precursor cells responded to the same threshold of stimulus, these low rates would not be possible. Noise in the system (variability in the abundance of key proteins in different cells) could allow only a few cells to differentiate, but then such variability would allow dedifferentiation as well, which is not observed. Ahrends *et al.* used computational modeling and protein measurements in single cells to show that multiple feedback loops in the regulatory circuits, along with noise, can allow both stable and infrequent differentiation. — LBR

Science, this issue p. 1384

PHOTO: CREDIT GOES HERE AS SHOWN; CREDIT GOES HERE AS SHOWN

Published by AAAS

REVIEW SUMMARY

SOCIAL COGNITION

The cultural evolution of mind reading

Cecilia M. Heyes[1]* and Chris D. Frith[2]

BACKGROUND: We use "theory of mind" or "mind reading" to understand our own thoughts and feelings and those of other agents. Mind reading has been a focus of philosophical interest for centuries and of intensive scientific inquiry for 35 years. It plays a pivotal role in human social interaction and communication. Mind reading allows us to predict, explain, mold, and manipulate each other's behavior in ways that go well beyond the capabilities of other animals; therefore, mind reading is crucial to understanding what it means to be human. In many respects, the capacity to read minds is like the capacity to read print: It involves the derivation of meaning from signs, depends on dedicated brain mechanisms, is subject to specific developmental disorders, shows cultural variation as well as cultural commonality, and has both interpretive (reading) and regulative (writing) functions. However, recent studies of mind reading in young infants suggest that, unlike print reading, mind reading develops very early in human ontogeny.

ADVANCES: In nonverbal tests of mind reading, infants' eye movements have been taken as evidence that infants expect an agent to reach toward a location where he or she believes a desirable object to be hidden, even when the agent's belief is false. This "implicit" mind reading could indicate that humans genetically inherit the specialized neurocognitive mechanisms used for "explicit," verbally mediated mind reading in adulthood. However, recent research with adults shows that, unlike explicit mind reading, implicit mind reading does not make demands on executive function. This indicates that, although they may be genetically inherited, the mechanisms that mediate implicit mind reading, whether specialized or general-purpose, are distinct from those controlling explicit mind reading. Furthermore, studies of twins, people with hearing impairments, and children from non-Western cultures, as well as typically developing Western children, suggest that, like print reading, explicit mind reading is culturally inherited. Rather than being constructed by simulation or theory-testing, explicit mind reading is a skill that is passed from one generation to the next by verbal instruction.

Most, possibly all, human neurocognitive skills are shaped by culture and many are culturally inherited, but the parallels between mind reading and print reading are extraordinary. In contrast, whereas linguistic communities vary in the ways that they categorize colors, color perception is not culturally inherited in the same way as print reading. Unlike print reading, color perception is rooted in highly specialized, genetically inherited mechanisms that humans share with other species. Though cultural input adjusts these mechanisms, it does not make them into a whole new neurocognitive system.

ON OUR WEBSITE

Read the full article at http://dx.doi.org/10.1126/science.1243091

OUTLOOK: The cultural evolutionary account of mind reading does not imply that mental states are mere fictions, but it does suggest that any aspect of mind reading—even those relating to knowledge and primary emotions—could show substantial cultural variation. More cross-cultural studies using sensitively translated test procedures are needed to chart extant variation. Similarly, although the cultural evolutionary account suggests that humans do not genetically inherit mechanisms that are specialized for the representation of mental states, it assumes that, as in the case of print reading, many of the neurocognitive raw materials for explicit mind reading are inborn. Therefore, priorities for future research are to identify the genetic "start-up kits" for both implicit and explicit mind reading and to find out exactly how the products of the former contribute to the development of the latter. Our view suggests that, like print reading, mind reading is a culturally inherited skill that facilitates the cultural inheritance of other, more specific skills; mind reading is a cultural gift that keeps on giving.

PHOTO: TETRA IMAGES/ALAMY

Learning to read minds is like learning to read print. The acquisition of explicit mind reading is a slow, effortful process in which a novice develops an important, culture-specific skill through expert tuition. Experts facilitate development by directing the novice's attention to signs that the novice is on the edge of understanding, as well as by explaining in conversation how these signs relate to their meaning.

[1]All Souls College and Department of Experimental Psychology, University of Oxford, Oxford OX1 4AL, UK. [2]Wellcome Trust Centre for Neuroimaging, University College London, London WC1N 3BG, UK.
*Corresponding author. E-mail: cecilia.heyes@all-souls.ox.ac.uk
Cite this article as C. M. Heyes, C. D. Frith, *Science* 344, 1243091 (2014). DOI: 10.1126/science.1243091

Published by AAAS

REVIEW

SOCIAL COGNITION

The cultural evolution of mind reading

Cecilia M. Heyes[1]* and Chris D. Frith[2]

It is not just a manner of speaking: "Mind reading," or working out what others are thinking and feeling, is markedly similar to print reading. Both of these distinctly human skills recover meaning from signs, depend on dedicated cortical areas, are subject to genetically heritable disorders, show cultural variation around a universal core, and regulate how people behave. But when it comes to development, the evidence is conflicting. Some studies show that, like learning to read print, learning to read minds is a long, hard process that depends on tuition. Others indicate that even very young, nonliterate infants are already capable of mind reading. Here, we propose a resolution to this conflict. We suggest that infants are equipped with neurocognitive mechanisms that yield accurate expectations about behavior ("automatic" or "implicit" mind reading), whereas "explicit" mind reading, like literacy, is a culturally inherited skill; it is passed from one generation to the next by verbal instruction.

"Why did she do that?" Neuroscience tries to answer this kind of question by referring to neural processes, but in everyday life we invoke the actor's thoughts and feelings. We predict and explain behavior by ascribing beliefs, desires, and intentions to the actor; for example, "She destroyed the evidence because she thought it was incriminating," or "She nodded at the auctioneer because she wanted to bid for the Miró." Our ability to ascribe mental states to ourselves and others is known as "theory of mind," "mentalizing," "folk psychology," or "mind reading." It has been a major focus of philosophical investigation for centuries and of scientific enquiry for 35 years (*1*). Mind reading has been studied intensively because it is thought to play a pivotal role in human social interaction and communication. Mind reading allows us to predict, explain, mold, and manipulate each other's behavior in ways that go well beyond the capabilities of other animals. Understanding mind reading is therefore crucial to understanding what it means to be human.

Until now, the term "mind reading" has been used in a casual, eye-catching way to suggest kinship with telepathy or to highlight a superficial resemblance between the ascription of mental states and print reading; both involve the derivation of meaning from signs. In print reading, the signs are marks on paper and their meaning relates to objects and events in the world. In mind reading, the signs are facial expressions, body movements, and utterances, and their meaning relates to the actor's mental states. In this article, we argue that the resemblance goes much deeper (Table 1). We suggest that mind reading, like print reading or literacy, is culturally inherited.

Literate people have neurocognitive mechanisms that are specialized for reading. If literacy were an ancient feature of human life, it would be natural to assume that these mechanisms evolved by genetic means. However, because literacy originated only 5 to 6 thousand years ago, these specialized neurocognitive mechanisms are thought to be products of cultural inheritance or cultural evolution. Cultural evolution has been modeled in a number of ways (*2*). The basic idea is that the reading and writing systems used across the world today have developed, diversified, and been honed by nongenetic evolutionary processes. These processes are evolutionary because they produce change through heritable variation in fitness. However, the inheritance occurs via social learning rather than genetic mechanisms, and fitness is defined by the number of individuals or groups who adopt the system through social learning, rather than by the number of biological offspring. On this kind of evolutionary analysis, when people are trained to read and write, they culturally inherit from their teachers a body of knowledge (for example, about rules governing character inscription and pronunciation) and a set of skills (for example, in distinguishing words from other objects) that are embodied in specialized neurocognitive mechanisms. These mechanisms are constructed or "recycled" (*3*) from genetically evolved mechanisms in the course of literacy training, but they have not been direct targets of gene-based natural selection.

We begin this Review by discussing features of mind reading—its neural bases, developmental disorders, cultural variation, and functions—that might be thought to show that mind reading depends on genetically evolved neurocognitive mechanisms. In each case, we point out that print reading has similar features. Because it is known that print reading is culturally rather than genetically inherited, these similarities between mind reading and print reading clear the way for us to consider the possibility that mind reading is also culturally inherited. In the second section, we discuss recent studies indicating that infants are capable of mind reading. These studies apparently support the view that mind reading depends on genetically evolved mechanisms because there is very little opportunity for cultural inheritance in the first few months of life. However, we will suggest that, when they seem to be mind reading, infants are not using the mechanisms that control "full-blown" or "explicit" mind reading in adults—mechanisms that allow us to deliberate and talk about mental states. In the third section, we turn to direct evidence that explicit mind reading is culturally inherited. This research indicates that, like learning to read print, learning to read minds in an explicit manner is a slow process that depends on instruction (Fig. 1).

Mind reading and print reading

Neural bases

Neuroimaging has shown that adults have cortical circuits specialized for mind reading. These circuits, which include the medial prefrontal cortex, temporo-parietal junction, and precuneus (Fig. 2), are more active when people are thinking about mental states than when they are performing similar tasks that do not involve thinking about mental states (*4*). It is tempting to assume that this sort of cortical specialization is due to genetic evolution. However, similar specialization has been found in the case of print reading. For example, in literate adults an area of the occipito-temporal cortex known as the "visual word form area" is more active during the presentation of words than comparable nonword stimuli (*5*).

Developmental disorders

Many people with autism spectrum conditions (ASCs) have a specific impairment in mind reading. Compared with IQ (intelligence quotient)–and language-matched controls, people with ASCs have difficulty working out what others are thinking and feeling (*6*). There is a substantial genetic contribution to the heritability of ASCs, which might suggest that neurocognitive mechanisms specialized for mind reading are usually genetically inherited and that people with ASCs genetically inherit atypical versions of these mechanisms. But dyslexia reminds us that this is only one of many candidate explanations for the mind-reading impairment associated with ASCs. Dyslexia is a genetically heritable developmental disorder that interferes with the acquisition of a culturally inherited skill: learning to read print (*7*).

Cultural variation

At first glance, it seems that print reading is characterized by cross-cultural diversity and mind reading by cross-cultural commonality. In the print domain, there is certainly a rich diversity of scripts, and the size of the speech units that are mapped onto printed units varies from whole words in Kanji, to syllables in Japanese Kana, to phonemes in alphabetic writing systems (*8*). Furthermore, in the mental domain, it is commonly assumed that

[1]All Souls College and Department of Experimental Psychology, University of Oxford, Oxford OX1 4AL, UK. [2]Wellcome Trust Centre for Neuroimaging, University College London, London WC1N 3BG, UK.
*Corresponding author. E-mail: cecilia.heyes@all-souls.ox.ac.uk

Table 1. Parallels between mind reading and print reading.

Feature	Mind reading	Print reading
Meaning from signs	Mental states from situations and behavior	Referents from inscriptions
Neural specialization	E.g., medial prefrontal cortex and temporo-parietal junction (*4*)	E.g., occipito-temporal "visual word form area" (*5*)
Developmental disorders	Autism spectrum conditions (*6*)	Dyslexias (*7*)
Cultural commonality	Thoughts and feelings can influence behavior (*11*)	Number of strokes per character and degree of redundancy (*9*)
Cultural variation	Importance, range, location, and causation of thoughts and feelings (*10*–*13*)	Importance, range, and medium of print; print-to-pronunciation rules (*8*)
Interpretation	Mental states from situations and behavior	Reading
Regulation	Promotes socially acceptable behavior (*15*, *16*)	Writing and spelling
Implicit competence	Accurate expectations about behavior (*17*–*19*, *25*–*29*)	Pictorial "reading"
Slow development	Specialization continues into late adolescence (*32*–*34*)	Specialization continues into late adolescence (*31*)
Cognitive effort	Uses executive processes (*26*)	Uses executive processes
Individual differences	Due to environmental rather than genetic factors (*35*)	Due to environmental rather than genetic factors (*41*)
Development depends on tuition: engineering	Desires and emotions before beliefs and knowledge (*43*–*45*)	Easy words before hard words
Development depends on tuition: instruction	Causal-explanatory relations among mental states, situations, and behavior (*38*–*41*, *43*–*48*)	Rules relating print to referents and pronunciation

the members of all cultures ascribe thoughts and feelings and understand these states to be related to behavior.

However, recent research suggests that print reading is more (and mind reading is less) uniform across cultures than was previously supposed. For example, featural analysis of 115 writing systems, contemporary and historical, has shown that most characters are formed by three strokes (*9*). In a complementary way, psychological experiments are beginning to reveal substantial cross-cultural variation in the development of mind reading. For example, children in Australia and the United States understand that different people can have different opinions ("diverse beliefs") before they understand that a person can be knowledgeable or ignorant about a particular fact ("knowledge access"). In contrast, children in China and Iran, where individualism and self-expression are less important, understand knowledge access before they understand diverse beliefs (*10*). Research of this kind supports earlier ethnographic data suggesting that cultures vary widely in the importance they assign to mental states, rather than situations, as causes of behavior; whether they take mental states to reside inside or outside the body; and the extent to which they regard mental states as subject to natural rather than supernatural laws (*11*). This research also converges with literary historical studies indicating that, in Western cultures, ideas about the mind and mental disorders have changed radically since ancient times (*12*, *13*).

Interpretation and regulation

Literacy has both interpretative (reading) and regulative (writing) aspects. As children are tutored in the writing conventions of their language, they learn not only to decode printed words (i.e., to relate them to spoken words and to meaning) but also to produce printed words that obey the conventions of their writing system and can therefore be decoded by others. Research on mind reading has emphasized its interpretive role: the way that the attribution of mental states allows us to explain and predict behavior. However, "mental literacy" also has an important regulative role (*14*). Novice mind readers learn that not only can behavior be produced by rational interactions among beliefs and desires, but also that it should be, and they are encouraged to make their own behavior obey these conventions. Recent research in social psychology and cognitive neuroscience has provided clear evidence in support of this regulative hypothesis. When adults are discouraged from believing in free will—for instance, when they are told that deterministic neurological processes, rather than mental states, control behavior—there is a weakening of neural signals

Fig. 1. Learning to read minds is like learning to read print. It is a slow, effortful process in which a novice develops an important, culture-specific skill through expert tuition. Experts facilitate the development of explicit mind reading by directing the novice's attention to signs [(**A**) behaviors, (**B**) words] that the novice is on the verge of understanding. Experts also explain in conversation how these signs relate to their meaning [(A) mental states, (B) objects and events].

associated with action planning (*15*), and they exhibit more antisocial cheating and aggressive behavior (*16*).

Implicit mind reading in infants and adults

In contrast, studies of infants suggest that the development of mind reading is very different from that of print reading. Western children do not typically acquire the skill of print reading until they are 5 or 6 years old, but infants as young as 7 months old seem to be capable of mind reading (*17*). The most notable results suggest that infants ascribe false beliefs to agents; they understand that an agent can believe something that does not match the physical reality of the situation. For example, in a typical experiment (*18*), infants first watch an adult placing a toy in one of two boxes, green rather than yellow, and subsequently reaching repeatedly for that box. Then they see the toy moved from the green box to the yellow box when the adult is present (true-belief condition) or absent (false-belief condition). In the final phase, infants in the true-belief condition show more surprise, measured by looking time, when the adult reaches for the green box rather than the yellow box, whereas infants in the false-belief condition are more surprised when she reaches for the yellow box. In both cases, the infant "expects" a reach toward the box where the adult believes the toy to be located.

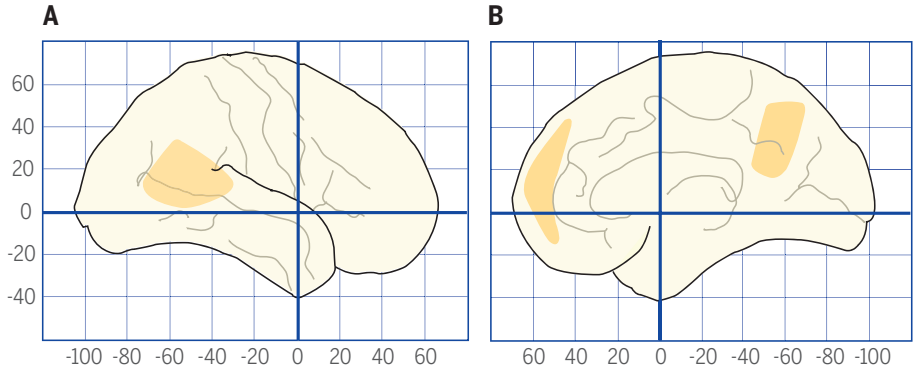

Fig. 2. Brain regions activated by tasks involving mind reading (4). (**A**) A region located on the border of the posterior temporal sulcus and temporo-parietal junction is shown on a diagram of the lateral surface of the right hemisphere embedded in Talairach coordinates. (**B**) Two regions, the medial prefrontal cortex (left) and the precuneus (right), are shown on a diagram of the medial surface of the right hemisphere embedded in Talairach coordinates.

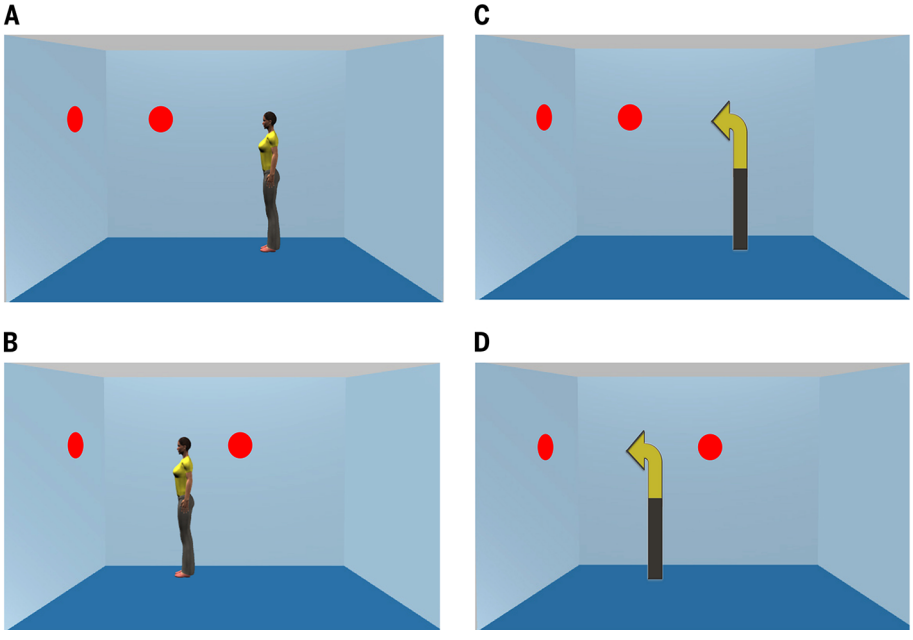

Fig. 3. Stimuli used in the dot perspective task. Adults are asked to report the number of dots they can see. Providing evidence of implicit mind reading, the adults make a faster judgment when all dots are in front of the avatar (**A**) than when some dots are behind the avatar (**B**). This difference also occurs when the central object is an arrow [(**C**) versus (**D**)], suggesting that it may be due to domain-general neurocognitive mechanisms that mediate automatic attentional orienting (*29*).

Research of this kind, which infers the occurrence of mind reading from nonverbal behavior such as looking time, is said to provide evidence of "implicit" mind reading. Implicit mind reading can be interpreted in three ways. The continuity interpretation suggests that it is controlled by the same neurocognitive mechanisms that mediate explicit mind reading in adults (*19*). The two-systems interpretation, favored by Frith, suggests that implicit and explicit mind reading arise from different neurocognitive mechanisms, but both systems are specialized for thinking about mental states (*20*, *21*). This is supported by the case of autism, in which there is evidence of specific failures in mind reading, whereas other domains remain intact (*22*). The implicit system develops early and tracks mental states in a fast and efficient way, whereas the explicit system develops later, operates more slowly, and makes heavier demands on executive functions such as working memory and inhibitory control. In common with the two-systems model, the submentalizing interpretation, favored by Heyes, assumes that explicit mind reading depends on specialized mechanisms that are late developing, slow, and effortful. However, the submentalizing view suggests that implicit mind reading depends on domain-general neurocognitive mechanisms, rather than mechanisms that are specialized for thinking about mental states (*23*, *24*).

The case of autism suggests that implicit and explicit mind reading depend on different mechanisms because explicit mind reading can be achieved in spite of continuing problems with implicit mind reading (*25*). Further evidence for this dissociation is found in studies of neurotypical adults. In tasks in which adults make verbal judgments about other people's thoughts and feelings (explicit mind reading), judgment accuracy is impaired by concurrent performance of an executive function task (*26*). In contrast, concurrent demands on executive function do not interfere with implicit mind reading (*27*). This dissociation is hard to reconcile with the continuity hypothesis but is compatible with the two-systems and submentalizing interpretations of implicit mind reading.

Evidence that implicit mind reading is automatic—that it does not make demands on executive function—comes from a "dot perspective task" in which participants see pictures of a room (Fig. 3). There is a human figure (an "avatar") in the middle of the room, facing to the right or left, and dots on the walls. The participant is required to report the total number of dots in each picture. Implicit mind reading is inferred from the fact that responses are slower and less accurate when some of the dots are behind the avatar than when they are all in front (*28*). On the two-systems account, this "self-other consistency" effect is due to automatic calculation by a specialized system of the number of dots that the avatar can see (i.e., of the content of the avatar's mental state). This automatic

calculation gives a different result from the calculation of the number of dots the participant can see and thus causes interference. On the submentalizing account, the effect is due to automatic attentional orienting to the gaze direction of the avatar (*29*); the same domain-general process that allows inanimate stimuli, such as arrows, to direct attention (*30*).

According to both accounts, however, explicit mind reading—the kind that allows us to deliberate about mental states and to express our thoughts about mental states in words—is like print reading: it develops slowly and is cognitively demanding. The slow development of print reading is reflected in the fact that event-related potentials indicative of reading fluency are not quite as fast in 16 year olds as in mature adults (*31*). Similarly, it is now known that in Western cultures, the neural systems implicated in explicit mind reading (Fig. 2) are among the last to reach maturity (*32*), and performance on explicit tests of mind reading (including perspective-taking, emotion recognition, and detection of pretense and irony) continues to improve between adolescence and adulthood (*33*, *34*).

Learning to read minds

Further evidence that the development of explicit mind reading depends on a slow process of learning, rather than the maturation of genetically inherited neurocognitive mechanisms, comes from a major twin study (*35*). When more than one thousand twin pairs were given a comprehensive battery of explicit mind-reading tests at 5 years old, the correlation in performance within pairs was the same (0.53) for nonidentical twins, with an average of 50% of genes in common, and for identical twins, who have all of their genes common. This indicates a "substantial shared environmental influence but negligible genetic influence on individual differences in theory of mind" (*35*).

However, by itself, this twin study does not tell us about the nature of the environmental influence or the kind of learning involved in the development of explicit mind reading. There are two well-established accounts of mind reading: simulation theory and theory-theory. Although they were previously treated as competing approaches to the explanation of mind reading, it is now widely accepted that these are complementary accounts with theory-theory having a role in explicit high-level mind reading, whereas simulation theory is more relevant to implicit low-level mind reading (*36*). Theory-theory proposes that children learn like scientists, developing explicit theories of how mental states cause behavior through observation and hypothesis testing (*37*). In this case, the ideas are not only honed and tested, but also generated by the novice mind reader herself. In contrast, our cultural evolutionary view suggests that the novice's ideas about the mind are derived primarily not from observation but from instruction, from what the novice is told about the mind by the expert mind readers in her social world.

A "natural experiment" has provided compelling evidence that language-based tuition is crucial in the development of mind reading. This natural experiment was the emergence in the 1970s of a new sign language (NSL) among deaf people in Nicaragua. Pyers and Senghas compared false-belief understanding in two adult cohorts of NSL users. They found that the first cohort, who learned NSL when it was still a rudimentary language, was less able to understand false beliefs than the second cohort, who learned NSL ~10 years later when it included many more signs for mental states. This suggests that although adults in the first cohort were 10 years older—and therefore had 10 years more opportunity to reflect on their own mental states and to watch the behavior of social partners—their understanding of false belief lagged behind that of adults in the second cohort because, lacking mental-state vocabulary, they had not been able to receive instruction about the mind (*38*). These results are supported by a recent study showing that children in Samoa, where it is considered improper to talk about mental states, develop an understanding of false belief at ~8 years of age, 4 or 5 years later than children in Europe and North America (*39*).

In combination with other research involving typically and atypically developing children (*40*, *41*), the NSL and Samoan studies indicate that we learn about the mind through conversation about the mind. In principle, the appropriate conversational experience could come from eavesdropping; that is, by listening to what expert mind readers say when they have no intention of teaching a novice. However, many studies suggest that experts, especially mothers, tailor or "epistemically engineer" (*42*) their conversation about the mind so that it helps children to learn (*43*–*45*). For example, in conversation with their 15 month old children, mothers make proportionally more references to desires and emotions than to thoughts and knowledge, and the frequency of desire/emotion talk selectively predicts the children's explicit mind-reading performance at 24 months. In contrast, at 24 months, mothers talk proportionally more about thoughts/knowledge than desires/emotions, and it is the frequency of references to thoughts/knowledge that predicts explicit mind reading at 33 months (*43*). Desires/emotions are easier to understand because infants and children are constantly attempting to fulfil their desires, and emotions are often reflected in distinctive facial expressions. Therefore, these findings suggest that, just as novice print readers are introduced to easy words before hard words, novice mind readers are introduced to easy states before hard states, and this epistemic engineering of the child's learning environment promotes the development of mind reading.

The development of explicit mind reading is not only predicted by the frequency with which mothers use mental state terms—such as "think," "want," and "happy"—in conversation with their children; it is also predicted by the frequency of mothers' "causal-explanatory" statements about the mind, specifying relations between situations, mental states, and observable behavior. For example, "She is smiling because she is happy," and "She thinks the toy is in the green box because she didn't see it moved to the yellow box" (*41*). In addition, Lohmann and Tomasello (*46*) found that training sessions in which 3 and 4 year olds conversed with an adult about deceptive objects (e.g., a pen that looks like a flower) were especially effective at improving false-belief understanding when the adult used sentential complement syntax: sentences such as "What do you think it is?" and "You say it is a flower," which take a full clause as their object complement. Research on causal-explanatory statements and sentential complements (*47*) suggests that conversation about the mind does not merely teach children labels for mental states. It also teaches them mental state concepts—what it is to "think" or to "feel" something, to be "happy" or "doubtful"—and gives them a format in which to represent these concepts. In other words, children culturally inherit from their parents, and other mind-reading experts (*48*), mechanisms that are specialized for the representation of mental states.

In emphasizing the importance of conversation and the possibility of marked cross-cultural variation, our view is similar to social constructivist accounts of mind reading (*49*). However, unlike many social constructivists, and in common with theory-theory, we assume that the processes involved in the development of explicit mind reading are broadly rational and yield conceptual knowledge about the mind. It is likely that some elements of mind reading, such as those relating to knowing or to primary emotions, will be found to show less cross-cultural variation than others, but our framework allows substantial variation, even in the "heartland" of mind reading. For example, given the structure of the human nervous system, it is likely that, in all cultures, looking is predictive of behaviors that, in many cultures, are understood to indicate knowing. But there could still be substantial variation in beliefs about the relation between seeing and knowing (*50*). Distinctive assumptions about the origin, location, and functioning of mental states will lead the members of different cultures to attend to different aspects of observable behavior, and because mind reading has regulative as well as interpretive functions, distinctive beliefs about the mind will lead to different patterns of observable behavior.

Start-up kit

In contrast with nativist theories of mind reading, our cultural evolution hypothesis suggests that humans do not genetically inherit neurocognitive mechanisms that are specialized for the development of explicit mind reading. Nonetheless, we naturally assume that genetically evolved mechanisms provide much of the raw material for the construction of explicit mind reading: the mechanisms that become specialized for representation of mental states and the processes that make cultural inheritance possible. Our perspective implies that a priority for future research is to identify the genetic "start-up kit" (*22*) for the cultural inheritance of mind reading. No one has made a concerted attempt to train chimpanzees to read minds, but few, if any, researchers would expect this enterprise to be a success. Why? What

are the genetically inherited neurocognitive resources that enable humans, but not chimpanzees, to culturally inherit mind reading?

Implicit mind reading

The healthy human infant comes into the world armed with a number of brain mechanisms that have a critical role in learning about the behavior of others. Some of these mechanisms are primitive and held in common with many other species. However, their presence in humans, in conjunction with dramatically enhanced learning processes, creates the potential for acquiring powerful social abilities. From birth, human infants attend to face-like stimuli and, by the end of their first year, can use faces to recognize identity, race, emotion, and gaze direction (*51*). Human infants also show a preference for observing moving limbs (*52*) and, by the age of 12 months, show predictive eye movements when observing the actions of others (*53*). In other words, they can predict where a movement will end, given how it starts. Infants are also attending to their own movements, thereby creating the link between action observation and action production that generates the motor resonance fundamental to accounts of low-level mind reading associated with simulation theory (*54*).

Much further work is needed to discover how and to what extent these low-level observational mechanisms contribute to the development of explicit mind reading. Again, the analogy with print reading may be helpful. Through listening to speech, the infant discovers statistical regularities that define components such as words and syllables (*55*). The implicit knowledge of such components is a vital precursor for learning how to map sounds onto strings of letters. Likewise, there are detectable statistical regularities associated with body movements derived, in part, from the physical constraints created by gravity and the construction of mammalian bodies (*56*), which define a vocabulary of action components. At the same time, infants, through the experience of their own instrumental actions, are learning to categorize actions in terms of features such as success and efficiency (*57*). This implicit knowledge not only provides a basis for expectations about the outcomes of observed actions (*58*), but also provides predetermined targets for instructions about how mental states are related to actions.

Explicit mind reading

Implicit mind reading emerges from observing the behavior of others. This is a one-way process. The learner observes the actor, who need not be aware that he or she is being observed. In contrast, explicit mind reading emerges from the deliberately instructive behavior of others. This is essentially a two-way process. The behavior of the actor is designed to help the observer learn, and both actor and observer are actively engaged in a communicative process. Components of a start-up kit for such processes might include the preference of newborn infants for faces making eye contact and the preference of very young infants for objects that respond to their own actions with high contingency. By 4 months, gaze following is much more likely to occur if it is preceded by direct eye contact (*59*). Between 12 and 18 months, infants can use eye contact and pointing behavior as signals that distinguish between communicative and noncommunicative interactions (*60*, *61*). This phenomenon of joint attention, in which both parties are aware that they are jointly attending, seems to be distinctly human (*62*).

Conclusions and future directions

We have argued that explicit mind reading is culturally inherited in the same way as print reading. The neurocognitive mechanisms that allow us to deliberate and talk about mental states are constructed, or recycled (*3*), from mechanisms that evolved genetically to fulfill more general functions (to parse and predict dynamic sequences of events and to get information from others), and the construction process depends on tuition. Expert mind readers communicate mental-state concepts, and ways of representing these concepts, to novices. As the present generation of novices becomes expert, it passes on the knowledge and skill of mind reading to the next cultural generation.

Most, possibly all, human neurocognitive skills are shaped by culture, and many are culturally inherited, but the parallels between mind reading and print reading are extraordinary. For example, linguistic communities vary in the ways that they categorize colors, but color perception is not culturally inherited in the same way as print reading. Unlike print reading, color perception is rooted in highly specialized, genetically inherited mechanisms that humans share with other species. Although cultural input adjusts these mechanisms, it does not make them into a whole new neurocognitive system.

The analogy between print reading and mind reading is not perfect. "Sound symbolism" shows that the relations between inscriptions and their corresponding speech sounds and referents often depend on structural features of the nervous system (*63*), but it is likely that these relations are more arbitrary than the relations between observable behavior and mental states. In this respect, numeracy may be a better analog than literacy. However, explicit mind reading is comparable to print reading, not only in terms of its weak dependence on specialized genetically inherited mechanisms and strong dependence on tuition, but also in the shape and size of the cultural legacy. Like print reading, explicit mind-reading mechanisms represent representational relations—between mental states, behavior, and events in the world—and allow the mind reader to regulate and interpret a virtually limitless range of mental contents. Consequently, the print reading and mind reading legacies are also alike in promoting the cultural inheritance of other, more specific skills. Reading and writing enable us to teach others almost anything we know through the written word, and mind reading improves the efficiency of all teaching by allowing the expert to represent what the novice does and does not already understand. Like print reading, mind reading is a cultural gift that goes on giving, a culturally inherited skill that facilitates the cultural inheritance of an enormous range of other, more specific skills (*64*).

We have suggested that in infancy, when the enculturation process is only beginning, implicit mind-reading mechanisms produce, under some circumstances, accurate expectations about the behavior of agents. A priority for future research is to find out whether these implicit mechanisms are specialized for mind reading, or whether implicit mind reading is mediated by domain-general mechanisms. In either case, it is clear that implicit mind-reading mechanisms continue to operate throughout the life cycle, enabling swift social coordination of behavior when time is short and other demands on the neurocognitive system are heavy. It is possible that the outputs of these implicit mechanisms also contribute to the development of explicit mind reading by, for example, segmenting the stream of observable behavior into units that can subsequently be aligned with mental categories. However, in our view, implicit mind reading is radically insufficient for the development of explicit mind reading. Our view suggests that no amount of individual learning—implicit mind reading, introspection, and watching the behavior of others—would be enough for the development of explicit mind reading. If a group of human infants managed to survive on a desert island, in a cruel *Lord of the Flies*–like experiment, they would be no more likely to develop a theory of mind and become explicit mind readers than to develop a writing system and become literate print readers.

REFERENCES AND NOTES

1. D. Premack, G. Woodruff, Does the chimpanzee have a theory of mind? *Behav. Brain Sci.* **1**, 515–526 (1978). doi: 10.1017/S0140525X00076512
2. R. Boyd, P. J. Richerson, J. Henrich, The cultural niche: Why social learning is essential for human adaptation. *Proc. Natl. Acad. Sci. U.S.A.* **108** (suppl. 2), 10918–10925 (2011). doi: 10.1073/pnas.1100290108; pmid: 21690340
3. S. Dehaene, L. Cohen, Cultural recycling of cortical maps. *Neuron* **56**, 384–398 (2007). doi: 10.1016/j.neuron.2007.10.004; pmid: 17964253
4. F. Van Overwalle, Social cognition and the brain: A meta-analysis. *Hum. Brain Mapp.* **30**, 829–858 (2009). doi: 10.1002/hbm.20547; pmid: 18381770
5. S. Dehaene, L. Cohen, The unique role of the visual word form area in reading. *Trends Cogn. Sci.* **15**, 254–262 (2011). doi: 10.1016/j.tics.2011.04.003; pmid: 21592844
6. U. Frith, Mind blindness and the brain in autism. *Neuron* **32**, 969–979 (2001). doi: 10.1016/S0896-6273(01)00552-9 pmid: 11754830
7. S. Paracchini, T. Scerri, A. P. Monaco, The genetic lexicon of dyslexia. *Annu. Rev. Genomics Hum. Genet.* **8**, 57–79 (2007). doi: 10.1146/annurev.genom.8.080706.092312; pmid: 17444811
8. S. Dehaene, *Reading in the Brain: The New Science of How We Read* (Penguin Books, New York, 2009).
9. M. A. Changizi, Q. Zhang, H. Ye, S. Shimojo, The structures of letters and symbols throughout human history are selected to match those found in objects in natural scenes. *Am. Nat.* **167**, E117–E139 (2006). doi: 10.1086/502806; pmid: 16671005
10. A. Shahaeian, C. C. Peterson, V. Slaughter, H. M. Wellman, Culture and the sequence of steps in theory of mind development. *Dev. Psychol.* **47**, 1239–1247 (2011). doi: 10.1037/a0023899; pmid: 21639620
11. A. Lillard, Ethnopsychologies: Cultural variations in theories of mind. *Psychol. Bull.* **123**, 3–32 (1998). doi: 10.1037/0033-2909.123.1.3; pmid: 9461850

12. W. Harris, *Mental Disorders in the Classical World* (Brill, Leiden, Netherlands, and Boston, 2013).
13. C. Burrow, *Epic Romance: Homer to Milton* (Clarendon Press, Oxford, 1993).
14. V. McGeer, "The regulative dimension of folk psychology." in *Folk Psychology Re-Assessed*, D. Hutto, M. M. Ratcliffe, Eds. (Springer, Dordrecht, Netherlands, 2007), pp. 137–156.
15. D. Rigoni, S. Kühn, G. Sartori, M. Brass, Inducing disbelief in free will alters brain correlates of preconscious motor preparation: The brain minds whether we believe in free will or not. *Psychol. Sci.* **22**, 613–618 (2011). doi: 10.1177/0956797611405680; pmid: 21515737
16. R. F. Baumeister, E. J. Masicampo, C. N. Dewall, Prosocial benefits of feeling free: Disbelief in free will increases aggression and reduces helpfulness. *Pers. Soc. Psychol. Bull.* **35**, 260–268 (2009). doi: 10.1177/0146167208327217 pmid: 19141628
17. Á. M. Kovács, E. Téglás, A. D. Endress, The social sense: Susceptibility to others' beliefs in human infants and adults. *Science* **330**, 1830–1834 (2010). doi: 10.1126/science.1190792; pmid: 21205671
18. K. H. Onishi, R. Baillargeon, Do 15-month-old infants understand false beliefs? *Science* **308**, 255–258 (2005). doi: 10.1126/science.1107621; pmid: 15821091
19. R. Baillargeon, R. M. Scott, Z. He, False-belief understanding in infants. *Trends Cogn. Sci.* **14**, 110–118 (2010). doi: 10.1016/j.tics.2009.12.006; pmid: 20106714
20. I. A. Apperly, *Mindreaders: The Cognitive Basis of "Theory of Mind"* (Psychology Press, Hove, UK, and New York, 2011).
21. J. Perner, "Who took the cog out of cognitive science? Mentalism in an era of anti-cognitivism." in *Cognition and Neuropsychology: International Perspectives on Psychological Science*, P. A. Frensch, R. Schwarzer, Eds. (Psychology Press, London, 2010), vol. 1, chap. 15, pp. 241–261.
22. U. Frith, Why we need cognitive explanations of autism. *Q. J. Exp. Psychol.* **65**, 2073–2092 (2012). doi: 10.1080/17470218.2012.697178; pmid: 22906000
23. C. Heyes, False belief in infancy: A fresh look. *Dev. Sci.* (2014). doi: 10.1111/desc.12148; pmid: 24666559
24. C. Heyes, Submentalizing: I am not really reading your mind. *Perspect. Psychol. Sci.* **9**, 131–143 (2014). doi: 10.1177/1745691613518076
25. A. Senju, V. Southgate, S. White, U. Frith, Mindblind eyes: An absence of spontaneous theory of mind in Asperger syndrome. *Science* **325**, 883–885 (2009). doi: 10.1126/science.1176170; pmid: 19608858
26. R. Bull, L. H. Phillips, C. A. Conway, The role of control functions in mentalizing: Dual-task studies of theory of mind and executive function. *Cognition* **107**, 663–672 (2008). doi: 10.1016/j.cognition.2007.07.015; pmid: 17765214
27. A. W. Qureshi, I. A. Apperly, D. Samson, Executive function is necessary for perspective selection, not Level-1 visual perspective calculation: Evidence from a dual-task study of adults. *Cognition* **117**, 230–236 (2010). doi: 10.1016/j.cognition.2010.08.003; pmid: 20817158
28. D. Samson, I. A. Apperly, J. J. Braithwaite, B. J. Andrews, S. E. Bodley Scott, Seeing it their way: Evidence for rapid and involuntary computation of what other people see. *J. Exp. Psychol. Hum. Percept. Perform.* **36**, 1255–1266 (2010). doi: 10.1037/a0018729; pmid: 20731512
29. I. Santiesteban, C. Catmur, S. Coughlan Hopkins, G. Bird, C. Heyes, Avatars and arrows: Implicit mentalizing or domain-general processing? *J. Exp. Psychol. Hum. Percept. Perform.* **40**, 929–937 (2014).pmid: 24377486
30. J. Tipples, Orienting to counterpredictive gaze and arrow cues. *Atten. Percept. Psychophys.* **70**, 77–87 (2008). doi: 10.3758/PP.70.1.77; pmid: 18306962
31. S. Brem *et al*., Evidence for developmental changes in the visual word processing network beyond adolescence. *Neuroimage* **29**, 822–837 (2006). doi: 10.1016/j.neuroimage.2005.09.023; pmid: 16257546
32. S.-J. Blakemore, The social brain in adolescence. *Nat. Rev. Neurosci.* **9**, 267–277 (2008). doi: 10.1038/nrn2353; pmid: 18354399
33. I. Dumontheil, I. A. Apperly, S. J. Blakemore, Online usage of theory of mind continues to develop in late adolescence. *Dev. Sci.* **13**, 331–338 (2010). doi: 10.1111/j.1467-7687.2009.00888.x; pmid: 20136929
34. N. C. Vetter, K. Leipold, M. Kliegel, L. H. Phillips, M. Altgassen, Ongoing development of social cognition in adolescence. *Child Neuropsychol.* 1–15 (2012). pmid: 22934659
35. C. Hughes *et al*., Origins of individual differences in theory of mind: From nature to nurture? *Child Dev.* **76**, 356–370 (2005). doi: 10.1111/j.1467-8624.2005.00850_a.x; pmid: 15784087
36. A. I. Goldman, *Simulating Minds: The Philosophy, Psychology, and Neuroscience of Mindreading* (Oxford Univ. Press, Oxford, 2006).
37. A. Gopnik, H. M. Wellman, Reconstructing constructivism: Causal models, Bayesian learning mechanisms, and the theory theory. *Psychol. Bull.* **138**, 1085–1108 (2012). doi: 10.1037/a0028044; pmid: 22582739
38. J. E. Pyers, A. Senghas, Language promotes false-belief understanding: Evidence from learners of a new sign language. *Psychol. Sci.* **20**, 805–812 (2009). doi: 10.1111/j.1467-9280.2009.02377.x; pmid: 19515119
39. A. Mayer, B. E. Träuble, Synchrony in the onset of mental state understanding across cultures? A study among children in Samoa. *Int. J. Behav. Dev.* **37**, 21–28 (2013). doi: 10.1177/0165025412454030
40. M. Meristo, E. Hjelmquist, G. Morgan, "How access to language affects theory of mind in deaf children." in *Access to Language and Cognitive Development*, M. Siegal, L. Surian, Eds. (Oxford Univ. Press, Oxford, 2012), p. 44.
41. V. Slaughter, C. C. Peterson, "How conversational input shapes theory of mind development in infancy and early childhood." in *Access to Language and Cognitive Development*, M. Siegal, L. Surian, Eds. (Oxford Univ. Press, Oxford, 2012), pp. 3–22.
42. K. Sterelny, *The Evolved Apprentice* (The MIT Press, Cambridge, MA, 2013).
43. M. Taumoepeau, T. Ruffman, Stepping stones to others' minds: Maternal talk relates to child mental state language and emotion understanding at 15, 24, and 33 months. *Child Dev.* **79**, 284–302 (2008). doi: 10.1111/j.1467-8624.2007.01126.x; pmid: 18366424
44. M. Taumoepeau, T. Ruffman, Mother and infant talk about mental states relates to desire language and emotion understanding. *Child Dev.* **77**, 465–481 (2006). doi: 10.1111/j.1467-8624.2006.00882.x; pmid: 16611184
45. E. Meins, "Social relationships and children's understanding of mind: Attachment, internal states, and mind-mindedness." in *Access to Language and Cognitive Development*, M. Siegal, L. Surian, Eds. (Oxford Univ. Press, Oxford, 2012), pp. 23–43.
46. H. Lohmann, M. Tomasello, The role of language in the development of false belief understanding: A training study. *Child Dev.* **74**, 1130–1144 (2003). doi: 10.1111/1467-8624.00597; pmid: 12938709
47. P. A. de Villiers, J. G. de Villiers, Deception dissociates from false belief reasoning in deaf children: Implications for the implicit versus explicit theory of mind distinction. *Br. J. Dev. Psychol.* **30**, 188–209 (2012). doi: 10.1111/j.2044-835X.2011.02072.x; pmid: 22429041
48. K. O'Brien, V. Slaughter, C. C. Peterson, Sibling influences on theory of mind development for children with ASD. *J. Child Psychol. Psychiatry* **52**, 713–719 (2011). doi: 10.1111/j.1469-7610.2011.02389.x; pmid: 21418062
49. J. I. M. Carpendale, C. Lewis, Constructing an understanding of mind: The development of children's social understanding within social interaction. *Behav. Brain Sci.* **27**, 79–96 (2004). doi: 10.1017/S0140525X04000032; pmid: 15481944
50. A. Seeger, *Nature and Society in Central Brazil: The Suyá Indians of Mato Grosso* (Harvard Univ. Press, Cambridge, MA, 1981).
51. M. C. Frank, E. Vul, S. P. Johnson, Development of infants' attention to faces during the first year. *Cognition* **110**, 160–170 (2009). doi: 10.1016/j.cognition.2008.11.010; pmid: 19114280
52. N. F. Troje, C. Westhoff, The inversion effect in biological motion perception: Evidence for a "life detector"? *Curr. Biol.* **16**, 821–824 (2006). doi: 10.1016/j.cub.2006.03.022 pmid: 16631591
53. T. Falck-Ytter, G. Gredebäck, C. von Hofsten, Infants predict other people's action goals. *Nat. Neurosci.* **9**, 878–879 (2006). doi: 10.1038/nn1729; pmid: 16783366
54. V. Gallese, A. Goldman, Mirror neurons and the simulation theory of mind-reading. *Trends Cogn. Sci.* **2**, 493–501 (1998). doi: 10.1016/S1364-6613(98)01262-5; pmid: 21227300
55. P. W. Jusczyk, How infants begin to extract words from speech. *Trends Cogn. Sci.* **3**, 323–328 (1999). doi: 10.1016/S1364-6613(99)01363-7; pmid: 10461194
56. S. M. Thurman, H. Lu, Physical and biological constraints govern perceived animacy of scrambled human forms. *Psychol. Sci.* **24**, 1133–1141 (2013). doi: 10.1177/0956797612467212; pmid: 23670885
57. M. Schlesinger, J. Langer, Infants' developing expectations of possible and impossible tool-use events between ages 8 and 12 months. *Dev. Sci.* **2**, 195–205 (1999). doi: 10.1111/1467-7687.00068
58. A. E. Skerry, S. E. Carey, E. S. Spelke, First-person action experience reveals sensitivity to action efficiency in prereaching infants. *Proc. Natl. Acad. Sci. U.S.A.* **110**, 18728–18733 (2013). doi: 10.1073/pnas.1312322110; pmid: 24167247
59. G. Csibra, Teleological and referential understanding of action in infancy. *Philos. Trans. R. Soc. London Ser. B* **358**, 447–458 (2003). doi: 10.1098/rstb.2002.1235; pmid: 12689372
60. D. A. Baldwin *et al*., Infants' reliance on a social criterion for establishing word-object relations. *Child Dev.* **67**, 3135–3153 (1996). doi: 10.2307/1131771; pmid: 9071774
61. T. Behne, M. Carpenter, M. Tomasello, One-year-olds comprehend the communicative intentions behind gestures in a hiding game. *Dev. Sci.* **8**, 492–499 (2005). doi: 10.1111/j.1467-7687.2005.00440.x; pmid: 16246240
62. M. Carpenter, J. Call, "How joint is the joint attention of apes and human infants?" in *Agency and Joint Attention*, J. Metcalfe, H. S. Terrace, Eds. (Oxford Univ. Press, New York, 2013), pp. 49–61.
63. O. Ozturk, M. Krehm, A. Vouloumanos, Sound symbolism in infancy: Evidence for sound-shape cross-modal correspondences in 4-month-olds. *J. Exp. Child Psychol.* **114**, 173–186 (2013). doi: 10.1016/j.jecp.2012.05.004 pmid: 22960203
64. C. Heyes, Grist and mills: On the cultural origins of cultural learning. *Philos. Trans. R. Soc. London Ser. B* **367**, 2181–2191 (2012). doi: 10.1098/rstb.2012.0120; pmid: 22734061

ACKNOWLEDGMENTS

We thank I. Apperly, J. Call, M. Eimer, U. Frith, A. Gopnik, D. Sperber, and two anonymous referees for their comments on the manuscript (especially the most challenging); V. McGeer, J. Nagel, and N. Shea for valuable discussion in the early stages; and I. Court, T. Court, and C. Catmur for the photographs in Fig. 1.

10.1126/science.1243091

RESEARCH ARTICLE

HUMAN EVOLUTION

Neandertal roots: Cranial and chronological evidence from Sima de los Huesos

J. L. Arsuaga,[1,2]* I. Martínez,[3,1] L. J. Arnold,[4,5] A. Aranburu,[6] A. Gracia-Téllez,[3,1] W. D. Sharp,[7] R. M. Quam,[8,9,1] C. Falguères,[10] A. Pantoja-Pérez,[1,2] J. Bischoff,[11] E. Poza-Rey,[1,2] J. M. Parés,[4] J. M. Carretero,[12] M. Demuro,[4,13] C. Lorenzo,[14,15,1] N. Sala,[1] M. Martinón-Torres,[4] N. García,[1,2] A. Alcázar de Velasco,[1] G. Cuenca-Bescós,[16] A. Gómez-Olivencia,[1,10,17] D. Moreno,[10,12] A. Pablos,[1,4,12] C.-C. Shen,[18] L. Rodríguez,[12] A. I. Ortega,[4] R. García,[12] A. Bonmatí,[1,2] J. M. Bermúdez de Castro,[4] E. Carbonell[15,14,19]

Seventeen Middle Pleistocene crania from the Sima de los Huesos site (Atapuerca, Spain) are analyzed, including seven new specimens. This sample makes it possible to thoroughly characterize a Middle Pleistocene hominin paleodeme and to address hypotheses about the origin and evolution of the Neandertals. Using a variety of techniques, the hominin-bearing layer could be reassigned to a period around 430,000 years ago. The sample shows a consistent morphological pattern with derived Neandertal features present in the face and anterior vault, many of which are related to the masticatory apparatus. This suggests that facial modification was the first step in the evolution of the Neandertal lineage, pointing to a mosaic pattern of evolution, with different anatomical and functional modules evolving at different rates.

The course of human evolution in the Middle Pleistocene is controversial (*1*–*4*). Most of the debate has focused on taxonomic and phylogenetic questions, particularly surrounding the origin of Neandertals and modern humans (*5*–*9*). The European Middle Pleistocene fossil record is important for the timing and pattern of emergence of the Neandertals, but it is composed mainly of isolated and geographically dispersed remains of diverse chronologies. This complicates the evaluation of competing evolutionary scenarios. One of these scenarios, known as the "accretion model," rests on two hypotheses: one regarding the timing of the origin of the Neandertal lineage and the other regarding the pattern of morphological change (*1*, *5*, *10*). Under this model, the Neandertals would have deep roots in the Middle Pleistocene, branching off as early as Marine Isotope Stage 11 [around 400,000 years ago (400 ka)] (*5*, *11*), or even earlier. In addition, the model suggests that the full suite of derived Neandertal features (anatomical and functional modules) did not emerge as a single package, but that different features appeared separately and at different times. In particular, Neandertal facial morphology evolved first, followed by changes in the neurocranium.

Here we analyze a collection of 17 well-dated skulls, including several previously unpublished specimens [Fig. 1, supplementary text S1 (*12*), and table S1], that can be used to test the two pillars of the accretion model. This sample comes from the Sima de los Huesos (SH) Middle Pleistocene site in the Sierra de Atapuerca (Spain) and derives from a single paleo-deme (p-deme). Because the accretion model is based mainly on nonmetric traits (*5*), our analysis emphasizes the pattern of expression of morphological features in the SH hominins, although the descriptive statistics for the principal craniometrical variables in the SH sample are also provided (table S2).

A new age for SH hominins

The SH site is a small chamber at the foot of a shaft located deep inside an underground karst

Fig. 1. Cranium 9 (top left), Cranium 15 (top right), and Cranium 17 (bottom) from SH. Scale bar: 3 cm.

[1]Centro Mixto UCM-ISCIII de Evolución y Comportamiento Humanos, Madrid, Spain. [2]Departamento de Paleontología, Facultad Ciencias Geológicas, Universidad Complutense de Madrid, Spain. [3]Área de Paleontología, Departamento de Geología, Geografía y Medio Ambiente, Universidad de Alcalá, Spain. [4]Centro Nacional de Investigación sobre la Evolución Humana Burgos, Spain. [5]School of Earth and Environmental Sciences, the Environment Institute, and the Institute for Photonics and Advanced Sensing (IPAS), University of Adelaide, Australia. [6]Departamento Mineralogía y Petrología, Facultad de Ciencia y Tecnología, Universidad del País Vasco, Spain. [7]Berkeley Geochronology Center, Berkeley, CA, USA. [8]Department of Anthropology, Binghamton University (State University of New York), Binghamton, NY, USA. [9]Division of Anthropology, American Museum of Natural History, New York, NY, USA. [10]Département de Préhistoire, Muséum National d'Histoire Naturelle, Paris, France. [11]U.S. Geological Survey, Menlo Park, CA, USA. [12]Laboratorio de Evolución Humana, Departamento de Ciencias Históricas y Geografía, Universidad de Burgos, Spain. [13]Institute for Photonics and Advanced Sensing (IPAS), School of Chemistry and Physics, University of Adelaide, Australia. [14]Àrea de Prehistòria, Departamento d'Història i Història de l'Art, Universitat Rovira i Virgili (URV), Tarragona, Spain. [15]Institut Català de Paleoecologia Humana i Evolució Social, Tarragona, Spain. [16]Paleontología, Aragosaurus-IUCA and Facultad Ciencias, Universidad de Zaragoza, Spain. [17]PAVE Research Group, Division of Biological Anthropology, Cambridge, UK. [18]High-Precision Mass Spectrometry and Environment Change Laboratory (HISPEC), Department of Geosciences, National Taiwan University, Taiwan ROC. [19]Institute of Vertebrate Paleontology and Paleoanthropology of Beijing (IVPP), China.
***Corresponding author. E-mail: jlarsuaga@isciii.es**

system (*13*). To date, more than 6500 human fossils from at least 28 individuals are represented in a single stratigraphic level that we have redated using a suite of numerical and relative dating methods (*12*).

The SH sedimentary record can be subdivided into 12 lithostratigraphic units (LU-1 to LU-12) (supplementary text S2). Of these, only LU-6 and LU-7 contain hominin and carnivore remains (Fig. 2). LU-6 consists of plastic red-brown clays with a high density of hominin and carnivore fossils and varying amounts of speleothem intraclasts. U-series dating of a cave raft speleothem deposited directly on a hominin cranium (cranium 4) from LU-6 yielded a mean age of 434 +36/–24 ka (n = 5; supplementary text S3 and S4). We interpret this age to be pene-contemporaneous with the deposition of the cranium. The new age is consistent with the early-Middle to mid-Middle Pleistocene age for the faunal assemblage of LU-6 and LU-7 (supplementary text S5). New paleomagnetic samples collected from four stratigraphic exposures yielded exclusively normal polarities for LU-6 (n = 28; supplementary text S6), consistent with previous paleomagnetic interpretations that the hominin bones accumulated during the Brunhes chron (<780 ka) (*14*). Combined electron spin resonance/uranium-series (ESR/U-series) analysis of a bear tooth from LU-6 provided an age of 261 +26/–25 ka, which is interpreted as a minimum age owing to uncertainties with the geochemical and dosimetry histories of this specimen (supplementary text S7).

The overlying sediments (LU-7) were transported into SH as a debris flow that incorporated large-carnivore bones, mainly those of bears previously accumulated in the Ramp section of the site, and locally eroded and incorporated some hominin and bear fossils from LU-6. The magnetic polarity of LU-7 is normal and consistent with a Brunhes depositional age (n = 9; supplementary text S6). All six of the TT-OSL and pIR-IR ages (428 ± 27 to 441 ± 25 ka for K-feldspar and 396 ± 35 to 429 ± 32 ka for quartz; supplementary text S8) and one of the ESR quartz ages (443 ± 90 ka; supplementary text S7) for this unit are statistically indistinguishable and support sedimentological evidence for a short-lived depositional episode. Although two additional ESR quartz samples taken from LU-7 yielded significantly older ages of 0.9 to 1.5 Ma, these are interpreted as maximum ages owing to potential methodological complications.

Cranial capacities and encephalization quotient (EQ)

The cranial capacity can only be measured directly in crania (Cr.) 4, 5, and 6 (*15*, *16*). Twelve other crania in the SH collection are sufficiently well preserved to allow for a good estimation of the cranial capacity on the basis of endocast scaling (Fig. 3 and supplementary text S9). The mean of the SH cranial capacities (1232 cm^3; n = 15, table S3) is clearly above the Asian *Homo erectus* mean. It is also well below the Neandertal and Pleistocene *H. sapiens* means and similar to the mean of the non–*H. erectus* Middle Pleistocene sample (fig. S1). The mean EQ obtained for the SH hominins (3.27) is lower

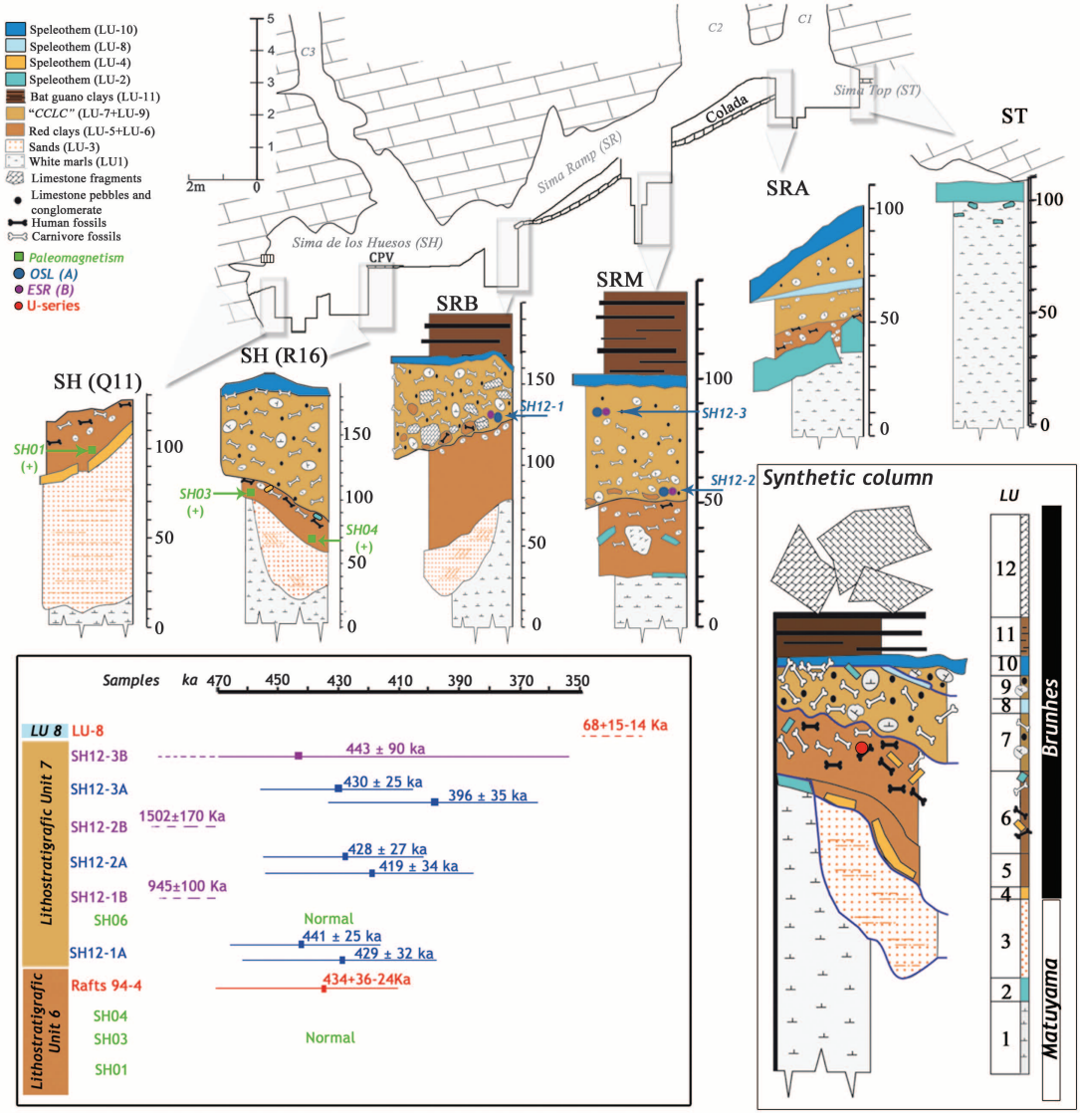

Fig. 2. Cross-section of SH showing the different stratigraphic columns exposed throughout the site. The composite stratigraphic section is shown, as are the sampling positions and ages obtained. The colors used correspond to those of the Munsell color for wet sediment. The inferred geomagnetic polarity zones are based on the results presented in this study for LU-5 to LU-7, and results for LU-2 to LU-10 were presented in (*14*, *45*).

than in modern humans and Neandertals (tables S4 and S5).

Cranial regions (Table 1)

Cranial vault

In the SH crania, the opisthocranion lies on the occipital plane, but the difference with the cranial length taken on the occipital torus is small. In contrast, in early *Homo* and Asian *H. erectus*, the opisthocranion always falls on the occipital torus. This same condition can be found at Ceprano. In *H. sapiens* and Neandertals, the opisthocranion lies clearly on the occipital plane of the occipital bone, well above the superior nuchal line. Although the SH occipital plane exhibits a certain degree of curvature, it is considerably less curved than in Neandertals, and there is no occipital bun ("chignon").

The temporal squama outline is consistently very convex in the SH sample, with an arched or subtriangular superior border, as seen in African and European Middle Pleistocene hominins (MPHs), Neandertals, and *H. sapiens*. The angular torus is absent in most SH specimens, although there are hints of it in some cases (Cr. 2, 5, 7), and it is more clearly expressed in Cr. 4. Arago and Ceprano are the only other European MPHs that clearly show this structure.

The maximum cranial breadth consistently lies in a low position, but the lateral cranial walls are either parallel or slightly convergent superiorly. This condition is similar to other European MPHs (Swanscombe, Steinheim, Reilingen, Petralona) and departs from the primitive state of convergent lateral walls of the braincase in early *Homo* and Asian *H. erectus* (*17*, *18*). It is also different from the derived conditions seen in Neandertals (circular outline) and most *H. sapiens* (divergent lateral walls with marked parietal bosses) (*19*–*21*).

The occipital torus of the SH specimens is generally weak, and mainly developed in the central region of the occipital squama, fading out toward the asterion. The tori are straight, do not have depressions in the middle, and are not bilaterally projecting, in contrast to Neandertals. Above the torus there is always a large central semicircular area, which is flat or even slightly convex and shows a concentration of small circular excavations. This pattern is attenuated, however, in Cr. 1, 4, and 5 (all mature adults). The flat, central, and semicircular supratoral area is clearly distinguishable from the rest of the occipital plane, and the opisthocranion lies precisely on its superior limit. A similar suprainiac morphology can be found in the Swanscombe sample. However, this individual shows more of a depression and the occipital torus is bilaterally projecting, as in Steinheim and Neandertals. Although the "cratered" surface of the SH specimens could be interpreted as reminiscent of the Neandertal suprainiac fossa (*16*, *19*), the latter is smaller, clearly sunken, and more inferiorly oriented. The SH condition is also different from that of the Vertëszöllos sample, which exhibits a high and slightly inflated occipital "torus" without a flat or depressed suprainiac area (*20*).

Most of the SH crania show a supraorbital torus that is double-arched and rounded (smoothly rolled) in a parasagittal section (though Cr. 13 shows a slight "torsion" between the glabellar segment and the more lateral parts of the ridge). There is no division of the torus into separate arches, although a shallow depression can be seen occasionally in the glabellar region (e.g., Cr. 13). The general SH pattern closely approaches the derived Neandertal morphology of the supraorbital torus and is clearly different from that of Arago, Kabwe, and Ceprano (being closer to Petralona).

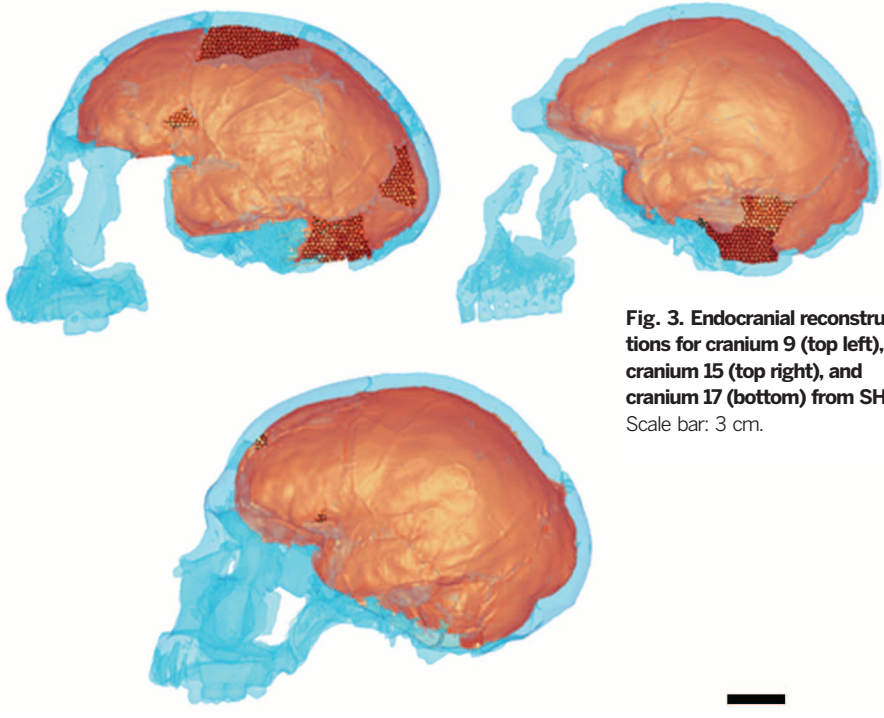

Fig. 3. Endocranial reconstructions for cranium 9 (top left), cranium 15 (top right), and cranium 17 (bottom) from SH. Scale bar: 3 cm.

Facial skeleton

The inferior malar border in the SH sample is gently arched, and the zygomatic root is located midway between the low (Neandertal) and the high (modern human) placements. The nasal root projects sagittally to the same degree as glabella (i.e., it is not depressed), and the nasal bones are horizontally oriented. In addition, the nasal spine is placed in a forward position in the SH specimens, with zygomaxillary angles within the Neandertal range of variation (fig. S10). There is some maxillary flexion, so that the infraorbital plate and the lateral wall of the nasal cavity do not form the same plane. Thus, there is an advanced degree of midfacial prognathism in the SH midface, but it is not as inflated, smooth, and retreating as in Neandertals.

Unlike the nasal morphology of Neandertals (*22*), a raised rim of the internal nasal margin is not formed in any SH cranium, and the transition between the clivus and the nasal cavity floor is smooth. The lateral nasal crest fades out in the nasoalveolar clivus at the level of the I^2, without merging with the spinal crest or reaching the nasal spine. Moreover, as has been noted by others (*23*), the "medial projection" [a wide, broad-base mass in the nasal wall that protrudes medially into the nasal cavity (*22*)] typical of the Neandertals is not seen in the SH sample. Finally, the nasal floor of the SH specimens is level or sloped and never sunken or bilevel, as is found in many Neandertals (*24*).

The dental arcade of the SH hominins generally shows approximately parallel postcanine toothrows and a frontal alignment of the anterior dentition, resulting in a fairly square outline. A more exaggerated expression of this dental arcade shape can be seen in Petralona and is also variably present in Neandertals.

Basicranium

The mastoid processes are more projecting than the weakly developed juxtamastoid eminence, particularly in the adult individuals, and no anterior mastoid tubercle is present in the SH sample. For these three features, the SH sample displays primitive morphology and contrasts with the derived Neandertal condition (*10*, *21*). The tympanic plate is coronally oriented in nearly all the SH specimens, which is a primitive condition also seen in Neandertals. The styloid process is fused to the basicranium, which is the primitive character state for the genus *Homo*, with Asian *H. erectus* showing a derived (non-fused) styloid process (*25*). Unlike in Neandertals (*26*), the styloid process is aligned with the stylomastoid foramen and the digastric groove in the SH sample.

A large postglenoid process is characteristic of Neandertals (*27*) and European MPHs (e.g., Steinheim, Bilzingsleben G1), but in the SH crania it is even more developed. In contrast, the articular

Table 1. Morphological traits in SH crania. See figs. S2 to S9 for illustration of the traits on the SH cranial sample and table S6 for the individual scores.

Trait	State
Occipital torus shape	Straight in inferior and posterior views: *N* = 9
Occipital torus extension	Fading toward the asterion: *N* = 8 Extends to the asterion: *N* = 2 (Cr. 1, Cr.4)
Oval-shaped area of dense "cratered" surface placed above the occipital torus	Present: *N* = 10
Maximum cranial breadth	At the supramastoid crest: *N* = 12
Parietal wall sides orientation in posterior view	Slightly convergent or parallel: *N* = 13
Opisthocranium location	At the upper margin of the suprainiac surface: *N* = 8
Opisthocranium not coincident with inion	Yes: *N* = 7 Absent: *N* = 13
Parietal angular torus	Weak: *N* = 3 Strong: *N* = 1 (Cr. 4)
Temporal squama	High and very convex (arched or triangular) superior border: *N* = 12
Mastoid process	Well projecting from the surrounding occipitomastoid region: *N* = 9
Anterior mastoid tubercle	Absent: *N* = 12
Postglenoid process	Well developed: *N* = 11
Articular eminence	Flattened: *N* = 11
Tympanic plate orientation	Coronally: *N* = 10 Sagittally: *N* = 1 (Cr. 4)
Styloid process	Fused to the basicranium: *N* = 12
Styloid process position	Aligned with the stylomastoid foramen and the digastric groove: *N* = 12
Supraorbital torus shape	Continuity of the lateral, orbital and glabellar segments: *N* = 10 Change of plane between the glabellar and orbital segments: *N* = 1 (Cr. 13)
Glabellar region shape	Inflated region without a midline depression: *N* = 10 Inflated but with a midline depression: *N* = 1 (Cr. 13)
Nasal bones projection	Projecting: *N* = 5
Nasal root sagittal position	At the same level as the glabella: *N* = 7
Internal nasal rim	Absent: *N* = 7
Middle projection of the walls of the nasal cavity	Absent: *N* = 7
Infraorbital plate morphology	The infraorbital plate is not diagonally oriented as in Neanderthals, nor coronally as in modern humans; the maxilla is inflated and there is no canine fossa; the zygomaxillaryalveolar crest is straight or gently arched and the root is placed midway between the low (Neandertal) and the high (modern human) character states: *N* = 7
Maxillary torus	Present: *N* = 1 (Cr. 15; but reduced to tubercles) Absent: *N* = 5

eminence is weakly developed in the SH sample, as in Neandertals and European MPHs (*25*, *28*). These traits could be functionally related to the low position of the mandibular condyle present in SH, and in some other European MPHs and Neandertals (*29*) (see below). Thus, the anterior portion of the temporal bone (functionally related to the masticatory apparatus) shows derived Neandertal features, whereas the posterior (occipitomastoid) region remains primitive.

Mandibles and dentition

The SH mandibles also show several derived Neandertal features (*30*, *31*). The sample is morphologically consistent, although some size-related variation is present, with larger specimens generally showing more posteriorly placed structures of the lateral corpus and larger retromolar spaces than smaller individuals (fig. S9). In addition, the SH mandibles show an asymmetrical configuration of the superior margin of the ramus, with a relatively low position of the condyle, a medial insertion of the incisure crest at the condyle. and a well-developed lateral pterygoid fossa on the medial aspect of the condylar neck. This suite of ramus features has been suggested to reflect a masticatory specialization in Neandertals (*29*).

Besides these derived Neandertal features, some distinctions from the Neandertals, reflecting the retention of primitive features, are also apparent. The SH mandibles show a more retreating symphyseal angle, and wider bigonial breadth (table S2), reflecting the general absence of truncation and inversion of the gonial margin typical of Neandertals. The ramus is wider in SH and the horizontal/oval (H-O) form of the mandibular foramen is absent (except in AT-2553). Finally, on the internal aspect of the mandibular corpus, the mylohyoid line is less diagonally inclined, and the submandibular fossae are shallower for the SH hominins.

The SH dentition presents most of the morphological traits usually considered characteristic of the Neandertals (*32*). In addition, the SH hominins have some likely homoplastic features that are particular to this population and are comparable to those of modern humans but are not found in other archaic *Homo* taxa (*33*). These include absolutely small posterior teeth (*34*), similar intermolar size ratios, frequent absence of hypoconulid and hypocone, and the pattern of cusp proportions in the M^1 (*33*, *35*, *36*).

Discussion

The chronology established for LU-6 and LU-7, on the basis of several independent techniques with reproducible results, provides a minimum age of ~430 ka for the SH human fossils, which is some 100 ka younger than previously reported (*37*). With this new age, the SH hominins are now the oldest reliably dated hominins to show clear Neandertal apomorphies. Notably, the improved chronology for the SH assemblage is compatible with the latest dental and genetic evidence for Middle Pleistocene evolutionary divergences (*38*, *39*) and enables us to state with certainty that the modern human/Neandertal most recent common ancestor dates to sometime before ~430 ka (pre–MIS 11).

The considerably enlarged SH cranial sample is morphologically quite homogeneous. In addition to some plesiomorphic traits in the cranial vault (such as the low position of the maximum cranial breadth), derived Neandertal traits are present in the midfacial projection, morphology of the supraorbital torus, and the glenoid cavity. Although the occipital morphology is not Neandertal-like, there is a flat supratoral surface that may be derived in the direction of the Neandertals. Finally, the SH mandibles and the dentition also show a derived Neandertal pattern, together with some distinctive dental features. In sum, the SH sample shows a constellation of derived Neandertal facial, dental, mandibular, and glenoid features that appears to represent a single functional masticatory complex. At the same time, the cranial vault lacks Neandertal specializations. This mosaic pattern fits the prediction of the accretion model for the first stage of Neandertal evolution.

Concerning the taxonomy of the SH fossils, we have long maintained that the SH hominins are members of the Neandertal lineage (*16*, *40*). Based on the cranial evidence, we have proposed that the SH fossils, as well as the rest of the European early and middle Middle Pleistocene specimens, should be assigned to the species *Homo heidelbergensis* defined in a broad sense to include fossils with a generally more primitive morphology than the late Middle Pleistocene and Late Pleistocene Neandertals, even if they exhibit some derived Neandertal traits (*19*). However, the difficulty with identifying derived Neandertal features in the Mauer mandible, the type specimen of *H. heidelbergensis*, contrasts strongly with the presence of numerous Neandertal apomorphies in the SH mandibles (*41*). On this basis, we suggest that the SH sample be removed from the *H. heidelbergensis* hypodigm. An alternative view of *H. heidelbergensis* is as a Middle Pleistocene taxon that includes only fossils that lack any Neandertal apomorphies, and, in this restricted sense, the species is seen as the stem group for Neandertals and modern humans (*7*).

In addition, the new evidence presented here based on cranial morphology confirms that the SH population differs from some other European MPHs, such as Ceprano and Arago, that do not exhibit the suite of derived Neandertal features seen in SH. Thus, more than one evolutionary lineage appears to have coexisted during the European Middle Pleistocene (*42*), with that represented by the SH sample being phylogenetically closer (i.e., a sister group) to the Neandertals.

Some authors have, indeed, recommended that the SH fossils be included in *H. neanderthalensis* (*5*, *7*) as early members of this evolutionary lineage. However, although we agree that the SH hominins are members of the Neandertal clade, the present analysis has shown that they differ from Neandertals in several cranial regions that are considered taxonomically diagnostic of *H. neanderthalensis*. We argue that the SH p-deme is sufficiently different from that of *H. neanderthalensis* so as to be considered a separate taxon. Whether this difference should be recognized on the specific or subspecific level is currently an open question.

Related to this, a nearly complete mitochondrial genome recently sequenced from a SH femur (*43*) groups with two Denisovan individuals rather than with Neandertals. This surprising result might seem to contradict our morphological interpretation of the SH population belonging to the Neandertal clade. However, based on analysis of their nuclear genome, the Denisovans are considered a sister group to Neandertals (*44*). It is possible that two deeply divergent mitochondrial DNA (mtDNA) lineages coexisted in the SH population, one that later characterizes the Denisovans and another (as yet undocumented) mtDNA lineage that became fixed in Neandertals. Alternatively, it is possible that gene flow from another hominin population (not belonging to the Neandertal clade) brought the Denisova-like mtDNA into the SH population or its ancestors. The latter scenario would imply that two different hominin clades (the Neandertal clade and another more primitive clade) coexisted in Europe for some time, an interpretation that is not contradicted by the fossil evidence. Retrieving additional mitochondrial or nuclear DNA sequences from the SH sample may help clarify our understanding.

It is important to underline that the morphology of the SH crania, mandibles, and teeth is very constant for those features that have been considered taxonomically relevant, without polymorphisms or different trait combinations. This finding was not a foregone conclusion, because the SH variation could have encompassed the range of variation found among different European fossils that are broadly contemporaneous. However, it is clear that there is more variation between demes in the European mid Middle Pleistocene than there is within the SH deme. The morphological variability among a single p-deme can be used to distinguish between anagenetic (linear) or cladogenetic (branching) patterns of evolution. The former implies that the population as a whole (of which any particular p-deme is but one component) evolves in a similar direction throughout its geographic range, and that the individual p-demes show a large degree of intrademe morphological variation. In contrast, the latter is more consistent with the cladogenetic model and implies that evolutionary change occurs via sorting between p-demes, which individually show little intrademe variation.

Although the accretion model is potentially consistent with either an anagenetic or cladogenetic mode of evolution, our morphological analysis of the SH sample fits the latter more closely. Moreover, the scenario of several demographic crashes influenced by climatic crisis throughout the European Middle Pleistocene would produce p-deme sorting, with extinction of some populations and replacement by others (*5*). The presence in the SH skulls of Neandertal-derived regions that can be functionally related in modules, together with others that remain primitive, combined with the pre-MIS 11 age of the sample, confirms the accretion model of Neandertal origins. Finally, the finding that these derived Neandertal features are functionally related with the masticatory complex suggests that the origin of the Neandertal clade coincides with a masticatory specialization.

REFERENCES AND NOTES

1. J.-J. Hublin, *Geobios Mem. Spec.* **15**, 345–357 (1982).
2. G. P. Rightmire, *Evol. Anthropol.* **17**, 8–21 (2008).
3. C. B. Stringer, in *Ancestors: The Hard Evidence*, E. Delson, Ed. (Liss, New York, 1985), pp. 285–295.
4. J. H. Schwartz, I. Tattersall, *Am. J. Phys. Anthropol.* **143** (suppl. 51), 94–121 (2010).
5. J. J. Hublin, *Proc. Natl. Acad. Sci. U.S.A.* **106**, 16022–16027 (2009).
6. G. P. Rightmire, *Evol. Anthropol.* **6**, 218–227 (1998).
7. C. Stringer, *Evol. Anthropol.* **21**, 101–107 (2012).
8. I. Tattersall, *Proc. Natl. Acad. Sci. U.S.A.* **106**, 16018–16021 (2009).
9. M. H. Wolpoff, in *The Human Revolution: Behavioural and Biological Perspectives in the Origins of Modern Humans*, P. Mellars, C. Stringer, Eds. (Edinburgh Univ. Press, Edinburgh, 1989), pp. 62–108.
10. D. Dean, J. J. Hublin, R. Holloway, R. Ziegler, *J. Hum. Evol.* **34**, 485–508 (1998).
11. C. B. Stringer, J. Hublin, *J. Hum. Evol.* **37**, 873–877 (1999).
12. Supplementary materials are available on *Science* Online.
13. J. L. Arsuaga *et al.*, *J. Hum. Evol.* **33**, 109–127 (1997).
14. J. M. Parés, A. Pérez-González, A. B. Weil, J. L. Arsuaga, *Am. J. Phys. Anthropol.* **111**, 451–461 (2000).
15. J. L. Arsuaga, I. Martínez, A. Gracia, *Anthropologie* **105**, 161–178 (2001).
16. J. L. Arsuaga, I. Martínez, A. Gracia, J. M. Carretero, E. Carbonell, *Nature* **362**, 534–537 (1993).
17. P. Andrews, *Cour. Forsch. Inst. Senckenberg* **69**, 167–175 (1984).
18. B. A. Wood, *Cour. Forsch. Inst. Senckenberg* **69**, 99–111 (1984).
19. J. L. Arsuaga, I. Martínez, A. Gracia, C. Lorenzo, *J. Hum. Evol.* **33**, 219–281 (1997).
20. J. J. Hublin, *C. R. Acad. Sci. Paris Ser. D* **287**, 923-926 (1978).
21. C. B. Stringer, J. J. Hublin, B. Vandermeersch, in *The Origin of Modern Humans: A World Survey of the Fossil Evidence*, F. H. Smith, F. Spencer, Eds. (Liss, New York, 1984), pp. 51–135.
22. J. H. Schwartz, I. Tattersall, *Proc. Natl. Acad. Sci. U.S.A.* **93**, 10852–10854 (1996).
23. J. H. Schwartz, I. Tattersall, M. Teschler-Nicola, *Anat. Rec.* **291**, 1517–1534 (2008).
24. R. G. Franciscus, *J. Hum. Evol.* **44**, 701–729 (2003).
25. I. Martínez, J. L. Arsuaga, *J. Hum. Evol.* **33**, 283–318 (1997).
26. M. Elyatqine, thesis, Université Bordeaux I, France (1995).
27. S. Condemi, in *L'Homme de Neandertal*, E. Trinkaus, Ed. (Etudes et Recherche Archéologiques de l'Université de Liége, Liège, France), 1988), vol. 3, pp. 49–53.
28. I. Martínez, R. Quam, J. L. Arsuaga, *Period. Biol.* **108**, 309–317 (2006).
29. Y. Rak, A. Ginzburg, E. Geffen, *Am. J. Phys. Anthropol.* **119**, 199–204 (2002).
30. J. Daura *et al.*, *J. Hum. Evol.* **49**, 56–70 (2005).
31. A. Rosas, *Am. J. Phys. Anthropol.* **114**, 74–91 (2001).
32. M. Martinón-Torres, J. M. Bermúdez de Castro, A. Gómez-Robles, L. Prado-Simón, J. L. Arsuaga, *J. Hum. Evol.* **62**, 7–58 (2012).
33. M. Martinón-Torres *et al.*, *J. Anat.* **223**, 353–363 (2013).
34. J. M. Bermúdez de Castro, *J. Hum. Evol.* **15**, 265–287 (1986).
35. J. M. Bermúdez de Castro, M. E. Nicolas, *Am. J. Phys. Anthropol.* **96**, 335–356 (1995).
36. A. Gómez-Robles, J. M. Bermúdez de Castro, M. Martinón-Torres, L. Prado-Simón, J. L. Arsuaga, *J. Hum. Evol.* **63**, 512–526 (2012).
37. J. L. Bischoff *et al.*, *J. Archaeol. Sci.* **34**, 763–770 (2007).
38. P. Endicott, S. Y. W. Ho, C. Stringer, *J. Hum. Evol.* **59**, 87–95 (2010).
39. A. Gómez-Robles, J. M. Bermúdez de Castro, J.-L. Arsuaga, E. Carbonell, P. D. Polly, *Proc. Natl. Acad. Sci. U.S.A.* **110**, 18196–18201 (2013).
40. J. L. Arsuaga, J. M. Carretero, I. Martínez, A. Gracia, *J. Hum. Evol.* **20**, 191–230 (1991).

41. Y. Rak *et al.*, *Am. J. Phys. Anthropol.* **144**, 247 (2011).
42. I. Tattersall, in *Continuity and Discontinuity in the Peopling of Europe: One Hundred Fifty Years of Neanderthal Study*, S. Condemi, G.-C. Weniger, Eds. (Springer Science+Business Media B.V., New York, 2011), chap. 4.
43. M. Meyer *et al.*, *Nature* **505**, 403–406 (2014).
44. M. Meyer *et al.*, *Science* **338**, 222–226 (2012).
45. L. J. Arnold *et al.*, *J. Hum. Evol.* **67**, 85–107 (2014).

ACKNOWLEDGMENTS

We are grateful to the Atapuerca team, especially A. Esquivel for work in SH and M. C. Ortega for restoration of the SH fossils, and to K. Ludwig, J. Rofes, and J. M. López-García for constructive discussions. E. Santos assisted with computed tomography scanning and J. Trueba provided the photos. For access to the comparative materials, we thank P. Mennecier, A. Froment, H. de Lumley, D. Grimaud-Hervé, C. B. Stringer, R. Kruszynski, G. D. Koufous, D. Mania, D. Lieberman, and J. Haas. A.G.-T. has a contract from the Ramón y Cajal Program (RYC-2010-06152). R.M.Q. received financial support from BU-SUNY and the AMNH. A.P.-P. has a MECD grant (AP-2009-4096). E.P.-R. has a CAM grant (S2010/BMD-2330). A.A.V. has a MINECO grant (BES-2010-039961). A.G.-O. and M.D. have a Marie Curie–IEF and a Marie Curie–IRG (PIRG8-GA-2010-276810) contracts. N.S., A.B., L.R., A.P.-P., A.A.V., and R.G. received Fundación Atapuerca grants. L.J.A. has an ARCFF grant (FT130100195). Dating at the Berkeley Geochronology Center was supported by the Ann and Gordon Getty Foundation. U-Th isotopic analysis at the HISPEC was supported by Taiwan ROC MOST and NTU grants (100-2116-M-002-009, 101-2116-M-002-009, 101R7625). Thanks to SGIker-UPV/EHU for their research facilities. This research was supported by the MINECO (CGL2012-38434-C03-01 and 03) and the JCyL (BU005A09, DGR 2009 SGR-324) projects. Fieldwork was funded by the JCyL and the Fundación Atapuerca. Junta de Castilla y León is the repository of the fossils.

SUPPLEMENTARY MATERIALS

www.sciencemag.org/content/344/6190/1358/suppl/DC1
Materials and Methods
Supplementary Text S1 to S9
Figs. S1 to S39
Tables S1 to S15
References (*46*–*178*)

26 March 2014; accepted 12 May 2014
10.1126/science.1253958

REPORTS

QUANTUM MECHANICS

An electronic quantum eraser

E. Weisz,* H. K. Choi,* I. Sivan, M. Heiblum,† Y. Gefen, D. Mahalu, V. Umansky

The quantum eraser is a device that illustrates the quantum principle of complementarity and shows how a dephased system can regain its lost quantum behavior by erasing the "which-path" information already obtained about it. Thus far, quantum erasers were constructed predominantly in optical systems. Here, we present a realization of a quantum eraser in a mesoscopic electronic device. The use of interacting electrons, instead of noninteracting photons, allows control over the extracted information and a smooth variation of the degree of quantum erasure. The demonstrated system can serve as a first step toward a variety of more complex setups.

Complementarity in quantum measurements is a core concept of quantum mechanics (*1*), closely related to Heisenberg's uncertainty principle, although the exact relation between the two remains a source of debate (*2*–*8*). An example of complementarity is the double-slit interference experiment: If we measure a particle's position, the measurement will quench its wavelike nature; vice versa, observing the wave behavior via interference implies lack of knowledge of the particle's path. A canonical system for exploring complementarity is the quantum eraser, predominantly studied in photonic systems (*9*–*16*). A quantum eraser is an interference experiment consisting of two stages. First, one of the interfering paths is coupled to a "which-path" detector, resulting in loss of interference due to acquisition of which-path information. Second, the which-path information is being "erased" by projecting the detector's wave function on an adequately chosen basis; this renders the which-path information inaccessible, which allows reconstruction of the interference pattern.

Here, we present an implementation of a quantum eraser in an electronic system. Our system consists of two identical electronic Mach-Zehnder interferometers (MZIs) (*17*) entangled via Coulomb interactions. Initially proposed by Kang (*18*) and studied theoretically in (*19*, *20*), this setup consists of two MZI: one serving as a path detector and the other as the system interferometer, where the visibility of the Aharonov-Bohm (AB) oscillation in the system can be controlled by the detector (*21*–*23*).

An electronic MZI is formed by manipulating quasi–one-dimensional, chiral edge channels, which are formed in the integer quantum Hall effect regime (*17*). Potential barriers, formed by quantum point contacts (QPCs), take the role of optical beam splitters, transmitting and reflecting impinging electrons with amplitudes t_i and r_i, respectively, where $|t_i|^2 + |r_i|^2 = 1$ and $t_i, r_i \in R$. Two such coupled MZIs are shown in Fig. 1, where the coupling is mediated by the lower path of the system and the upper path of the detector, referred to as interacting paths (shaded area in Fig. 1A).

Starting with the system, an electron injected from source S1 arrives at SQPC1 and is put into a superposition of being reflected into the interacting path and transmitted into the noninteracting path, namely, $|S\rangle = r_1|\uparrow\rangle_S + t_1|\downarrow\rangle_S$, with $|\uparrow\rangle_S$ and $|\downarrow\rangle_S$ standing for the interacting and noninteracting paths of the system, respectively. The paths recombine and interfere at SQPC2, with the electron's probability of reaching the drain D2 being $P(\mathrm{D2}) = |r_1 r_2 e^{i\phi_S} - t_1 t_2|^2 = T_0 - T_1\cos(\phi_S)$, where $T_0 \equiv |t_1 t_2|^2 + |r_1 r_2|^2$, $T_1 \equiv 2t_1 t_2 r_1 r_2$, $\phi_S = 2\pi AB/\Phi_0$ is the AB phase (*24*), $\Phi_0 = h/e$ is the magnetic flux quantum, A the area enclosed by the two paths, and B the magnetic field. The visibility of the interfering pattern at D2 is defined as $v_{\mathrm{D2}} \equiv \frac{\max[P(\mathrm{D2})] - \min[P(\mathrm{D2})]}{\max[P(\mathrm{D2})] + \min[P(\mathrm{D2})]} = \frac{T_1}{T_0}$. Throughout our experiments, all the QPCs were tuned to have equal transmission and reflection amplitudes, $|r_i|^2 = |t_i|^2 = \frac{1}{2}$; $i = 1...4$.

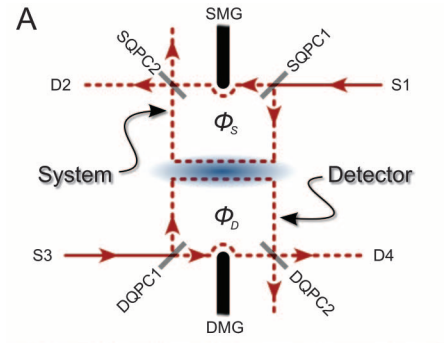

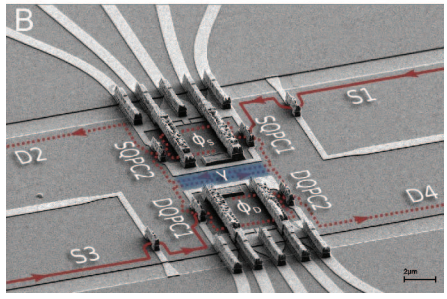

Fig. 1. Schematics and micrograph of the device under study. (**A**) The electronic quantum eraser consists of two identical electronic Mach-Zehnder interferometers (MZIs) entangled via Coulomb interactions. Quantum point contacts (QPCs) serve as beam splitters (full lines represent full beams, and dashed lines partitioned beams). (**B**) A scanning electron microscope micrograph of the fabricated structure, which was realized in a GaAs-AlGaAs heterostructure harboring a high-mobility two-dimensional electron gas. The edge channels were manipulated by biasing surface gates (bright gray) and surface etching. Ohmic contacts serve as sources (S1, S3) and drains (D2, D4), which allow electric access to the electron gas lying underneath the surface. The nanostructures were defined using electron-beam lithography.

Braun Center for Submicron Research, Department of Condensed Matter Physics, Weizmann Institute of Science, Rehovot 76100, Israel.
*These authors contributed equally to this work. **†Corresponding author. E-mail: moty.heiblum@weizmann.ac.il**

The Coulomb interaction between two electrons passing simultaneously in the interacting paths causes a slight mutual repulsion, which affects their trajectories and reduces the AB area in each MZI by δA_γ, which therefore adds a phase shift $\gamma = \delta A_\gamma B/\Phi_0$ (*25*). The closer the interacting edges, the larger the phase shift. The states of the detector are $|0\rangle_D = \frac{1}{\sqrt{2}}\,(e^{i\phi_D}|\uparrow\rangle_D + |\downarrow\rangle_D)$, if the system's electron passes through the noninteracting path, and $|\gamma\rangle_D = \frac{1}{\sqrt{2}}(e^{i(\phi_D+\gamma)}|\uparrow\rangle_D + |\downarrow\rangle_D)$, if it passes through the interacting path. The system-detector complex is thus in an entangled state $|\Psi\rangle = \frac{1}{\sqrt{2}}(|\downarrow\rangle_S|0\rangle_D + e^{i\phi_S}|\uparrow\rangle_S|\gamma\rangle_D)$, where the detector's state provides which-path information about the system. Consequently, the system is dephased, as is evident from its transmission probability $P(\mathrm{D2}) = \frac{1}{2} - \frac{1}{2}\mathrm{Re}(e^{i\phi_S}\langle 0|\gamma\rangle_D) = \frac{1}{2} - \frac{1}{4}[\cos(\phi_S) + \cos(\phi_S + \gamma)]$. This can be understood as the average of two interference patterns of the system: one with the unperturbed AB phase and one with the added interaction phase γ (Fig. 2, inset). An equivalent view (*26*) stems from the realization that the detector's interacting path carries shot noise (because of the current partitioning by DQPC1), which leads to an at least partial dephasing of the system.

The visibility of the system, an indicator of its coherence, is determined by the overlap of the detector states, $\langle 0|\gamma\rangle_D$: $v_{\mathrm{D2}} = |\langle 0|\gamma\rangle_D| = \cos(\gamma/2)$. In reality, the visibility of the system, without the presence of a detector, is limited because of uncontrolled dephasing from the external environment. Thus, the measured visibility of the system is

$$v_{\mathrm{D2}} = \xi\cos(\gamma/2) \qquad (1)$$

where $0 \le \xi \le 1$.

The detector states' distinguishability (D), its efficacy in acquiring the which-path information, is complementary to the system's interference visibility, namely, $D^2 + {v_{\mathrm{D2}}}^2 = 1$ (*27*–*29*), hence $D = \sin(\gamma/2)$in the ideal case $\xi = 1$; in other words, having the particle's which-path information, encoded in the detector's phase, comes at the expense of observing the particle's wavelike nature.

One can define the knowledge (K), the which-path information measured in our detector at drain D4, as

$$K(\phi_D) \equiv |P(\mathrm{D4}|\uparrow_S) - P(\mathrm{D4}|\downarrow_S)| = |D\,\sin(\phi_D + \frac{\gamma}{2})|, \qquad (2)$$

namely, the difference in the detector's output currents, for a certain AB phase ϕ_D, when the system's electron takes either of the possible paths. Whereas the distinguishability D indicates the which-path information encoded in the detector state, the knowledge K indicates how much of it is actually accessible. Naturally, the knowledge is bound by the distinguishability, $K \le D$. The knowledge K can be continuously tuned by altering the detector's AB phase ϕ_D between gaining full which-path information ($K = D$) and fully erasing it ($K = 0$).

Erasing the which-path information to allow recovery of the electron's wavelike nature can be accomplished by postselecting readings of the system's output according to the detector's reading. Experimentally, we measure the correlation between the current fluctuations in drains D2 (system) and D4 (detector) (*19*, *20*, *23*, *30*), which is proportional to the reduced joint-probability for simultaneously detecting electrons at the two drains

$$P(\delta\mathrm{D2} \times \delta\mathrm{D4}) = \frac{1}{4}\cos\left(\phi_S + \frac{\gamma}{2}\right)\cos\left(\phi_D + \frac{\gamma}{2}\right)\sin^2\left(\frac{\gamma}{2}\right) \qquad (3)$$

Note that the joint probability $P(\delta D2 \times \delta D4)$ is symmetric with regard to system and detector, which stresses the arbitrariness of their labeling. The expected visibility of the AB oscillation in the reduced joint probability is $v_{\mathrm{D2D4}} = \sin\left(\frac{\gamma}{2}\right)\cos\left(\phi_D + \frac{\gamma}{2}\right)$, which also obeys a complementarity relation with the which-path knowledge: ${v_{\mathrm{D2D4}}}^2 + K^2 = D^2$ (*18*).

We realized the system-detector complex in a two-dimensional electron gas (2DEG) embedded in a GaAs-AlGaAs heterostructure. A quantizing magnetic field (B = 4.4 T) put the 2DEG in the second filling factor of the quantum Hall effect, with a base temperature of 12 mK and an electron temperature of ~30 mK. Only the outer chiral edge channels (the lowest spin split Landau level) participated in the interference and the interaction, whereas the inner edge channels were fully reflected at QPC0, which precede QPC1 of both MZIs and, thus, played no active role. The outer edge channel, emanating from source contact S1 (S3), was split at SQPC1 (DQPC1) into two paths that subsequently interfered at SQPC2 (DQPC2). The AB phase is controlled by changing the area enclosed between the interfering paths via the system's modulation gate SMG (detector's DMG). The second filling factor was chosen because the devices were more stable and the visibility of the AB oscillation was reasonably high under these conditions; however, the two interacting paths were partly screened by the adjacent unbiased inner channels, which weakened the mutual interaction. The system's output current $\langle I_{D2}\rangle$ ($\langle I_{D4}\rangle$), measured in drain contact D2 (D4), was proportional to the phase-dependent transmission probability P(D2) [P(D4)]. For half transmission of QPC1 and QPC2, $|t_1|^2 = |t_2|^2 = \frac{1}{2}$, the visibility reached $\xi = 0.66$ in each MZI. Interaction between system and detector via the interacting paths, counterpropagating along 6 μm and separated by less than 2 μm, was controlled by surface gates, while avoiding tunneling between the interacting paths.

Under these conditions, the system's differential visibility v_{D2} was measured as a function of the detector's source current I_{S3} (Fig. 2). The visibility v_{D2} decreased by some 15% when

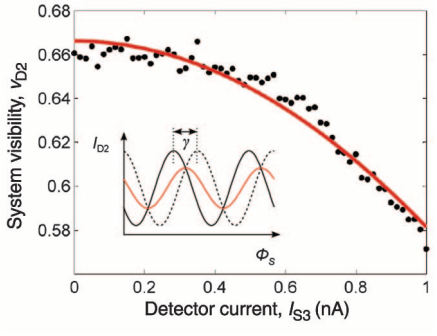

Fig. 2. Dephasing of the system by entanglement with the detector. The system visibility is reduced as the detector current is increased (dots). Red solid line: fit to Eq. 1 yielding $\xi = 0.66$ and $\gamma = \pi/6$ at I_{S3} = 1 nA. (**Inset**) Schematic representation of the AB-dependent current at D2, shown separately for electrons that did (dashed black line) and did not (solid black line) receive a "γ shift." The average of the two (red line) has AB oscillations with the same periodicity but reduced amplitude (partial dephasing).

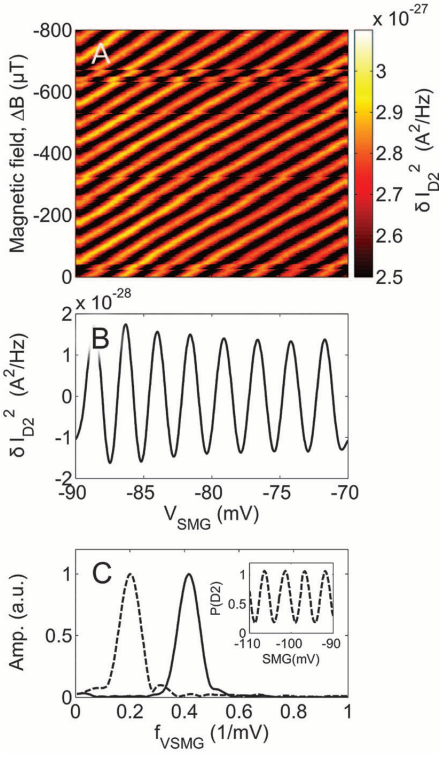

Fig. 3. AB dependence of the autocorrelation in the system. (**A**) The system's autocorrelation was measured while letting the magnetic field decay slowly (ΔB) and varying the system's area with the modulation gate (SMG) faster. (**B**) The average autocorrelation signal oscillates at half the periodicity of the AB oscillation in conductance, as seen in (**C**) discrete Fourier transforms of the AB oscillations in conductance (dashed line, 0.2 mV^{-1}) and in autocorrelation (full line, 0.4 mV^{-1}). (Inset) AB oscillations in conductance.

increasing the input current to 1 nA. This can be understood in two ways: (i) With the increased current, more electrons pass at any time through the interacting path of the detector, which increases the total phase shift a system electron undergoes and consequently the acquired which-path information, and (ii) in terms of interaction, potential fluctuations in the detector's interacting path increase with current, which leads to stronger dephasing of the system. If one assumes a linear dependence of γ on I_{S3}, the data fit theory with $\gamma \approx \pi/6$ at I_{S3} = 1 nA (Fig. 2, red line). Although dephasing due to power dissipation could also take place, it would not affect our main results; thermally induced dephasing is irreversible and, as such, cannot contribute to phase recovery by quantum erasure. Moreover, the consistence between the above value for γ and that obtained from the cross-correlation data (see below) suggests that dephasing due to power dissipation is minor. Also, note that the transmission of DQPC2 was varied and was found to have no effect on the dephasing of the system.

After quantifying the strength of interaction, equal source currents I_S = 0.5 nA were fed into both MZIs. The interacting paths were set to obtain maximal interaction, void of interchannel tunneling. Three zero-frequency correlation signals were measured simultaneously: (i and ii) autocorrelation of each drain current, $\langle \delta I_{D2}{}^2 \rangle$ and $\langle \delta I_{D4}{}^2 \rangle$, and (iii) cross-correlation of the two drain currents $\langle \delta I_{D2} \delta I_{D4} \rangle$. All three were measured as a function of SMG, which affected the system's phase ϕ_S, and the decaying magnetic field, which affected both ϕ_S and ϕ_D.

The autocorrelation of each interferometer is proportional to its shot noise. In the case of the system

$$\langle \delta I_{D2}{}^2 \rangle \propto S_{MZI} = 2eI_{S1}P(\mathrm{D2})[1 - P(\mathrm{D2})] = \frac{1}{4}eI_{S1}[1 - \cos(2\phi_S)] \quad (4)$$

where $P(D2)$ is the average transmission of the system. The shot noise oscillated at half the periodicity of the conductance (Fig. 3, B and C). The color plot in Fig. 3A was obtained by letting the magnetic field decay slowly while the voltage of SMG was scanned faster. Note that the magnitude of the shot noise in each MZI was considerably larger than predicted by Eq. 4, a phenomenon that was previously observed (*23*). Although this phenomenon remains unexplained, it could result from unobservable high-frequency charge fluctuations, which cause fluctuations in the AB phase that lower the visibility right from the start, as they are down-converted to the measured frequency by the partitioning of QPC2.

Our main result lies in the AB dependence of the zero-frequency cross-correlation between current fluctuations in D2 and D4, $\langle \delta I_{D2} \delta I_{D4} \rangle$ (Fig. 4A). The cross-correlation signal, merely 4×10^{-30} A^2/Hz, was extracted by a digital band-pass filter and compensated for the unavoidable magnetic field dependence of the system's interference pattern.

It may be easier to understand the cross-correlation color plot with two cuts at specific magnetic fields (Fig. 4B): One cut at ΔB = 103 μT (relative to B = 4.4 T), with rather strong oscillations in the cross-correlation as a function of V_{SMG}, and another at ΔB = 140 μT, with reduced cross-correlation oscillations. The AB oscillations in the cross-correlation retrace qualitatively the lost interference; the dependence of the cross-correlation visibility on ΔB is plotted in Fig. 4C.

The amplitude of the "checkerboard" pattern, observed in Fig. 4A, drops as γ^2 when the interaction is reduced (Eq. 3, $\gamma << \pi$). Therefore, as the interacting edges were separated, the distinctive checkerboard pattern vanished altogether (fig. S1); future works should be able to see the gradual quenching of the pattern as the interacting edges are carefully brought apart. This behavior is consistent with the system-detector's mutual interaction acting as the dominant source for the observed results.

In a more quantitative fashion, we compared the visibility of the cross-correlation oscillation (a wavelike property) with the which-path knowledge K (a particle-like property), which is obtained by an approximation of Eq. 2: for $\gamma << \pi, K(\phi_D) \propto |\gamma \frac{dI_{D4}}{d\phi_D}|$. Although being available from the AB conductance oscillation in the detector, we obtained the above derivative from the autocorrelation signal $\langle \delta I_{D4}{}^2 \rangle$, which was measured simultaneously with the cross-correlation signal. Plotting the cross-correlation visibility (Fig. 4C) and the knowledge, K (Fig. 4D), their anticorrelated dependence on ΔB is evident. The small shift between the two dependencies is attributed to the finite γ, which we estimate from the shift to be $\gamma \approx \pi/12$ for I_{S3} = 0.5 nA; this is consistent with the previously found $\gamma \approx \pi/6$ for I_{S3} = 1 nA. The oscillations in the cross-correlation visibility are larger than the expected $\sin^2(\gamma/2) = 0.017$ (Eq. 3), similar to the excess noise in the autocorrelation. The anticorrelation between the cross-correlation visibility and the which-path knowledge demonstrates that erasing which-path information allows recovery of the system's wavelike nature.

Two major differences between electrons and photons, which are customarily used in this type of experiments, are their exchange statistics and strong coulomb interaction. The former allows a highly controlled autocorrelation and noise-free current, because of Pauli's exclusion principle; the latter makes the electrons vulnerable to dephasing but, at the same time, allows control of the entanglement strength and phase manipulation. Our work can be expanded upon by realizing a delayed choice (*31*) or a spin-entangled device (*32*), or a three-electron–entangled (GHZ) state (*33*). Moreover, the electronic quantum eraser could be used to measure weak values (*34*) or the Bell inequality (*35*) for the entangled electrons.

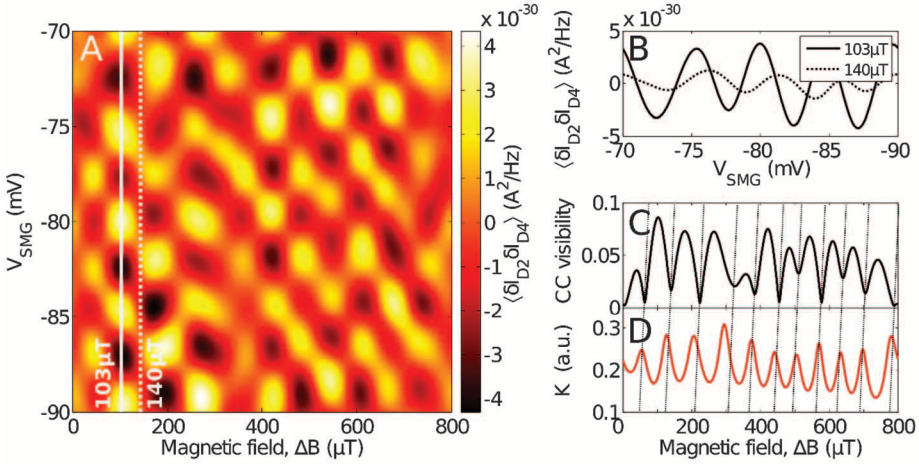

Fig. 4. Phase recovery by quantum erasure. (**A**) The cross-correlation of the system and detector output currents. (**B**) Cuts of the color plot in (A) for two values of the magnetic field, as marked in (A). There is near anticorrelation between (**C**) the oscillation visibility and (**D**) the which-path knowledge, which shows that quantum erasure allows the recovery of interference; the dashed lines serve as guides to the eye. The slight shift from perfect anticorrelation allows us to estimate $\gamma \approx \pi/12$ for I_{S3} = 0.5 nA.

REFERENCES AND NOTES

1. N. Bohr, *Nature* **121**, 580–590 (1928).
2. R. Feynman, R. Leighton, M. Sands, *The Feynman Lectures on Physics*, vol. 3, *Quantum Mechanics* (Addison-Wesley, Reading, MA, 1965).
3. M. O. Scully, B. G. Englert, H. Walther, *Nature* **351**, 111–116 (1991).
4. B. G. Englert, M. O. Scully, H. Walther, *Nature* **375**, 367–368 (1995).
5. E. P. Storey, S. M. Tan, M. J. Collett, D. F. Walls, *Nature* **375**, 368–368 (1995).
6. D. I. Chang *et al.*, *Nat. Phys.* **4**, 205–209 (2008).
7. S. Dürr, T. Nonn, G. Rempe, *Nature* **395**, 33–37 (1998).
8. P. Bertet *et al.*, *Nature* **411**, 166–170 (2001).
9. M. O. Scully, K. Drühl, *Phys. Rev. A* **25**, 2208–2213 (1982).
10. P. G. Kwiat, A. M. Steinberg, R. Y. Chiao, *Phys. Rev. A* **45**, 7729–7739 (1992).
11. T. J. Herzog, P. G. Kwiat, H. Weinfurter, A. Zeilinger, *Phys. Rev. Lett.* **75**, 3034–3037 (1995).
12. P. G. Kwiat, A. M. Steinberg, R. Y. Chiao, *Phys. Rev. A* **49**, 61–68 (1994).
13. Y. H. Kim, R. Yu, S. P. Kulik, Y. Shih, M. O. Scully, *Phys. Rev. Lett.* **84**, 1–5 (2000).
14. X. S. Ma *et al.*, *Proc. Natl. Acad. Sci. U.S.A.* **110**, 1221–1226 (2013).
15. A. Peruzzo, P. Shadbolt, N. Brunner, S. Popescu, J. L. O'Brien, *Science* **338**, 634–637 (2012).
16. F. Kaiser, T. Coudreau, P. Milman, D. B. Ostrowsky, S. Tanzilli, *Science* **338**, 637–640 (2012).
17. Y. Ji *et al.*, *Nature* **422**, 415–418 (2003).
18. K. Kang, *Phys. Rev. B* **75**, 125326 (2007).

19. J. Dressel, Y. Choi, A. N. Jordan, *Phys. Rev. B* **85**, 045320 (2012).
20. F. Buscemi, P. Bordone, A. Bertoni, *Eur. Phys. J. D* **66**, 312–323 (2012).
21. E. Buks, R. Schuster, M. Heiblum, D. Mahalu, V. Umansky, *Nature* **391**, 871–874 (1998).
22. D. Sprinzak, E. Buks, M. Heiblum, H. Shtrikman, *Phys. Rev. Lett.* **84**, 5820–5823 (2000).
23. I. Neder, M. Heiblum, D. Mahalu, V. Umansky, *Phys. Rev. Lett.* **98**, 036803 (2007).
24. Y. Aharonov, D. Bohm, *Phys. Rev.* **115**, 485–491 (1959).
25. B. Rosenow, Y. Gefen, *Phys. Rev. Lett.* **108**, 256805 (2012).
26. A. Stern, Y. Aharonov, Y. Imry, *Phys. Rev. A* **41**, 3436–3448 (1990).
27. W. K. Wootters, W. H. Zurek, *Phys. Rev. D Part. Fields* **19**, 473–484 (1979).
28. G. Jaeger, A. Shimony, L. Vaidman, *Phys. Rev. A* **51**, 54–67 (1995).
29. B. G. Englert, *Phys. Rev. Lett.* **77**, 2154–2157 (1996).
30. I. Neder *et al.*, *Nature* **448**, 333–337 (2007).
31. J. Wheeler, W. Zurek, *Quantum Theory and Measurement* (Princeton Univ. Press, Princeton, NJ, 1983).
32. W. Chen *et al.*, *Phys. Rev. B* **87**, 155308 (2013).
33. A. A. Vyshnevyy, G. B. Lesovik, T. Jonckheere, T. Martin, *Phys. Rev. B* **87**, 165417 (2013).
34. V. Shpitalnik, Y. Gefen, A. Romito, *Phys. Rev. Lett.* **101**, 226802 (2008).
35. A. A. Vyshnevyy, A. V. Lebedev, G. B. Lesovik, G. Blatter, *Phys. Rev. B* **87**, 165302 (2013).

ACKNOWLEDGMENTS

We thank K. Kang, Y. Chung, I. Neder, and H. Inoue for useful discussions. M.H. and Y.G. acknowledge the partial support of the Israeli Science Foundation, the Minerva foundation, and the U.S.-Israel Binational Science Foundation (BSF). M.H. acknowledges also the support of the European Research Council under the European Community's Seventh Framework Program (FP7/2007-2013)/ERC grant agreement no. 227716, and the German Israeli Project Cooperation (DIP).

SUPPLEMENTARY MATERIALS

www.sciencemag.org/content/344/6190/1363/suppl/DC1
Materials and Methods
Supplementary Text
Figs. S1 to S3
References (*36*, *37*)

13 November 2013; accepted 23 May 2014
10.1126/science.1248459

NANOMAGNETISM

Nanoscale imaging and control of domain-wall hopping with a nitrogen-vacancy center microscope

J.-P. Tetienne,[1,2] T. Hingant,[1,2] J.-V. Kim,[3] L. Herrera Diez,[3] J.-P. Adam,[3] K. Garcia,[3] J.-F. Roch,[1] S. Rohart,[4] A. Thiaville,[4] D. Ravelosona,[3] V. Jacques[1,2]*

The control of domain walls in magnetic wires underpins an emerging class of spintronic devices. Propagation of these walls in imperfect media requires defects that pin them to be characterized on the nanoscale. Using a magnetic microscope based on a single nitrogen-vacancy (NV) center in diamond, we report domain-wall imaging on a 1-nanometer-thick ferromagnetic nanowire and directly observe Barkhausen jumps between two pinning sites spaced 50 nanometers apart. We further demonstrate in situ laser control of these jumps, which allows us to drag the domain wall along the wire and map the pinning landscape. Our work demonstrates the potential of NV microscopy to study magnetic nano-objects in complex media, whereas controlling domain walls with laser light may find an application in spintronic devices.

Magnetic domain walls (DWs) represent nanoscale objects that form the cornerstone of a number of emerging spintronic applications, such as the racetrack memory (*1*), the magnetic random access memory (*2*), or the magnetic memristor (*3*). In such schemes, precise control of the positioning and motion of a single DW or a sequence of DWs along a track is paramount for their operation (*4*). However, in materials important for technology, such as ultrathin films with perpendicular magnetic anisotropy (*5*), defects can result in considerable pinning that impedes wall propagation. This pinning effect has two important consequences. First, it introduces a stochastic component into the wall dynamics, whereby thermally driven processes involving hopping over energy barriers, or Barkhausen jumps, become important. Second, these processes can involve deformations in the DW profile itself, resulting in more complex two-dimensional (2D) dynamics such as creep in the low-velocity regime (*6*, *7*). It is therefore an important challenge to quantify these aspects experimentally for realistic sample geometries.

The capacity to directly image DWs in nanostructures would provide valuable insight into how the structure of a DW deforms as it navigates through a complex energy landscape shaped by a random network of material defects. However, experimental techniques that allow this for practical spintronic devices with the requisite nanoscale spatial resolution are scarce. Techniques based on x-ray (*8*) or electron (*9*) microscopy, for example, suffer from a lack of signal because of the small interaction volumes in nanometer-thick films, whereas magnetic force microscopy is usually not suitable because DWs in ultrathin films are highly sensitive to magnetic perturbations. Other techniques, such as spin-polarized scanning tunneling microscopy (*10*) and spin-polarized low-energy electron microscopy (*11*), can provide sufficient resolution to image wall structures but are limited to model systems.

Over the past few years, scanning nitrogen-vacancy (NV) center microscopy has emerged as a powerful magnetic imaging technique that provides quantitative measurements of the stray magnetic field emanating from a micromagnetic structure (*12*–*16*). This method is highly sensitive (*17*), produces no detectable magnetic backaction on the sample, and allows for a spatial resolution ultimately limited by the atomic size of the probe. This technique recently enabled stray-field imaging of a single electron spin (*18*) and of the vortex core in a magnetic microdot (*19*, *20*). Here, we use scanning NV center microscopy to image, study, and control DWs in perpendicularly magnetized ultrathin wires.

The scanning NV center microscope employs the electronic spin of a single NV defect hosted in a diamond nanocrystal, which is attached to the tip of an atomic force microscope (*21*) and used as a magnetic field sensor (Fig. 1A). The magnetic field is evaluated within an atomic-size detection volume by encoding Zeeman shifts of the electron spin sublevels onto the spin-dependent photoluminescence (PL) intensity of the NV defect (*16*). To this end, a laser beam at the wavelength $\lambda = 532$ nm is tightly focused onto the NV defect with a high–numerical aperture microscope objective, whereas a radiofrequency source allows for manipulation of its electron spin state. The spin-dependent red PL intensity of the NV defect is collected by the same objective and forms the magnetometer signal, which gives information about the projection $|B_{NV}|$ of the local magnetic field along the NV center's quantization axis u_{NV} (Fig. 1A) (*19*, *22*).

We studied a 1.5-μm-wide Ta/CoFeB(1 nm)/MgO wire that exhibits perpendicular magnetic anisotropy (Fig. 1B). After preparing well-isolated DWs by applying short magnetic field pulses (*22*), the stray magnetic field was measured while operating the scanning NV center microscope in the "dual iso-B" imaging mode, which provides two different iso–magnetic field (iso-B) contours (*19*, *21*). Figure 1C shows a typical magnetic field map

[1]Laboratoire Aimé Cotton, CNRS, Université Paris-Sud and ENS Cachan, UPR CNRS 3321, 91405 Orsay, France.
[2]Laboratoire de Photonique Quantique et Moléculaire, ENS Cachan and CNRS, UMR CNRS 8537, 94235 Cachan, France.
[3]Institut d'Electronique Fondamentale, Université Paris-Sud and CNRS, UMR CNRS 8622, 91405 Orsay, France.
[4]Laboratoire de Physique des Solides, Université Paris-Sud and CNRS, UMR CNRS 8502, 91405 Orsay, France.
***Corresponding author. E-mail: vjacques@ens-cachan.fr**

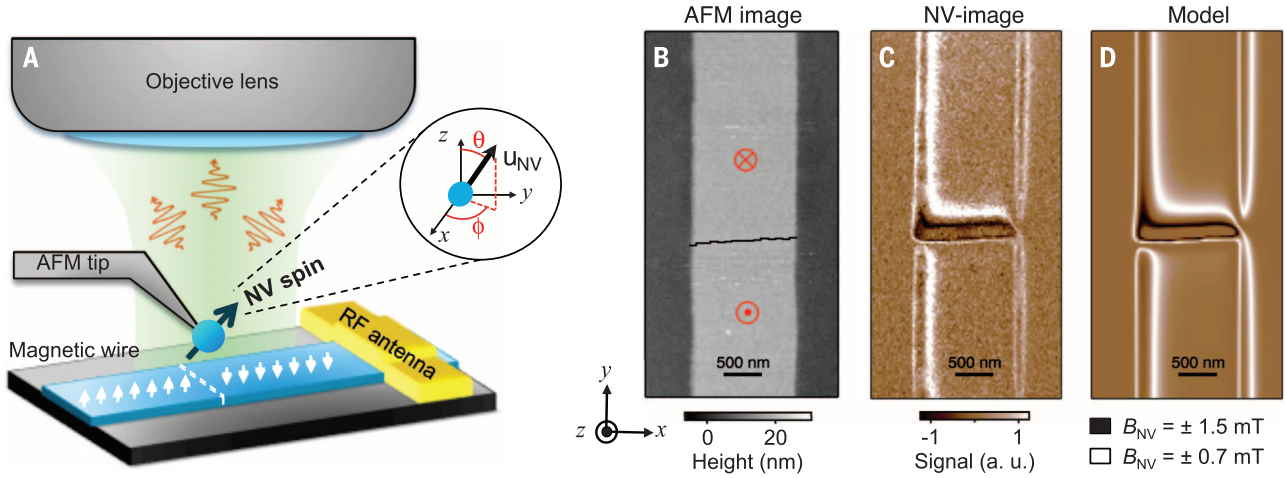

Fig. 1. Imaging a DW in a 1-nm-thick magnetic wire. (**A**) Schematic of the experimental setup. Magnetic field measurements are performed by a single NV defect placed at the apex of an atomic force microscope tip. The quantization axis u_{NV} of the NV defect used in this work is characterized by spherical angles $\theta = 122°$ and $\phi = 45°$. RF, radiofrequency. (**B**) AFM image of the magnetic sample, a 1.5-μm-wide Ta/CoFeB(1 nm)/MgO wire. The red symbols indicate the magnetization direction. (**C**) Dual iso-B image recorded above the magnetic wire, revealing a single DW. Positive magnetometer signal (bright) indicates $B_{NV} = \pm 0.7$ mT, whereas negative magnetometer signal (dark) indicates $B_{NV} = \pm 1.5$ mT. a. u., arbitrary units. (**D**) Data fitting with micromagnetic calculations (*22*). The resulting DW profile is shown in (B) as a black line overlaid on the AFM image. In these experiments, the probe-sample distance is ≈110 nm, with the magnetic layer buried 7 nm below the sample surface. The acquisition time is 50 ms per pixel.

above the wire, with iso-B contours corresponding to $B_{NV} = \pm 0.7$ and ± 1.5 mT. The field exhibits local maxima above the edges of the wire, but also along a line across the wire: this is the signature of a single DW. In such perpendicularly magnetized samples, the stray field is generated near regions of abrupt magnetization changes—that is, above the edges or DWs (*22*). By fitting the data to micromagnetic calculations (Fig. 1D), the spatial position profile $y_{DW} = f(x)$ of the DW can be extracted with a standard error ≈30 nm in the y direction (*22*). Here, the DW is found to be nearly straight, with a 3° tilt with respect to the x axis (black line in Fig. 1B).

For an ideal magnetic sample, the DW should be straight and perpendicular to the wire axis to minimize the DW energy. However, the presence of structural or fabrication defects locally modifies the energy landscape, creating pinning sites for the DW. To occupy a local energy minimum, the DW is distorted. While repeating magnetic field measurements above the magnetic wire, we observed discrete jumps of the DW between two pinning sites, labeled 1 and 2 in Fig. 2A. The position profiles of the DW in each pinning site (Fig. 2B) reveal a spatial separation ranging from 50 ± 30 nm (near the right-hand edge of the wire) to 200 ± 30 nm (left-hand edge). The hopping of the DW between the two pinning sites, driven by thermal fluctuations, is known as the Barkhausen effect (*23*–*25*). Movie S1 further illustrates the observation of this effect in our experiment, performed in zero external magnetic field and at room temperature.

To analyze the dynamics of the hopping process, we monitored the magnetometer signal over time at a fixed position on the wire, above site 2 (Fig. 2A, close-up views). The resulting traces exhibit well-defined jumps between two magnetometer signal levels, reflecting DW hopping over an

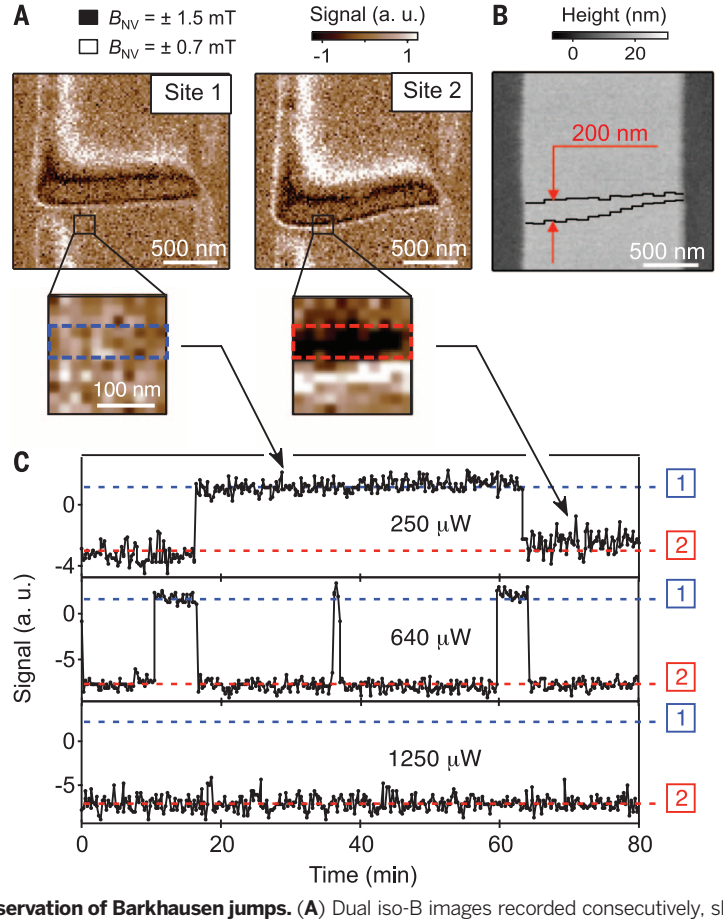

Fig. 2. Observation of Barkhausen jumps. (**A**) Dual iso-B images recorded consecutively, showing the DW in two different pinning sites, labeled 1 and 2. (**B**) DW position profile in each site (black lines) extracted from data fitting with micromagnetic calculations and overlaid on the AFM image. (**C**) Magnetometer signal traces showing DW hopping between the two pinning sites for three values of the laser power. Each data point is obtained by reducing the scanning window to the black squares shown in (A) and integrating the magnetometer signal over the dashed rectangles [see close-up views in (A)]. The acquisition time per point is 3 s.

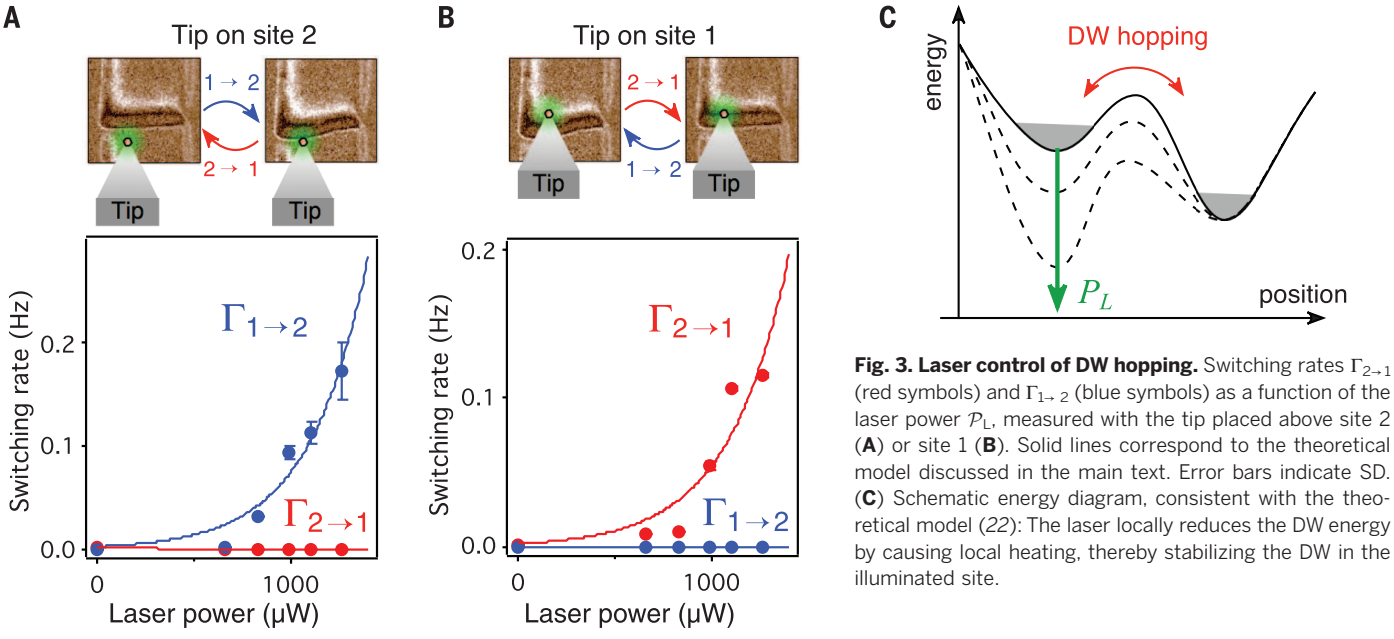

Fig. 3. Laser control of DW hopping. Switching rates $\Gamma_{2\to1}$ (red symbols) and $\Gamma_{1\to2}$ (blue symbols) as a function of the laser power $\mathcal{P}_L$, measured with the tip placed above site 2 (**A**) or site 1 (**B**). Solid lines correspond to the theoretical model discussed in the main text. Error bars indicate SD. (**C**) Schematic energy diagram, consistent with the theoretical model (*22*): The laser locally reduces the DW energy by causing local heating, thereby stabilizing the DW in the illuminated site.

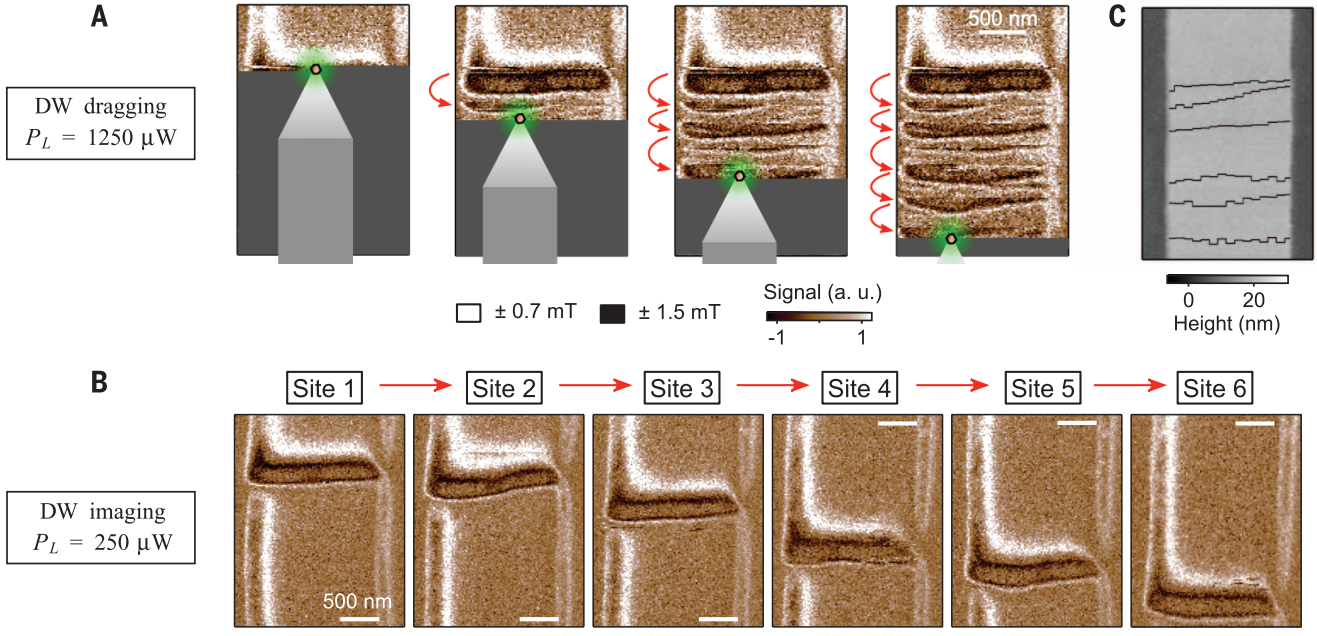

Fig. 4. Mapping the pinning sites in an ultrathin magnetic wire. (**A**) Laser-induced DW dragging: At high laser power ($\mathcal{P}_L$ = 1250 μW), the DW hops from site to site as the tip is scanned along the wire, as directly seen on the dual iso-B image recorded during the scan. (**B**) Iso-B images obtained at low laser power ($\mathcal{P}_L$ = 250 μW) after preparing the DW in different pinning sites through laser-induced DW dragging. The images show the six pinning sites found in the 2-μm-long wire portion that we investigated. Scale bars for all panels in (B), 500 nm. (**C**) Reconstructed DW position profiles of the six pinning sites (black lines) overlaid on the AFM image.

energy barrier (Fig. 2C). Notably, the switching rates dramatically depend on the laser power $\mathcal{P}_L$ used to optically excite the NV defect. The lifetime of site 2 becomes substantially longer when $\mathcal{P}_L$ increases; at sufficiently high laser power, there are no more switching events back to site 1. The laser spot—with a diffraction-limited Gaussian profile with waist ≈330 nm—is focused onto the NV center probe (i.e., mostly above site 2 in these experiments), which suggests a pinning action of the laser. Though the DW has no preferential site at low power, it is efficiently trapped into site 2 at high laser power, illustrating how laser light can be used to control DW hopping in an ultrathin magnetic wire. To get more insight into this process, the switching rates $\Gamma_{i\to j}$ from site i to site j were measured as a function of $\mathcal{P}_L$ following the preparation-readout procedure described in (*22*). These measurements were performed with the tip (i.e., the laser spot) placed above either site 1 or site 2 (Fig. 3, A and B). A similar behavior is observed in both cases: The switching rate toward the illuminated site increases with increasing $\mathcal{P}_L$. This clearly demonstrates that the laser tends to pin the DW in the nearest available site.

This effect can be explained by laser-induced local heating, which leads to a reduction in the DW energy through the decrease in saturation magnetization and anisotropy with increasing

temperature (*26*, *27*), as depicted in Fig. 3C. To verify this hypothesis, we developed a model of the thermally activated hopping by applying Kramer's transition rate theory to 1D stochastic DW dynamics (*22*). The two pinning sites are modeled as pointlike defects with an increase in the DW energy for the transition from site 1 to site 2 because of a 14-nm elongation in the wall length, as observed experimentally (Fig. 2B). The spatial profile of the laser-induced heating is assumed to mirror the Gaussian profile of the laser beam. The DW energy then acquires an additional spatial dependence as a result of this local heating, with an energy minimum at the laser spot center, which leads to an additional force that drives the DW toward this minimum. With the use of the micromagnetic parameters determined for our system from other experiments (*28*) and including the temperature dependence of the saturation magnetization, we find that this leads to an exponential increase in the hopping rate toward the pinning site under laser focus and confirms the intuitive picture shown in Fig. 3C. Furthermore, quantitative agreement is found with the experiment (solid lines in Fig. 3, A and B) if one assumes (i) pinning fields of 1.1 mT at site 1 and 1.8 mT at site 2, in good agreement with field-induced DW propagation measurements (*29*), and (ii) a temperature increase of ~6 K per milliwatt of applied power in the ferromagnetic wire at the position of the laser spot. This is in reasonable agreement with the ≈20-K/mW temperature increase measured with the same NV center employed as a nanoscale thermometer (*22*, *30*).

To explore the pinning in the wire, we then used laser-controlled hopping of the DW. By scanning the sample with a high laser power ($\mathcal{P}_L$ > 1 mW), the DW is forced to hop toward the pinning site nearest to the tip, thereby jumping from site to site following the scan direction. Such a laser-induced DW dragging is directly observed on the magnetic field image (Fig. 4A). The DW can be efficiently prepared in a given pinning site by simply turning the laser off as soon as the DW is detected in the desired site. Following this laser-assisted preparation, the DW can be subsequently imaged with no major perturbation by using a low laser power ($\mathcal{P}_L$ = 250 μW). We used this dragging-imaging procedure to clearly identify six different pinning sites over the 2-μm-long wire portion that we investigated (Fig. 4B). From the magnetic images, we inferred the DW position profiles in each site, which are overlaid on the atomic force microscopy (AFM) image in Fig. 4C. The mean spacing between consecutive stable pinning sites is ≈300 nm. This is consistent with structural studies performed on such Ta/CoFeB/MgO films with x-ray diffraction (*29*), indicating a very low density of structural defects (interface roughness, grain boundaries, crystalline texture) with respect to other materials with perpendicular anisotropy such as Co/Pt, Co/Pd, or Co/Ni.

Our technique allows for the determination of the density of pinning sites in magnetic nanowires and for the evaluation of individual pinning strengths in the event of a local gradient in thermal energy, two important aspects of magnetic recording applications involving magnetic DW motion and thermally assisted magnetization switching. This work also highlights the potential for NV center microscopy to manipulate micromagnetic structures at the nanoscale.

REFERENCES AND NOTES

1. S. S. P. Parkin, M. Hayashi, L. Thomas, *Science* **320**, 190–194 (2008).
2. M. Yamanouchi *et al.*, *Appl. Phys. Lett.* **102**, 212408 (2013).
3. A. Chanthbouala *et al.*, *Nat. Phys.* **7**, 626–630 (2011).
4. M. Hayashi, L. Thomas, R. Moriya, C. Rettner, S. S. P. Parkin, *Science* **320**, 209–211 (2008).
5. S. Ikeda *et al.*, *Nat. Mater.* **9**, 721–724 (2010).
6. S. Lemerle *et al.*, *Phys. Rev. Lett.* **80**, 849–852 (1998).
7. P. J. Metaxas *et al.*, *Phys. Rev. Lett.* **99**, 217208 (2007).
8. M.-Y. Im, L. Bocklage, P. Fischer, G. Meier, *Phys. Rev. Lett.* **102**, 147204 (2009).
9. M. Kläui *et al.*, *Phys. Rev. Lett.* **95**, 026601 (2005).
10. S. Meckler *et al.*, *Phys. Rev. Lett.* **103**, 157201 (2009).
11. G. Chen *et al.*, *Phys. Rev. Lett.* **110**, 177204 (2013).
12. B. M. Chernobrod, G. P. Berman, *J. Appl. Phys.* **97**, 014903 (2005).
13. J. M. Taylor *et al.*, *Nat. Phys.* **4**, 810–816 (2008).
14. C. L. Degen, *Appl. Phys. Lett.* **92**, 243111 (2008).
15. G. Balasubramanian *et al.*, *Nature* **455**, 648–651 (2008).
16. L. Rondin *et al.*, *Rep. Prog. Phys.* **77**, 056503 (2014).
17. J. R. Maze *et al.*, *Nature* **455**, 644–647 (2008).
18. M. S. Grinolds *et al.*, *Nat. Phys.* **9**, 215–219 (2013).
19. L. Rondin *et al.*, *Nat. Commun.* **4**, 2279 (2013).
20. J.-P. Tetienne *et al.*, *Phys. Rev. B* **88**, 214408 (2013).
21. L. Rondin *et al.*, *Appl. Phys. Lett.* **100**, 153118 (2012).
22. Supplementary materials are available on *Science* Online.
23. A. Chizhik *et al.*, *Appl. Phys. Lett.* **97**, 012502 (2010).
24. A. Schwarz *et al.*, *Phys. Rev. Lett.* **92**, 077206 (2004).
25. J. A. J. Burgess *et al.*, *Science* **339**, 1051–1054 (2013).
26. P. Möhrke, J. Rhensius, J.-U. Thiele, L. J. Heyderman, M. Kläui, *Solid State Commun.* **150**, 489–491 (2010).
27. G. V. Astakhov *et al.*, *Phys. Rev. Lett.* **106**, 037204 (2011).
28. T. Devolder *et al.*, *Appl. Phys. Lett.* **102**, 022407 (2013).
29. C. Burrowes *et al.*, *Appl. Phys. Lett.* **103**, 182401 (2013).
30. D. M. Toyli, C. F. de las Casas, D. J. Christle, V. V. Dobrovitski, D. D. Awschalom, *Proc. Natl. Acad. Sci. U.S.A.* **110**, 8417–8421 (2013).

ACKNOWLEDGMENTS

We thank L. Rondin, O. Boulle, G. Gaudin, L. Vila, and B. Ocker for experimental assistance and fruitful discussions. The research has been partially funded by the European Community's Seventh Framework Programme (FP7/2007-2013) under grant agreements 611143 (DIADEMS) and 257707 (MAGWIRE); the French Agence Nationale de la Recherche through the projects DIAMAG, FRIENDS, and ELECMADE; and C'Nano Ile-de-France (NANOMAG).

SUPPLEMENTARY MATERIALS

www.sciencemag.org/content/344/6190/1366/suppl/DC1
Materials and Methods
Supplementary Text
Figs. S1 to S10
Table S1
References (*31*–*38*)
Movie S1

23 December 2013; accepted 8 May 2014
10.1126/science.1250113

NANOPHOTONICS

Controlling graphene plasmons with resonant metal antennas and spatial conductivity patterns

P. Alonso-González,[1] A. Y. Nikitin,[1,2] F. Golmar,[1,3] A. Centeno,[4] A. Pesquera,[4] S. Vélez,[1] J. Chen,[1] G. Navickaite,[5] F. Koppens,[5] A. Zurutuza,[4] F. Casanova,[1,2] L. E. Hueso,[1,2] R. Hillenbrand[2,6]*

Graphene plasmons promise unique possibilities for controlling light in nanoscale devices and for merging optics with electronics. We developed a versatile platform technology based on resonant optical antennas and conductivity patterns for launching and control of propagating graphene plasmons, an essential step for the development of graphene plasmonic circuits. We launched and focused infrared graphene plasmons with geometrically tailored antennas and observed how they refracted when passing through a two-dimensional conductivity pattern, here a prism-shaped bilayer. To that end, we directly mapped the graphene plasmon wavefronts by means of an imaging method that will be useful in testing future design concepts for nanoscale graphene plasmonic circuits and devices.

Surface plasmon polaritons—coupled excitations of photons and mobile charge carriers—in metals and doped semiconductors offer intriguing opportunities to control light in nanoscale devices (*1*–*7*). Plasmons provide both a strong local field enhancement and confinement, accompanied by an appreciable reduction of the wavelength relative to free-space radiation. However, plasmons in metals exhibit relatively strong losses and cannot be controlled by electrical fields. Consequently, novel plasmonic materials are being sought (*8*). Among them, doped graphene is advantageous because of its two-dimensional nature

[1]CIC nanoGUNE, 20018 Donostia-San Sebastián, Spain. [2]IKERBASQUE, Basque Foundation for Science, 48011 Bilbao, Spain. [3]I.N.T.I.-CONICET and ECyT-UNSAM, San Martín, Buenos Aires, Argentina. [4]Graphenea SA, 20018 Donostia-San Sebastián, Spain. [5]ICFO-Institut de Ciéncies Fotoniques, Mediterranean Technology Park, 08860 Casteldefells, Barcelona, Spain. [6]CIC nanoGUNE and UPV/EHU, 20018 Donostia-San Sebastián, Spain.
***Corresponding author. E-mail: r.hillenbrand@nanogune.eu**

and high carrier mobility, supporting plasmons with an extreme confinement and a wavelength that can be strongly reduced relative to photons of the same frequency (*9*–*14*). More importantly, the carrier concentration in graphene can be tuned by electrical gating, opening exciting avenues for nanoscale electrical control of light (*15*–*21*). The ultrashort graphene plasmon (GP) wavelengths, however, come at the expense of a large momentum mismatch with photonic modes of the same frequency (*22*–*25*). Future graphene plasmonic circuits (*15*) will thus critically depend on converting incident light into propagating GPs, and on controlling their propagation and focusing to enhance light-matter interactions.

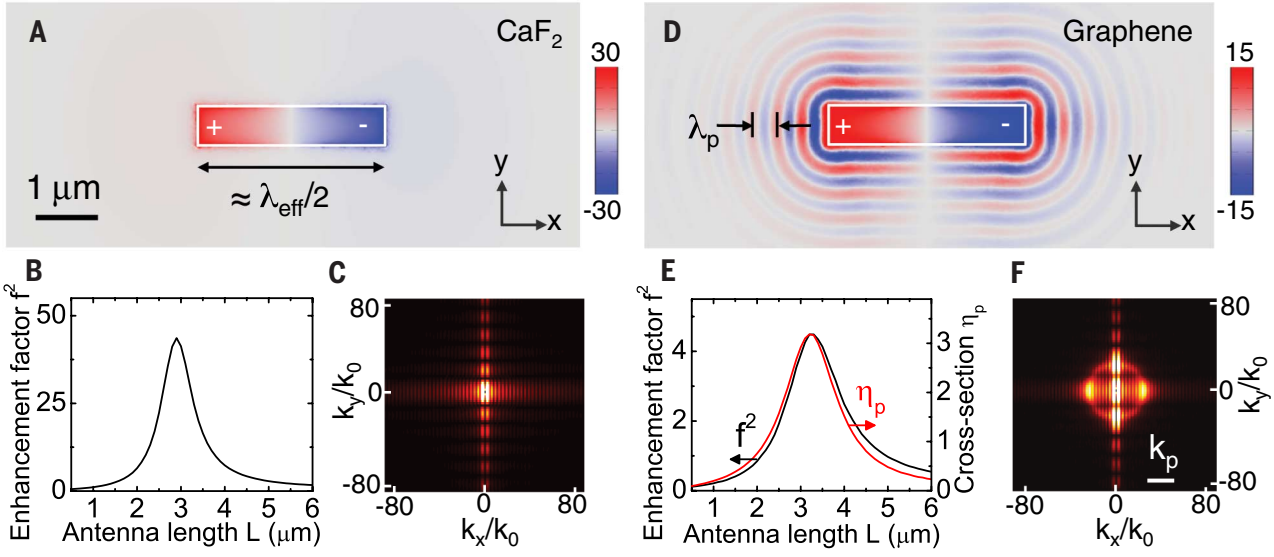

Fig. 1. Numerical study of launching propagating GPs with resonant dipole antennas at λ_0 = 10.20 μm. (**A**) Near-field distribution of a resonant antenna (length L = 2.9 μm, width w = 0.6 μm, height h = 40 nm) on a CaF_2 substrate. (**B**) Near-field intensity enhancement factor f^2 as a function of L. (**C**) Absolute value of the Fourier transform of the near field in (A). (**D**) Near-field distribution of a resonant antenna (L = 3.2 μm, w = 0.6 μm, h = 40 nm) on graphene on a CaF_2 substrate. (**E**) Enhancement factor f^2 and η_p as a function of L. (**F**) Absolute value of the Fourier transform of the near field in (D). The images in (A) and (D) show the real part of the near-field z-component 5 nm above the antenna surface, normalized to $|E_0|$.

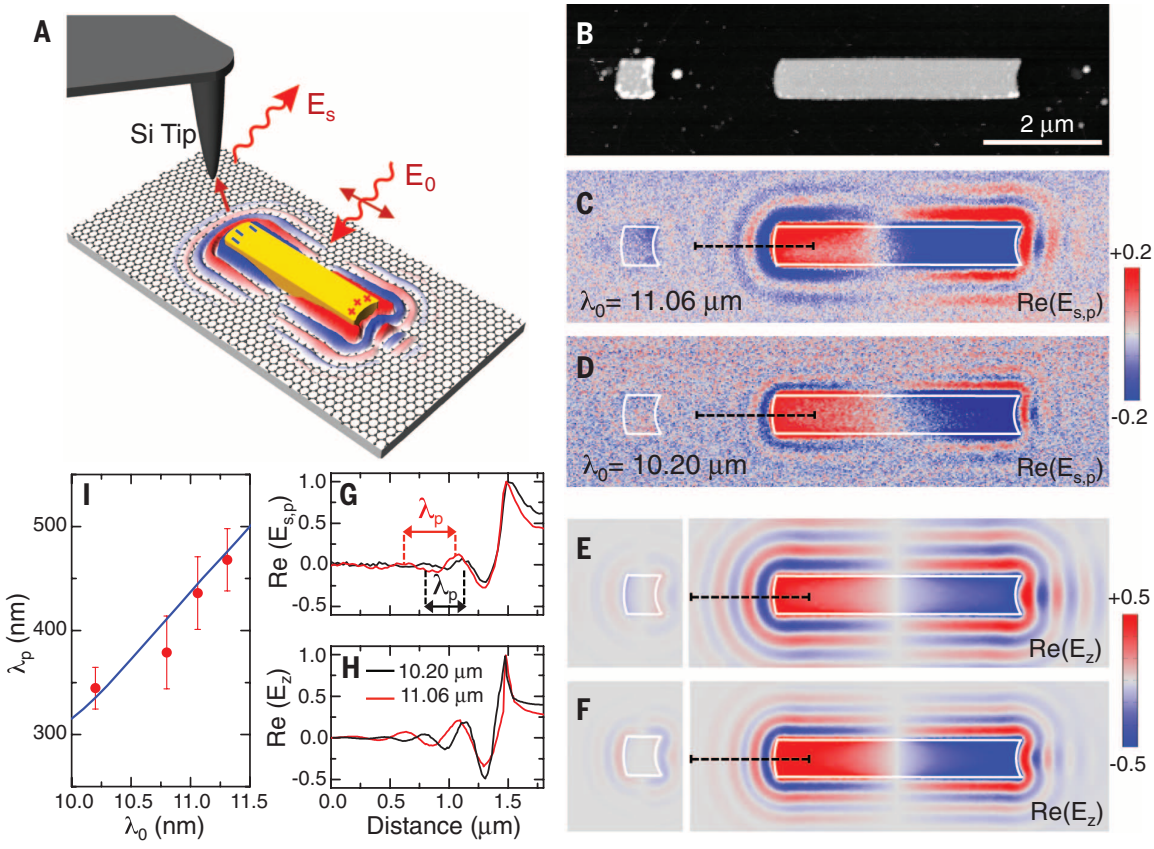

Fig. 2. Verification of an antenna-based GP launcher. (**A**) Illustration of the experiment. (**B**) Topography image of an off- and on-resonance dipole antenna (left and right, respectively). (**C** and **D**) Experimental and (**E** and **F**) calculated images illustrating the real part of the vertical near-field component of the antennas shown in (B) for λ_0 = 11.06 μm and 10.20 μm, respectively. (**G**) Experimental and (**H**) calculated near-field profiles along the dashed black lines in (C) and (D) and in (E) and (F), respectively. Data in (C) to (H) are normalized to the near-field signals at the left antenna extremity. (**I**) Experimental (symbols) and calculated (solid line) GP wavelength λ_p as a function of λ_0. Error bars denote SD of the averaged GP wavelengths obtained form adjacent near-field profiles.

Figure 1 introduces the launching of GPs by metal antennas. The calculations (*26*) consider gold rods of length L acting as resonant dipole antennas. As shown in Fig. 1A, they provide strong near fields of opposite polarity at the rod extremities. For the fixed illumination wavelength λ_0 = 10.20 μm, the near-field intensity enhancement factor $f^2 = (E/E_0)^2$ indicates the fundamental dipolar antenna resonance at L = 2.9 μm, where E is the electric field averaged over the antenna surface and E_0 is the incident electric field. The Fourier transform (FT) of Fig. 1A reveals antenna near fields with momentum increased by orders of magnitude relative to the incident wave vector k_0 (Fig. 1C). When such an antenna is placed on graphene (assuming a Fermi energy E_F = 0.44 eV and a carrier mobility μ = 1136 $cm^2 V^{-1} s^{-1}$), the high-momentum near-field components match the GP wave vector, thus exciting propagating GPs. Indeed, we observed an oscillating near-field distribution around the antenna on graphene (Fig. 1D). The distance between the field maxima of the same polarity (same color) yields the GP wavelength, λ_p = 380 nm, which is smaller than λ_0 by a factor of 27 (*24*, *25*). Accordingly, the FT of Fig. 1D yields a bright ring of diameter $k_p = 2\pi/\lambda_p = 27k_0$, corroborating propagating GPs (Fig. 1F). As expected, the excitation of GPs broadens and shifts the antenna resonance (black curve in Fig. 1E).

To analyze how efficiently GPs are excited, we calculated the quantity $\eta_p = P_p/(I_0 A_{ant})$ (red curve in Fig. 1E), where P_p is the power transferred into graphene, I_0 is the illuminating intensity, and A_{ant} is the geometrical antenna cross section. The value of η_p provides a good estimate for the cross section of exciting GPs relative to the antenna's geometrical cross section (*26*). It clearly follows the antenna's resonance. Relative to nonresonant antennas [e.g., with a quadratic cross section (600 nm × 600 nm)], the efficiency on resonance is enhanced by a factor of 28. The resonant near-field enhancement around the antenna is thus the source for strong GP excitation.

Intriguingly, we observed plane GP wavefronts parallel to the antenna axis, in contrast to metal surface plasmon polaritons launched by dipole antennas (Fig. 1D) (*27*). We explain these plane wavefronts by the weak diffraction of the GPs, which results from their short wavelength relative to the antenna length. The antenna can thus be considered as an extended plasmon source with a length of several GP wavelengths.

For an experimental demonstration, we fabricated gold rods on chemical vapor deposition–grown graphene transferred onto a 5-nm-thick SiO_2 layer on a CaF_2 substrate (*26*). We imaged the near-field distribution with a scattering-type scanning near-field microscope using a dielectric Si tip (Fig. 2A). The tip and sample were illuminated with *s*-polarized light (electric field E_0) parallel to the antenna axis, thus efficiently exciting the antenna. While scanning the sample, the real part of the *p*-polarized tip-scattered light, $\mathrm{Re}(E_{s,p})$, is recorded simultaneously with topography (*26*). On metal plasmonic antennas, such an imaging scheme yields the vertical near-field component, $\mathrm{Re}(E_z)$ (*28*). This scheme also allows for mapping the vertical near field of the GP wavefronts launched by the antenna. This represents a fundamental difference from earlier experiments (*24*, *25*) in which a metal tip was used to both excite and detect GPs, yielding complex images of plasmon interference.

Figure 2B shows the topography of two Au antennas on graphene being strongly off resonance (left) and near resonance (right). Near-field images at λ_0 = 11.06 μm and λ_0 = 10.20 μm (Fig. 2, C and D) verify the dipolar mode on the right antenna. We also observed short-range spatial near-field oscillations around this antenna. Their period is about 400 nm, matching the GP wavelength at mid-infrared frequencies (*24*, *25*). Our experimental observations agree well with numerical simulations (Fig. 2, E and F) assuming E_F = 0.44 eV and μ = 1136 $cm^2 V^{-1} s^{-1}$. These values, used in all the calculations throughout this work, are consistent with our earlier experiments in which similarly grown graphene was used (*24*, *26*). Because of the relatively low mobility, the field oscillations decay within a few plasmon wavelengths. For quantitative comparison, we show in Fig. 2, G and H, the experimental and calculated near-field profiles, $\mathrm{Re}(E_{s,p})$ and $\mathrm{Re}(E_z)$, along the dashed black lines indicated in Fig. 2, C and D, and Fig. 2, E and F, respectively. We found excellent agreement, particularly for the oscillation periods and relative field strengths.

Figure 2I depicts the plasmon wavelength λ_p extracted from near-field images taken at different illumination wavelengths λ_0. Good agreement with the calculations is found, confirming the GP origin of the near-field oscillations. Note that the experimental images directly reveal the plasmon wavefronts and wavelength λ_p [the latter

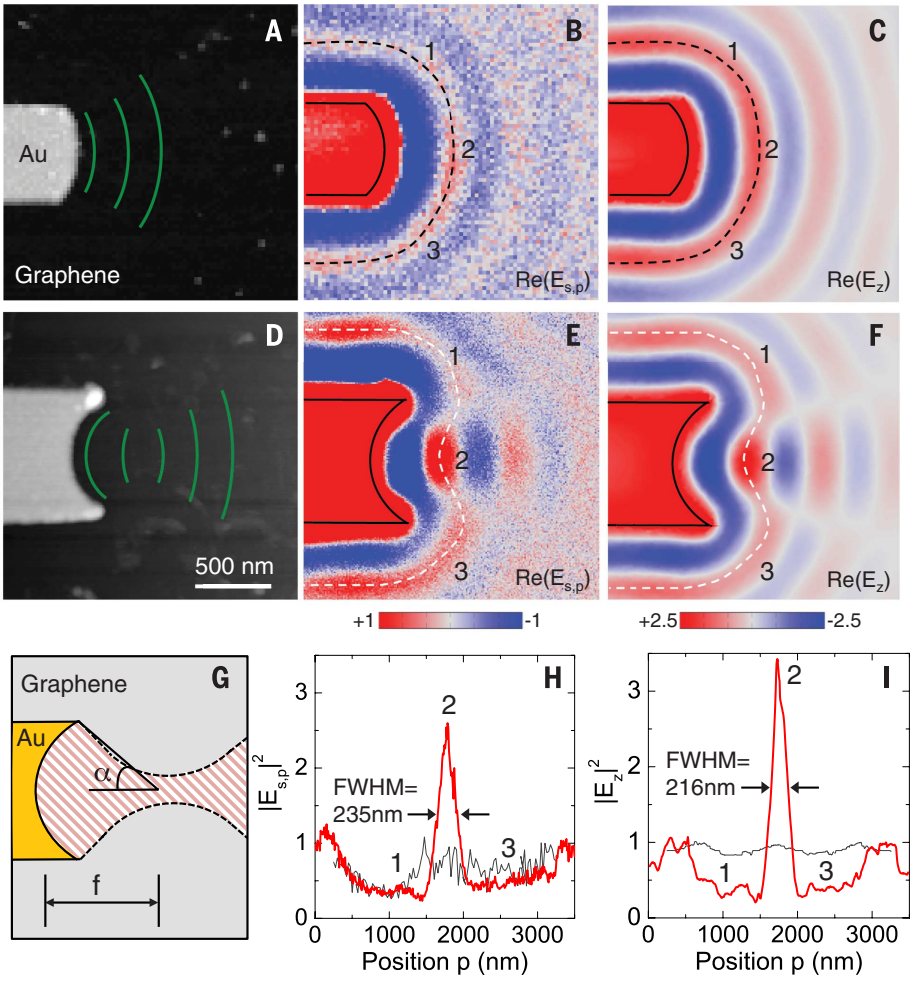

Fig. 3. Wavefront engineering of GPs. (**A** and **D**) Topography, (**B** and **E**) experimental near-field images $\mathrm{Re}(E_{s,p})$, and (**C** and **F**) calculated near-field images $\mathrm{Re}(E_z)$ of a convex and a concave antenna extremity, respectively (λ_0 = 11.06 μm). The green lines in the topography images illustrate the GP wavefronts. (**G**) Illustration of GP focusing with a concave antenna extremity. (**H** and **I**) Experimental and calculated near-field intensity (red curves) along the white dashed lines in (E) and (F), respectively. The dark gray curves show the experimental and calculated near-field intensity along the black dashed lines in (B) and (C), respectively. All curves and near-field images are normalized to their maximum in the lower left corners of (E) and (F).

given by the distance between two consecutive field maxima of the same polarity (color)], rather than local density of states (LDOS) maps and $\lambda_p/2$ as observed in (*24*, *25*).

We also fabricated and imaged much shorter antennas (left structure in Fig. 2, B to F) being strongly off resonance with the incident wavelength. Owing to the weak field enhancement, we did not observe GPs around them (Fig. 2, C and D). For the same reason, some asperities remaining from the lithography process do not launch GPs. This result proves that GPs are launched by the resonant antenna near fields and not by the tip.

Resonant antennas can be simultaneously used for engineering the GP wavefronts, as we demonstrated with the use of concave and convex antenna extremities. While the convex extremity launches diverging GPs (Fig. 3, A to C; same data as shown in Fig. 2, A, C, and E), the concave extremity launches converging GPs (Fig. 3, D to F), yielding a focus at a distance of about 400 nm, as discerned by the change of the wavefront curvature (green lines in Fig. 3D).

The concave extremity represents a 2D lens for focusing GPs (Fig. 3G). The focal length f is determined by the cavity radius, which nominally is 400 nm, and thus agrees well with the focus position observed in Fig. 3E. To analyze the focus, we plot in Fig. 3, H and I, the experimental and calculated near-field intensities, $|E_{s,p}|^2$ and $|E_z|^2$, along the white dashed lines in Fig. 3, E and F, respectively (red curves). The dashed lines trace the field at a constant distance of 400 nm around the antenna extremity. We observed a strongly localized intensity at the focus position (position 2 in Fig. 3, E and F), which is enhanced by a factor of about 6 relative to positions 1 and 3. The plasmon focus yields an intensity enhancement by a factor of ~3 with respect to the convex antenna extremity (dark gray curves in Fig. 3, H and I).

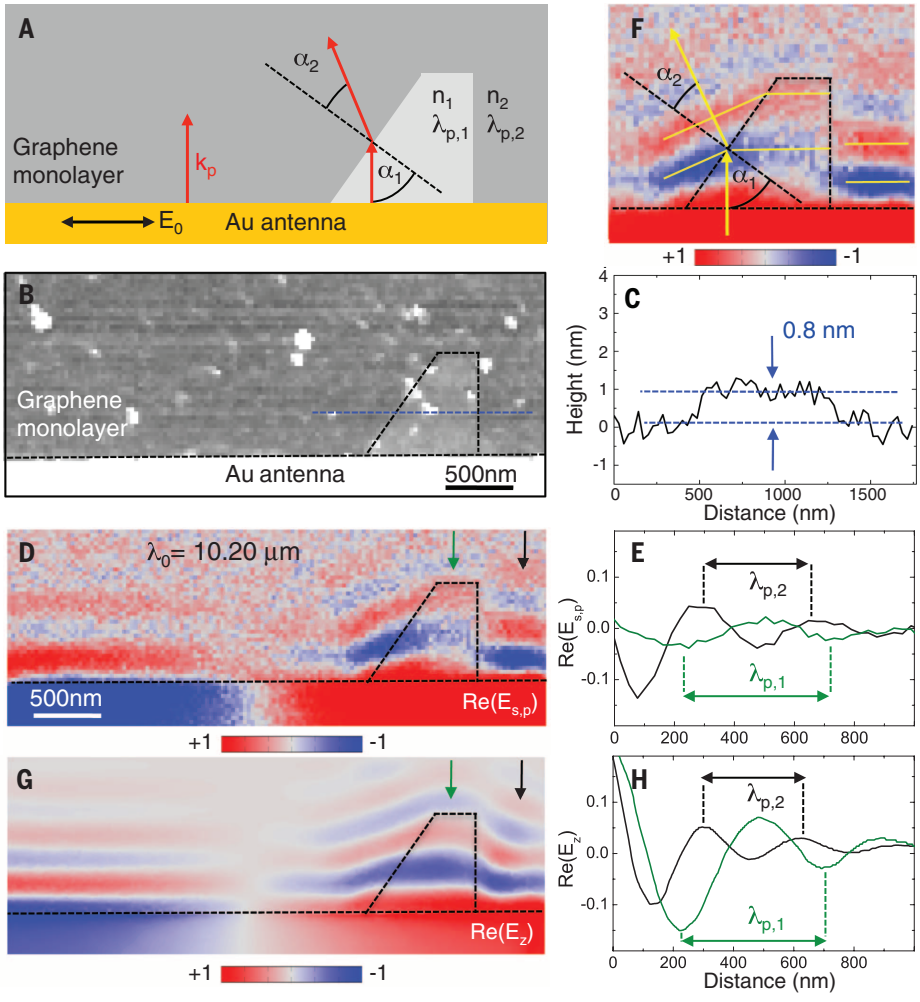

Fig. 4. Refraction of GPs at a graphene bilayer prism. (**A**) Illustration of our experiment and Snell's law of refraction. (**B**) Topography image of a graphene bilayer prism next to a resonant Au antenna. (**C**) Height profile along the dashed line in Fig. 3B. (**D**) Near-field image, Re($E_{s,p}$), recorded simultaneously with the topography shown in (B). (**E**) Near-field profiles taken at the positions marked by black and green arrows in (D). (**F**) Analysis of the GP wavefronts. Image extracted from Fig. 4D. (**G**) Calculated near-field image, Re(E_z). (**H**) Near-field profiles taken at the positions marked by black and green arrows in (G). All near-field data are shown in arbitrary units.

The GP focus is determined by the numerical aperture (NA) of the concave extremity and the GP wavelength, analogous to diffraction-limited optics. Generally, the full width at half maximum (FWHM) of a focus size at wavelength λ can be estimated by FWHM ≈ $\lambda/(2NA)$, where NA = sin(α). With α = 70° (from Fig. 3D) and λ_p = 436 nm, we calculate FWHM = 232 nm, which agrees well with FWHM = 235 nm in the experimental near-field profile (Fig. 3H) and FWHM = 216 nm in the calculated (Fig. 3I) near-field profile (red curves), respectively. Note that the focus size can be tailored by varying the NA. In Fig. 2C, where the opening angle α of the cavity and thus the numerical aperture are smaller (α = 29°, NA = 0.485), we measure a larger FWHM = 458 nm (fig. S2), in agreement with the expected FWHM = 450 nm (*26*).

Both the launching of GPs by antennas and wavefront mapping offer unique possibilities for studying fundamental and applied aspects of graphene plasmonics. In Fig. 4 we demonstrate that the propagation direction of GPs can be controlled by 2D refractive elements based on spatial conductivity patterns, as recently proposed (*15*). Our experiment is illustrated in Fig. 4A. A resonant gold antenna is illuminated with field E_0 parallel to the antenna axis. The antenna fields launch GPs propagating perpendicular to the antenna, which are refracted at a prism structure where the Fermi energy and thus the GP wavelength are locally modified.

In the experiment, the prism consists of a graphene bilayer (*26*), which is outlined by a dashed black line in the topography image (Fig. 4B). Its height is 0.8 nm (Fig. 4C). In the near-field image (Fig. 4D), Re($E_{s,p}$), we observed horizontal GP wavefronts above both the left side and the end of the right side of the antenna (wavelength $\lambda_{p,2}$), as in Figs. 2 and 3. Inside the prism, we found an increased plasmon wavelength, $\lambda_{p,1}$ = 1.4 $\lambda_{p,2}$ (Fig. 4E). We explain it by a locally increased conductivity. Note that the conductivity, and thus the wavelength λ_p, scales with the Drude weight D (*29*). For stacks of decoupled graphene layers (where interlayer hopping of electrons is neglected), the Drude weight scales as $D \sim n_G^{1/2} l$ (*29*), where n_G is the carrier density per layer and l is the number of layers. Assuming that the carriers are equally distributed between the layers (*30*), we obtain $n_G = n/l$, and subsequently $D \sim n^{1/2} l^{1/2}$, where n is the total carrier density equal to that of the monolayer graphene. For a bilayer, the conductivity is thus 1.41 larger than in a monolayer, yielding $\lambda_{p,1}/\lambda_{p,2} = D$ = 1.41, in agreement with our experimental finding.

Outside the left prism boundary, the wavefronts are tilted by 24°. For the propagation directions we found α_1 = 50° and α_2 = 26°, yielding $\sin(\alpha_1)/\sin(\alpha_2)$ = 1.75 (Fig. 4F). Our findings, $\lambda_{p,1}/\lambda_{p,2} > 1$ and $\sin(\alpha_1)/\sin(\alpha_2) > 1$, demonstrate that GPs qualitatively follow the most fundamental law of refraction, Snell's law:

$$\frac{\sin\alpha_1}{\sin\alpha_2} = \frac{n_2}{n_1} = \frac{\lambda_1}{\lambda_2} \quad (1)$$

In Fig. 4G we corroborate the GP refraction with a numerical calculation, assuming $E_{F,2}$ = 0.44 eV

for the graphene monolayer (as in Figs. 2 and 3). For the bilayer, we increased the conductivity to match the experimental wavelength ratio, $\lambda_{p,1} = 1.4\lambda_p$ (Fig. 4H). We measured $\alpha_1 = 50°$ and $\alpha_2 = 30°$, yielding $\sin(\alpha_1)/\sin(\alpha_2) = 1.53$, qualitatively following Snell's law (Eq. 1). The quantitative discrepancy found in both experiment and theory [i.e., $\sin(\alpha_1)/\sin(\alpha_2) > \lambda_{p,1}/\lambda_{p,2}$] is attributed to the strong GP damping. In strongly absorbing media, Snell's law deviates from its simple form (Eq. 1), as fronts of constant amplitude and phase may exhibit different diffraction angles (*31*), which is not considered in our analysis. Although further studies are required for a better quantitative understanding, our results demonstrate that GP propagation can be controlled by refraction. In the future, local gating of graphene could open exciting avenues for electrically tunable refractive elements, such as for steering of GPs.

Launching and control of propagating GPs by resonant metal antennas and spatial conductivity patterns could lead to various applications, including GP focusing into gated graphene waveguides, resonators, modulators, or plasmon interferometers for communication and sensing. Through the use of improved doping strategies and carrier mobility in graphene, we expect GPs to propagate over distances of many wavelengths at mid-infrared, near-infrared, and telecommunication wavelengths. Resonant antenna devices might also be used for converting the GPs into far-field radiation, which would enable a purely optical readout of graphene plasmonic circuits or wireless on-chip communication between them.

REFERENCES AND NOTES

1. W. L. Barnes, A. Dereux, T. W. Ebbesen, *Nature* **424**, 824–830 (2003).
2. S. A. Maier, *Plasmonics: Fundamentals and Applications* (Springer-Verlag, New York, 2007).
3. P. Mühlschlegel, H. J. Eisler, O. J. F. Martin, B. Hecht, D. W. Pohl, *Science* **308**, 1607–1609 (2005).
4. S. I. Bozhevolnyi, V. S. Volkov, E. Devaux, J.-Y. Laluet, T. W. Ebbesen, *Nature* **440**, 508–511 (2006).
5. F. López-Tejeira *et al.*, *Nat. Phys.* **3**, 324–328 (2007).
6. J. Lin *et al.*, *Science* **340**, 331–334 (2013).
7. F. J. Rodríguez-Fortuño *et al.*, *Science* **340**, 328–330 (2013).
8. A. Boltasseva, H. A. Atwater, *Science* **331**, 290–291 (2011).
9. K. W. K. Shung, *Phys. Rev. B* **34**, 979–993 (1986).
10. O. Vafek, *Phys. Rev. Lett.* **97**, 266406 (2006).
11. G. W. Hanson, *J. Appl. Phys.* **103**, 064302 (2008).
12. M. Jablan, H. Buljan, M. Soljačić, *Phys. Rev. B* **80**, 245435 (2009).
13. B. Wunsch, T. Stauber, F. Sols, F. Guinea, *New J. Phys.* **8**, 318 (2006).
14. M. Polini *et al.*, *Phys. Rev. B* **77**, 081411 (2008).
15. A. Vakil, N. Engheta, *Science* **332**, 1291–1294 (2011).
16. Z. Fang *et al.*, *ACS Nano* **6**, 10222–10228 (2012).
17. Y. Yao *et al.*, *Nano Lett.* **13**, 1257–1264 (2013).
18. H. Yan *et al.*, *Nat. Photonics* **7**, 394–399 (2013).
19. L. Ju *et al.*, *Nat. Nanotechnol.* **6**, 630–634 (2011).
20. A. N. Grigorenko, M. Polini, K. S. Novoselov, *Nat. Photonics* **6**, 749–758 (2012).
21. F. J. García de Abajo, *Science* **339**, 917–918 (2013).
22. A. Y. Nikitin, F. Guinea, F. J. Garcia-Vidal, L. Martin-Moreno, *Phys. Rev. B* **84**, 195446 (2011).
23. F. H. L. Koppens, D. E. Chang, F. J. García de Abajo, *Nano Lett.* **11**, 3370–3377 (2011).
24. J. Chen *et al.*, *Nature* **487**, 77–81 (2012).
25. Z. Fei *et al.*, *Nature* **487**, 82–85 (2012).
26. See supplementary materials on *Science* Online.
27. Y. Liu *et al.*, *Nano Lett.* **12**, 4853–4858 (2012).
28. M. Schnell *et al.*, *Nat. Photonics* **3**, 287–291 (2009).
29. H. Yan *et al.*, *Nat. Nanotechnol.* **7**, 330–334 (2012).
30. Y.-M. Lin *et al.*, *Nano Lett.* **8**, 2119 (2008).
31. M. Born, E. Wolf, *Principles of Optics* (Pergamon, New York, 1959).

ACKNOWLEDGMENTS

We thank P. S. Carney, A. Kuzmenko, I. Nechaev, and F. Guinea for stimulating discussions. Supported by the European Union through ERC starting grants (TERATOMO, SPINTROS and CarbonLight), NMP (HINTS and Grafol), Marie Curie Career Integration Grants (ITAMOSCINOM and GRANOP); the European Commission under Graphene Flagship (contract no. CNECT-ICT-604391); the Spanish Ministry of Economy and Competitiveness (National Projects MAT2012-36580 and MAT2012-37638) and from the Basque Government (Project PI2011-1). F.K. acknowledges support from the Fundacio Cellex Barcelona. R.H. is co-founder of Neaspec GmbH, a company producing scattering-type scanning near-field optical microscope systems such as the one used in this study. All other authors declare no competing financial interests.

SUPPLEMENTARY MATERIALS

www.sciencemag.org/content/344/6190/1369/suppl/DC1
Materials and Methods
Figs. S1 and S2
References (*32*–*35*)

11 March 2014; accepted 8 May 2014
Published online 22 May 2014;
10.1126/science.1253202

LOW-DENSITY MATERIALS

Ultralight, Ultrastiff Mechanical Metamaterials

Xiaoyu Zheng,[1]* Howon Lee,[2] Todd H. Weisgraber,[1] Maxim Shusteff,[1] Joshua DeOtte,[1] Eric B. Duoss,[1] Joshua D. Kuntz,[1] Monika M. Biener,[1] Qi Ge,[2] Julie A. Jackson,[1] Sergei O. Kucheyev,[1] Nicholas X. Fang,[2]* Christopher M. Spadaccini[1]*

The mechanical properties of ordinary materials degrade substantially with reduced density because their structural elements bend under applied load. We report a class of microarchitected materials that maintain a nearly constant stiffness per unit mass density, even at ultralow density. This performance derives from a network of nearly isotropic microscale unit cells with high structural connectivity and nanoscale features, whose structural members are designed to carry loads in tension or compression. Production of these microlattices, with polymers, metals, or ceramics as constituent materials, is made possible by projection microstereolithography (an additive micromanufacturing technique) combined with nanoscale coating and postprocessing. We found that these materials exhibit ultrastiff properties across more than three orders of magnitude in density, regardless of the constituent material.

Nature has found a way to achieve mechanically efficient materials by evolving cellular structures. Natural cellular materials, including honeycomb (*1*) (wood, cork) and foamlike structures, such as trabecular bone (*2*), plant parenchyma (*3*), and sponge (*4*), combine low weight with superior mechanical properties. For example, lightweight balsa has a stiffness-to-weight ratio comparable to that of steel along the axial loading direction (*5*). Inspired by these naturally occurring cellular structures, human-made lightweight cellular materials fabricated from a wide array of solid constituents are desirable for a broad range of applications including structural components (*6*, *7*), energy absorption (*8*, *9*), heat exchange (*10*, *11*), catalyst supports (*12*), filtration (*13*, *14*), and biomaterials (*15*, *16*).

However, the degradation in mechanical properties can be drastic as density decreases (*17*, *18*). A number of examples among recently reported low-density materials include graphene elastomers (*19*), metallic microlattices (*20*), carbon nanotube foams (*21*), and silica aerogels (*22*, *23*). For instance, the Young's modulus of low-density silica aerogels (*22*, *23*) decreases to 10 kPa (0.00001% of bulk) at a density of less than 10 mg/cm^3 (<0.5% of bulk).

This loss of mechanical performance is because most natural and engineered cellular solids with random porosity, particularly at relative densities less than 0.1%, exhibit a quadratic or stronger scaling relationship between Young's modulus and density as well as between strength and density. Namely, $E/E_s \propto (\rho/\rho_s)^n$ and $\sigma_y/\sigma_{ys} \propto (\rho/\rho_s)^n$, where E is Young's modulus, ρ is density, σ_y is yield strength, and s denotes the respective bulk value of the solid constituent material property. The power n of the scaling relationship between relative material density and the relative mechanical property depends on the material's microarchitecture. Conventional cellular foam materials with stochastic porosity

[1]Lawrence Livermore National Laboratory, Livermore, CA 94550, USA. [2]Department of Mechanical Engineering, Massachusetts Institute of Technology, Cambridge, MA 02139, USA.
*Corresponding author. E-mail: zheng3@llnl.gov (X.Z.); spadaccini2@llnl.gov (C.M.S.); nicfang@mit.edu (N.X.F.)

are known to deform predominantly through bending of their cell walls and struts (*24*). This type of deformation results in relative stiffness scaling with $n = 2$ or 3. A number of approaches in recent years have aimed to reduce this coupling between mechanical properties and mass density (*5*, *17*, *18*, *20*, *25*–*31*). Among these, few fabrication processes are capable of building arbitrary three-dimensional microarchitectures with controlled micro- and nanostructure across a wide range of mass density and material constituents. The desired material properties are thus limited to a narrow density range and specific loading directions.

Improved mechanical properties can arise from a material that contains micro- and nanoscale building blocks arranged in an ordered hierarchy. Among these new designs are metallic microlattices with high recoverability when compressed (*20*, *26*), TiN nanotrusses (*32*, *33*), and ceramic composite trusses (*34*) that show enhanced fracture toughness of coating materials when the thickness of coating materials is reduced to the nanoscale.

We report a group of ultralight mechanical metamaterials that maintain a nearly linear scaling between stiffness and density spanning three orders of magnitude in density, over a variety of constituent materials. We use the term "mechanical metamaterials" to refer to materials with certain mechanical properties defined by their geometry rather than their composition. The materials described here are highly ordered, nearly isotropic, and have high structural connectivity within stretch-dominated, face-centered cubic (fcc) architectures. The ultralow-density regime is accessed by fabricating microlattices with critical features ranging from ~20 μm down to ~40 nm. The densities of samples produced in this work ranged from 0.87 kg/m^3 to 468 kg/m^3, corresponding to 0.025% to 20% relative density.

A stretch-dominated unit cell structure, consisting of b struts and j frictionless joints and satisfying Maxwell's criterion, $M = b - 3j + 6 > 0$, is substantially more mechanically efficient—with a higher stiffness-to-weight ratio (defined as E/ρ)—than its bend-dominated counterpart. This is attributed to its struts carrying load under compression or tension rather than bending (*17*). A fundamental lattice building block of this type is the octet-truss unit cell (Fig. 1A), whose geometric configuration was proposed by Deshpande *et al.* (*35*). The cell has a regular octahedron as its core, surrounded by eight regular tetrahedra distributed on its faces (fig. S1). All the strut elements have identical aspect ratios, with 12 solid rods or hollow tubes connected at each node. The cubic symmetry of the cell's fcc structure generates a material with nearly isotropic behavior (*36*). The relative density of such octet-truss unit cells can be approximated by $\rho = 26.64(d/L)^2$ (*35*), where L and d are the length and diameter of each beam element. On the macroscale, under uniaxial compressive loading, the relative compressive stiffness and yield strength of these structures theoretically show linear scaling relationships: $E/E_s \propto (\rho/\rho_s)$ and $\sigma/\sigma_s \propto (\rho/\rho_s)$ (*35*). A cubic lattice is readily constructed by periodic packing of the unit cell along its three principal directions (Fig. 1, B and C) (*37*, *38*). Alternate orientations of the bulk lattice relative to the unit cell's principal axes can likewise be constructed (fig. S2), with the fundamental tessellation of space by the unit cell remaining the same.

To study how the loading direction and lattice orientation of an octet-truss lattice affects its E-ρ scaling relationship, we analyzed, fabricated, and tested them in a variety of orientations (*39*) (figs. S1 to S5). In addition to these stretch-dominated lattices, as a point of comparison, a bend-dominated tetrakaidecahedron unit cell (*40*, *41*) of the same size scale was generated and the corresponding cubic-symmetric foams (known as Kelvin foams) were fabricated with a variety of densities (Fig. 1, D to F).

The fabrication of these microlattices is enabled by projection microstereolithography, a layer-by-layer additive micromanufacturing process capable of fabricating arbitrary three-dimensional microscale structures (*42*, *43*). In contrast to other three-dimensional (3D) rapid prototyping methods such as 3D printing and ultraviolet (UV) projection waveguide systems (*44*), this type of fabrication technology is ideal for 3D lattices with high structural complexity and with feature sizes ranging from tens of micrometers to centimeters. By combining projection microstereolithography with nanoscale coating methods, 3D lattices with ultralow relative densities below 0.1% can be created. The process begins with a photosensitive polymer resin bath; we use either 1,6-hexanediol diacrylate (HDDA) or poly(ethylene glycol) diacrylate (PEGDA). Shown schematically in Fig. 2A, the apparatus uses a spatial light modulator—in this case a liquid-crystal-on-silicon chip—as a dynamically reconfigurable digital photomask. A three-dimensional CAD model is first sliced into a series of closely spaced horizontal planes. These two-dimensional image slices are sequentially transmitted to the reflective liquid-crystal-on-silicon chip, which is illuminated with UV light from a light-emitting diode array. Each image is projected through a reduction lens onto the surface of the photosensitive resin. The exposed liquid cures, forming a layer in the shape of the two-dimensional image, and the substrate on which it rests is lowered, reflowing a thin film of liquid over the cured layer. The image projection is then repeated, with the next image slice forming the subsequent layer. Our polymer microlattices were fabricated in tens of minutes and have features spanning size scales from 10 to 500 μm. For mechanical testing purposes, all materials described here were fabricated as blocks of various sizes consisting of multiple unit cells (table S1). Scanning electron microscopy (SEM) images of the as-built polymer lattice and unit cell are shown in Fig. 2, B and F.

Although projection microstereolithography requires a photopolymer, other constituent materials such as metals and ceramics can be incorporated with additional processing. Using the base polymer lattice as a template, we are able to convert the structures to metallic and ceramic microlattices. Metallic lattices were generated via electroless nickel plating on the as-formed HDDA. The thickness of the metal coating is

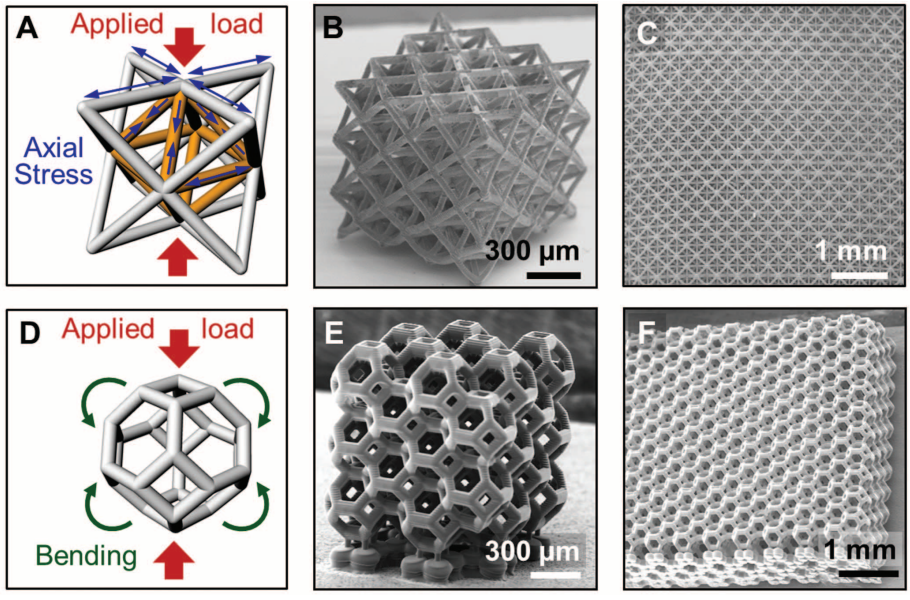

Fig. 1. Architecture of stretch-dominated and bend-dominated unit cells and lattices. (**A**) Mechanical response to compressive loading of a stretch-dominated octet-truss unit cell. (**B**) Octet-truss unit cells packed into a cubic microlattice. (**C**) SEM image of a stretch-dominated lattice material composed of a network of octet-truss unit cells. (**D**) Mechanical response to compressive loading of a bend-dominated tetrakaidecahedron unit cell. (**E**) Tetrakaidecahedron unit cell packed into a cubic bend-dominated lattice (Kelvin foam). (**F**) SEM image of a bend-dominated lattice composed of a network of tetrakaidecahedron unit cells.

controlled by the plating time, yielding metal films from 100 nm to 2 μm. The polymer template is subsequently removed by thermal decomposition, leaving behind the hollow-tube nickel-phosphorus (Ni-P) stretch-dominated microlattice shown in Fig. 2, C and G.

A similar templating approach is used to generate hollow-tube aluminum oxide (amorphous Al_2O_3, alumina) microlattices; however, the coating is produced by atomic layer deposition (ALD), a gas-phase process, rather than liquid-phase processing. The resulting hollow-tube microlattices have alumina thicknesses from ~40 to 210 nm, with an example shown in Fig. 2, D and H, with corresponding material weight density ranging from less than 1 kg/m^3 to 10.2 kg/m^3.

Loading the resin bath with nanoparticles can further expand the base material set. Solid Al_2O_3 ceramic lattices were prepared in the microlithography system by using photosensitive PEGDA liquid prepolymer loaded with ~150-nm alumina nanoparticles (Baikowski Inc., ~12.5% alumina by volume). The same sequential lithographic exposure process produced a microlattice made of a hybrid of solid PEGDA and alumina nanoparticles. These hybrid lattices are converted to pure Al_2O_3 octet-truss microlattices through a sintering procedure (*39*). An example of this structure is shown in Fig. 2, E and I. The parameters and properties for a selection of our stretch-dominated mechanical metamaterials and bend-dominated foams are summarized in table S1. The densities of all samples were calculated by measuring the weight and fabricated dimensions of the completed microlattices.

The microstructured mechanical metamaterials were tested to determine their Young's modulus E and uniaxial compressive strength σ_y, defined as the crushing stress of the material. Uniaxial compression studies of all microlattices with the same cubic dimensions were conducted on an MTS Nano Indenter XP, equipped with a flat punch stainless steel tip with a diameter of 1.52 mm. During 20 consecutive compression cycles up to 10% strain, we observed typical viscoelastic behavior for the polymer microlattices with pronounced hysteresis and loading rate–dependent Young's modulus. The Young's moduli for all polymer microlattices and foams were extracted at a loading rate at 87.2 nN/s, corresponding to a strain rate of 10^{-3} s^{-1}. Uniaxial compression of these structures is shown in movies S1 to S3. Representative stress-strain curves from uniaxial compression crushing tests for determining the compressive strength of octet-truss microlattices made of solid HDDA polymer, hollow-tube Ni-P metal, and solid alumina are shown in fig. S7, A and B, and fig. S8A, respectively. Bulk HDDA polymer, cured by UV cross-linking a solid sample of similar dimensions to the octet-truss lattices, was determined to have Young's modulus E_s = 530 MPa and yield stress σ_{ys} = 86 MPa. [See (*39*) for detailed measurement methods and bulk property values for other constituent materials.]

The results of these mechanical tests, together with the bend-dominated tetrakaidecahedron-based Kelvin foams fabricated from the base HDDA polymer, are summarized in Fig. 3, A and B, which respectively plot relative Young's modulus and strength against relative mass density. Figure 4 shows the location of these material properties on the stiffness versus density material selection chart, together with other recently reported ultralight materials for comparison. The stretch-dominated microlattices populate the highly desirable ultralight, ultrastiff space toward the upper left of the chart (*17*) and have stiffness-to-weight ratios that do not substantially degrade as density decreases by several orders of magnitude. In contrast to the common bend-dominated $E/E_s \propto (\rho/\rho_s)^2$ scaling of open-cell stochastic foams such as silica aerogels and carbon foams, our stretch-dominated microlattice materials demonstrate the desired linear relationship of $E/E_s \propto \rho/\rho_s$, approaching the theoretical limit, and exhibit this remarkable scaling relationship over three orders of magnitude in density and across all constituent materials studied. These octet-truss lattice materials are highly isotropic, so the scaling of stiffness with density does not vary with the orientation of the lattice (fig. S4), as confirmed by our studies of different loading directions. These lattices have the highest specific stiffness when the lattice is loaded normal to the (111) plane, which is closest-packed within the fcc architecture.

In the ultralow-density regime (relative density <0.1%), we observed markedly different compression behavior in hollow-tube ALD ceramic octet-truss microlattices relative to solid ceramic lattices at higher relative densities (8 to 20%). The hollow-tube ceramic microlattices with nanoscale wall thicknesses showed smoother behavior with progressively fewer discontinuities in their stress-strain curves (fig. S8, A and B), in contrast to solid microstrut ceramic lattices with catastrophic, fracture-dominated behavior. The loading-unloading curves of hollow-tube Al_2O_3 lattices revealed elastic behavior followed by a nonlinear response on each loading cycle. Although relative compressive stiffness and relative density initially follow a nearly linear scaling law, the transition from conventional brittle behavior (in low-density ceramic materials) to more "ductile" mechanical behavior (in ultralight materials with nanoscale wall thicknesses) suggests

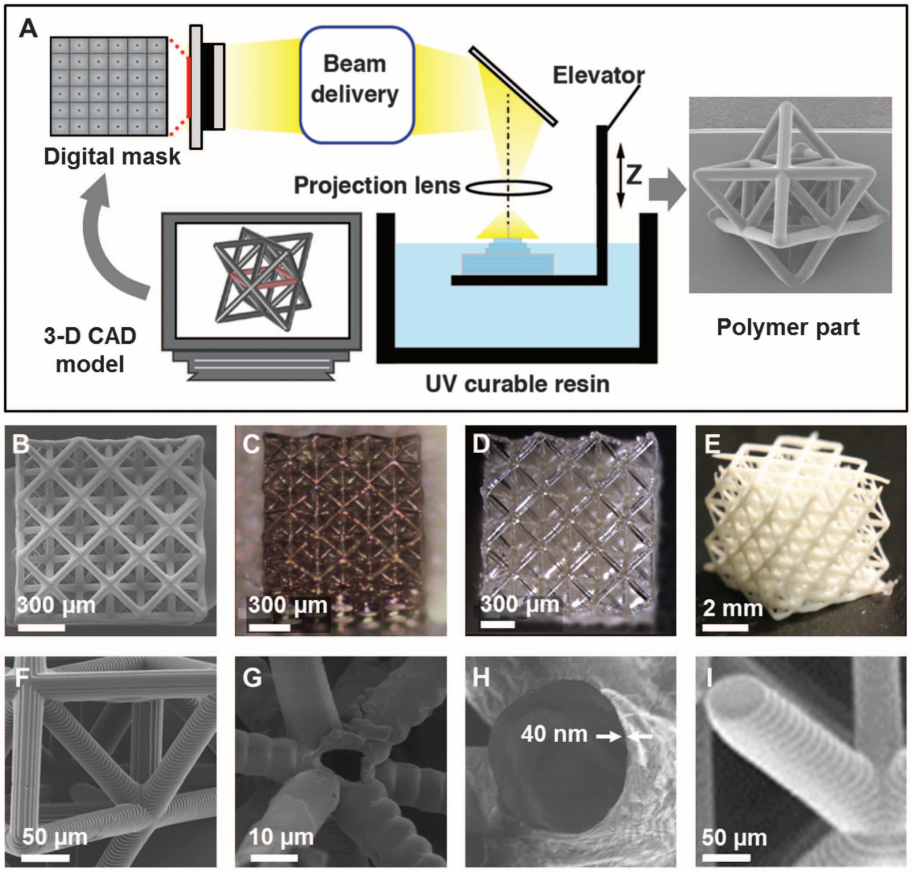

Fig. 2. Fabrication of ultralight, ultrahigh-stiffness stretch-dominated microlattices. (**A**) Projection microstereolithography, a layer-by-layer technique capable of fabricating arbitrary, microscale, three-dimensional structures with resolution of ~5 μm. As the structure builds, the substrate is lowered into the liquid resin by an elevator traveling vertically (marked as Z-direction); the SEM image at the right is the fabricated octet-truss unit cell. (**B** to **E**) Octet-truss microlattices with varied constituent materials and configurations: (B) solid polymer HDDA; (C) hollow-tube metallic Ni-P; (D) hollow-tube ceramic (alumina); (E) solid ceramic (alumina). (**F** to **I**) Magnified views of the struts of the microlattices in (B) to (E), respectively.

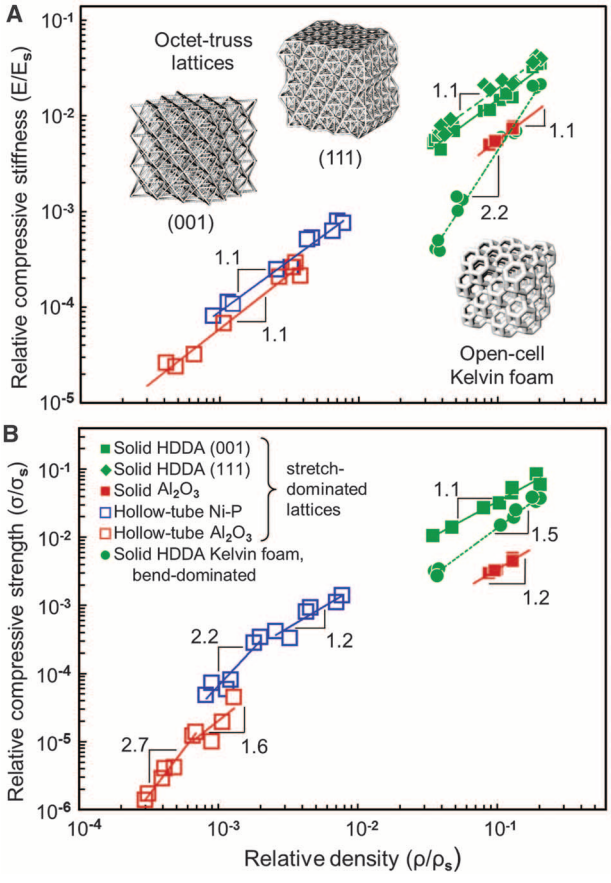

Fig. 3. Measurement of the material properties of stretch-dominated microlattices and Kelvin foams as a function of relative density. (**A**) Relative stiffness as a function of relative density for stretch-dominated and bend-dominated microlattices. Stretch-dominated materials exhibit a linear stiffness-density relationship of $E \propto \rho$, whereas bend-dominated materials soften as $E \propto \rho^2$ or worse, as shown by their slopes in the plot. (**B**) Relative strength as a function of relative density for stretch-dominated and bend-dominated microlattices.

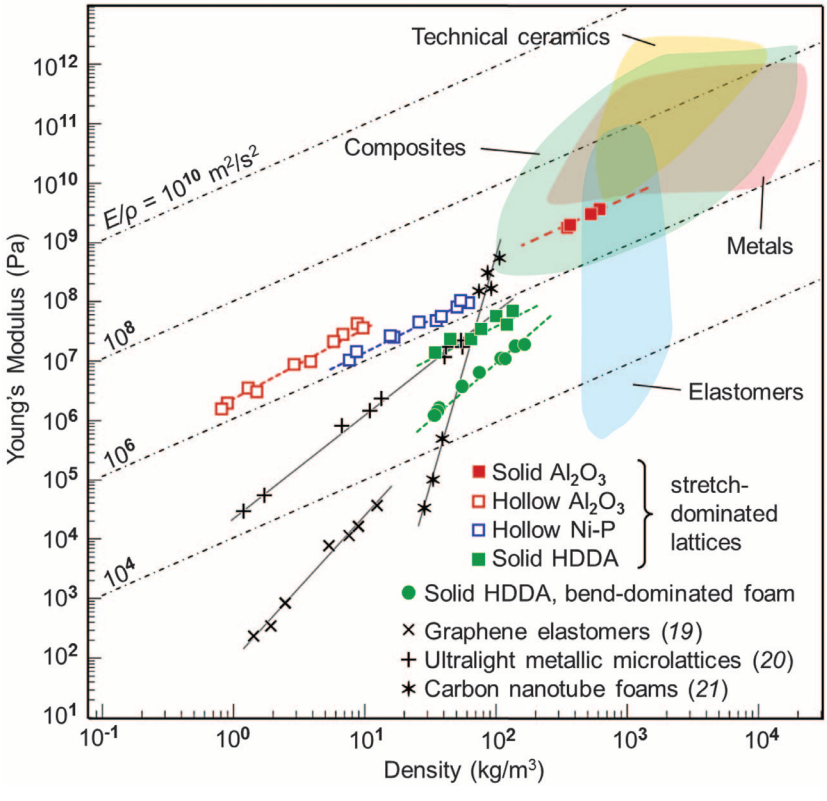

Fig. 4. An Ashby chart plotting compressive stiffness versus density for ultralight, ultrastiff mechanical metamaterials and other previously reported materials. Dotted lines indicate contours of constant stiffness-density ratio $c = E/\rho$ (m^2/s^2).

a transition from a fracture-dominated failure mode to a buckling-dominated failure mode, with suppression of the catastrophic failure seen in solid Al_2O_3 octet-truss lattices.

These differences in compressive behavior between solid and hollow-tube ceramic octet-truss lattices are primarily attributed to local buckling induced by the high aspect ratio of the strut length to nanoscale wall thickness, in contrast to nanoscale TiN trusses (*32*) and ceramic composite (*34*), whose aspect ratios are low enough to allow the nanoscale strengthening effect of the wall thickness to dominate. For example, the ratio of strut length to nanoscale wall thickness in fig. S8B is about 1400:1 and contributes to its large compression strain, governed by $\varepsilon \propto (1/\rho)^{0.5}$ (*17*). Thus, the relative compressive strength makes a transition from the nearly linear scaling law governing the stretch-dominated failure mode at an approximate density near 0.08% to a scaling power of 2.7, as indicated in Fig. 3B. In the same figure, a similar transition from yielding-dominated to buckling-dominated failure at an approximate relative density of 0.2% is evident in Ni-P lattices, consistent with the trend observed for bend-dominated metallic microlattices (*26*).

When an ultralow-density metallic microlattice is bend-dominated, its stiffness degrades substantially with reduced density. An example of this is the Ni-P lattice reported by Schaedler *et al.* (*20*), whose specific stiffness (stiffness-to-weight ratio) degrades from 0.23×10^6 m^2/s^2 to 0.05×10^6 m^2/s^2 as density is reduced from 40 mg/cm^3 to 14 mg/cm^3 (*45*). By contrast, our Ni-P stretch-dominated metallic lattice is not only much stiffer in the same density range, its specific stiffness stays nearly constant, measured as 1.8×10^6 m^2/s^2 and 2.1×10^6 m^2/s^2 at densities of 14 mg/cm^3 and 40 mg/cm^3, respectively. Similarly, in a recent report of high-strength microarchitected ceramic composites (*34*), their strength performance approaches the linear scaling relationship over a narrow density range, and only when loaded in a direction optimized for their anisotropic architecture. Our metamaterials, in contrast, maintain their mechanical efficiency over a broad density regime without substantial degradation in specific stiffness, owing to the nearly linear E-ρ scaling relationship.

We have shown that these high mechanical efficiencies are possible across a range of constituent materials. Fabricating ordered lattice structures at these length scales brings them into the regime in which it becomes possible to design microstructured functional materials with superior bulk-scale properties.

REFERENCES AND NOTES

1. K. Ando, H. Onda, *J. Wood Sci.* **45**, 120–126 (1999).
2. T. M. Ryan, C. N. Shaw, *Proc. R. Soc. B* **280**, 20130172 (2013).
3. P. Van Liedekerke *et al.*, *Phys. Biol.* **7**, 026006 (2010).
4. J. H. Shen, Y. M. Xie, X. D. Huang, S. W. Zhou, D. Ruan, *Key Eng. Mater.* **535–536**, 465–468 (2013).
5. J. A. Kepler, *Compos. Sci. Technol.* **71**, 46–51 (2011).
6. L. Valdevit, A. J. Jacobsen, J. R. Greer, W. B. Carter, *J. Am. Ceram. Soc.* **94**, s15–s34 (2011).
7. N. Lyu, B. Lee, K. Saitou, *J. Mech. Des.* **128**, 527 (2006).
8. T. A. Schaedler *et al.*, *Adv. Eng. Mater.* **16**, 276–283 (2014).

9. K. J. Maloney *et al.*, *APL Mater.* **1**, 022106 (2013).
10. L. Valdevit, A. Pantano, H. A. Stone, A. G. Evans, *Int. J. Heat Mass Transfer* **49**, 3819–3830 (2006).
11. M. Q. Li, X. Shi, *Rare Metal Mater. Eng.* **36**, 575 (2007).
12. O. Y. Kwon, H. J. Ryu, S. Y. Jeong, *J. Ind. Eng. Chem.* **12**, 306 (2006).
13. R. A. Olson, L. C. B. Martins, *Adv. Eng. Mater.* **7**, 187–192 (2005).
14. P. Day, H. Kind, *Mod. Cast.* **74**, 16 (1984).
15. S. Baudis *et al.*, *Biomed. Mater.* **6**, 055003 (2011).
16. K. Arcaute, B. K. Mann, R. B. Wicker, *Tissue Eng. C* **17**, 27–38 (2010).
17. J. L. Gibson, F. M. Ashby, *Cellular Solids: Structure and Properties* (Cambridge Univ. Press, Cambridge, 2001).
18. H. Fan *et al.*, *Nat. Mater.* **6**, 418–423 (2007).
19. L. Qiu, J. Z. Liu, S. L. Y. Chang, Y. Wu, D. Li, *Nat. Commun.* **3**, 1241 (2012).
20. T. A. Schaedler *et al.*, *Science* **334**, 962–965 (2011).
21. M. A. Worsley, S. O. Kucheyev, J. H. Satcher, A. V. Hamza, T. F. Baumann, *Appl. Phys. Lett.* **94**, 073115 (2009).
22. T. M. Tillotson, L. W. Hrubesh, *J. Non-Cryst. Solids* **145**, 44–50 (1992).
23. S. O. Kucheyev *et al.*, *Adv. Mater.* **24**, 776–780 (2012).
24. L. J. Gibson, *MRS Bull.* **28**, 270–274 (2003).
25. K. Tantikom, Y. Suwa, T. Aizawa, *Mater. Trans.* **45**, 509–515 (2004).
26. A. Torrents, T. A. Schaedler, A. J. Jacobsen, W. B. Carter, L. Valdevit, *Acta Mater.* **60**, 3511–3523 (2012).
27. C. Q. Dam, R. Brezny, D. J. Green, *J. Mater. Res.* **5**, 163–171 (1990).
28. J. K. Cochran, K. J. Lee, D. McDowell, T. Sanders, Multifunctional metallic honeycombs by thermal chemical processing. In *Processsing and Properties of Lightweight Cellular Metals and Structures*, A. K. Ghosh, T. H. Sanders, T. D. Claar, Eds. (Minerals, Metals and Materials Society, Seattle, WA, 2002), p. 127–136.
29. J. Zhang, M. F. Ashby, *Int. J. Mech. Sci.* **34**, 475–489 (1992).
30. D. Rayneau-Kirkhope, Y. Mao, R. Farr, *Phys. Rev. Lett.* **109**, 204301 (2012).
31. K. C. Cheung, N. Gershenfeld, *Science* **341**, 1219–1221 (2013).
32. D. Jang, L. R. Meza, F. Greer, J. R. Greer, *Nat. Mater.* **12**, 893–898 (2013).
33. L. Meza, J. Greer, *J. Mater. Sci.* **49**, 2496–2508 (2014).
34. J. Bauer, S. Hengsbach, I. Tesari, R. Schwaiger, O. Kraft, *Proc. Natl. Acad. Sci. U.S.A.* **111**, 2453–2458 (2014).
35. V. S. Deshpande, N. A. Fleck, M. F. Ashby, *J. Mech. Phys. Solids* **49**, 1747–1769 (2001).
36. J. D. Renton, *Elastic Beams and Frames* (Horwood, Chichester, UK, ed. 2, 2002).
37. S. Hyun, J. E. Choi, K. J. Kang, *Comput. Mater. Sci.* **46**, 73–82 (2009).
38. H. L. Fan, F. N. Jin, D. N. Fang, *Mater. Des.* **30**, 511–517 (2009).
39. See supplementary materials on *Science* Online.
40. W. Y. Jang, S. Kyriakides, A. M. Kraynik, *Int. J. Solids Struct.* **47**, 2872–2883 (2010).
41. Y. Takahashi, D. Okumura, N. Ohno, *Int. J. Mech. Sci.* **52**, 377–385 (2010).
42. X. Zheng *et al.*, *Rev. Sci. Instrum.* **83**, 125001 (2012).
43. C. Sun, N. Fang, D. M. Wu, X. Zhang, *Sens. Actuators A* **121**, 113–120 (2005).
44. A. J. Jacobsen, W. Barvosa-Carter, S. Nutt, *Adv. Mater.* **19**, 3892–3896 (2007).
45. L. M. Moreau *et al.*, *Nano Lett.* **12**, 4530–4539 (2012).

ACKNOWLEDGMENTS

This work was performed under the auspices of the U.S. Department of Energy by Lawrence Livermore National Laboratory under contract DE-AC52-07NA27344. Supported by LDRD Strategic Initiative 11-SI-005 and DARPA MCMA (Materials with Controlled Microstructural Architecture, Program Manager J. Goldwasser). The authors at Lawrence Livermore National Laboratory thank H. Rathbun for useful discussions on modeling the lattice structures, M. Worsley for taking SEM images, and C. Harvey for technical support. N.X.F. thanks S. Cai at University of California San Diego for insightful input regarding buckling modes in ceramic octet-truss lattices (LLNL-JRNL-640334).

SUPPLEMENTARY MATERIALS

www.sciencemag.org/content/344/6190/1373/suppl/DC1
Materials and Methods
Figs. S1 to S9
Table S1
Movies S1 to S3
References (*46*–*55*)

17 February 2014; accepted 16 May 2014
10.1126/science.1252291

NANOMATERIALS

Long-range orientation and atomic attachment of nanocrystals in 2D honeycomb superlattices

M. P. Boneschanscher,[1] W. H. Evers,[2,3] J. J. Geuchies,[1] T. Altantzis,[4] B. Goris,[4] F. T. Rabouw,[1] S. A. P. van Rossum,[1] H. S. J. van der Zant,[3] L. D. A. Siebbeles,[2] G. Van Tendeloo,[4] I. Swart,[1] J. Hilhorst,[5] A. V. Petukhov,[1] S. Bals,[4] D. Vanmaekelbergh[1]*

Oriented attachment of synthetic semiconductor nanocrystals is emerging as a route for obtaining new semiconductors that can have Dirac-type electronic bands such as graphene, but also strong spin-orbit coupling. The two-dimensional (2D) assembly geometry will require both atomic coherence and long-range periodicity of the superlattices. We show how the interfacial self-assembly and oriented attachment of nanocrystals results in 2D metal chalcogenide semiconductors with a honeycomb superlattice. We present an extensive atomic and nanoscale characterization of these systems using direct imaging and wave scattering methods. The honeycomb superlattices are atomically coherent and have an octahedral symmetry that is buckled; the nanocrystals occupy two parallel planes. Considerable necking and large-scale atomic motion occurred during the attachment process.

In oriented attachment, a single nanocrystal (NC) is formed from two adjacent NCs through atomically matched bond formation between two specific facets. Controlled oriented attachment is currently emerging as a route to form extended one- and two-dimensional single-crystalline semiconductors of II-VI and IV-VI compounds (*1*–*5*). These superlattices are of interest in optoelectronics. Truncated nanocubes of the Pb-chalcogenide family (fig. S1) have been recently used to create two-dimensional (2D) atomically coherent ultrathin quantum wells (*4*) as well as superlattices with square or honeycomb geometries (fig. S2) (*5*). The formation of such systems is remarkable, given that several demanding conditions must be fulfilled. The NC building blocks must be nearly monodisperse in size and shape, and attachment should only occur with a geometrically defined subset of NC facets. The long-range atomic and nanoscale order in such systems is far from understood. For extended, atomically coherent PbSe superlattices with honeycomb geometry, immediate questions emerge regarding the large-scale crystallographic orientation of the NCs, the role of surface passivation of specific facets, and the atomic mechanism of attachment.

Here, we report on the atomic and nanoscale analysis of atomically coherent PbSe, PbS, and CdSe honeycomb superlattices. Using high-angle annular dark-field scanning transmission electron microscopy (HAADF-STEM) tomography, we show that the honeycomb structures are buckled—the NCs occupy two parallel planes—and hence show nanoscale analogy with the proposed atomic silicene honeycomb structure. The specific orientation of the NCs in the 2D superlattice extends over hundreds of unit cells, suggesting that such types of single crystals must be formed from a preordered state, for example at the suspension/air interface. Compared with the native building blocks, the NCs in the honeycomb structure are considerably elongated in the direction of the NC-NC bond. This finding points to bond formation via necking accompanied with a gradual release of the capping molecules and considerable atomic motion within the NCs. Moreover, the 2D honeycomb structures of PbSe with a rocksalt atomic lattice were robust enough to be transformed into 2D CdSe lattices with a zinc blende atomic lattice through cation-exchange and keep the nanoscale honeycomb geometry intact. This method opens a route to a new class of 2D semiconductors with tunable composition. In these structures, the nanoscale honeycomb geometry has been predicted to result in both valence and conduction bands that can be filled with Dirac-type charge carriers as in graphene but, unlike graphene, with strong spin-orbit coupling (*6*).

The PbSe NCs have the shape of a cantellated cube, approaching that of a rhombicuboctahedron (fig. S1), implying that the NCs are terminated with {100}, {110}, and {111} facets. We estimated the NC size from the radially averaged diameter of the TEM projections for >1000 particles (5.3 ± 0.4 nm) (fig. S3). The oriented attachment of these NCs resulted in structures with long-range periodicity, as visualized by means of an equilateral triangle spanning the same number of unit cells along each vertex in the HAADF-STEM image (Fig. 1A).

[1]Debye Institute for Nanomaterials Science, University of Utrecht, Post Office Box 80.000, 3508 TA Utrecht, Netherlands. [2]Opto-electronic Materials Section, Delft University of Technology, Julianalaan 136, 2628 BL Delft, Netherlands. [3]Kavli Institute of Nanoscience, Delft University of Technology, Post Office Box 5046, 2600 GA Delft, Netherlands. [4]Electron Microscopy for Materials Science (EMAT), University of Antwerp, Groenenborgerlaan 171, 2020 Antwerp, Belgium. [5]European Synchrotron Radiation Facility (ESRF), Grenoble, Beamline ID01, France.
***Corresponding author. E-mail: d.vanmaekelbergh@uu.nl**

Zooming in on the honeycomb structure (Fig. 1B) reveals that the ⟨111⟩ axes of the NCs are perpendicular to the substrate and that the NC-NC bonds are perpendicular to three of the ⟨110⟩ axes (a discussion on atomic contrast in HAADF-STEM images is available in fig. S4). This result is also corroborated by electron diffraction (ED) patterns (Fig. 1C). The structures have a high degree of crystallinity, as observed with the occurrence of sharp spots in ED patterns recorded on selected areas with a diameter of 200 nm (Fig. 1C; a full analysis of all peaks in the diffraction pattern is available in fig. S5 and tables S1 and S2) (*7*).

There are three different models for attachment of the NCs that result in a honeycomb structure with the nanocrystal ⟨111⟩ axes perpendicular to the substrate: attachments via the {110}, {111}, or {100} facets, respectively (Fig. 1, D to I). The three structures appear similar from the top but have a very different 3D geometry. Attachment via {110} facets results in a planar, trigonal structure with bond angles between the NCs of 120° (Fig. 1, D and E). If the NCs attach via the {111} facets, the overall structure of the superlattice is slightly buckled, with a tetrahedral symmetry and NC bond angles of 109.5° (Fig. 1, F and G). Attachment via {100} facets results in a highly buckled geometry, with an octahedral symmetry and NC bond angles of 90° (Fig. 1, H and I). We used various imaging techniques to show that the experimental structure is of the octahedral type, but that the bond lengths are longer than expected on the basis of a simple block model.

In the trigonal model, the attachment takes place via the {110} facets, meaning that the ⟨110⟩ axes are parallel to the NC bonds. However, both the high-resolution HAADF-STEM images and the ED patterns show that in our experiment, the ⟨110⟩ axes are perpendicular to the NC bonds (Fig. 1, B and C), so we could discard the trigonal model. In the buckling of the honeycomb, the HAADF-STEM images showed additional scattering strength on the NC bonds, indicating a larger-than-average thickness of the sample at that position. In this respect, both the tetrahedral and octahedral model are buckled and have three of the ⟨110⟩ NC axes perpendicular to the NC bonds, so it was impossible to discriminate between these remaining models by ED or 2D projections from high-resolution HAADF-STEM. Thus, we needed to use a combination of scanning tunneling microscopy (STM), grazing-incidence small-angle x-ray scattering

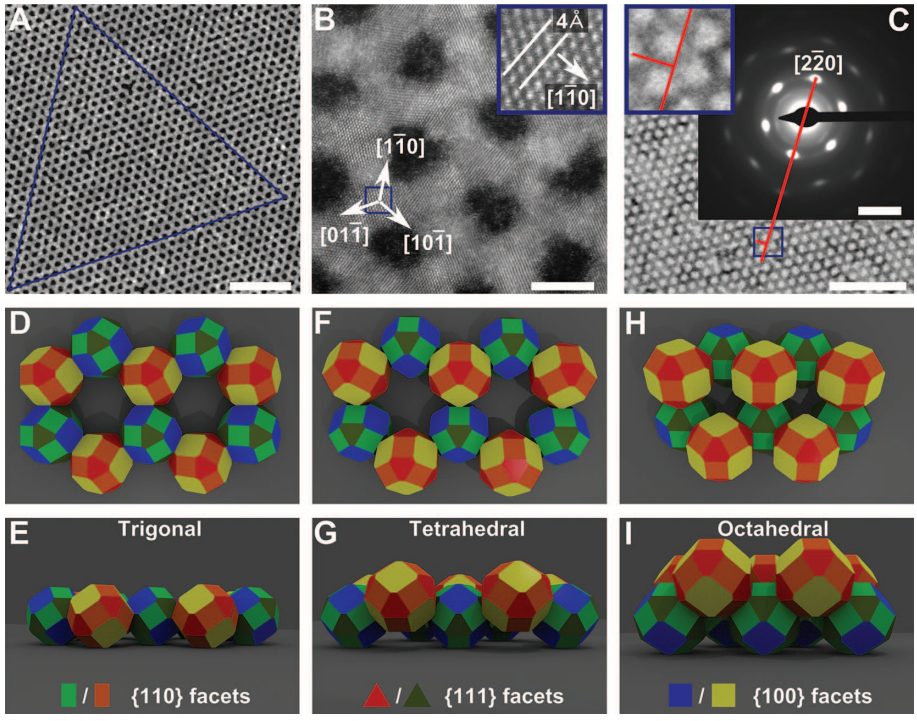

Fig. 1. Single-crystalline PbSe honeycomb structures created by means of oriented attachment. (**A**) HAADF-STEM image of the honeycomb structure (bright on a dark background). The equilateral triangle shows the long-range ordering of the structure. Scale bar, 50 nm. (**B**) High-resolution HAADF-STEM image showing that the ⟨111⟩ NC axes are perpendicular to the honeycomb plane, and three of the ⟨110⟩ axes are perpendicular to the NC bonds. (Inset) Zoom-in on the atomic columns indicated by the blue box. Scale bar, 5 nm. (**C**) Electron diffraction pattern showing the high degree of crystallinity. TEM image in the background shows the area on which the ED pattern was recorded (the honeycomb appears dark on a bright background). Red line and inset show the orientation of the diffraction spots with respect to the honeycomb structure, confirming that the ⟨110⟩ axes are perpendicular to the NC bonds. Scale bars, 50 nm (TEM); 5 nm^{-1} (ED). (**D** to **I**) Models of the honeycomb structure, with cantellated cubes as nanocrystals. The two inequivalent sites in the honeycomb lattice are indicated by yellow/red and blue/green NCs. Rectangles (orange and light green) represent {110} facets, triangles (red and dark green) represent {111} facets, and squares (yellow, blue) represent {100} facets. (D) and (E) are the top and side view of the trigonal structure, respectively. (F) and (G) are top and side view of the tetrahedral structure, respectively. (H) and (I) are the top and side view of the octahedral structure, respectively.

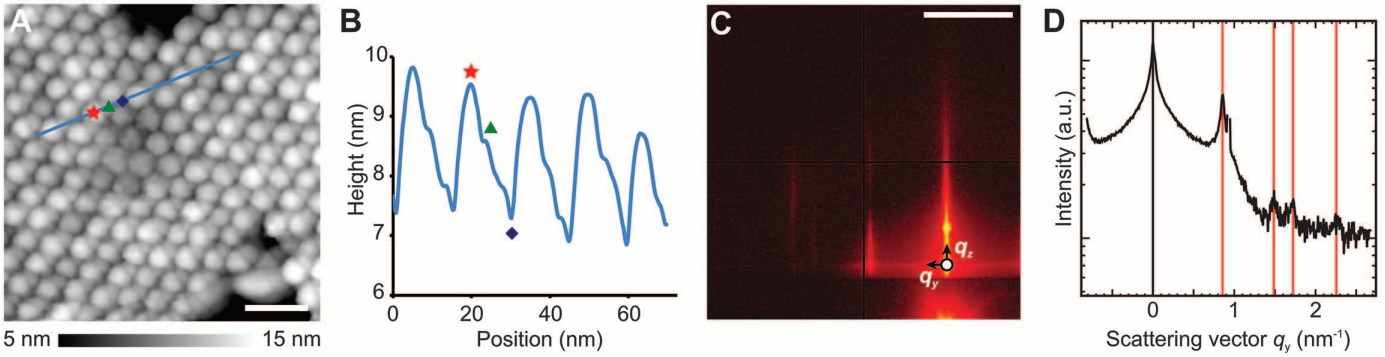

Fig. 2. STM and GISAXS measurements of the PbSe honeycomb structures. (**A**) Constant-current STM measurement showing high (red star) and low (green triangle) nanocrystals forming a honeycomb structure. Feedback settings are 3.5 V and 20 pA. Scale bar, 20 nm. (**B**) Height profile along the blue line indicated in (A). The position of a high NC (star), low NC (triangle), and hollow site (diamond) are indicated. (**C**) GISAXS pattern of a honeycomb structure on top of a Si(100) substrate, under an angle of incidence of 0.7°. Scale bar, 1 nm^{-1}. (**D**) Line trace in the horizontal direction indicated in (C), revealing the in-plane order. Red lines mark diffraction peaks with relative positions of $1:\sqrt{3}:2:\sqrt{7}$, arising from the hexagonal order of the holes in the structure.

(GISAXS), and electron tomography to fully resolve the honeycomb structure.

The STM measurements showed that the honeycomb structure is indeed buckled (Fig. 2, A and B). However, topography in STM is a complicated convolution of NC height and tip radius (fig. S6), so no quantitative height data could be extracted. We cannot measure bond lengths and angles directly in STM, but we could reliably determine the distance between next-nearest neighbors (NNNs) at the same height (8.5 ± 0.8 nm, for >500 measurements). From GISAXS (Fig. 2, C and D, and fig. S7), we observed scattering peaks arising from the hexagonal order of the holes in the honeycomb structure with relative positions of $1:\sqrt{3}:2:\sqrt{7}$, as expected from a honeycomb structure (Fig. 2, C and D). Looking at the absolute peak positions in Fig. 2D, we found a hole-hole distance of 8.5 nm, which is in accordance with the NNN distances observed in STM. Assuming perfect honeycomb models, this distance implies a bond length of 5.2 nm for the tetrahedral and 6.0 nm for the octahedral honeycomb structure.

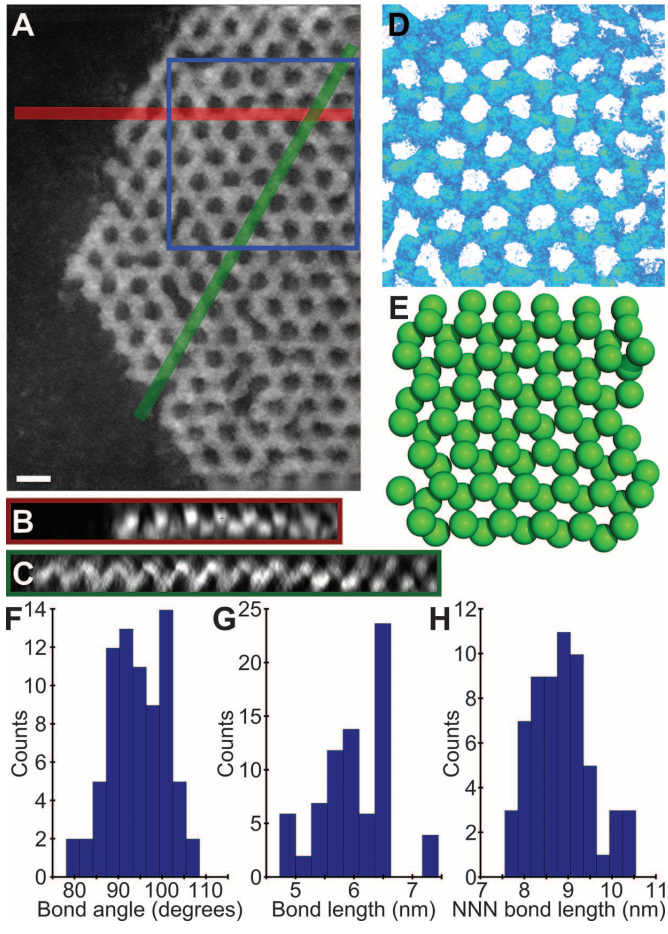

Fig. 3. HAADF-STEM tomography on a PbSe honeycomb structure. (**A**) Overview of the honeycomb structure obtained by averaging the tomographic reconstruction in the direction perpendicular to the substrate. Scale bar, 10 nm. (**B** and **C**) Slices through the tomogram perpendicular to (A), along the (B) red or (C) green line indicated in (A). (**D**) Isovolume rendering of the tomographic reconstruction in the region indicated with the blue box in (A). (**E**) Equally sized spheres plotted on the coordinates obtained by means of automated particle detection in the region indicated in blue in (A). (**F**) Bond angles measured from the coordinates in (E), showing a bond angle of 95 ± 5°. (**G**) Bond lengths to nearest neighbors, showing a bond length of 6.0 ± 0.5 nm. (**H**) Bond lengths to NNNs, showing a NNN bond length of 8.9 ± 0.6 nm.

The tomographic reconstruction of a PbSe honeycomb structure obtained with electron tomography is shown in Fig. 3 (movie S1) (*7*–*10*). Slices through the reconstruction in the direction perpendicular to the substrate indicate that the two inequivalent NCs in the honeycomb unit cell are located on different heights (Fig. 3, B and C) (*11*). We performed automated particle detection (*7*) on the region of interest indicated in Fig. 3D. We remark that the effect of the missing wedge in our tomography data results in a blurring of the contrast along the *z* direction. In (*7*), we used simulated tomography data to show that the missing wedge in this case does not impede objective particle detection (fig. S8). From the resulting coordinates, we constructed a model resembling the tomographic reconstruction (Fig. 3E). Using a Voronoi method, we could measure important parameters such as bond angle, bond length, and NNN bond length (Fig. 3, F to H).

The obtained bond angle of 95° ± 5° (Fig. 3F) shows that the honeycomb structure is of the octahedral type, with bonds between the {100} facets. We can compare the ratio between bond length (6.0 ± 0.5 nm) and NNN bond length (8.9 ± 0.6 nm) that we find with the theoretical values for the different structures—for the octahedral type, one would expect $1:\sqrt{2}$; for the tetrahedral type, $1:\sqrt{8/3}$; and for the trigonal type, $1:\sqrt{3}$. The ratio we find here (1:1.48) is a bit higher than the expected ratio for an octahedral structure, which is in agreement with the bond angles being slightly higher than 90°. The same measurement on a tomogram of a CdSe honeycomb structure shows bond angles of 85° ± 6°, which is slightly lower than expected (figs. S9 and S10 and movie S2).

We established that the NCs attach via the {100} facets into a honeycomb structure with octahedral symmetry (Fig. 1, H and I). Next, we returned to the bond lengths of the honeycomb structure, as extracted from TEM (fig. S11), STM, GISAXS, and tomography. All four techniques give an independent measure of 6.0 nm for the NC bond lengths, which is an increase of 13% of the original NC diameter. The increased bond lengths shed light on the microscopic mechanism of facet-to-facet atomic attachment. Li *et al.* (*12*) showed that in the process of oriented attachment, the NCs are continuously rotating and moving in close proximity by means of Brownian motion to find an optimum configuration before enduring attachment takes place. We propose that during the rotation and Brownian motion as described by Li *et al.* (*12*), atomic-scale necking took place as a first step in the attachment. After necking had started, the capping molecules that remain bound to the facet were gradually removed,

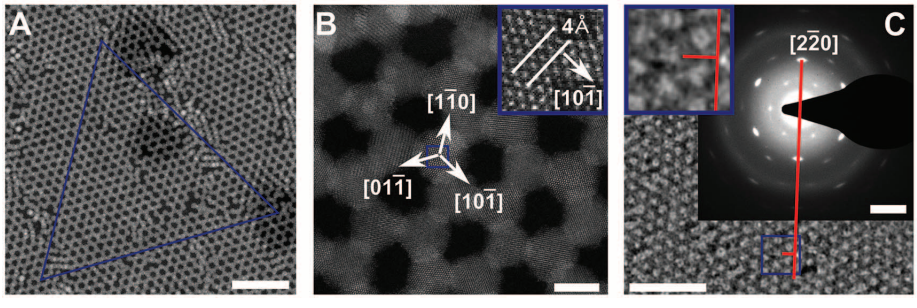

Fig. 4. Single crystalline CdSe honeycomb structures created by cation exchange. (**A**) HAADF-STEM image of the CdSe honeycomb structure. The honeycomb appears bright on a dark background. The equilateral triangle shows that the long-range ordering of the structure is retained. Scale bar, 50 nm. (**B**) High-resolution HAADF-STEM image showing that the orientation of the Se anion lattice with respect to the superlattice geometry is preserved. (Inset) Zoom-in on the area indicated by the blue box. Scale bar, 5 nm. (**C**) An ED pattern showing that the high degree of crystallinity is preserved. TEM image in the background shows the area on which the ED pattern was recorded (the honeycomb appears dark on a bright background). Red line and inset show the orientation of the diffraction spots with respect to honeycomb structure, confirming that the ⟨110⟩ axes are perpendicular to the NC bonds. Scale bars, 50 nm (TEM); 5 nm^{-1} (ED).

and the neck extended perpendicular to the bond axis through large-scale atomic motion. For PbSe NCs, considerable atomic reconfigurations have been reported (*13*, *14*). The necking explains the elongation of the bond lengths, which also results in a considerably more open honeycomb structure than can be obtained from geometric attachment of rigid block models (Fig. 1H, as compared with the real structures in Figs. 1, A to C, 3, and 4). In the mechanism that we propose, not all of the capping molecules have to be released at once from a facet, resulting in pathways with lower activation energy. Oriented attachment accompanied with neck formation has been reported before as a pathway for the growth of various metal nanoparticles (*15*, *16*).

Since the emergence of graphene (*17*), there has been a general interest in the properties of electrons confined in a honeycomb lattice (*18*–*23*). We show that oriented attachment can form the basis of a generally applicable two-step method for the preparation of 2D semiconductors with nanoscale honeycomb geometry: assembly and oriented attachment of Pb-chalcogenide NCs with truncated cubic shape, followed by cation exchange. It has been predicted that honeycomb semiconductors of zinc blende compounds (such as CdSe) show a truly new electronic band structure, with a valence hole Dirac band and one or two conduction electron Dirac bands combined with strong spin-orbit coupling (*6*). We transformed PbSe honeycomb structures into CdSe superlattices via a cation exchange reaction (*24*, *25*) and showed that honeycomb structures can also be prepared from PbS NCs (figs. S12 and S13).

The successful exchange of a PbSe honeycomb lattice into a CdSe honeycomb is presented in Fig. 4. The complete transformation of the PbSe lattice into CdSe is confirmed by means of energy-dispersive x-ray spectroscopy (fig. S14). HAADF-STEM and ED measurements show that the orientation of the Se anion lattice with respect to the honeycomb periodicity is preserved (Fig. 4, A to C). This result is in agreement with earlier described mechanisms in which the anion lattice is preserved during cation exchange (*26*, *27*) and is corroborated with high-resolution HAADF-STEM measurements of honeycomb structures at intermediate stages of cation exchange (*7*).

REFERENCES AND NOTES

1. C. Pacholski, A. Kornowski, H. Weller, *Angew. Chem. Int. Ed. Engl.* **41**, 1188–1191 (2002).
2. K.-S. Cho, D. V. Talapin, W. Gaschler, C. B. Murray, *J. Am. Chem. Soc.* **127**, 7140–7147 (2005).
3. W. K. Koh, A. C. Bartnik, F. W. Wise, C. B. Murray, *J. Am. Chem. Soc.* **132**, 3909–3913 (2010).
4. C. Schliehe *et al.*, *Science* **329**, 550–553 (2010).
5. W. H. Evers *et al.*, *Nano Lett.* **13**, 2317–2323 (2013).
6. E. Kalesaki *et al.*, *Phys. Rev. X* **4**, 011010 (2014).
7. Materials and methods are available as supplementary materials on *Science* Online.
8. H. Friedrich *et al.*, *Nano Lett.* **9**, 2719–2724 (2009).
9. M. P. Boneschanscher *et al.*, *Nano Lett.* **13**, 1312–1316 (2013).
10. P. A. Midgley, M. Weyland, *Ultramicroscopy* **96**, 413–431 (2003).
11. The PbSe honeycombs suffer from beam damage, making it hard to obtain high-quality tomographic reconstructions. CdSe, on the other hand, is more stable under the electron beam, resulting in higher-quality tomographic reconstructions (Fig. 3 as compared with fig. S9, for example. Both images are obtained under the same conditions).
12. D. Li *et al.*, *Science* **336**, 1014–1018 (2012).
13. M. A. van Huis *et al.*, *Nano Lett.* **8**, 3959–3963 (2008).
14. M. A. van Huis *et al.*, *Adv. Mater.* **21**, 4992–4995 (2009).
15. J. M. Yuk *et al.*, *Science* **336**, 61–64 (2012).
16. J. M. Yuk *et al.*, *Chem. Commun. (Camb.)* **49**, 11479–11481 (2013).
17. A. H. Castro Neto, N. M. R. Peres, K. S. Novoselov, A. K. Geim, *Rev. Mod. Phys.* **81**, 109–162 (2009).
18. K. K. Gomes, W. Mar, W. Ko, F. Guinea, H. C. Manoharan, *Nature* **483**, 306–310 (2012).
19. G. De Simoni *et al.*, *Appl. Phys. Lett.* **97**, 132113 (2010).
20. M. Gibertini *et al.*, *Phys. Rev. B* **79**, 241406 (2009).
21. C.-H. Park, S. G. Louie, *Nano Lett.* **9**, 1793–1797 (2009).
22. C.-H. Park, L. Yang, Y.-W. Son, M. L. Cohen, S. G. Louie, *Phys. Rev. Lett.* **101**, 126804 (2008).
23. A. Singha *et al.*, *Science* **332**, 1176–1179 (2011).
24. J. M. Luther, H. Zheng, B. Sadtler, A. P. Alivisatos, *J. Am. Chem. Soc.* **131**, 16851–16857 (2009).
25. B. J. Beberwyck, Y. Surendranath, A. P. Alivisatos, *J. Phys. Chem. C* **117**, 19759–19770 (2013).
26. S. Bals *et al.*, *Nano Lett.* **11**, 3420–3424 (2011).
27. M. Casavola *et al.*, *Chem. Mater.* **24**, 294–302 (2012).

ACKNOWLEDGMENTS

We thank ESRF (Grenoble, France) for providing the synchrotron beamtime and the staff of ESRF beamline ID-01 for their support. We thank C. van Overbeek for his help on the PbS sample. This research is part of the programs "Control over Functional Nanoparticle Solids (FNS)" and "Designing Dirac Carriers in semiconductor honeycomb superlattices (DDC)," which are supported by the Foundation of Fundamental Research on Matter (FOM), which is part of the Dutch Research Council (NWO). The authors also acknowledge financial support from the European Research Council (ERC Advanced Grant 24691-COUNTATOMS and ERC Starting Grant #335078-COLOURATOM). The authors also appreciate financial support from the European Union under the Seventh Framework Program [Integrated Infrastructure Initiative 262348 European Soft Matter Infrastructure (ESMI)]. This work was supported by the Flemish Fund for Scientific Research (FWO Vlaanderen) through a Ph.D. research grant to B.G.

SUPPLEMENTARY MATERIALS

www.sciencemag.org/content/344/6190/1377/suppl/DC1
Materials and Methods
Figs. S1 to S14
Tables S1 to S2
References (*28*, *29*)
Movies S1 to S2

25 February 2014; accepted 13 May 2014
Published online 29 May 2014;
10.1126/science.1252642

NANOMATERIALS

Hydroxylation of the surface of PbS nanocrystals passivated with oleic acid

Danylo Zherebetskyy,[1] Marcus Scheele,[1,2] Yingjie Zhang,[1,3] Noah Bronstein,[2] Christopher Thompson,[1,2] David Britt,[4] Miquel Salmeron,[1] Paul Alivisatos,[1,2] Lin-Wang Wang[1]*

Controlling the structure of colloidal nanocrystals (NCs) is key to the generation of their complex functionality. This requires an understanding of the NC surface at the atomic level. The structure of colloidal PbS NCs passivated with oleic acid has been studied theoretically and experimentally. We show the existence of surface OH^- groups, which play a key role in stabilizing the PbS(111) facets, consistent with x-ray photoelectron spectroscopy as well as other spectroscopic and chemical experiments. The role of water in the synthesis process is also revealed. Our model, along with existing observations of NC surface termination and passivation by ligands, helps to explain and predict the properties of NCs and their assemblies.

The structure of the interior of nanocrystals (NCs) can be determined quite accurately by crystallography, but the structure of their surfaces cannot be obtained from this analysis because of the complexity of the organic capping ligands (*1*–*6*). However, the NC surface structure controls the growth and solubility and strongly influences the physical and chemical properties (*7*–*12*). We took advantage of improved insights into the mechanisms of NC growth (*3*–*6*), combined with extensive ab initio total energy calculations, to create a testable model for the atomic surface passivation structure of the exposed facets of a PbS NC. The model made specific, and at first surprising, predictions about the surface-bound species that were subsequently verified experimentally. PbS is ideal for this study because of the high symmetry of its rock-salt structure and its propensity to form NCs with well-defined (111) and (001) facets (*13*, *14*). PbS NCs with controlled size and shape can be produced from a PbO lead precursor, hexamethyldisilathiane (TMS_2S) sulfur precursor, and oleic acid that binds to exposed Pb atoms to stabilize the surface (*1*–*6*).

We performed ab initio electronic structure calculations on relevant subsystems and on the reaction steps involved in the synthetic process, including studies of immediate precursors, the fate of byproducts of the initial decomposition step, NC-ligand interactions, and ligand-ligand and ligand-solvent

[1]Materials Sciences Division, Lawrence Berkeley National Laboratory, Berkeley, CA 94720, USA. [2]Department of Chemistry, University of California at Berkeley, Berkeley, CA 94720, USA. [3]Applied Science and Technology Graduate Program, University of California at Berkeley, Berkeley, CA 94720, USA. [4]The Molecular Foundry, Lawrence Berkeley National Laboratory, One Cyclotron Road, Berkeley, CA 94720, USA.
***Corresponding author. E-mail: lwwang@lbl.gov**

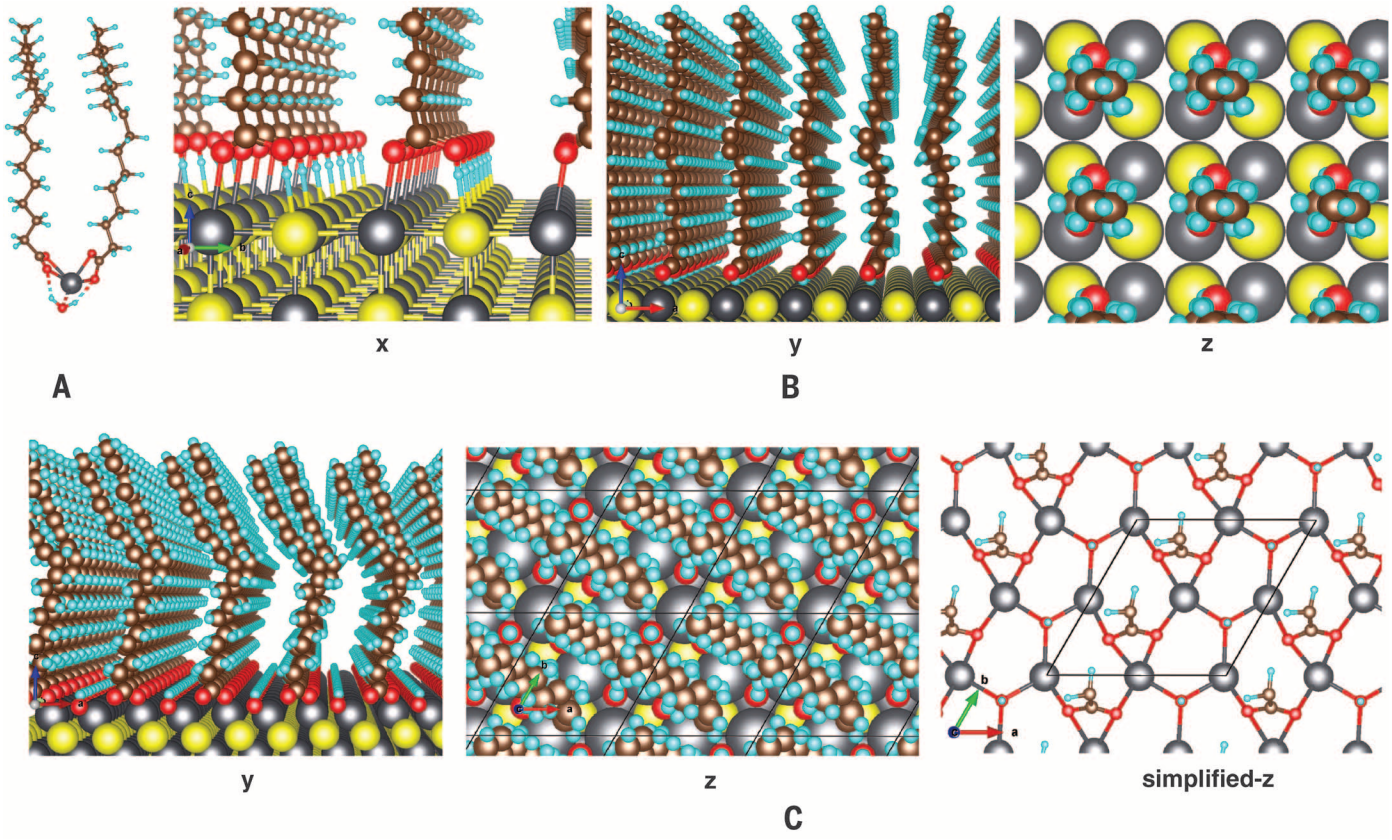

Fig. 1. Optimized molecular configurations. (**A**) A water molecule formed during NC synthesis is bound to the $Pb(OA)_2$ molecule, forming a $Pb(OA)_2\cdots H_2O$ complex. (**B**) Relaxed configuration of OAH molecules on the PbS(001) surface (*x*,*y*,*z* views). (**C**) Relaxed lowest-energy configuration of OA^- and OH^- molecules on the PbS(111) surface: *y* and *z* views. On the right, a simplified *z*-view schematic is shown with truncated tail chains. Pb, gray; S, yellow; O, red; H, blue; C, brown.

interactions. Our methods (*15*) are density functional theory (DFT) in the generalized gradient approximation (GGA). The GGA is not accurate enough to describe the van der Waals (vdW) interactions, and the entropic contributions in the solvent are prohibitively time-consuming at present to be calculated directly. However, we have taken advantage of likely cancellations of these terms when comparing different systems. We found the following features in our theoretically derived model: (i) The Pb:S atomic ratio is roughly 1.2:1 (Pb_{excess}:S ~ 0.2:1) for ~5-nm NCs. (ii) The ratio between the number of surface oleate molecules and the number of excess Pb atoms is ~1:1. (iii) The ligands can be easily removed from the (001) surface. (iv) The average (111)/(001) surface-to-center distance ratio of the truncated octahedral shape is about 0.82:1. (v) OH^- groups are present on the NC (111) facet. These features are consistent with prior and current experimental studies, including Rutherford backscattering (RBS), transmission electron microscopy (TEM), x-ray photoelectron spectroscopy (XPS), sum frequency generation (SFG) spectroscopy, nuclear magnetic resonance (NMR), and Fourier transform infrared spectroscopy (FTIR) (*5*, *6*, *16*–*18*). The presence of hydroxide groups on the surface predicted in the calculation as by-products of precursor decomposition was verified with XPS and SFG. The existence of water in the precursor was supported with NMR and FTIR measurements.

Table 1. Surface and ligand binding energies for the (001) and (111) surfaces of a PbS NC. The (001) and (111) surface areas per OAH (OA^-) molecule are 35.2 and 30.5 $Å^2$, respectively.

	(001)	(111)
Unpassivated surface (meV/$Å^2$)	12.31	23.47*
Binding *E* per OAH (or OA^-) (eV)	−0.16	−0.52
Total surface energy (meV/$Å^2$)	7.76	6.33

*Reconstructed surface.

The colloidal PbS NCs (*4*, *5*) are synthesized by dissolving PbO in hot oleic acid (*15*). One of the by-products of the reaction is water, which was proposed to remain as free molecules in the solution (*4*, *5*). Our calculations, however, show that it is energetically more favorable for water to bind to the Pb precursor (*15*). Thus, the first reaction step can be written as

$$PbO + 2 \times OAH \rightarrow Pb(OA)_2\cdots H_2O \quad (1)$$

where OAH denotes oleic acid. The DFT-optimized structure of the $Pb(OA)_2\cdots H_2O$ is shown in Fig. 1A. In the experiment, the reaction products were degassed at 110°C under vacuum for 1 hour. To determine whether such degassing removed all of the water in the precursor as previously suggested, we used NMR and FTIR. Although NMR demonstrated the absence of liquid water, it was unable to distinguish water molecules bound to the $Pb(OA)_2$ complexes (*15*). Using FTIR measurements and deuterated oleic acid (d1-OA), we distinguished O-H stretching modes associated with water bound to $Pb(OA)_2$ (*15*). The d1-OA was prepared so that only the acid H was exchanged for D. A major part of the water remained after degassing in sufficient amounts to provide the required 20% of water in Eq. 1 for the surface passivation described below (Pb_{excess}:S = 0.2:1, one OH^- per excess Pb). The existence of water is consistent with the observation that the $Pb(OA)_2$ precursors often form clusters (*19*). As a further demonstration of the role of water, we added acetic anhydride (*20*) as a drying agent during the reaction of Eq. 1, followed by evacuation to remove acetic acid and excess anhydride (*15*). The subsequent formation of PbS NCs was much slower and the NCs were of reduced size, from 8 to 10 nm (for that particular synthesis condition) to 4 nm. Also, the particle shapes became rather irregular, with many (001) surfaces (*15*), which is consistent with our model.

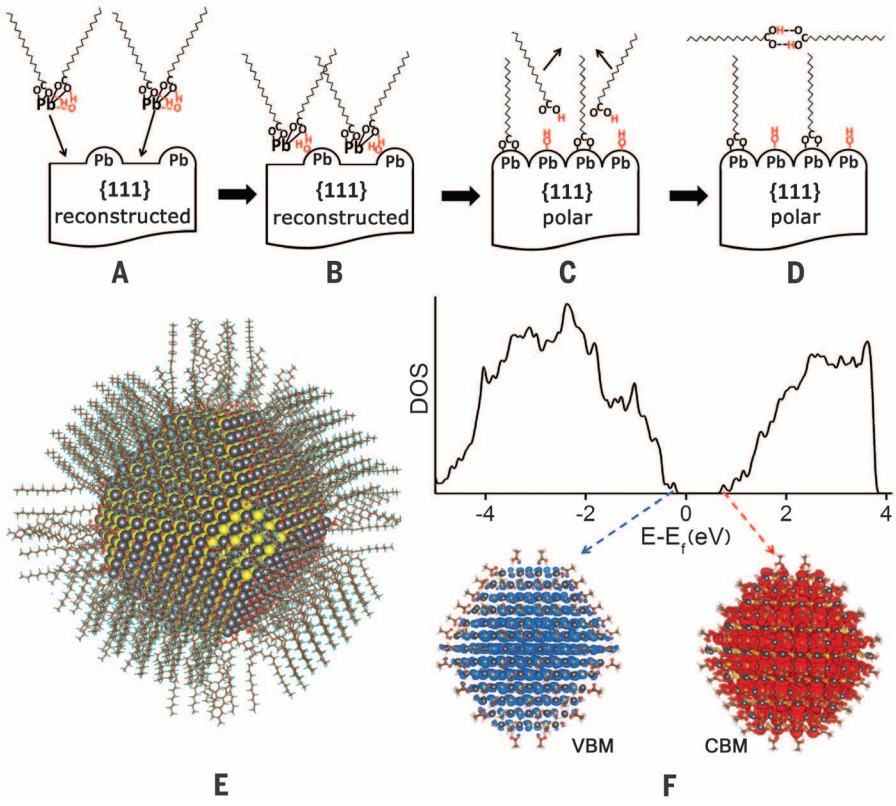

Fig. 2. Model of a PbS NC in colloidal solution. (**A** to **D**) Multistep process for building up the (111) facets of a PbS NC. (A) $Pb(OA)_2\cdots H_2O$ precursors approach the nonpolar and stoichiometric (111) facets. (B) Pb ions bind to surface vacancies. (C) One of the two OA^- in each $Pb(OA)_2\cdots H_2O$ complex is removed because of steric effects, and the water molecule dissociates to provide an OH^- group to the surface and H^+ for desorbing OA^-. (D) The desorbed OAH molecules dimerize in the solvent. (**E**) Calculated atomic structure of a 5-nm-diameter NC passivated with OA^- and OH^- ligands [coordinates in (*15*)]. (**F**) Electron density of states, showing the valence band maximum (VBM) and conduction band minimum (CBM) levels, of a NC passivated with truncated oleic acid alkyl chains [coordinates in (*15*)].

In the second step, TMS_2S dissolved in trioctylphosphine (TOP) is injected into the heated $Pb(OA)_2\cdots H_2O$ precursor dissolved in octadecene

$$Pb(OA)_2\cdots H_2O + (TMS)_2S \rightarrow PbS + (TMS)_2O + 2 \times OAH \quad (2)$$

The calculated Gibbs energy (ΔG) of Eq. 2 is –2.13 eV. It was suggested that the end product from oleic acid is $(oleyl\text{-}CO)_2O$ (*4*, *5*). It is also known, and computationally confirmed, that water will react with $(oleyl\text{-}CO)_2O$ to form two oleic acid molecules. Thus, during NC synthesis, oleic acid, $Pb(OA)_2\cdots H_2O$ [from excess $Pb(OA)_2$ precursor], $(TMS)_2O$, TOP, and octadecene are present in the solution as possible passivants. In the following, we consider passivations of the (001) and (111) surfaces separately.

Our calculation shows that oleic acid has the strongest binding energy to the (001) surface, because of its -COOH group (*15*). The (001) surface covered by OA^- (*9*) has a much higher energy than when covered by OAH, because the OA^- can bind with a cation in the solvent and thus has a much lower chemical potential in the solvent than OAH. On the PbS (001) surface, the -COOH groups form bidentate bridges between Pb and S atoms (–C=O···Pb and -COH···S bonds; Fig. 1B). This model contains one OAH molecule per two surface PbS pairs: one pair bound to one OAH and the other unbound. A high-density packing, with one OAH per PbS pair, is unfavorable because of steric repulsions between the oleyl tails. The binding energy between oleic acid and the PbS (001) surface is calculated as

$$E(\text{bind}) = E(\text{mol/surf}) - [E(\text{mol}) + E(\text{surf})] \quad (3)$$

Here E(mol/surf) is the energy of the whole system, E(surf) is the energy of the unpassivated nonpolar PbS(001) surface after atomic relaxation, and E(mol) is the free energy of the passivating molecule in the solvent, including solvent binding effects. There are two types of solvent binding effects: hydrogen bonding (H bonding) between functional groups and vdW interactions between alkane chains; of these, only H bonding can be described accurately by the GGA method. For the vdW interaction, we have removed the GGA vdW alkyl chain-chain interaction energy from the E(mol/surf) term in Eq. 3, because the chain-chain vdW interactions will approximately cancel each other between the E(mol/surf) term and E(mol) term (*15*). For E(mol), we included the –0.83-eV binding energy of the H-bonded OAH-OAH dimer. We also ignored the entropy change of the ligand molecules, which we deem to be small (*15*). The final calculated (001) binding energy is –0.16 eV per oleic acid (Table 1).

Table 2. Ligand patterns binding energies (in eV) on the (111) PbS NC surface for a 4-Pb-atom area. For $Pb(OA)_2$ cases, the binding energy of H_2O with $Pb(OA)_2$ and the binding of liquid water [after $Pb(OA)_2$ is bound to the surface] are taken into account. The 2 OA^-, 2 OH^- (current model) value is twice that shown in Table 1, because the surface area is twice as large here. The 2 OA^-, O^{2-} corresponds to the case where 2 OH^- form one O^{2-} on the surface and one H_2O leaving the surface.

2 OA^-, 2 OH^-	–1.04
2 OA^-, O^{2-}	–0.60
$Pb(OA)_2$ half-filled	–0.03
2$Pb(OA)_2$ full-filled	+3.78

Assessing the energetics of capping the polar (111) facets is more complicated because of the need for charge compensation (*21*, *22*) to satisfy the electron counting rule (*23*–*25*). The NCs formed in Eq. 2 have equal numbers of Pb and S, with stoichiometric nonpolar (111) facets with only half of the terminal Pb atoms (*22*, *26*). We then considered whether the $Pb(OA)_2\cdots H_2O$ group in the solvent can fill in the surface vacancies (the missing Pb atoms). We found that, in agreement with Bealing *et al.* (*9*), it is sterically impossible to fill every missing Pb atom of the (111) surface with one $Pb(OA)_2$, but one OA^- per missing Pb is possible. Hence, an anionic species is needed for charge balance. This species is OH^-, provided by the dissociation of bound H_2O, while the H^+ is used to form OAH

$$(PbS)_N(111) + Pb(OA)_2\cdots H_2O \rightarrow OA - Pb_{N+1}S_N(111) - OH + OAH \quad (4)$$

Here $(PbS)_N(111)$ denotes the reconstructed nonpolar (111) surface, and $Pb_{N+1}S_N(111)$ denotes the full Pb-terminated polar surface (Fig. 2, A to D). The binding energy of this passivation, which equals to the ΔG of the reaction (*4*), is –0.52 eV per oleate (Table 1), which is much larger than the (001) surface binding energy. The minimum energy configuration (*15*) of OA-$Pb_{N+1}S_N$(111)-OH is shown in Fig. 1C, where the OA^- group stabilizes the Pb ions via μ^2-bidentate bridging bonds, and the OH^- group stabilizes the Pb ions via μ^3-Pb_3–OH bonds. In the calculation of ΔG, we included the OAH-OAH dimer interaction of –0.83 eV and removed the alkyl chain-chain vdW interaction at the surface as in the (001) surface case. Although we have considered other possible passivation stoichiometries and configurations (*15*), none was found to be as stable as the ones considered above (Table 2).

In order to predict the shape of the PbS NC, we calculated the surface energies of the (001) and (111) surfaces, which are equal to the unpassivated surface energies [nonpolar for (111)] plus the binding energies calculated above. The unpassivated

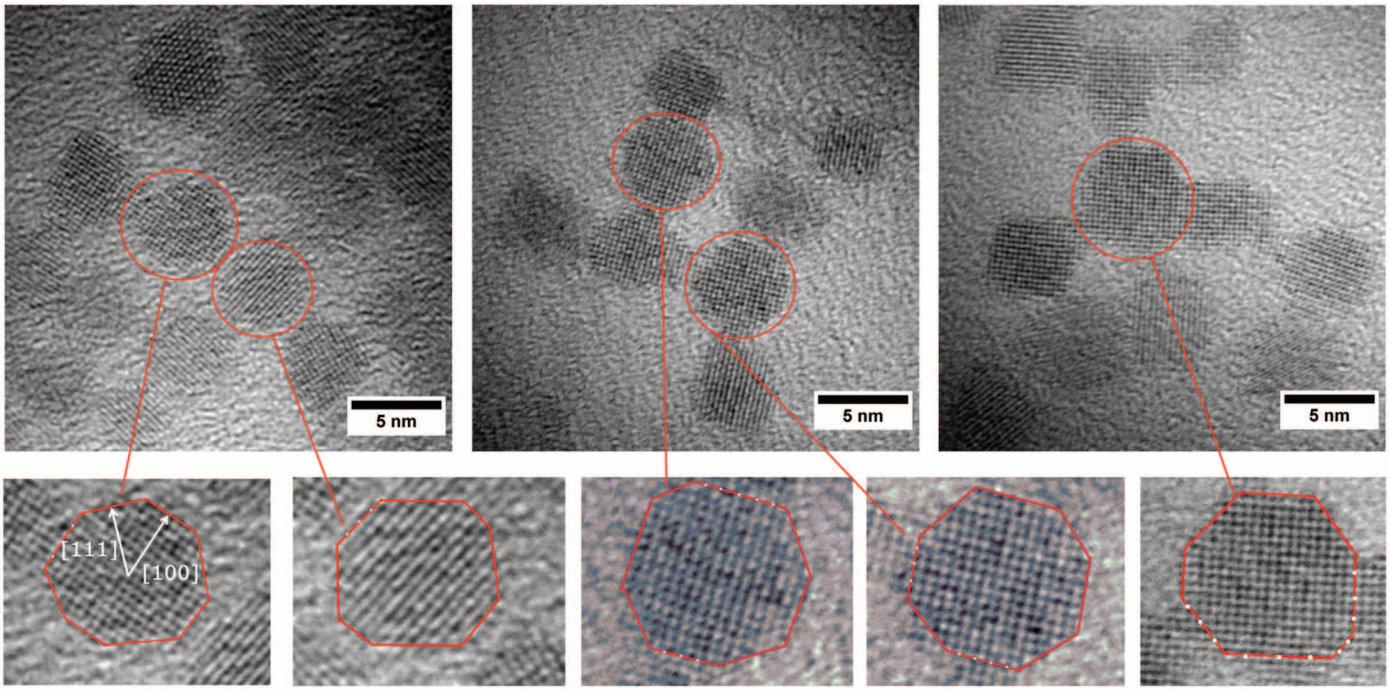

Fig. 3. TEM images of PbS NCs. High-resolution TEM images of the synthesized PbS NCs, with enlarged views of selected NCs shown below. The (111)/(001) Wulff ratios of center-to-surface distances of NCs are 0.820, 0.762, 0.866, 0.847, and 0.792 from left to right, respectively, with an average ratio of 0.817, in good agreement with the calculated value.

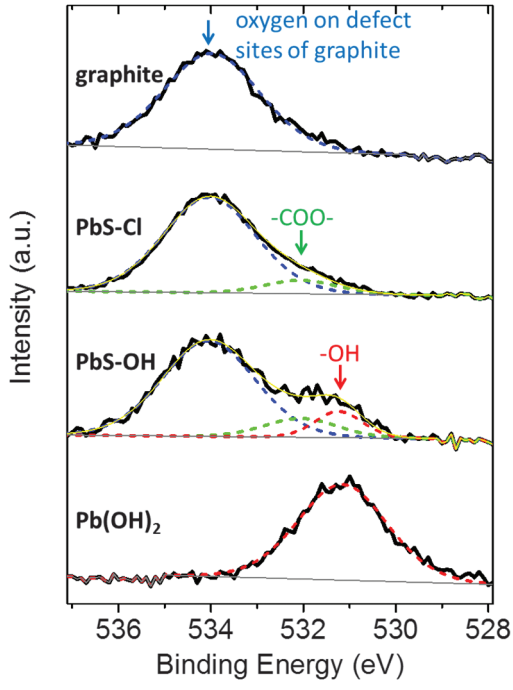

Fig. 4. The XPS spectra of PbS NCs. O 1s XPS showing peaks at 531.2eV (red) from O in OH^- groups, and at 532.1eV (green) from O in carboxyl groups. The peak at 534 eV is due to substrate O bound to graphite. a.u., arbitrary units.

surface energies were calculated from the energies of the slabs minus the corresponding bulk values. The resulting energies (Table 1) were used in a Wulff construction model (*27*–*29*) to determine the equilibrium NC shape. We obtained a (001)-to-(111) Wulff ratio of 0.82, which is in excellent agreement with the average 0.82 value derived from TEM images (Fig. 3). With this procedure, we constructed a model NC with all the surface passivation features (*15*) and with OH^- groups placed at the edges to determine whether it provides good passivation of edges and corners. To simplify the calculation, we truncated the alkyl chains of the oleic acids to the shorter acetic acid, which is not expected to change the NC surface electronic structure. We subsequently relaxed the atomic structure of the 2325-atom, 4–nm-diameter NC using DFT/GGA (*15*). The final system showed perfect surface passivation, with a clean band gap, without impurity or defect-induced states (Fig. 2F) and with good edge and corner passivation. Thus, we propose that the three-dimensional (3D) bulk structure determines the 2D surface passivation structure, which in turn determines the 1D edge passivation. For a 5-nm NC, our model (*15*) also provides the ratio between excess Pb and S atoms of 0.19:1 and between excess Pb and surface OA molecules of 1.18:1 respectively, which agree closely with experimentally observed values of 0.21:1 (measured by RBS) and 0.97:1 reported in (*6*). In our model, the ligand binding energy on the (001) surface is much smaller than that on the (111) surface, consistent with the images in Fig. 3, where all NCs are standing up on (001) facets, with some in direct contact via (001) facets. Both observations indicate that it is easy to remove the ligand molecules from the (001) facets.

One of the most interesting features of our passivation model is the existence of the OH^- groups on the (111) facet. Water readily dissociates into OH^- and H^+ on transition-metal or oxide surfaces (*30*–*33*), and the binding of H_2O to $Pb(OA)_2$ in the solvent provides a natural kinetic pathway for this reaction (Fig. 2, A to D). The presence of small-sized anions is also required to establish charge neutrality over the entire quantum dot that could not be achieved by the sterically hindered OA^- molecules alone. The coexistence of sterically demanding ligands such as OA^-, and small anions to fill the gaps and fulfill the electron counting rule, could apply to other metal chalcogenide systems as well.

To probe the existence of OH^-, two NC samples were synthesized, one as described above (denoted PbS-OH) and another following the procedure developed by Moreels *et al.* (*17*) that uses Cl^- and no water during synthesis [denoted PbS-Cl (*15*)]. In the PbS-Cl sample, the Cl^- anion has effectively replaced OH^-. Both samples were spin-coated on freshly cleaved graphite, followed by thorough washing with acetone to remove unbound ligands, to form a submonolayer film. The XPS data, including those for the two control samples, graphite and $Pb(OH)_2$ powder, are shown in Fig. 4. Although the graphite is freshly cleaved in an Ar glove box (with an oxygen concentration of less than 1 part per million), it is slightly oxidized (*34*, *35*), showing an O 1s peak at 534.0 eV. Because of the incomplete surface coverage (*15*), this substrate peak is also present in the PbS-Cl and PbS-OH NC samples. After subtracting this peak, the PbS-Cl shows only one additional peak at 532.1 eV, probably from the oleate species. The PbS-OH sample contains three peaks at 534.0, 532.1, and 531.2 eV. The new peak at 531.2 eV is assigned to OH^-, in agreement with the $Pb(OH)_2$ powder single peak at 531.2 eV and with reported values for other metal-OH groups' XPS peaks (*36*, *37*). In the PbS-Cl sample, this feature is absent, whereas the Cl species produced a peak in the XPS (*15*). The 534.0-eV and 532.1-eV peaks have the same widths in different samples in Fig. 4. The SFG measurement also indicates the existence of OH^- in the sample (*15*). Although the present work applies to PbS-NCs, we expect the general applicability of this approach to other colloidal NCs.

REFERENCES AND NOTES

1. P. Alivisatos, *Science* **271**, 933–937 (1996).
2. B. Murray *et al.*, *IBM J. Res. Dev.* **45**, 47–56 (2001).
3. Y. Yin, A. P. Alivisatos, *Nature* **437**, 664–670 (2005).
4. J. S. Steckel, B. K. Yen, D. C. Oertel, M. G. Bawendi, *J. Am. Chem. Soc.* **128**, 13032–13033 (2006).
5. H. Liu, J. S. Owen, A. P. Alivisatos, *J. Am. Chem. Soc.* **129**, 305–312 (2007).
6. I. Moreels, B. Fritzinger, J. C. Martins, Z. Hens, *J. Am. Chem. Soc.* **130**, 15081–15086 (2008).
7. J. Li, L. W. Wang, *Nano Lett.* **3**, 1357–1363 (2003).
8. J. Schrier, L. W. Wang, *J. Phys. Chem. C* **112**, 11158–11161 (2008).
9. C. R. Bealing, W. J. Baumgardner, J. J. Choi, T. Hanrath, R. G. Hennig, *ACS Nano* **6**, 2118–2127 (2012).
10. P. L. McEuen, D. L. Klein, R. Roth, A. K. L. Lim, A. P. Alivisatos, *Nature* **389**, 699–701 (1997).
11. D. V. Talapin, J. S. Lee, M. V. Kovalenko, E. V. Shevchenko, *Chem. Rev.* **110**, 389–458 (2010).
12. A. H. Ip *et al.*, *Nat. Nanotechnol.* **7**, 577–582 (2012).
13. Y. W. Jun, J. H. Lee, J. S. Choi, J. Cheon, *J. Phys. Chem. B* **109**, 14795–14806 (2005).
14. S.-M. Lee, Y. W. Jun, S.-N. Cho, J. Cheon, *J. Am. Chem. Soc.* **124**, 11244–11245 (2002).
15. Materials and methods are available as supplementary materials on *Science* Online.
16. I. Moreels *et al.*, *Chem. Mater.* **19**, 6101–6106 (2007).
17. I. Moreels *et al.*, *ACS Nano* **5**, 2004–2012 (2011).
18. V. Petkov, I. Moreels, Z. Hens, Y. Ren, *Phys. Rev. B* **81**, 241304 (2010).
19. D. Britt, Y. Yoon, P. Ercius, T. D. Ewers, A. P. Alivisatos, *Chem. Mater.* **25**, 2544–2548 (2013).
20. A. J. Houtepen, R. Koole, D. Vanmaekelbergh, J. Meeldijk, S. G. Hickey, *J. Am. Chem. Soc.* **128**, 6792–6793 (2006).
21. Y. Gai, H. Peng, J. Li, *J. Phys. Chem. C* **113**, 21506–21511 (2009).
22. K. Shiraishi, *J. Phys. Soc. Jpn.* **59**, 3455–3458 (1990).
23. P. Srivastava, *Rep. Prog. Phys.* **60**, 561–613 (1997).
24. L. Manna, L. W. Wang, R. Cingolani, A. P. Alivisatos, *J. Phys. Chem. B* **109**, 6183–6192 (2005).
25. C. Fang, M. A. van Huis, D. Vanmaekelbergh, H. W. Zandbergen, *ACS Nano* **4**, 211–218 (2010).
26. K. Kimura, K. Nakajima, Y. Fujii, M. Mannami, *Surf. Sci.* **318**, 363–367 (1994).
27. G. Wulff, *Z. Krystallog.* **34**, 449 (1901).
28. E. Ringe, R. P. Van Duyne, L. D. Marks, *Nano Lett.* **11**, 3399–3403 (2011).
29. S. Polarz, *Adv. Funct. Mater.* **21**, 3214–3230 (2011).
30. P. J. Eng *et al.*, *Science* **288**, 1029–1033 (2000).
31. P. J. Feibelman, *Science* **295**, 99–102 (2002).
32. S. U. Khan, M. Al-Shahry, W. B. Ingler Jr., *Science* **297**, 2243–2245 (2002).
33. H. J. Shin *et al.*, *Nat. Mater.* **9**, 442–447 (2010).
34. W. T. Pong, C. Durkan, *J. Phys. D Appl. Phys.* **38**, R329–R355 (2005).
35. S. Wu, R. Yang, D. Shi, G. Zhang, *Nanoscale* **4**, 2005–2009 (2012).
36. X. Deng *et al.*, *Langmuir* **24**, 9474–9478 (2008).
37. K. Andersson, A. Nikitin, L. Pettersson, A. Nilsson, H. Ogasawara, *Phys. Rev. Lett.* **93**, 196101 (2004).

ACKNOWLEDGMENTS

We thank R. Cai and Z. Zhu for helpful discussions and J. Engel for help in the XPS experiments. This work was supported by the Director, Office of Science, the Office of Basic Energy Sciences, Materials Sciences and Engineering Division of the U.S. Department of Energy (DOE) through the organic/inorganic nanocomposite program under contract DE-AC02-05CH11231. It used resources of the National Energy Research Scientific Computing Center, the Molecular Foundry, and the Advanced Light Source, which are supported by the Office of Science of the DOE. Computations also used resources of the Oak Ridge Leadership Computing Facility at the Oak Ridge National Laboratory, which is supported by the Office of Science of the DOE under contract no. DE-AC05-00OR22725, with computational time allocated by the Innovative and Novel Computational Impact on Theory and Experiment project. M.S. thanks the Alexander von Humboldt-Foundation for a Feodor Lynen-Fellowship. Materials and methods, supporting information, and the coordinates of NC models are included in the supplementary materials.

SUPPLEMENTARY MATERIALS

www.sciencemag.org/content/344/6190/1380/suppl/DC1
Materials and Methods
Supplementary Text
Figs. S1 to S19
Tables S1 to S3
References (*38*–*82*)
Databases S1 and S2

27 February 2014; accepted 14 May 2014
Published online 29 May 2014;
10.1126/science.1252727

COMPUTATIONAL BIOLOGY

Controlling low rates of cell differentiation through noise and ultrahigh feedback

Robert Ahrends, Asuka Ota, Kyle M. Kovary, Takamasa Kudo, Byung Ouk Park, Mary N. Teruel*

Mammalian tissue size is maintained by slow replacement of de-differentiating and dying cells. For adipocytes, key regulators of glucose and lipid metabolism, the renewal rate is only 10% per year. We used computational modeling, quantitative mass spectrometry, and single-cell microscopy to show that cell-to-cell variability, or noise, in protein abundance acts within a network of more than six positive feedbacks to permit pre-adipocytes to differentiate at very low rates. This reconciles two fundamental opposing requirements: High cell-to-cell signal variability is needed to generate very low differentiation rates, whereas low signal variability is needed to prevent differentiated cells from de-differentiating. Higher eukaryotes can thus control low rates of near irreversible cell fate decisions through a balancing act between noise and ultrahigh feedback connectivity.

Understanding how large populations of cells direct small subsets to a different state is crucial for understanding the differentiation of precursor cells and stem cells, as well as cancer progression (*1*). Adipocyte differentiation is of fundamental importance for disease-associated conditions such as insulin resistance, obesity, and cancer and is also an accessible experimental system for investigating mammalian cell fate decisions. Adipocytes have a large pool of precursor cells that reside in the fat tissue—about one for every five differentiated cells (*2*)—which means that only about 1 cell out of 60 embarks on a differentiation path during the up to 12 days it takes to differentiate (*3*) (supplementary text). These pre-adipocytes differentiate through a bistable switch mechanism with a single threshold for activation in each cell that involves positive feedback between two key transcription factors, CCAAT/enhancer binding protein α (CEBPA) and peroxisome proliferator-activated receptor γ (PPARG) (Fig. 1A) (*4*). In a bistable system, if the precursor population were truly uniform, there would be a single critical threshold stimulus below which 100% of the cells remain precursor cells and above which 100% of the cells differentiate. Thus, it is a conundrum how a graded response is observed experimentally (Fig. 1B) (*5*), with weak stimuli inducing very low differentiation rates that increase as the stimuli intensity increases rather than causing all cells to convert at one critical stimulus threshold.

By extension of results from bacterial differentiation (*6*), it is plausible that the observed regulated mammalian differentiation rates are generated by noise, or cell-to-cell variability, in the abundance of key regulatory proteins (*7*–*10*).

Department of Chemical and Systems Biology, Stanford University, Stanford, CA 94305, USA.
***Corresponding author. E-mail: mteruel@stanford.edu**

Noise in the cell population makes it possible for only a small fraction of cells to differentiate at low receptor stimuli, R, but can also interfere with maintenance of the differentiated state by temporarily lowering the abundance of a key regulatory protein below a critical threshold. This dual effect of noise may explain why de-differentiation occurs in adipose (*11*), pancreatic beta (*12*), neuronal (*13*), epithelial (*14*), and cardiac cells (*15*). Thus, organisms have a fundamental optimization problem. They need noise to be able to regulate fractional rates of differentiation, but this same noise can also cause unwanted and stochastic de-differentiation.

We explored these competing requirements computationally. We used a working model that includes the established feedback between PPARG (X_0) and CEBPA (X_1) as a driver for adipogenesis (Fig. 1C) (*4*). Figure 1D shows a steady-state representation of this model in which the positive feedback loop generates bistability. If an activating receptor input R exceeds a critical threshold R_{on}, the cell switches to the differentiated state. If R were later to decrease below R_{off}, the differentiated cell would drop back into the undifferentiated state. Irreversible differentiation requires that there is a basal activity R_0 that remains higher than R_{off} when the stimulus is turned off.

The typically observed noise for mammalian protein abundance is 30% and stems from intrinsic noise in the synthesis and degradation of mRNA and proteins (*16*). Our simulations demonstrated that noise added to each of the two feedback components enabled receptor stimuli to control low fractional rates of differentiation:

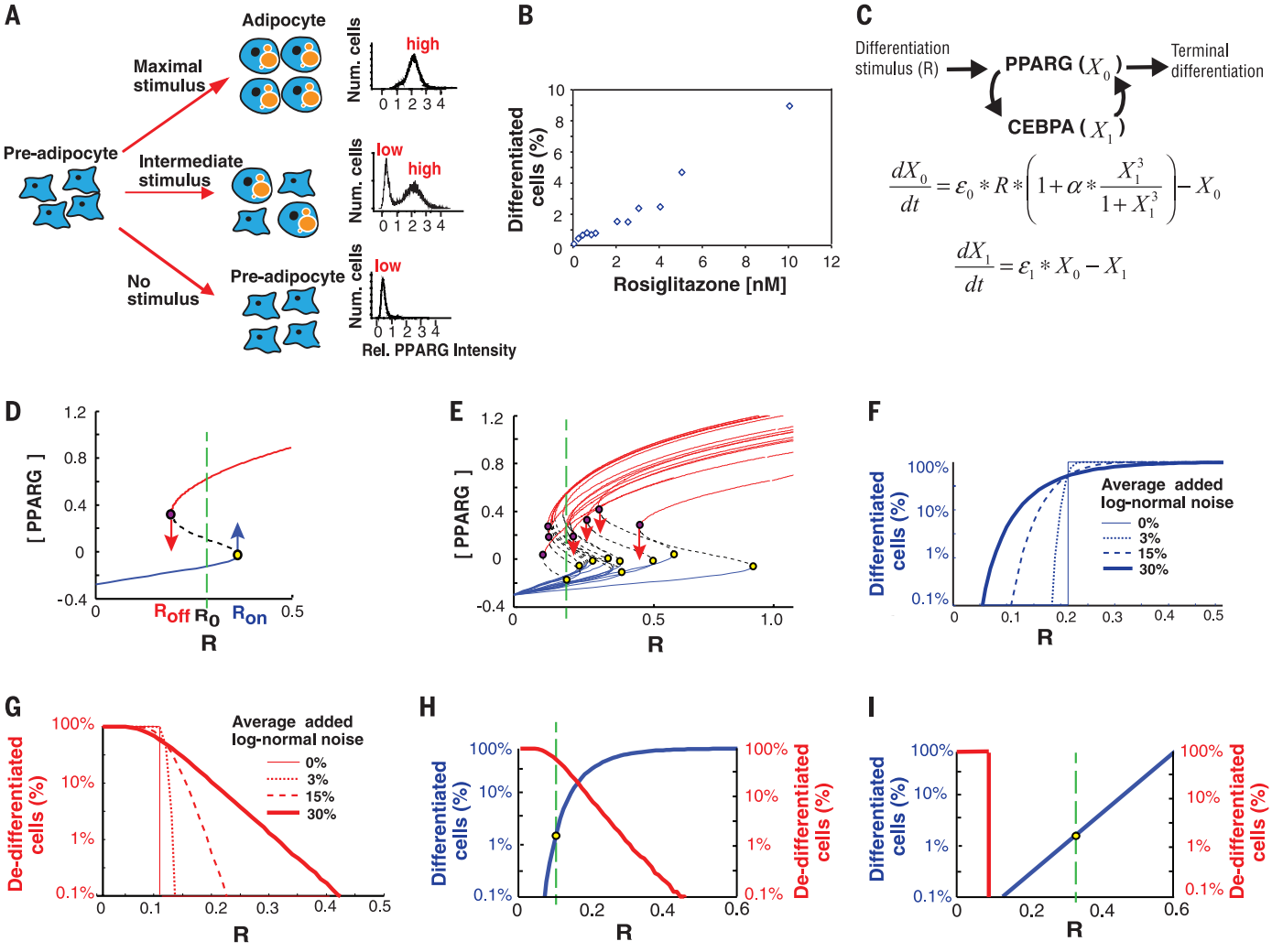

Fig. 1. Description of the control problem. (**A**) Schematic of the bistable switch from pre-adipocyte to adipocyte. Right, bimodality in single cell abundance of PPARG. (**B**) Control of very low rates of adipocyte differentiation by increasing the stimulus, R, applied to mouse OP9 preadipocyte cells. Here, R is rosiglitazone, a PPARG agonist, which directly induces adipogenesis in these cells (*7*). (**C**) Quantitative model of the protein network controlling the terminal differentiation decision in adipocytes. ε_0 and ε_1 represent noise in the abundance of X_0 and X_1, respectively. α is a feedback amplification term experimentally measured to be ~15 (*7*). (**D**) Steady-state plot of a one-feedback loop system with cooperativity, $n = 3$. As the receptor stimulus R is increased, R_{on} is the level of R at which the modeled cell triggers into the differentiated state (yellow dot). As R is decreased, R_{off} is the level of R at which the cell loses the differentiated state (purple dot). R_0 is the level of basal receptor activity. (**E**) Sample steady-state plots of the system in (D) but with 30% log-normal noise randomly added to each simulation. At the stimulus intensity marked by the green line, only one cell differentiated but several differentiated cells de-differentiated (red arrows). (**F** and **G**) The relationship between R and number of cells differentiating or de-differentiating becomes more graded as more noise is added. Each curve in these plots summarizes the R_{on} (F) or R_{off} (G) values obtained from 20,000 simulations. Noise was added randomly to each simulation to result in an average of no noise (thin solid line) up to 30% log-normal noise (thick solid line). (**H**) Plot showing the probabilities of triggering differentiation (blue) versus losing the differentiated state (red) as a function of the stimulus intensity R [20,000 simulations of the system described in (E)]. Such a system would be unable to maintain tissue size because, at the rate of preadipocyte differentiation observed in vivo (1.65%, as marked by dashed green line), ~80% of adipocytes would de-differentiate. (**I**) Plot showing ideal condition which allows for graded control of low rates of differentiation but with no de-differentiation.

For a specific receptor stimulus (marked with a green line in Fig. 1E), only 1 out of 15 cells switched to the differentiated state. Plots in which different amounts of noise were stochastically added to each simulation showed that the ability to regulate the rate of differentiation by increasing receptor stimuli markedly improved as the amount of noise increased (Fig. 1F). Nevertheless, this same noise also caused increasing fractions of cells in the population to lose the differentiated state over time, even for high-stimulus amplitudes (Fig. 1, E and G). The constraints that allow regulation of low rates of differentiation and also locking of cells in the differentiated state can be appreciated in a combined graph (Fig. 1H). To lose less than 0.33% of the differentiated cells and thereby maintain the 10% yearly rate of mature adipocyte turnover (*5*, *17*), the minimal basal receptor activity R_0 value must be higher than 0.4. At the same time, a much smaller R_0 of 0.1 is required to regulate the observed in vivo rate of pre-adipocyte differentiation of less than 2% every 12 days (Fig. 1H, left axis, and supplementary text). Thus, this system cannot be optimized because R_0 cannot be both more than 0.4 and less than 0.1, simultaneously. An ideal system must instead have differentiation and de-differentiation rates closer to the ones shown in the scheme in Fig. 1I. Although cell death may also contribute to maintaining constant cell numbers in tissues, recent studies indicate that de-differentiation might be an equally or more relevant process (*12*–*15*).

Regulatory systems with bistability typically have cooperativities of 2 to 4, although in a few cases higher cooperativities have been found (*18*). As shown in Fig. 2A, increasing the cooperativity from 3 to 6, and to 12, broadened the window between R_{off} and R_{on}. However, the higher cooperativity combined with the co-dependence between the feedback loop mediators, X_0 and X_1, resulted in a large increase in the total parameter noise of the system (Fig. 2B). Thus, increasing the cooperativity in a single loop system improves the system's performance but still does not allow optimization (Fig. 2B and fig. S1).

We explored whether increasing the number of feedback loops would help. Dual positive feedback, with one of the feedbacks being much slower, allows high-frequency signaling noise to be rejected (*19*). We noticed in our simulations that a system with two loops connected in an AND-gate configuration reduced the rate of de-differentiation by a mechanism that does not require different time constants of the loops. The improvement in system performance was still insufficient to allow optimization, so we tested whether a large number of feedbacks might be even better (model 2 in Fig. 2C). A system architecture with ultrahigh feedback connectivity—that is, more than six positive feedbacks, each having a cooperativity of only two—resulted in an optimized system that successfully balanced very low rates of cell differentiation with stability of the differentiated state (Fig. 2, D and E). There are two main reasons for this marked improvement in performance of this ultrahigh feedback loop system: First, by connecting different loops required for adipogenesis in an AND-gate configuration, the cooperativities of the feedback loops can be added together to give a high overall system cooperativity. Second, the noise in protein abundance in each feedback loop is independent and random from each other, leading to a reduction in overall system noise compared with a system with fewer feedback loops and the same overall cooperativity (Fig. 2, C and F, and supplementary text).

We wanted to test our prediction that adipocyte differentiation requires ultrahigh feedback connectivity. To identify feedback loops and evaluate their importance, one needs a method

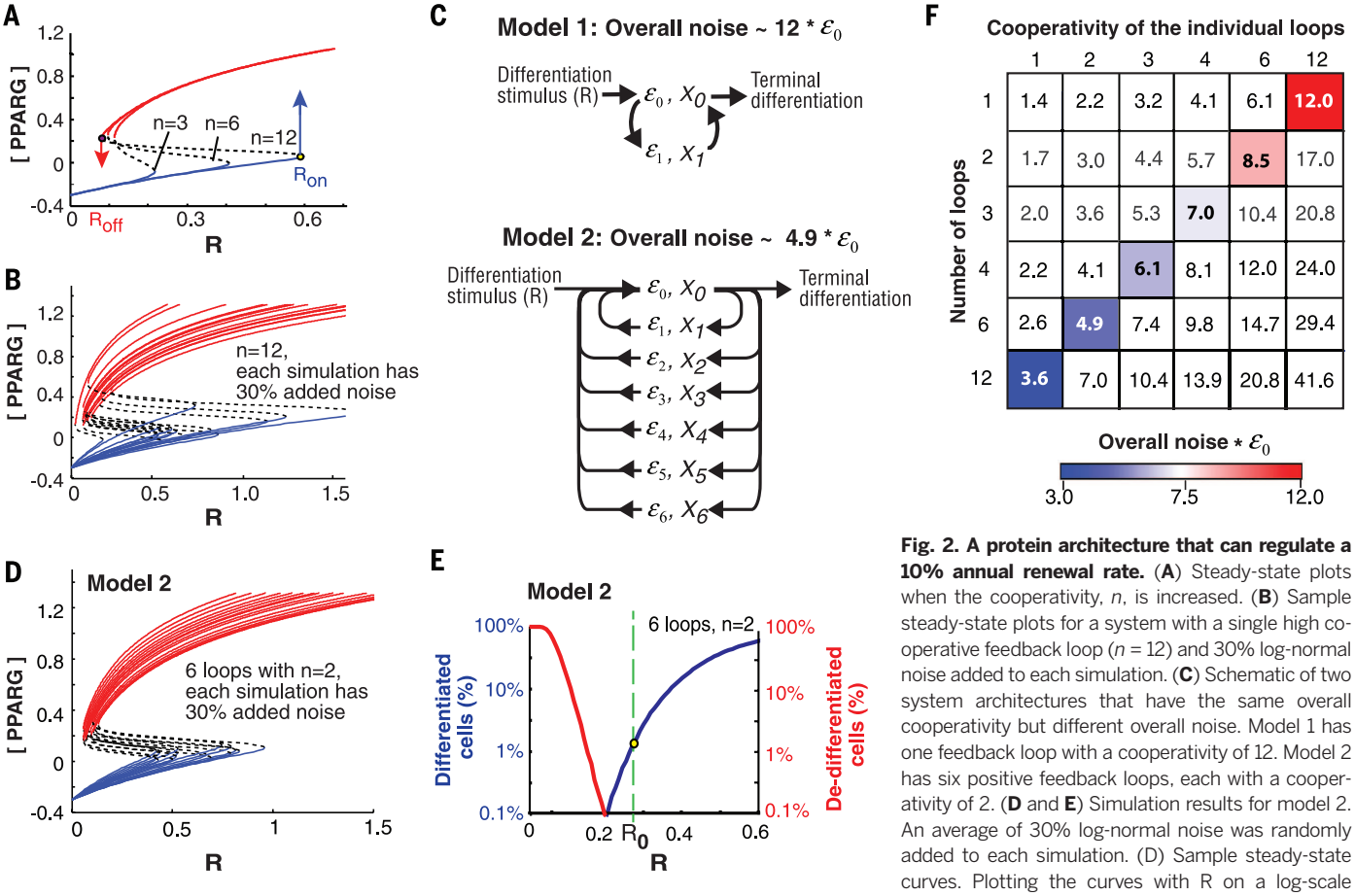

Fig. 2. A protein architecture that can regulate a 10% annual renewal rate. (**A**) Steady-state plots when the cooperativity, *n*, is increased. (**B**) Sample steady-state plots for a system with a single high cooperative feedback loop ($n = 12$) and 30% log-normal noise added to each simulation. (**C**) Schematic of two system architectures that have the same overall cooperativity but different overall noise. Model 1 has one feedback loop with a cooperativity of 12. Model 2 has six positive feedback loops, each with a cooperativity of 2. (**D** and **E**) Simulation results for model 2. An average of 30% log-normal noise was randomly added to each simulation. (D) Sample steady-state curves. Plotting the curves with R on a log-scale shows that the variability in R_{on} and R_{off} is similar (fig. S1C). (E) Results of 20,000 simulations showing that such a system can maintain tissue size. At the low differentiation rate needed to renew adipose tissue (1.65%, yellow dot), less than 0.1% of differentiated cells would lose the differentiated state. (**F**) The matrix shows the overall system noise as a function of number of feedback loops versus cooperativity of the individual loops. The colored boxes mark systems with the same total cooperativity ($n = 12$), but with decreasing system noise as the number of feedback loops increases.

to perturb a protein in the network and then measure the effect of that perturbation over time on many other proteins, that is, the candidate feedback loop partners. We used mouse OP9 cells, a bone marrow–derived adipocyte model, as a cell model that shares key regulatory processes with adipogenesis in vivo (*7*, *20*–*23*). We selected 60 nuclear proteins—including PPARG, CEBPB, CEBPA, and other proteins implicated as important in adipogenesis from the literature or from our small interfering RNA (siRNA) knockdown screening data (table S1)—as our candidate network to identify the prevalence of feedback loops coupled to PPARG and used selected reaction monitoring mass spectrometry (SRM-MS) to quantitatively measure the abundance of these proteins (figs. S2 to S8) (*24*, *25*).

For a protein to be classified as being in a feedback loop with PPARG, it had to meet four criteria. First, because the abundance of PPARG changes dramatically during adipogenesis, we assumed that the abundance of a protein in a feedback loop with PPARG also had to change over the time course of adipogenesis (figs. S9 and S10). Second, to confirm a link from PPARG to the candidate feedback loop protein, changing PPARG abundance with siRNA or small molecules needed to result in a corresponding change in the abundance of the candidate feedback loop protein (Fig. 3A and figs. S11 and S12). Third, to confirm a link from the candidate protein back to PPARG, changing the abundance of the candidate protein by siRNA-mediated depletion needed to result in a corresponding change in the abundance of PPARG (Fig. 3B and fig. S13). As a fourth criterion, titration of the PPARG activator rosiglitazone onto undifferentiated cells at basal conditions had to result in a direct change of expression of the candidate protein (Fig. 4A and fig. S14). Out of 60 candidate proteins (table S1), we identified seven positive feedback mediators of PPARG that satisfied these four criteria: three previously unknown positive feedback mediators (the CCAAT-box DNA binding protein CEBPZ, the fatty-acid binding protein FABP4, and the phosphatidic acid phosphohydrolase enzyme LPIN1), two new mediators of double negative feedback loops that function analogously to positive feedback loops (the actin-binding protein FLNA and transcription factor RUNX2), and validated two known positive feedback mediators (the transcription factors CEBPB and CEBPA) (*7*) (Fig. 4B).

Supporting the assumption that different feedback loops regulate PPARG expression independently, the identified feedback mediators interacted with PPARG in very different ways. For example, the promoter of CEBPZ has several predicted CEBPA binding elements (*26*), suggesting that the observed up-regulation of CEBPZ expression by PPARG activation is likely through PPARG-mediated increase in accumulation of CEBPA. FABP4 likely activates PPARG by transporting PPARG-activating ligands into the nucleus (*27*). LPIN1 activates PPARG by releasing a corepressor of PPARG (*28*).

To understand whether the newly identified feedback loops contribute to differentiation, we used siRNA to deplete the feedback loop proteins in undifferentiated OP9 cells; induced differentiation by adding the PPARG activator rosiglitazone for 24 hours (*7*, *29*); and then fixed, imaged, and analyzed the cells (Fig. 4C, left column). To understand the feedback loop contributions to preventing de-differentiation, we terminally differentiated OP9 preadipocytes into adipocytes by adding rosiglitazone for 48 hours and then used siRNA to deplete the feedback loop proteins in these cells (Fig. 4C, right column). The effect of the feedback loops on differentiation and de-differentiation was not necessarily symmetrical. For example, depletion of CEBPB or LPIN1 had a greater effect on differentiation than on de-differentiation, suggesting that these loops promote differentiation and are less important for keeping cells in the terminally differentiated state.

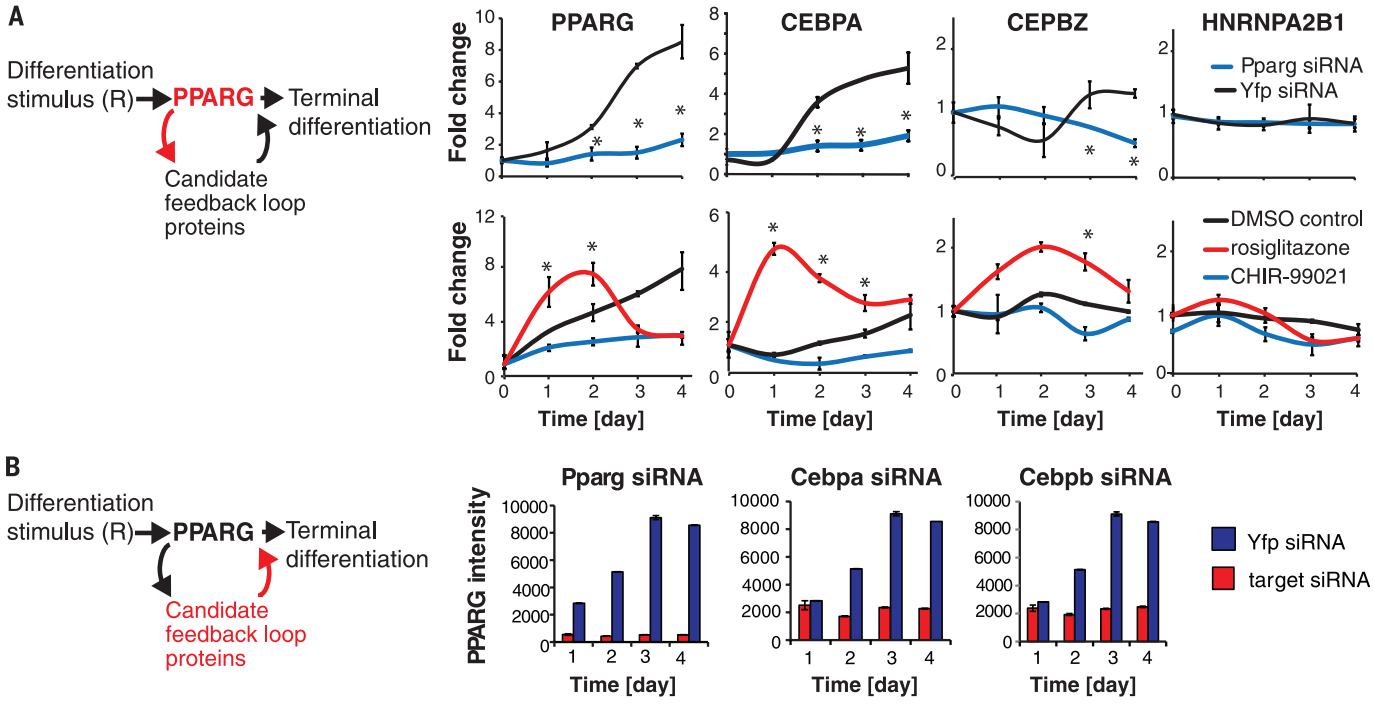

Fig. 3. A method to systematically uncover feedback loops in a protein network. (**A**) SRM-MS was used to measure changes in nuclear protein concentrations over the timecourse of adipogenesis in response to siRNA or chemical perturbations to PPARG (see also figs. S10 to S12). OP9 preadipocytes were induced to differentiate into mature adipocytes in 4 days by addition of the adipogenic cocktail (dexamethasone, isobutylmethylxanthine, and insulin). (Top) Cells were transfected with siRNA targeting PPARG (blue) or yellow fluorescent protein (YFP) as a control (black) 24 hours before addition of the adipogenic factors. (Bottom) A PPARG agonist (rosiglitazone) or PPARG inhibitor (CHIR-99021) was added together with the adipogenic mix. All values were normalized to the control value at day 0. Each data point is the average of three biological replicates (error bars show standard deviation). A protein was classified as regulated by PPARG activity if its abundance in the perturbed versus control (YFP) samples varied significantly at one or more time points, $P < 0.05$ (*) calculated using the student's t test, two-tailed, two-sample equal variance. (**B**) siRNA-mediated depletion of the candidate feedback loop partners was used to determine which ones regulate PPARG. The knockdown effect in OP9 cells was measured by immunocytochemistry staining for PPARG. Each bar in the plots represents ~10,000 cells. Error bars show standard error. See also fig. S13.

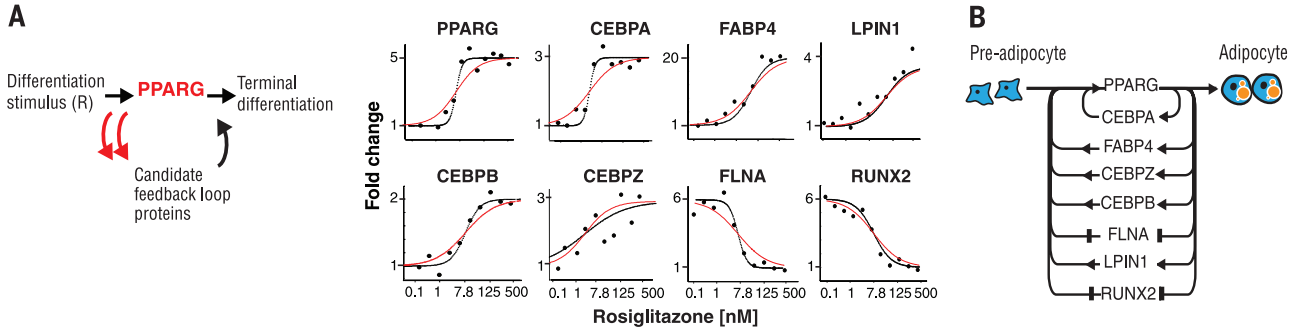

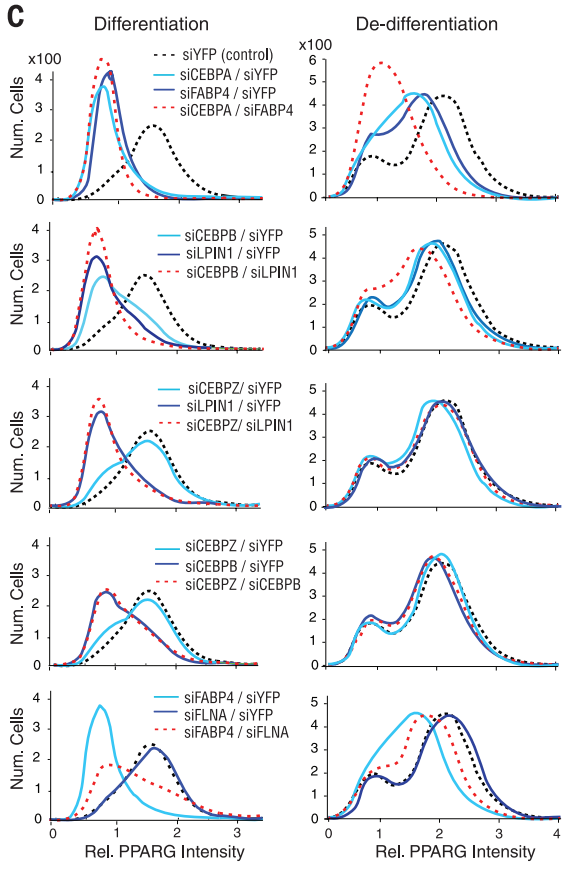

Fig. 4. Differentiation from pre-adipocyte to adipocyte is regulated by a single module consisting of multiple positive-feedback loops connecting back to PPARG. (**A**) Test for feedback connectivity by directly activating PPARG. The PPARG agonist rosiglitazone was titrated into the medium of undifferentiated OP9 cells, and the protein abundance of the candidate feedback loop mediators was measured by SRM-MS 48 hours later, a time point at which PPARG is maximally expressed (*7*). Curves show the best fits to the data using an optimized Hill coefficient (black) versus a Hill coefficient of 1 (red). (**B**) Schematic of the seven identified feedback loops. (**C**) Contributions of the identified feedback loops to switching pre-adipocytes (low PPARG peak) to adipocytes (high PPARG peak) and to preventing de-differentiation. To measure contributions to differentiation, we transfected OP9 cells with siRNA 24 hours before the start of the experiment to remove the specified feedback loop components. The cells were then stimulated with 1 μM rosiglitazone for 24 hours and fixed (left column). To measure contributions to de-differentiation, OP9 cells were first differentiated into adipocytes by adding 1 μM rosiglitazone to the culture media for 48 hours, then transfected with the specified siRNA and fixed 24 hours later (right column). PPARG abundance was quantified by immunocytochemistry staining with anti-PPARG and then imaged.

At least four of the identified feedback loop proteins—CEBPA, FABP4, CEBPB, and LPIN1—are required for adipogenesis and are thus connected as AND-gates. siRNA-mediated depletion of each of these proteins during adipogenesis resulted in a nearly complete lack of adipogenesis in most cells (enrichment of cells in the low PPARG abundance peak as shown by the solid lines in the top two plots in the left column of Fig. 4C). Nevertheless, the specific regulatory mechanisms by which each of the identified feedback loops acts is likely not the same and may include a mixture of additive (OR-gate) and multiplicative (AND-gate) features. In addition, the differential effects of the feedback loops on adipogenesis indicate that the cooperativity is likely different for the different loops and that our model in which all loops have equal cooperativity is a simplification.

This ultrahigh feedback system with multiple AND-gate feedback loops creates the ultrasensitivity needed to create a robust bistable switch that can be triggered at variable activation thresholds within the cell population and at the same time limits the noise within a range that permits both low rates of differentiation and locking of cells into the differentiated state. Furthermore, a system with a large number of feedback loops with various regulatory proteins can integrate information from a broad range of signaling, metabolic, and stress inputs to regulate and better control the fraction of differentiating cells. The advantages of such a system design suggest that the combination of noise with ultrahigh feedback is a ubiquitous regulatory feature that applies to other cell fate decisions in multicellular organisms. Our integrated approach combining SRM-MS, chemical and genetic perturbations, and single-cell microscopy may be useful to identify and understand such feedback loop circuits in other cell fate decisions.

REFERENCES AND NOTES

1. J. Zuber *et al.*, *Nature* **478**, 524–528 (2011).
2. Y. D. Tchoukalova, M. G. Sarr, M. D. Jensen, *Am. J. Physiol.* **287**, R1132 (2004).
3. A. Chawla, E. J. Schwarz, D. D. Dimaculangan, M. A. Lazar, *Endocrinology* **135**, 798–800 (1994).
4. E. D. Rosen *et al.*, *Genes Dev.* **16**, 22–26 (2002).
5. K. L. Spalding *et al.*, *Nature* **453**, 783–787 (2008).
6. G. M. Süel, R. P. Kulkarni, J. Dworkin, J. Garcia-Ojalvo, M. B. Elowitz, *Science* **315**, 1716–1719 (2007).
7. B. O. Park, R. Ahrends, M. N. Teruel, *Cell Reports* **2**, 976–990 (2012).
8. H. H. Chang, M. Hemberg, M. Barahona, D. E. Ingber, S. Huang, *Nature* **453**, 544–547 (2008).
9. J. Hanna *et al.*, *Nature* **462**, 595–601 (2009).
10. S. Palani, C. A. Sarkar, *Cell Reports* **1**, 215–224 (2012).
11. A. Poloni *et al.*, *Stem Cells* **30**, 965–974 (2012).
12. C. Talchai, S. Xuan, H. V. Lin, L. Sussel, D. Accili, *Cell* **150**, 1223–1234 (2012).
13. T. Reiff *et al.*, *J. Neurosci.* **30**, 905–915 (2010).
14. P. R. Tata *et al.*, *Nature* **503**, 218–223 (2013).
15. S. E. Senyo *et al.*, *Nature* **493**, 433–436 (2013).
16. M. Niepel, S. L. Spencer, P. K. Sorger, *Curr. Opin. Chem. Biol.* **13**, 556–561 (2009).

17. Q. A. Wang, C. Tao, R. K. Gupta, P. E. Scherer, *Nat. Med.* **19**, 1338–1344 (2013).
18. N. B. Trunnell, A. C. Poon, S. Y. Kim, J. E. Ferrell Jr., *Mol. Cell* **41**, 263–274 (2011).
19. O. Brandman, J. E. Ferrell Jr., R. Li, T. Meyer, *Science* **310**, 496–498 (2005).
20. E. D. Rosen, O. A. MacDougald, *Nat. Rev. Mol. Cell Biol.* **7**, 885–896 (2006).
21. R. Berry, E. Jeffery, M. S. Rodeheffer, *Cell Metab.* **19**, 8–20 (2014).
22. D. C. Berry, D. Stenesen, D. Zeve, J. M. Graff, *Development* **140**, 3939–3949 (2013).
23. N. E. Wolins *et al.*, *J. Lipid Res.* **47**, 450–460 (2006).
24. E. Abell, R. Ahrends, S. Bandara, B. O. Park, M. N. Teruel, *Proc. Natl. Acad. Sci. U.S.A.* **108**, 14485–14490 (2011).
25. P. Picotti, B. Bodenmiller, L. N. Mueller, B. Domon, R. Aebersold, *Cell* **138**, 795–806 (2009).
26. M. I. Lefterova *et al.*, *Genes Dev.* **22**, 2941–2952 (2008).
27. S. D. Ayers, K. L. Nedrow, R. E. Gillilan, N. Noy, *Biochemistry* **46**, 6744–6752 (2007).
28. H. E. Kim *et al.*, *Biochem. J.* **453**, 49–60 (2013).
29. P. Tontonoz, B. M. Spiegelman, *Annu. Rev. Biochem.* **77**, 289–312 (2008).

ACKNOWLEDGMENTS

We thank T. Meyer, S. Collins, G. Anderson, S. Spencer, together with members of the Teruel lab, for thoughtful comments and discussions. This work is supported by Stanford University New Faculty Startup Funds and NIH P50GM107615 (M.N.T.), Deutsche Forschungsgemeinschaft Fellowship AH 220/1-1 (R.A.), and American Heart Association Fellowship 13POST17090092 (A.O.).

SUPPLEMENTARY MATERIALS

www.sciencemag.org/content/344/6190/1384/suppl/DC1
Materials and Methods
Supplementary Text
Figs. S1 to S14
Tables S1 to S3
References (*30*, *31*)

11 February 2014; accepted 30 May 2014
10.1126/science.1252079

AGING CELL BIOLOGY

Life-span extension by a metacaspase in the yeast *Saccharomyces cerevisiae*

Sandra Malmgren Hill, Xinxin Hao, Beidong Liu,* Thomas Nyström*

Single-cell species harbor ancestral structural homologs of caspase proteases, although the evolutionary benefit of such apoptosis-related proteins in unicellular organisms is unclear. Here, we found that the yeast metacaspase Mca1 is recruited to the insoluble protein deposit (IPOD) and juxtanuclear quality-control compartment (JUNQ) during aging and proteostatic stress. Elevating *MCA1* expression counteracted accumulation of unfolded proteins and aggregates and extended life span in a heat shock protein Hsp104 disaggregase– and proteasome-dependent manner. Consistent with a role in protein quality control, genetic interaction analysis revealed that *MCA1* buffers against deficiencies in the Hsp40 chaperone *YDJ1* in a caspase cysteine–dependent manner. Life-span extension and aggregate management by Mca1 was only partly dependent on its conserved catalytic cysteine, which suggests that Mca1 harbors both caspase-dependent and independent functions related to life-span control.

The cysteine-dependent aspartate-directed proteases, or caspases, are a family of proteases required for apoptosis [programmed cell death (PCD)] (*1*–*3*). PCD is vital for proper development, tumor suppression, immunity, and neuron homeostasis (*4*). The yeast *Saccharomyces cerevisiae* expresses a single, type I metacaspase [ancestral structural caspase homolog (*5*)] called Mca1 (Yca1) (*6*). After particular stresses, *S. cerevisiae* display numerous markers of PCD, dependent on the presence of Mca1 (*6*–*8*). Although these results imply that Mca1 is a PCD executioner protein, other reports suggest that Mca1 has beneficial functions independent of PCD, for example, in protein quality control (PQC) (*9*–*13*). PQC ensures that individual proteins are accurately produced, folded, compartmentalized, degraded, and prevented from aggregating (*14*). When, for example, during severe stress and aging, PQC fails to fully prevent protein aggregation, a second line of defense, spatial PQC, ensures that aggregates are not equally inherited during cytokinesis, a phenomenon that resets age in one cell lineage (*15*–*19*). In the budding yeast *S. cerevisiae*, this mother cell–biased segregation of aggregated proteins requires the heat shock protein Hsp104 (*20*, *21*).

By crossing *HSP104* fused to green fluorescent protein, *HSP104-GFP* (*22*, *23*), into a synthetic genetic miniarray of yeast mutants lacking chaperones or cochaperones and Hsp104 interactors (*16*, *22*, *24*), we showed that Mca1 is required for keeping yeast daughter cells free of aggregated proteins generated during a transient heat shock (fig. S1A). Constitutively elevating Mca1 levels (fig. S1B) by exchanging the weak *MCA1* promoter with the strong promoter (P_{GPD}) of the *GPD* gene boosted aggregate asymmetry during cytokinesis (fig. S1A). Asymmetric aggregate distribution can be achieved by limiting inheritance (retention in mother cells) or by aggregate removal (disaggregation and/or retrograde transport) in daughter cells (*16*, *24*). These two processes were experimentally distinguished using fluorescent concanavalin A (Con A) staining of the cell wall (Fig. 1, A and B), which revealed that most genes required for establishing asymmetry (fig. S1A) were important for both aggregate removal and asymmetrical inheritance (Fig. 1C). However, deletions of *MCA1* and *SSA3* only affected aggregate removal (Fig. 1C). Consistently, Mca1 overproduction enhanced aggregate removal while leaving the process of inheritance unaffected (Fig. 1D).

Using genome-wide synthetic genetic array (SGA) analysis (*23*, *25*), we next identified genes that interacted negatively with *MCA1*, which demonstrated that Mca1 buffers against deficiencies in a few discrete functions (Fig. 2A and fig. S2A), including PQC, through negative interactions with *CDC48* and *RPT1* of the proteasome system. Among the nonessential genes, only one significant interaction was found: a strong negative interaction with *YDJ1*, which encodes the major cytosolic Hsp40 chaperone (Fig. 2, A to C). In addition, removing *MCA1* in the *ydj1*Δ mutant exacerbated cell shape abnormalities (large, elongated buds) (Fig. 2D) and aggregate morphology (multiple amorphous aggregate structures rather than inclusion bodies) (Fig. 2E and fig. S2, B and C). Like metazoan caspases, Mca1 contains a conserved active-site cysteine [cysteine C276, previously designated C297 (*6*, *26*)], and exchanging this single cysteine to alanine was sufficient to cause a negative genetic interaction with *ydj1*Δ (Fig. 2F).

In line with the suggested association of Mca1 with aggregates (*11*), Mca1 relocalized to Hsp104-associated cytosolic puncta during both heat stress (fig. S3A) and aging (Fig. 3A). We used the temperature-sensitive variant of the SUMO-conjugating enzyme, $Ubc9^{ts}$-RFP, with red fluorescent protein (RFP), as a marker for juxtanuclear quality-control compartment (JUNQ) and the Hsp104-enriched insoluble protein deposit (IPOD) inclusions (*17*, *27*). We found that Mca1 associated with aggregates within both these compartments (Fig. 3B) and that the JUNQ association (fig. S3B) was often close to the nucleolus (Fig. 3C) (*28*). During stress and aging, Mca1 relocated to inclusions independently of Ydj1, Hsp104, and Ssa1 and 2 (Fig. 3D and fig. S3C). Further, cells without Mca1, like cells lacking Ydj1, displayed increased numbers of inclusion in aged cells (Fig. 3, E and F), and age-related accumulation of inclusions was counteracted in both wild-type and *ydj1*Δ cells by overproducing Mca1, albeit to a higher degree in wild-type cells (Fig. 3F). The IPOD-specific reporter Rnq1 (*27*) revealed that most aggregates in old cells were IPODs and that Mca1 overproduction caused a 30% reduction in the accumulation of these inclusions (fig. S3, D and E). To test by which route Mca1 may prevent the buildup of such protein inclusions, we determined the effect of Mca1 dosage on luciferase folding (*29*) and the levels of the signal sequence–deficient, unfolded carboxypeptidase Y,

Department of Chemistry and Molecular Biology (CMB), University of Gothenburg, Medicinaregatan 9C, S-413 90 Göteborg, Sweden.
***Corresponding author. E-mail: thomas.nystrom@cmb.gu.se (T.N.); beidong.liu@cmb.gu.se (B.L.)**

Fig. 1. Mca1 dosage affects the establishment of aggregate asymmetry during cytokinesis. The aggregate reporter Hsp104-GFP was used to test if the genes identified as being required for establishing aggregate asymmetry (fig. S1A) during cytokinesis were doing so by preventing aggregate inheritance or by boosting aggregate removal in daughter cells. This analysis established that Mca1 is limiting for aggregate removal in yeast daughter cells. (**A**) Schematic overview of the Con A staining protocol to discriminate between aggregate inheritance and/or retention (unstained buds, produced after heat shock) and removal (stained buds, present during heat shock). (**B**) Experimental examples depicting aggregate removal (left) and retention (right). Top rows show successful events (+), bottom rows exemplify failed processes (−), generating daughter cells containing aggregate(s). Scale bar, 5 μm. (**C**) Defects in aggregate removal and/or retention in asymmetry mutants identified in fig. S1A. Data are plotted as the mutants' deviation from the wild type (WT) in aggregate inheritance (white bars; 100% increase means a twofold increase in mutant daughter cell inheritance compared with WT daughters) and removal (black bars; –100% means a twofold decrease in mutant daughter cell removal of aggregates compared with WT daughters). Data are means ± SD. $N = 3$ for *ssa1*Δ, *ssa2*Δ, *ssa3*Δ, *ssb1*Δ, *hsp82*Δ; $N = 4$ for *ydj1*Δ; $N = 5$ for *mca1*Δ. (**D**) Aggregate removal and inheritance in the Mca1-overproducing strain (P_{GPD}-*MCA1*). Data are means ± SD. $N = 3$. $^{*}P < 0.05$; $^{**}P < 0.005$; $^{***}P < 0.0005$.

CPY*, fused to Leu2 (hereafter called ΔssCL*) (*30*, *31*). We found that neither Mca1 overproduction nor an *mca1*Δ deletion affected folding activity (fig. S3F). In contrast, Mca1 overproduction reduced, whereas *mca1*Δ increased, the levels of the unfolded proteasome substrate ΔssCL* (Fig. 3, G and H), which suggested that Mca1 is required for efficient removal of terminally unfolded proteins.

In view of these data, we tested whether *MCA1* was acting as a pro- (executioner) or anti- (gerontogene) aging gene. The lack of Mca1 had little effect on the replicative life span in otherwise wild-type cells but accelerated aging of cells lacking Ydj1 (Fig. 4A), which confirmed that Mca1 becomes indispensable in the absence of Ydj1. Overproducing Mca1 extended life span (46 to 56%) in a manner partly dependent on Ydj1 (Fig. 4, B and C). That life-span extension by Mca1 overproduction was less efficient in cells lacking Ydj1 is consistent with a more pronounced reduction of aggregates in the former (Fig. 3F) and suggests that proper protein homeostasis is required to achieve full effects of elevated Mca1 levels. Indeed, overproduction of Mca1 did not result in a statistically significant extension of life span in the absence of Hsp104 (Fig. 4D) or a reduction in proteasome levels by deleting the proteasome regulator Rpn4 (*32*) (Fig. 4E). Thus, the removal of unfolded and aggregated proteins is a key feature of Mca1's role in life-span control.

The conserved catalytic cysteine-histidine dyad of Mca1 is, like metazoan caspases, activated under certain conditions including H_2O_2 exposure, to autocatalytically remove a small ~12-kD subunit on the Mca1 protein (*6*, *33*). We found that this 12-kD subunit accumulated in aged cells carrying the P_{GPD}-*MCA1* fusion, similar to cells exposed to H_2O_2 (Fig. 4F), which indicated that typical metacaspase processing is triggered upon mother cell aging. The $Mca1_{C276A}$ protein was, when overproduced, incapable of removing the 12-kD subunit during aging (Fig. 4F) and partially defective in counteracting aggregate accumulation (Fig. 4G) and extending life span (Fig. 4H). Overproduction of $Mca1_{C276A}$ in cells lacking Ydj1 reduced rather than extended life span (Fig. 4I), consistent with the requirement for the active-site cysteine in Ydj1-deficient cells (Fig. 2F). Thus, both cysteine-dependent and independent functions of Mca1 are required for life-span control of which the cysteine-independent one can only be realized in cells harboring functional Ydj1.

Here, we have shown that Mca1 has a beneficial cell-autonomous function in PQC that can compensate for the lack of the major Hsp40 chaperone of the yeast cytosol and facilitate the removal of an unfolded protein, counteract accumulation of protein aggregates, and prolong cellular life span in an Hsp104 disaggregase- and proteasome-dependent manner. The fact that the Hsp104 disaggregase is required for Mca1 to extend life span

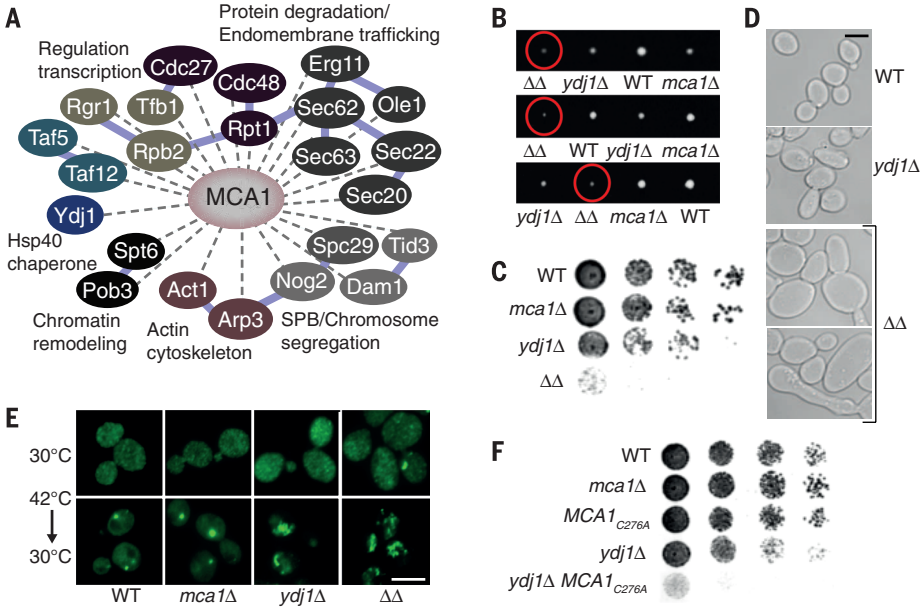

Fig. 2. *MCA1* displays negative genetic interactions with *YDJ1* and genes involved in PQC. To identify a possible function of Mca1 in PQC, the genetic interaction network of *MCA1* was determined for both essential and nonessential genes, which demonstrated that Mca1 is buffering against deficiencies in the major Hsp40 chaperone, Ydj1, and components of the proteasome. (**A**) Negative genetic interactions of *MCA1*, clustered in functional groups, connected by known physical interactions (purple lines). (**B**) Growth of spores after reconstructing *ydj1*Δ *mca1*Δ (ΔΔ, red circle) double mutants by genetic crossing. (**C**) Growth defect of a reconstructed *ydj1*Δ *mca1*Δ (ΔΔ) double mutant. (**D**) Cell morphologies of the WT, *ydj1*Δ, and *ydj1*Δ *mca1*Δ (ΔΔ) strains. (**E**) Aggregate morphology after heat treatment in WT, *ydj1*Δ, *mca1*Δ, and *ydj1*Δ *mca1*Δ (ΔΔ), visualized by Hsp104-GFP. Scale bar, 5 μm. (**F**) Growth defect of a *ydj1*Δ $MCA1_{C276A}$ double mutant. $N > 2$ for all tests in (B) to (F).

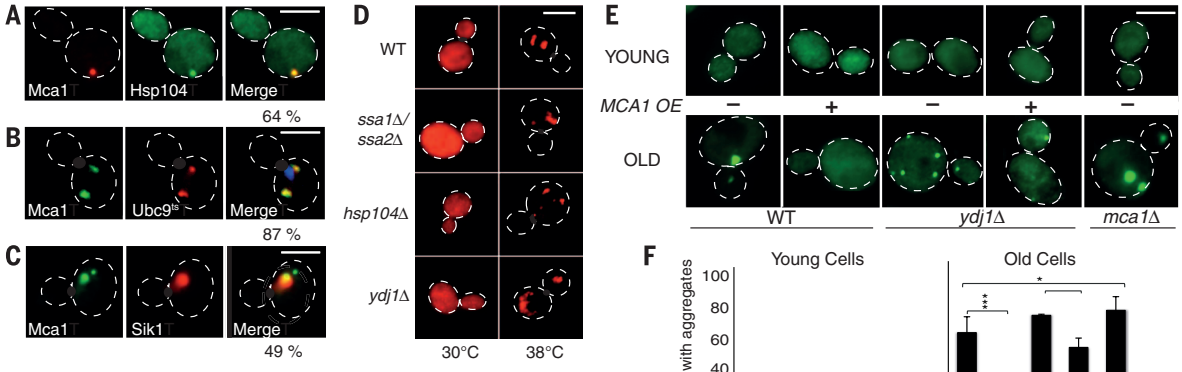

Fig. 3. Mca1 localizes to IPOD and JUNQ quality-control compartments and prevents accumulation of unfolded proteins and aggregates formed upon aging. (**A**) Colocalization of Mca1 and Hsp104 at aggregates in replicatively aged cells (12 generations). The fraction (%) of cells displaying colocalization is indicated near the micrograph; 400 cells were analyzed. $N > 2$. (**B**) Colocalization of Mca1 and Ubc9^{ts} at peripheral (IPOD) and juxtanuclear (JUNQ) compartments [4′,6′-diamidino-2-phenylindole (DAPI)–stained nucleus in blue]. The fraction (%) of Mca1 foci colocalizing with Ubc9^{ts} is indicated near the micrograph; 188 cells were analyzed. $N > 2$. (**C**) Mca1 localization to aggregates at peripheral sites and the nucleolus, visualized by Sik1-RFP. The fraction (%) of Mca1 foci colocalizing with Sik1 is indicated near the micrograph; 245 cells were analyzed. $N > 2$. (**D**) Mca1 association with aggregates in the absence of *SSA1*, *SSA2*, *HSP104*, and *YDJ1* as indicated. $N > 2$. (**E**) Visualization of Hsp104-GFP aggregates in young and replicatively aged cells as indicated with (+) and without (−) overexpression of *MCA1* (*MCA1 OE*). Scale bars, 5 μm. (**F**) Percentage of cells from (E) containing aggregates in young (0 generations) and aged cells (13 generations for WT and *mca1*Δ, 9 generations in *ydj1*Δ strains). $N = 6$ for *mca1*Δ and WT *MCA1 OE*, $N = 3$ for *ydj1*Δ and *ydj1*Δ *MCA1 OE*. Data are means ± SD. $^{*}P < 0.05$; $^{***}P < 0.0005$. (**G**) The ΔssCL* protein that misfolds in the cytoplasm and is degraded by the proteasome (*30*, *31*) was used to test if Mca1 is involved in facilitating removal of misfolded proteins. Cells expressing ΔssCL* (ΔssCPY* fused to Leu2) were spotted on indicated media and incubated for 3 days at 30°C. Enhanced growth on plates lacking leucine indicates stabilization of ΔssCL* (*30*, *31*), whereas reduced growth indicates increased degradation. $N = 3$. (**H**) Immunoblotting showing relative ΔssCL* levels of the indicated strains. Data are means ± SD. $N = 3$.

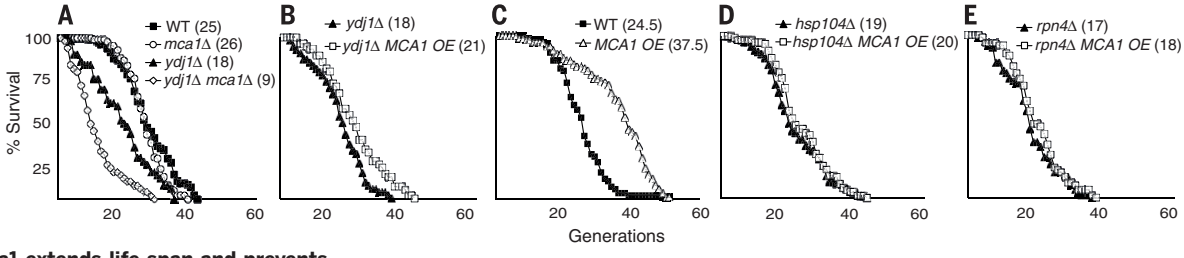

Fig. 4. Mca1 extends life span and prevents aggregate accumulation in a partially caspase cysteine–independent manner. To test if Mca1 acts as an executioner gene or gerontogene during the life history of yeast mother cells, the replicative life span of Mca1-deficient and Mca1-overproducing cells was determined. This analysis demonstrated that Mca1 acted as a life-span–extending gene and that life-span extension required both Hsp104-dependent disaggregase activity and fully functional proteasomes linking Mca1-dependent life-span control to the removal of damaged and aggregated proteins. (**A**) Replicative life span of WT, *ydj1*Δ, *mca1*Δ, and *ydj1*Δ *mca1*Δ. Life span of *ydj1*Δ is shorter than that of WT (P = 5.0E-4; 50 cells) and is further shortened when also deleting *MCA1* (P = 5.1E-5; 50 cells). No difference was seen between *mca1*Δ and WT (P = 0.99; 80 cells). (**B** and **C**) Life-span extension by Mca1 overproduction in cells lacking *YDJ1* (B) (P = 3.00E-2; 80 cells), and in WT cells (C) (P = 0.037; 80 cells). (**D** and **E**) Life span of the Mca1-overproducing strain lacking the disaggregase Hsp104 (P = 0.014; 80 cells) (D) and the proteasome regulator Rpn4 (E) (P = 0.16; 64 cells). (**F**) Mca1 proteolytic processing during aging and H_2O_2 exposure in cells overproducing Mca1 or the caspase-inactive Mca1$_{C276A}$. Red arrow indicates the 12-kD product typically cleaved off upon caspase activation. (**G**) Age-induced aggregation in cells overproducing caspase-inactive Mca1$_{C276A}$. Data are means ± SD. $N = 3$. $^{**}P < 0.005$. (**H** and **I**) Effect of overproducing the caspase-inactive Mca1$_{C276A}$ on the life span of WT (H) (P = 3.5E-5; 64 cells) and *ydj1*Δ (I) (P = 0.0082; 64 cells) cells.

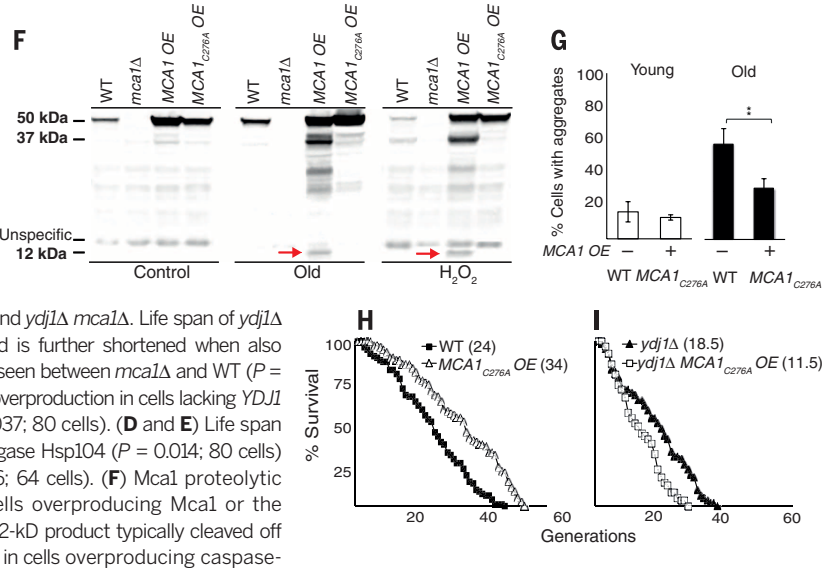

suggests that protein aggregates and/or inclusions are true aging factors in the yeast model system. Because the beneficial functions of Mca1 related to aggregate management and longevity are only partially dependent on the catalytic cysteine C276, it is conceivable that under some conditions, metacaspase-dependent PCD activities (*6*–*8*) may be balanced by both metacaspase-dependent and independent proteostasis. In addition, the data raise the possibility that caspases and/or metacaspases originally evolved as PQC-related cytoprotective factors that were later adopted as PCD-related executioners, perhaps upon their overinduction during severe stress. Elucidating the nature of the environmental cues regulating the switching of metacaspase functions between proteostasis and PCD might explain how decisions concerning survival are made at the level of the individual cell versus the cell community.

REFERENCES AND NOTES

1. J. Yuan, H. R. Horvitz, *Cell* **116**, (Suppl), S53–S56 (2004).
2. E. S. Alnemri *et al*., *Cell* **87**, 171 (1996).
3. N. N. Danial, S. J. Korsmeyer, *Cell* **116**, 205–219 (2004).
4. P. K. Gregersen, *N. Engl. J. Med.* **356**, 1263–1266 (2007).
5. A. G. Uren *et al*., *Mol. Cell* **6**, 961–967 (2000).
6. F. Madeo *et al*., *Mol. Cell* **9**, 911–917 (2002).
7. E. Herker *et al*., *J. Cell Biol.* **164**, 501–507 (2004).
8. F. Madeo, E. Fröhlich, K. U. Fröhlich, *J. Cell Biol.* **139**, 729–734 (1997).
9. A. Shrestha, L. A. Megeney, *Front. Oncol.* **2**, 78 (2012).
10. R. E. Lee, L. G. Puente, M. Kaern, L. A. Megeney, *PLOS One* **3**, e2956 (2008).
11. R. E. Lee, S. Brunette, L. G. Puente, L. A. Megeney, *Proc. Natl. Acad. Sci. U.S.A.* **107**, 13348–13353 (2010).
12. A. Shrestha, L. G. Puente, S. Brunette, L. A. Megeney, *J. Proteomics* **81**, 24–30 (2013).
13. A. Szallies, B. K. Kubata, M. Duszenko, *FEBS Lett.* **517**, 144–150 (2002).
14. F. U. Hartl, M. Hayer-Hartl, *Nat. Struct. Mol. Biol.* **16**, 574–581 (2009).
15. H. Aguilaniu, L. Gustafsson, M. Rigoulet, T. Nyström, *Science* **299**, 1751–1753 (2003).
16. B. Liu *et al*., *Cell* **140**, 257–267 (2010).
17. R. Spokoini *et al*., *Cell Reports* **2**, 738–747 (2012).
18. M. A. Rujano *et al*., *PLOS Biol.* **4**, e417 (2006).
19. M. R. Bufalino, B. DeVeale, D. van der Kooy, *J. Cell Biol.* **201**, 523–530 (2013).
20. N. Erjavec, L. Larsson, J. Grantham, T. Nyström, *Genes Dev.* **21**, 2410–2421 (2007).
21. P. Tessarz, M. Schwarz, A. Mogk, B. Bukau, *Mol. Cell. Biol.* **29**, 3738–3745 (2009).
22. J. R. Glover, S. Lindquist, *Cell* **94**, 73–82 (1998).
23. Materials and methods, figs. S1 to S3, and table S1 are available as supplementary materials on *Science* Online.
24. B. Liu *et al*., *Cell* **147**, 959–961 (2011).
25. A. H. Tong *et al*., *Science* **294**, 2364–2368 (2001).
26. A. H. Wong, C. Yan, Y. Shi, *J. Biol. Chem.* **287**, 29251–29259 (2012).
27. D. Kaganovich, R. Kopito, J. Frydman, *Nature* **454**, 1088–1095 (2008).
28. M. K. Sung, W. K. Huh, *Yeast* **24**, 767–775 (2007).
29. R. Gupta *et al*., *Nat. Methods* **8**, 879–884 (2011).
30. F. Eisele, D. H. Wolf, *FEBS Lett.* **582**, 4143–4146 (2008).
31. D. Öling, F. Eisele, K. Kvint, T. Nyström, *EMBO J.* **33**, 747–761 (2014).
32. U. Kruegel *et al*., *PLOS Genet.* **7**, e1002253 (2011).
33. D. Carmona-Gutierrez, K. U. Fröhlich, G. Kroemer, F. Madeo, *Cell Death Differ.* **17**, 377–378 (2010).

ACKNOWLEDGMENTS

The authors thank C. Boone for providing strain collections for the SGA analysis, L. Megeney for the *MCA1C276A* strain and the pLM1010 plasmid, W.-K. Huh for the pSIK1-RFP plasmid, D. Kaganovich for the pUBC9ts-RFP plasmid, D. Cyr for the pRS423-Cup1-Rnq1-mRFP plasmid, E. Deuerling for the Mca1 antibody, C. Andréasson and U. Hartl for the luciferase plasmids, F. Eisele for the pFE15 (CPY) plasmid, and A. Sigurdsson for assistance in complementation assays. This work was supported by grants from the Swedish Natural Research Council (VR) (T.N. and B.L.) and the Knut and Alice Wallenberg Foundation (Wallenberg Scholar) and European Research Council (Advanced Grant; QualiAge) to T.N., the Swedish Cancer Society (CAN 2012/601) and Stiftelsen Olle Engkvist Byggmästare Foundation to B.L.

SUPPLEMENTARY MATERIALS

www.sciencemag.org/content/344/6190/1389/suppl/DC1
Materials and Methods
Figs. S1 to S3
Table S1
References (*34*–*39*)

25 February 2014; accepted 9 May 2014
Published online 22 May 2014;
10.1126/science.1252634

HIV LATENCY

Screening for noise in gene expression identifies drug synergies

Roy D. Dar,[1] Nina N. Hosmane,[2] Michelle R. Arkin,[3,4]* Robert F. Siliciano,[2,5]* Leor S. Weinberger[1,6,7]†

Stochastic fluctuations are inherent to gene expression and can drive cell-fate specification. We used such fluctuations to modulate reactivation of HIV from latency—a quiescent state that is a major barrier to an HIV cure. By screening a diverse library of bioactive small molecules, we identified more than 80 compounds that modulated HIV gene–expression fluctuations (i.e., "noise"), without changing mean expression. These noise-modulating compounds would be neglected in conventional screens, and yet, they synergized with conventional transcriptional activators. Noise enhancers reactivated latent cells significantly better than existing best-in-class reactivation drug combinations (and with reduced off-target cytotoxicity), whereas noise suppressors stabilized latency. Noise-modulating chemicals may provide novel probes for the physiological consequences of noise and an unexplored axis for drug discovery, allowing enhanced control over diverse cell-fate decisions.

From infectious disease to stem cells and cancer, therapeutic manipulation of cell fate remains a fundamental goal. Efficient manipulation has proven difficult, in part, because cell-fate decisions are often regulated by stochastic cellular processes (*1*–*4*) that generate heterogeneity in signaling responses and result in substantial cell-to-cell variability. For pathogens that establish persistent states (e.g., HIV latency), therapeutic targeting and perturbation of the dormant-cell phenotype has proven exceptionally challenging.

HIV can enter a long-lived proviral latent state (Fig. 1A) that is a leading obstacle to a cure (*5*) and requires that infected individuals remain on lifelong antiretroviral therapy. A leading HIV-cure strategy attempts to stimulate the latent virus back into an active-replication state and simultaneously eliminate it by antiretroviral therapy (*6*). However, efficient reactivation of latent HIV has had limited success (*7*), perhaps because of the stochastic nature of latency (*8*–*11*).

Small-molecule compounds that promote HIV reactivation have been identified, primarily from reporter assays that detect amplification of the mean level of HIV gene expression (*12*), but these compounds fall short of completely reactivating latency (*10*). However, given the stochastic nature of gene expression (*13*), the mean represents only one aspect of expression. We examined whether compounds that affect fluctuations around the mean gene-expression level (i.e., "noise") synergize with existing drug candidates.

Noise in gene expression often results from promoter transitions between on and off states that generate episodic "bursts" of transcription (*13*–*17*). In this "two-state" model, RNA polymerase II stalls on the HIV long terminal repeat (LTR) promoter (*18*, *19*), but when the elongation stall is relieved, multiple polymerases can read through, which results in a burst of transcripts and highly variable expression levels (Fig. 1A, inset). If HIV expression reaches sufficient levels, HIV's autoregulatory gene products (i.e., Tat and Rev) drive reactivation and ultimately active replication. Transcriptional activators, such as tumor necrosis factor (TNF), typically activate the LTR by increasing transcriptional initiation, thereby increasing the frequency of transcriptional events (*18*, *19*) (Fig. 1B). In contrast, compounds that modulate elongation increase the

[1]The Gladstone Institutes, 1650 Owens Street, San Francisco, CA 94158, USA. [2]Department of Medicine, Johns Hopkins University School of Medicine, Baltimore, MD 21205, USA. [3]Small Molecule Discovery Center, University of California, San Francisco, Mission Bay Campus, CA 94158, USA. [4]Department of Pharmaceutical Chemistry, School of Pharmacy, University of California, San Francisco, CA 94143, USA. [5]Howard Hughes Medical Institute, Baltimore, MD 21205, USA. [6]QB3: California Institute for Quantitative Biosciences, University of California, San Francisco, CA 94158, USA. [7]Department of Biochemistry and Biophysics, University of California, San Francisco, CA 94143, USA.
*These authors contributed equally to this work. **†Corresponding author. E-mail: leor.weinberger@gladstone.ucsf.edu**

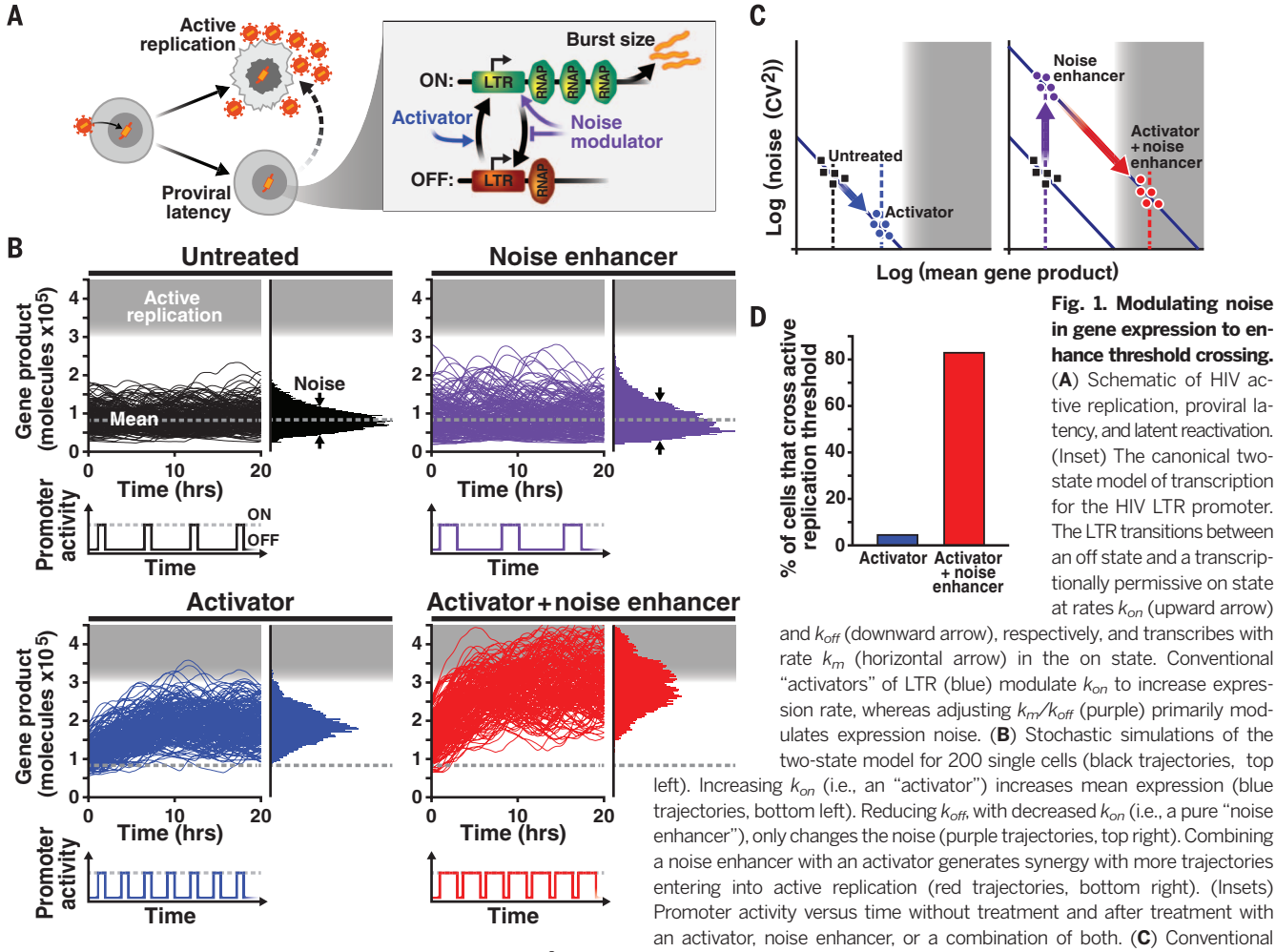

Fig. 1. Modulating noise in gene expression to enhance threshold crossing. (**A**) Schematic of HIV active replication, proviral latency, and latent reactivation. (Inset) The canonical two-state model of transcription for the HIV LTR promoter. The LTR transitions between an off state and a transcriptionally permissive on state at rates k_{on} (upward arrow) and k_{off} (downward arrow), respectively, and transcribes with rate k_m (horizontal arrow) in the on state. Conventional "activators" of LTR (blue) modulate k_{on} to increase expression rate, whereas adjusting k_m/k_{off} (purple) primarily modulates expression noise. (**B**) Stochastic simulations of the two-state model for 200 single cells (black trajectories, top left). Increasing k_{on} (i.e., an "activator") increases mean expression (blue trajectories, bottom left). Reducing k_{off}, with decreased k_{on} (i.e., a pure "noise enhancer"), only changes the noise (purple trajectories, top right). Combining a noise enhancer with an activator generates synergy with more trajectories entering into active replication (red trajectories, bottom right). (Insets) Promoter activity versus time without treatment and after treatment with an activator, noise enhancer, or a combination of both. (**C**) Conventional noise-versus-mean plots for quantitative comparison of noise levels (CV^2). Theoretical lines of constant burst size (i.e., k_m/k_{off} = constant) decrease with mean. Activators increase k_{on} to increase mean expression along lines of constant burst size (left). Noise enhancers transfer the system to a new higher burst-size line (right). Combining an activator with a noise enhancer results in more frequent transcriptional bursts that also have larger burst size, generating more mRNA and surpassing levels achieved by activator alone. (**D**) Percentage of trajectories in (C) that pass into the active-replication region during the simulation.

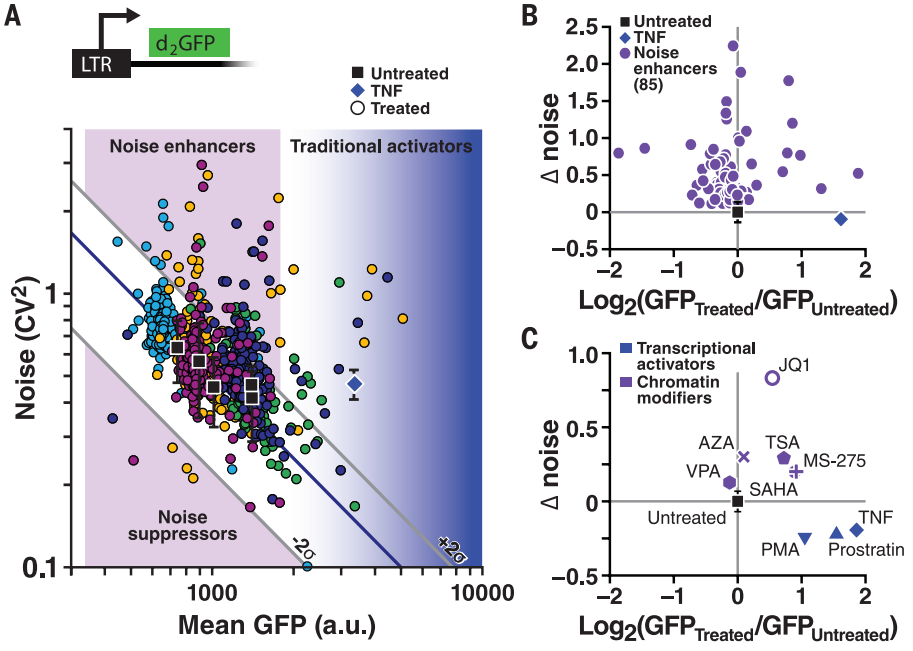

Fig. 2. Screening for compounds that modulate noise in HIV promoter expression. (**A**) Flow cytometry measurements of LTR-d_2GFP isoclonal cells exposed to 1600 small molecules (in 96-well plate format) for 24 hours. Each point represents the mean fluorescence and intrinsic noise (CV^2) for ~50,000 live cells under stringent forward-versus-side scatter gating (*21*) (a.u., arbitrary units). Each color represents a measurement cluster of compounds screened on a single day. Untreated controls (black squares) vary along the constant-burst-size line (diagonal blue line); error bars calculated from standard deviation for 28 measurements. TNF was used as a positive control for each measurement cluster (blue diamond). Noise-modulating compounds increased or suppressed noise by at least ±2σ from the constant burst-size line. (**B**) Change in noise and mean for 85 transcriptional noise enhancers identified by secondary filtering through the two-reporter assay (fig. S1). (**C**) Noise and mean changes for transcriptional modulators of the LTR. Transcriptional activators increased mean expression, whereas chromatin modifiers increase expression noise with minimal increases in expression mean.

duration in the on state, thereby increasing the transcriptional "burst size" and amplifying noise (*20*). Stochastic simulations showed that combining activators with noise enhancers generates a synergistic effect, increasing expression into the active replication regime (Fig. 1B). A convenient method to measure this synergy is to plot noise magnitude (the variance over the mean squared or coefficient of variation squared CV^2) versus mean expression (Fig. 1C). Activators, which increase burst frequency, are constrained to increasing expression along negatively sloped lines of constant burst size on these noise-versus-mean plots (*18*, *19*). In contrast, amplification of noise—which increases the burst size—transfers the system to a new diagonal line of greater burst size where each burst generates more gene product; so, an equivalent increase in burst frequency generates higher amounts of mean expression and substantially more reactivation (Fig. 1D). We tested this theory by searching for noise-enhancing compounds that might synergize with conventional transcriptional activators to enhance HIV reactivation from latency.

To identify noise-enhancing compounds, we screened (*21*) a diverse library of 1600 bioactive small molecules in an isoclonal Jurkat cell line that exhibits a well-characterized noise-versus-mean expression profile (*18*, *19*). This Jurkat T cell line contains one integrated copy of the HIV LTR promoter expressing a short-lived green fluorescent protein (GFP) reporter (d_2GFP)—the short GFP half-life focuses the screen toward identifying

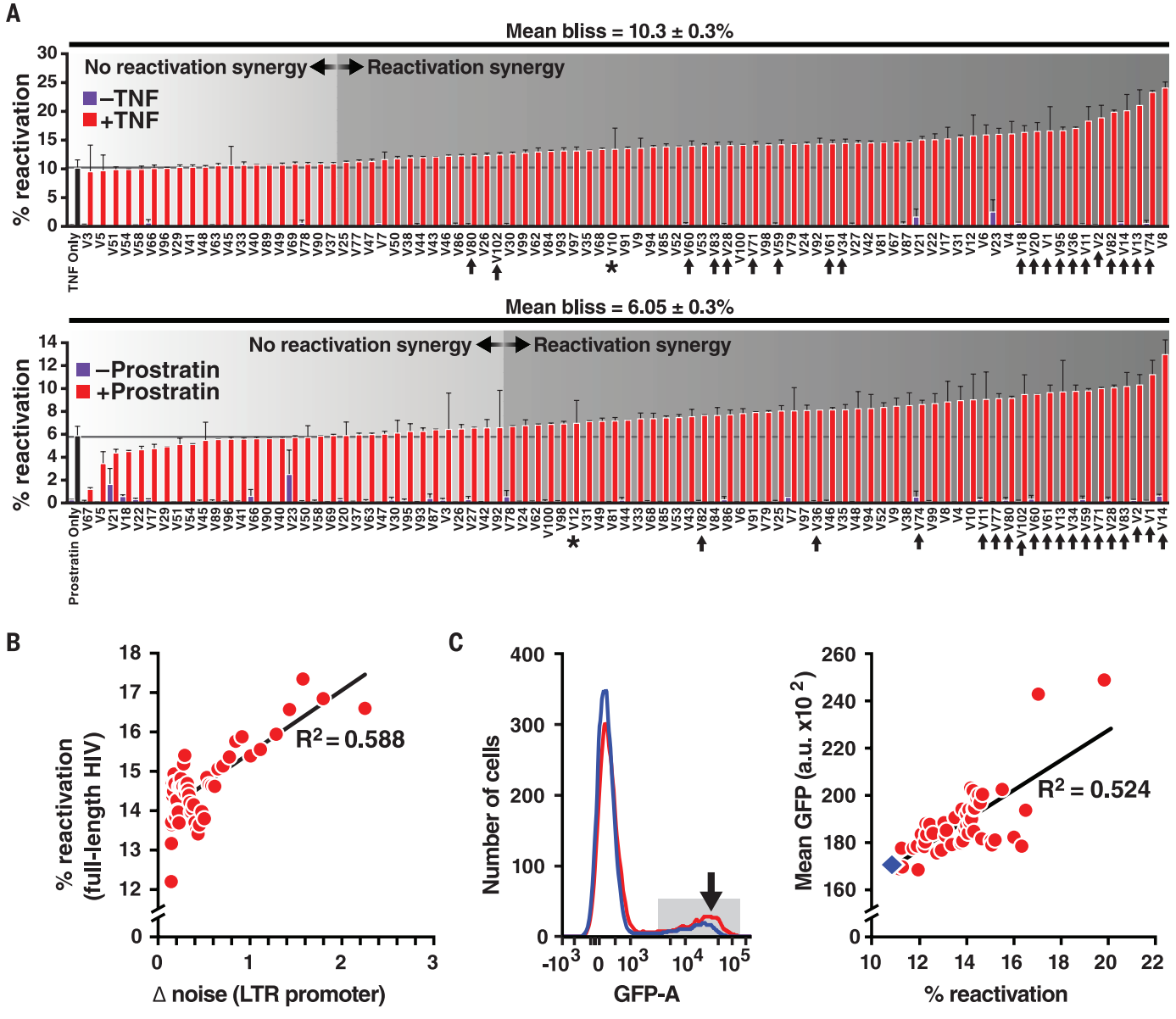

Fig. 3. Synergy of noise enhancers with conventional activators to amplify reactivation of full-length latent HIV. (**A**) Percent reactivation of latently infected J-Lat cells 24 hours after treatment with TNF alone (solid black bar, top), prostratin alone (solid black bar, bottom), or one of the 85 noise enhancers alone (purple bars) or in combination with TNF (red, top) or prostratin (red, bottom). Synergy (Bliss scores greater than the mean Bliss score) is calculated relative to TNF-only or prostratin-only control. The majority of noise enhancers synergize with TNF and prostratin to enhance latent reactivation. Black arrows identify noise enhancers analyzed in Fig. 4B. The asterisk indicates noise enhancers that increase reactivation but without significant synergy. (**B**) Correlation between a compound's noise enhancement (from Fig. 2B) and its reactivation synergy with TNF [from (A)]. Each data point represents a moving average of 10 compounds. (**C**) (Left) Representative flow cytometry histogram for reactivation with TNF + noise enhancer cocktail (red) compared with TNF alone (blue). Noise enhancers amplify mean expression when used in conjunction with an activator (black arrow). (Right) For all the noise enhancer + TNF combinations that synergized, the mean GFP positively correlates with reactivation percentage.

compounds that modulate transcription. Flow cytometry analysis identified more than 100 compounds that enhanced GFP-expression noise (CV^2) by > 2σ, without considerably altering mean-GFP expression (Fig. 2A). These noise-enhancer compounds would be neglected in conventional transcriptional activator screens, which only examine the mean GFP axis.

To find noise-enhancer compounds that might synergize with activators, we next identified which compounds were transcriptional modulators using a stable mCherry reporter driven off a second LTR integration (fig. S1). The differential stability of mCherry and d_2GFP allowed us to select compounds that enhanced transcriptional noise (*21*). This two-reporter assay filtered out 25 compounds, leaving 85 transcriptional noise-enhancer compounds (Fig. 2B and table S1). To ensure that the observed noise enhancement was not an artifact of a specific HIV-integration site, we used a single-cell microscopy approach (*19*) and observed noise enhancement across a broad spectrum of HIV-integration sites (fig. S2 and movie S1).

It was intriguing that previously known latency modulators act as noise enhancers (table S2). Previous analysis showed that chromatin remodelers [histone deacetylase (HDAC) inhibitors, methylation inhibitors, and bromodomain inhibitors] synergize with transcriptional activators [TNF, phorbol 12-myristate 13-acetate (PMA), and prostratin] to enhance HIV reactivation; e.g., the HDAC inhibitor (HDACi) suberanilohydroxamic acid (SAHA) synergizes with prostratin and TNF (*20*, *22*). Chromatin remodeling compounds were found to cause modest increases in noise, whereas known transcriptional activators primarily increased mean expression (Fig. 2C). This observation—that previously identified synergies between TNF or prostratin and HDACi's consist of a noise enhancer and an activator—supports the hypothesis that noise amplification may provide a generalized signature for compounds that synergize.

To test if the 85 newly identified noise enhancers synergized with transcriptional activators to enhance reactivation, we used a well-studied latency model in Jurkat cells (*23*). These cells contain a single, integrated copy of a full-length, latent HIV genome that encodes a GFP reporter (*21*). Upon stimulation with activators, a fraction of the latent cells reactivate, express GFP, and produce viral particles. We quantified synergy with the Bliss Independence Score (*21*), a threshold for strict additivity in the combination of two compounds. Despite noise-enhancer compounds not inducing reactivation on their own, pairwise Bliss scores show that >75% of compounds (64 of 85) significantly synergize with TNF ($P < 0.0001$) (Fig. 3A). Similar amounts of synergy were observed in combinations with prostratin (~64%), with some noise enhancers doubling the reactivation efficacy of TNF and prostratin (Fig. 3A). Noise enhancers tested on two alternate latency cell lines exhibited comparable synergies (fig. S3), which confirms that the observed synergy is not specific to a single HIV integration site.

Theory predicts that the magnitude of noise enhancement should forecast the degree of reactivation synergy (*21*). In agreement, the data exhibited a positive correlation between noise enhancement and reactivation (Fig. 3B) and larger increases in mean expression when noise enhancers and activators were combined (Fig. 3C and fig. S4). To exclude that observed synergies resulted from nonspecific bioactivity of the compounds, we tested combinations of noise enhancers among themselves (fig. S5) and in combination with HDAC and methylation inhibitors (fig. S6). None of these combinations yielded reactivation synergy. Moreover, when two random arrays of ~80 nonenhancers of noise were tested for synergy with TNF and prostratin (fig. S7), only ~6.4% synergized with TNF and 2.6% synergized with prostratin. Importantly, "extrinsic" variability (e.g., cellular microenvironments) did not predict synergy (fig. S8). Thus, noise enhancement is a good predictor of synergy with transcriptional activators.

To test whether reactivation could be further optimized, we varied the doses of noise enhancer and activator (fig. S9). The dose-response matrix for TNF or prostratin with cetirizine hydrochloride (noise enhancer V11) exhibited a peak in HIV reactivation at 25 μM V11 (table S2) and achieved greater reactivation than was caused by TNF or prostratin alone (Fig. 4A and fig. S10). Moreover, noise-enhancer cocktails exhibited substantially less off-target cytotoxicity than did other reactivation cocktails. We compared leading reactivation cocktails to 21 combinations of a noise enhancer with TNF + prostratin (Fig. 4B), and all noise-enhancing cocktails increased reactivation by ~150 to 200% over TNF + prostratin, with minimal cytotoxicity compared with SAHA—a leading candidate that enhances reactivation (*7*) but

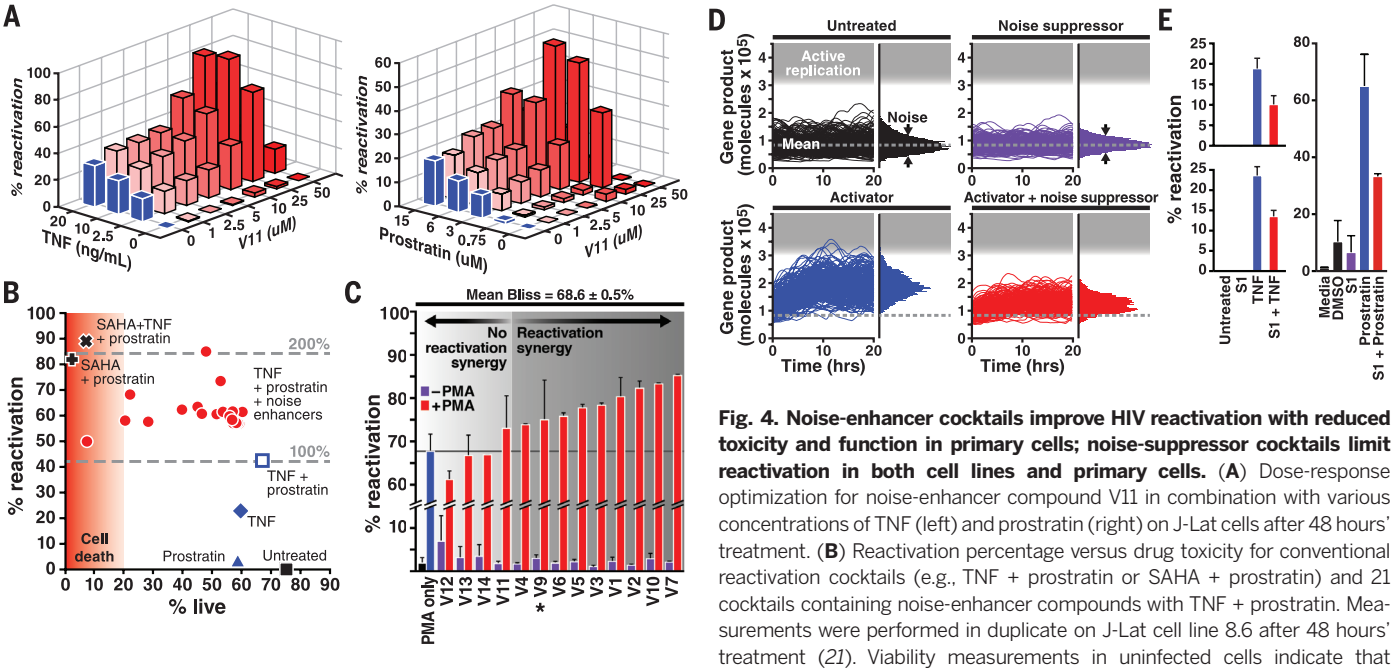

Fig. 4. Noise-enhancer cocktails improve HIV reactivation with reduced toxicity and function in primary cells; noise-suppressor cocktails limit reactivation in both cell lines and primary cells. (**A**) Dose-response optimization for noise-enhancer compound V11 in combination with various concentrations of TNF (left) and prostratin (right) on J-Lat cells after 48 hours' treatment. (**B**) Reactivation percentage versus drug toxicity for conventional reactivation cocktails (e.g., TNF + prostratin or SAHA + prostratin) and 21 cocktails containing noise-enhancer compounds with TNF + prostratin. Measurements were performed in duplicate on J-Lat cell line 8.6 after 48 hours' treatment (*21*). Viability measurements in uninfected cells indicate that reduced viability resulted from chemical cytotoxicity and not viral reactivation (fig. S10). (**C**) Primary T cell model of HIV latency 48 hours after reactivation with PMA or a subset of noise enhancers [reactivation percentage is calculated relative to maximal reactivation potential (*21*)]. Maximal increased activation was observed with PMA and V7 by ~20% or half the available range. (**D**) Stochastic simulations of noise suppression, which reduce noise without altering the mean level but limit reactivation induced by an activator. (**E**) Noise-suppressor molecule S1 decreased TNF-induced reactivation by ~40% in two J-Lat cell lines (top = J-Lat 15.4, bottom = J-Lat 8.6), and decreased prostratin-induced reactivation by ~50% in the primary T cell model (right).

generates substantial off-target cytotoxicity for uninfected cells (fig. S11) (*21*).

In a primary T cell model of HIV latency (*24*), >60% of noise enhancers tested synergized with PMA (Fig. 4C), with some compounds reactivating half of the remaining cells that PMA alone did not reactivate (e.g., mebendazole, V7). Moreover, in both Jurkat and primary T cell models, noise suppression with manidipine hydrochloride, or S1, substantially reduced latent reactivation, as predicted from theory (Fig. 4, D and E). Although there may be considerable technical challenge in identifying noise suppressors—due to the extrinsic noise threshold (*4*)—noise suppression could ultimately be used in strategies to limit spontaneous reactivation of latent HIV, stabilize other fate-specification processes, or identify antagonistic drug combinations.

Overall, the noise-modulating compounds are previously approved by the U.S. Food and Drug Administration and span diverse chemical classes and mechanisms of action [tables S1, S2, and (*21*)]. Although the effects of a single round of reactivation were incomplete (with about 50% of remaining latent cells responding for the best enhancers in primary T cells), latency-reversing strategies will likely require multiple rounds of treatment (10) and noise-enhancing compounds may allow each round of treatment to be more effective by including drugs with highly diverse mechanisms of action and nonoverlapping toxicities. Moreover, we identified these compounds in a fairly small screen of ~1600 compounds; a more extensive screen might identify compounds that work better to allow multiple rounds of reactivation to eliminate the virus. For fundamental cell-biology research on the roles of noise (e.g., in cell-fate specification), noise-modulating chemicals could provide an approach to complement existing genetic noise-perturbation methods (*25*–*28*). From a pharmaceutical science and drug-screening perspective, "noise screening" presents an orthogonal axis to detect synergistic drug combinations. Compared with random synergy screening, noise screening requires substantially fewer tests. Blind synergy searches for pairwise combinations of N compounds require ~N^2 tests; by contrast, noise screening permits ~N tests. Noise screening might help identify compounds for manipulating other fate-switching phenotypes such as cellular reprogramming, metastasis, and bacterial persistence.

REFERENCES AND NOTES

1. M. B. Elowitz, A. J. Levine, E. D. Siggia, P. S. Swain, *Science* **297**, 1183–1186 (2002).
2. J. M. Raser, E. K. O'Shea, *Science* **304**, 1811–1814 (2004).
3. W. J. Blake, M. Kærn, C. R. Cantor, J. J. Collins, *Nature* **422**, 633–637 (2003).
4. Y. Taniguchi *et al.*, *Science* **329**, 533–538 (2010).
5. D. D. Richman *et al.*, *Science* **323**, 1304–1307 (2009).
6. S. G. Deeks, *Nature* **487**, 439–440 (2012).
7. N. M. Archin *et al.*, *Nature* **487**, 482–485 (2012).
8. L. S. Weinberger, J. C. Burnett, J. E. Toettcher, A. P. Arkin, D. V. Schaffer, *Cell* **122**, 169–182 (2005).
9. L. S. Weinberger, R. D. Dar, M. L. Simpson, *Nat. Genet.* **40**, 466–470 (2008).
10. Y. C. Ho *et al.*, *Cell* **155**, 540–551 (2013).
11. A. D. Weinberger, L. S. Weinberger, *Cell* **155**, 497–499 (2013).
12. D. S. Ruelas, W. C. Greene, *Cell* **155**, 519–529 (2013).
13. M. Kærn, T. C. Elston, W. J. Blake, J. J. Collins, *Nat. Rev. Genet.* **6**, 451–464 (2005).
14. T. B. Kepler, T. C. Elston, *Biophys. J.* **81**, 3116–3136 (2001).
15. M. L. Simpson, C. D. Cox, G. S. Sayler, *J. Theor. Biol.* **229**, 383–394 (2004).
16. I. Golding, J. Paulsson, S. M. Zawilski, E. C. Cox, *Cell* **123**, 1025–1036 (2005).
17. A. Raj, C. S. Peskin, D. Tranchina, D. Y. Vargas, S. Tyagi, *PLOS Biol.* **4**, e309 (2006).
18. A. Singh, B. Razooky, C. D. Cox, M. L. Simpson, L. S. Weinberger, *Biophys. J.* **98**, L32–L34 (2010).
19. R. D. Dar *et al.*, *Proc. Natl. Acad. Sci. U.S.A.* **109**, 17454–17459 (2012).
20. D. Boehm *et al.*, *Cell Cycle* **12**, 452–462 (2013).
21. Materials and methods are available as supplementary materials on *Science* Online.
22. S. Reuse *et al.*, *PLOS ONE* **4**, e6093 (2009).
23. A. Jordan, D. Bisgrove, E. Verdin, *EMBO J.* **22**, 1868–1877 (2003).
24. H. C. Yang *et al.*, *J. Clin. Invest.* **119**, 3473–3486 (2009).
25. E. M. Ozbudak, M. Thattai, I. Kurtser, A. D. Grossman, A. van Oudenaarden, *Nat. Genet.* **31**, 69–73 (2002).
26. M. Acar, J. T. Mettetal, A. van Oudenaarden, *Nat. Genet.* **40**, 471–475 (2008).
27. W. J. Blake *et al.*, *Mol. Cell* **24**, 853–865 (2006).
28. N. Vardi, S. Levy, M. Assaf, M. Carmi, N. Barkai, *Curr. Biol.* **23**, 2051–2057 (2013).

ACKNOWLEDGMENTS

We thank I. Golding, J. Weissman, O. Weiner, E. Verdin, M. Simpson, C. Lee, A. Pai and the Weinberger lab for thoughtful discussions. We thank C. Wilson, M. Cavrois, M. Gesner, and M. Titus for technical expertise and assistance. R.D.D. was supported by an NIH National Research Service Award fellowship (AI104380). This work was supported by the NIH Director's New Innovator Award DP2-OD006677 (L.S.W.), the NIH Delaney Collaboratory of AIDS Researchers for a Cure (U19AI096113), a UCSF CTSI-SOS Award, UCSF-GIVI CFAR (P30AI027763), UCSF-CSSB (P50GM081879), the Pew Scholars in the Biomedical Sciences, and the Alfred P. Sloan Foundation.

SUPPLEMENTARY MATERIALS

www.sciencemag.org/content/344/6190/1392/suppl/DC1
Materials and Methods
Supplementary Text
Figs. S1 to S11
Tables S1 and S2
References (*29*–*51*)
Movie S1

26 December 2013; accepted 27 May 2014
Published online 5 June 2014;
10.1126/science.1250220

CANCER GENOMICS

Single-cell RNA-seq highlights intratumoral heterogeneity in primary glioblastoma

Anoop P. Patel,[*1,2,3,4] Itay Tirosh,[*3] John J. Trombetta,[3] Alex K. Shalek,[3] Shawn M. Gillespie,[2,3,4] Hiroaki Wakimoto,[1] Daniel P. Cahill,[1] Brian V. Nahed,[1] William T. Curry,[1] Robert L. Martuza,[1] David N. Louis,[2] Orit Rozenblatt-Rosen,[3] Mario L. Suvà,[2,3]†‡ Aviv Regev,[3,4,5]†‡ Bradley E. Bernstein[2,3,4]†‡

Human cancers are complex ecosystems composed of cells with distinct phenotypes, genotypes, and epigenetic states, but current models do not adequately reflect tumor composition in patients. We used single-cell RNA sequencing (RNA-seq) to profile 430 cells from five primary glioblastomas, which we found to be inherently variable in their expression of diverse transcriptional programs related to oncogenic signaling, proliferation, complement/immune response, and hypoxia. We also observed a continuum of stemness-related expression states that enabled us to identify putative regulators of stemness in vivo. Finally, we show that established glioblastoma subtype classifiers are variably expressed across individual cells within a tumor and demonstrate the potential prognostic implications of such intratumoral heterogeneity. Thus, we reveal previously unappreciated heterogeneity in diverse regulatory programs central to glioblastoma biology, prognosis, and therapy.

Tumor heterogeneity poses a major challenge to cancer diagnosis and treatment. It can manifest as variability between tumors, wherein different stages, genetic lesions, or expression programs are associated with distinct outcomes or therapeutic responses (*1*–*3*). Alternatively, cells from the same tumor may harbor different mutations or exhibit distinct phenotypic or epigenetic states (*4*–*7*). Such intratumoral heterogeneity is increasingly appreciated as a determinant of treatment failure and disease recurrence (*8*).

Glioblastoma is an archetypal example of a heterogeneous cancer and one of the most lethal human malignancies (*9*, *10*). Intratumoral heterogeneity and redundant signaling routes likely underlie the inability of conventional and targeted therapies to achieve long-term remissions (*11*–*13*). These tumors contain cellular niches enriched for distinct phenotypic properties, including transient quiescence and self-renewal (*14*–*16*), adaptation to hypoxia (*17*), and resistance to radiation-induced DNA damage (*18*, *19*). DNA and RNA profiles of bulk tumors have enabled genetic and transcriptional classification of glioblastomas (*20*, *21*). However, the relationships among different sources of intratumoral heterogeneity—genetic, transcriptional, and functional—remain obscure.

Single-cell transcriptome analysis by RNA sequencing (RNA-seq) (*22*, *23*) should in principle enable functional characterization from landmark genes and annotated gene sets, relate in vivo states to in vitro models, inform transcriptional classifications based on bulk tumors, and even capture genetic information for expressed transcripts. To analyze intratumoral heterogeneity systematically, we isolated individual cells from five freshly resected and dissociated human glioblastomas and generated single-cell full-length transcriptomes using SMART-seq (96 to 192 cells per tumor, total 672 cells; Fig. 1A). Before sorting, the suspension was depleted for $CD45^+$ cells to remove inflammatory infiltrate. As a control, we also generated population (bulk) RNA-seq profiles from the CD45-depleted tumor samples. All tumors were *IDH1/2* wild-type primary glioblastomas (fig. S1), and three were *EGFR* amplified as determined by routine clinical tests (table S1). We excluded genes and cells with low coverage (*24*), retaining ~6000 genes quantified in 430 cells from five patient tumors and population controls (table S1). The population-level controls correlated with the average of the single cells in that tumor (fig. S2), supporting the accuracy of the single-cell data. Individual cells from the same tumor were more correlated to each other than were cells from different tumors (fig. S2). Nevertheless, correlations between individual cells from the same tumor showed a broad spread (correlation coefficient r ~0.2 to 0.7) (fig. S2), consistent with intratumoral heterogeneity.

Although our isolation procedures specifically targeted glioblastoma cells, we tested whether our sampling also included normal cells. To distinguish normal from malignant, we attempted to infer large-scale copy-number alterations for each cell by averaging relative expression levels over large genomic regions (*24*). This allowed us to

[1]Department of Neurosurgery, Massachusetts General Hospital and Harvard Medical School, Boston, MA 02114, USA. [2]Department of Pathology and Center for Cancer Research, Massachusetts General Hospital and Harvard Medical School, Boston, MA 02114, USA. [3]Broad Institute of Harvard and Massachusetts Institute of Techonology (MIT), Cambridge, MA 02142, USA. [4]Howard Hughes Medical Institute Chevy Chase, MD 20815, USA. [5]Department of Biology, MIT, Cambridge, MA 02139, USA.
*These authors contributed equally to this work. †These authors contributed equally to this work. **‡Corresponding author. E-mail: bernstein.bradley@mgh.harvard.edu (B.E.B.); aregev@broadinstitute.org (A.R.); suva.mario@mgh.harvard.edu (M.L.S.)**

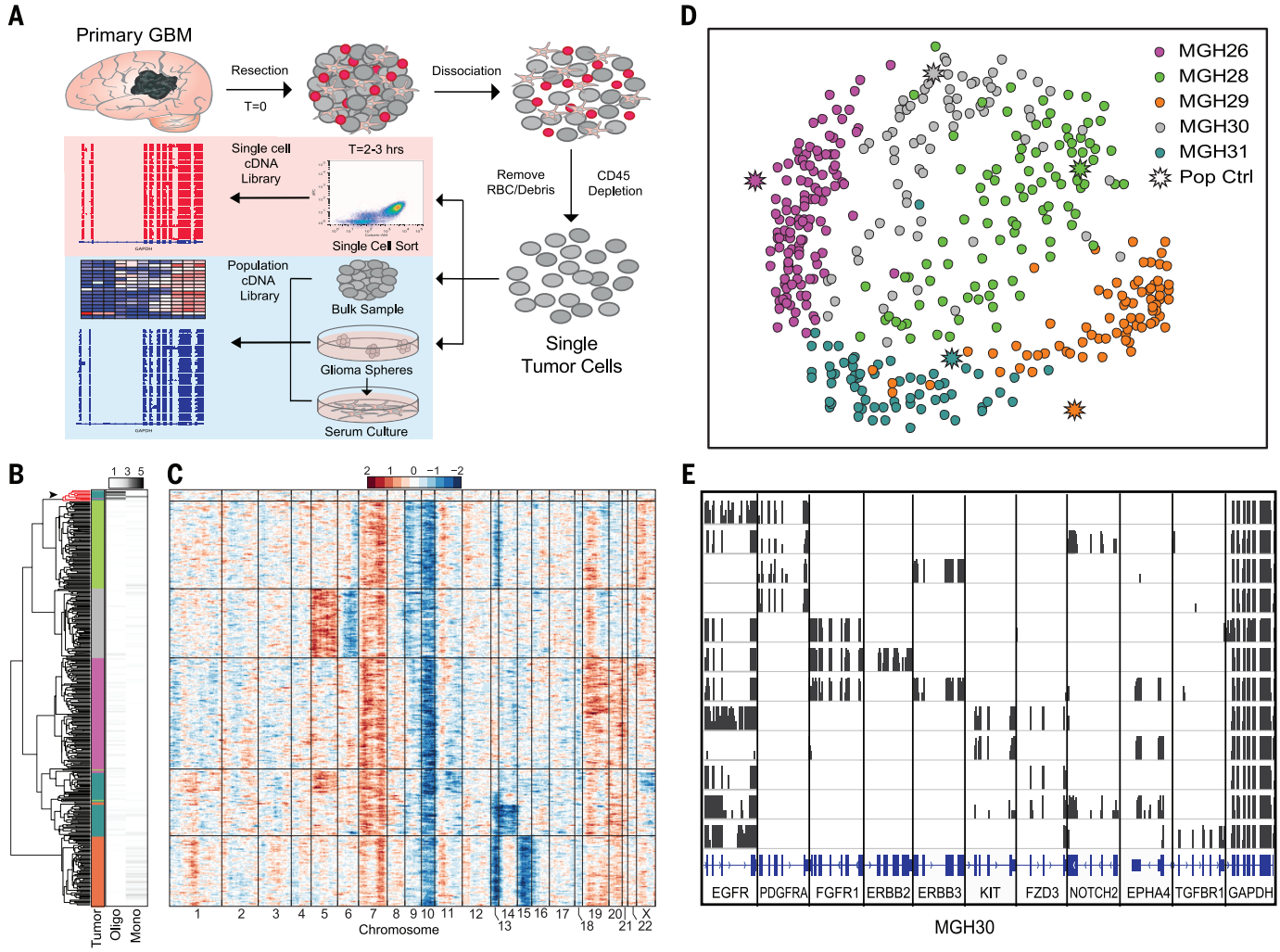

Fig. 1. Intratumoral glioblastoma heterogeneity quantified by single-cell RNA-seq. (**A**) Workflow depicts rapid dissociation and isolation of glioblastoma cells from primary tumors for generating single-cell and bulk RNA-seq profiles and deriving glioblastoma culture models. (**B**) Clustering of CNV profiles inferred from RNA-seq data for all single cells and a normal brain sample. Clusters (dendrogram) primarily reflect tumor-specific CNV [colored bar coded as in (D)]. Topmost cluster (red, arrow) contains the normal brain sample and 10 single cells, 9 of which correlate with normal oligodendrocyte expression profiles and 1 with normal monocytes ("Oligo" and "Mono," black and white heatmap). (**C**) Heatmap of CNV signal normalized against the "normal" cluster defined in (B) shows CNV changes by chromosome (columns) for individual cells (rows). All cells outside the normal cluster exhibit chromosome 7 gain (red) and chromosome 10 loss (blue), which are characteristic of glioblastoma. (**D**) Multidimensional scaling illustrates the relative similarity between all 420 single tumor cells and population controls. The distance between any two cells reflects the similarity of their expression profiles. Cells group by tumor (color code), but each tumor also contains outliers that are more similar to cells in other tumors. (**E**) RNA-seq read densities (vertical scale of 10) over surface receptor genes are depicted for individual cells (rows) from MGH30. Cell-to-cell variability suggests a mosaic pattern of receptor expression, in contrast to constitutively expressed *GAPDH*.

suppress individual gene-specific expression patterns and emphasize the signal of large-scale copy-number variations (CNVs). As a control, we included RNA-seq profiles from (bulk) normal human brain (*25*). Hierarchical clustering of all single cells and normal brain samples identified seven groups with concordant CNV profiles (Fig. 1B). The normal brain sample clustered with 10 single cells that presumably have "normal" copy number. In parallel, unsupervised transcriptional analysis identified nine outlier cells with increased expression of mature oligodendrocyte genes and down-regulation of glioblastoma genes (figs. S3 and S4). Notably, all nine of these expression outliers clustered with the normal brain in the CNV analysis (Fig. 1B). The one additional "normal" cell inferred from this CNV cluster correlated with a monocytic expression signature (*26*) (Fig. 1B). None of the remaining 420 cells show similarity to the transcriptional programs of nonmalignant brain or immune cell types (fig. S5) (*24*). Although nonmalignant cells are critical components of the tumor microenvironment, the combination of dissociation methods, $CD45^{+}$ depletion, flow cytometry gating, and computational filtering used in this study largely excluded nontumor cells.

Normalization of CNV profiles using signal from the "normal" cluster revealed coherent chromosomal aberrations in each tumor (Fig. 1C). Gain of chromosome 7 and loss of chromosome 10, the two most common genetic alterations in glioblastoma (*20*), were consistently inferred in every tumor cell. Chromosomal aberrations were relatively consistent within tumors, with the exception that MGH31 appears to contain two genetic clones with discordant copy-number changes on chromosomes 5, 13, and 14. Although these data suggest large-scale intratumoral genetic homogeneity, we recognize that heterogeneity generated by focal alterations and point mutations will be grossly underappreciated using this method. Nevertheless, such panoramic analysis of chromosomal landscapes effectively separated normal from malignant cells.

To analyze global transcriptional interrelationships, we used multidimensional scaling to represent the degree of similarity among the cells in the data set (Fig. 1D) (*24*). In contrast to the chromosome-scale analysis above, we observed extensive intratumoral heterogeneity at the transcriptional level. Although most cells grouped by tumor of origin, there were many examples of cells from one tumor crossing into the transcriptional space of another tumor. Moreover, the transcriptional diversity within each individual tumor was significantly greater than that observed for the normal oligodendrocytes (fig. S4) or for an in vitro model of stemlike tumor-propagating glioblastoma cells (GBM6 and GBM8) (*27*, *28*) (fig. S2).

Cell-to-cell variability is also evident in the expression and splicing patterns of signaling molecules such as receptor tyrosine kinases (RTKs), which are important therapeutic targets (*29*). Mosaic RTK amplification and redundant signaling pathways contribute to targeted therapy resistance in glioblastoma (*11*, *12*, *30*). We found mosaic expression for *EGFR*, *PDGFRA*, *PDGFA*, *FGFR1*, *FGF1*, *NOTCH2*, *JAG1*, and other surface receptors and ligands in pathways pertinent to glioblastoma (Fig. 1E and figs. S6 and S7). Notably, the transcripts encoding such genes are highly expressed in individual cells and in the aggregate profiles, increasing our confidence that their absence reflects true negatives (*23*). Additionally, multiple *EGFR* truncations and in-frame deletions have been described, including an oncogenic mutant form, *EGFRvIII*, which lacks the extracellular domain (de2-7) and is a putative target for immunotherapy (*31*). Of the three tumors with significant *EGFR* expression in our data set (MGH26, MGH30, and MGH31), MGH30 expresses *EGFRvIII*. By examining junction-spanning "spliced" reads at the single-cell level, we identified cells in MGH30 expressing wild-type *EGFR* (7%) and *EGFRvIII* (19%), as well as a second oncogenic variant [*de4* (*32*); 25%] (fig. S8). These variants were almost mutually exclusive, with just 1 to 2% of cells coexpressing wild-type *EGFR* and *EGFRvIII*. Moreover, several cells lack *EGFR* but express other tyrosine kinase receptors, suggesting potential alternative pathways for proliferative signaling (Fig. 1E and fig. S7). For example, *EGFR* expression is anticorrelated with *PDGFRA* and *PDGFC* expression in cells from MGH30 (fig. S9). These findings suggest that heterogeneous expression and/or mutational status of RTKs and other signaling molecules across individual glioblastoma tumor cells may compromise therapies targeting receptor immunogenicity or RTK signaling.

We next used hierarchical clustering and principal component analysis to define four meta-signatures, each composed of multiple related clusters that coherently vary across individual cells from a given tumor or the full data set (*24*) (Fig. 2A). These four meta-signatures were, respectively, enriched for genes related to cell cycle (Fig. 2B), hypoxia (Fig. 2C), complement/immune response (fig. S10), and oligodendrocyte function (demarcating the nine normal oligodendrocytes). We validated the coexpression of meta-signature genes by single-cell quantitative polymerase chain reaction (QPCR) on another 91 cells from MGH26 and 76 cells from MGH30 using primers for 24 genes (fig. S11). Although immune cells are an important component of the

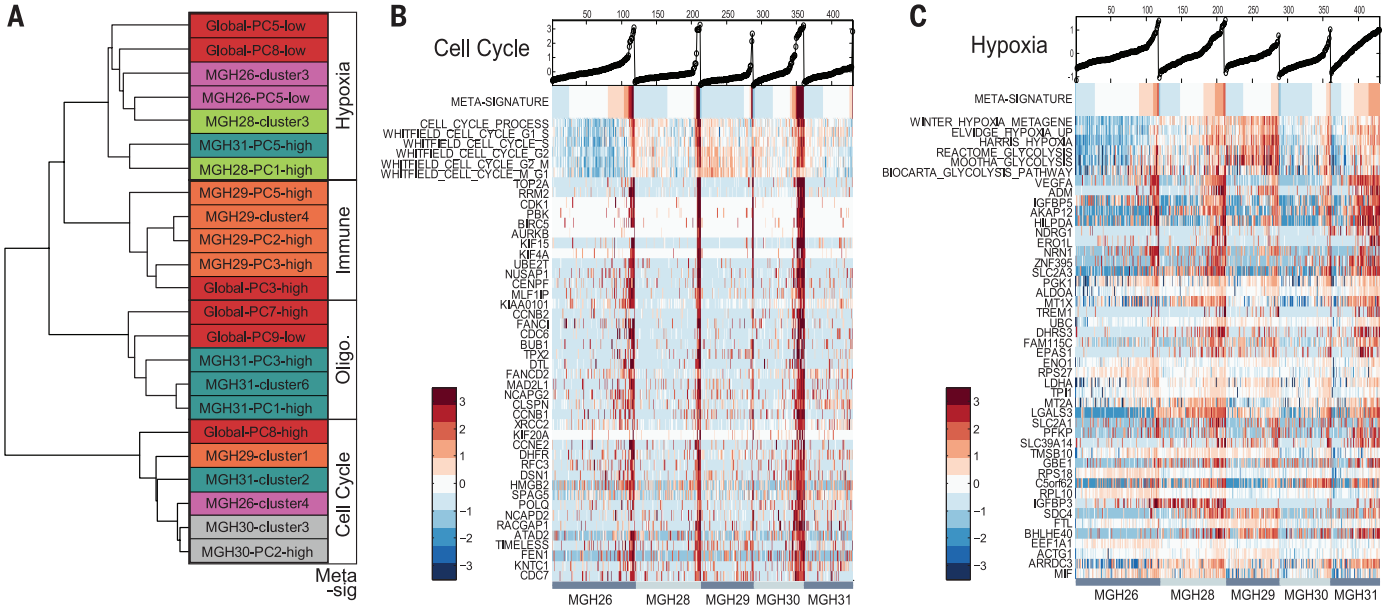

Fig. 2. Unbiased analysis of intratumoral heterogeneity reveals coherent transcriptional modules. (**A**) Gene sets that vary coherently between cells in specific tumors or across the global data set (colored boxes) were identified by principal component analysis or clustering (*24*). Hierarchical clustering of these gene sets across all cells (tree) reveals four meta-signatures related to hypoxia, complement/immune response, oligodendrocytes, and cell cycle. (**B**) Heatmap shows expression of the cell cycle meta-signature, selected cell cycle gene sets, and representative genes from the signature (rows) in individual glioblastoma cells (columns). Cells were grouped by tumor and ordered by meta-signature score (top). (**C**) Heatmap depicts hypoxia meta-signature as in (B).

tumor microenvironment, expression of complement and immune genes by malignant cells was somewhat unexpected. We validated this result using two approaches. MGH29 harbors a previously described p53 mutation, R248L (C→T) (*33*) (table S1). Although coverage of this transcript was relatively low, we identified three cells from MGH29 that clearly contain this oncogenic mutation. All of these cells also expressed C3 and other genes from the complement/immune module (fig. S12). Moreover, direct examination of additional cells scoring for the complement/immune signature confirmed chromosomal aberrations characteristic of glioblastoma (Fig. 1C). Notably, the module may be more generally relevant, as robust coexpression of these genes was detected in multiple cell lines derived from brain tumors in the Cancer Cell Line Encyclopedia (CCLE) (fig. S13) (*34*).

Another notable feature of the module analysis is the activity of the cell cycle program in a relatively small proportion of cells from each tumor, ranging from just 1.4% in MGH31 to 21.9% in MGH30 (table S2 and Fig. 2B). These values contrast markedly with those of the in vitro glioblastoma models in which almost 100% of cells scored positively for the cell cycle module, but are relatively consistent with Ki67^{+} quantifications for these tumors (figs. S14 and S15). We investigated several markers previously linked to quiescence, including *HES1*, *TSC22D1*, and *KDM5B* (*35*–*37*). Transcripts for *HES1* were not well detected in our data owing to low expression, but *TSC22D1* and *KDM5B* showed significantly higher expression in noncycling tumor cells (fig. S16A). *KDM5B*, which has been implicated in quiescence and therapeutic resistance in melanoma, was detected in 10 to 20% of individual cells across all tumors and confirmed to anticorrelate with cell cycle meta-signature by single-cell QPCR in MGH26 (fig. S16B).

Clustering of genes anticorrelated to the cell cycle meta-signature also revealed a group of 12 genes (fig. S17A), nine of which were in the hypoxia meta-signature (Fig. 2C). Indeed, these meta-signatures were diametrically opposed (fig. S17B). Although this meta-signature might be influenced by tissue-processing procedures, hypoxia has been studied extensively as a stimulus for angiogenesis (*17*) and transdifferentiation of glioblastoma stem cells into vascular endothelium (*38*–*40*). Reordering of the cells by hypoxic module score, which was pronounced in MGH28 and MGH31, demonstrated clear gradients in each sample (Fig. 2C), potentially reflecting variations in the tumor microenvironment that affect oxygen tension, blood supply, or nutritional source (*17*, *38*–*40*). Further studies are needed to understand the spatial relationships of these transcriptional niches in vivo. Thus, in vivo microenvironment and genes linked to quiescence may affect dormant and possibly refractory compartments in glioblastoma.

Glioblastomas likely contain a primitive subpopulation of stemlike cells (GSCs) with preferential

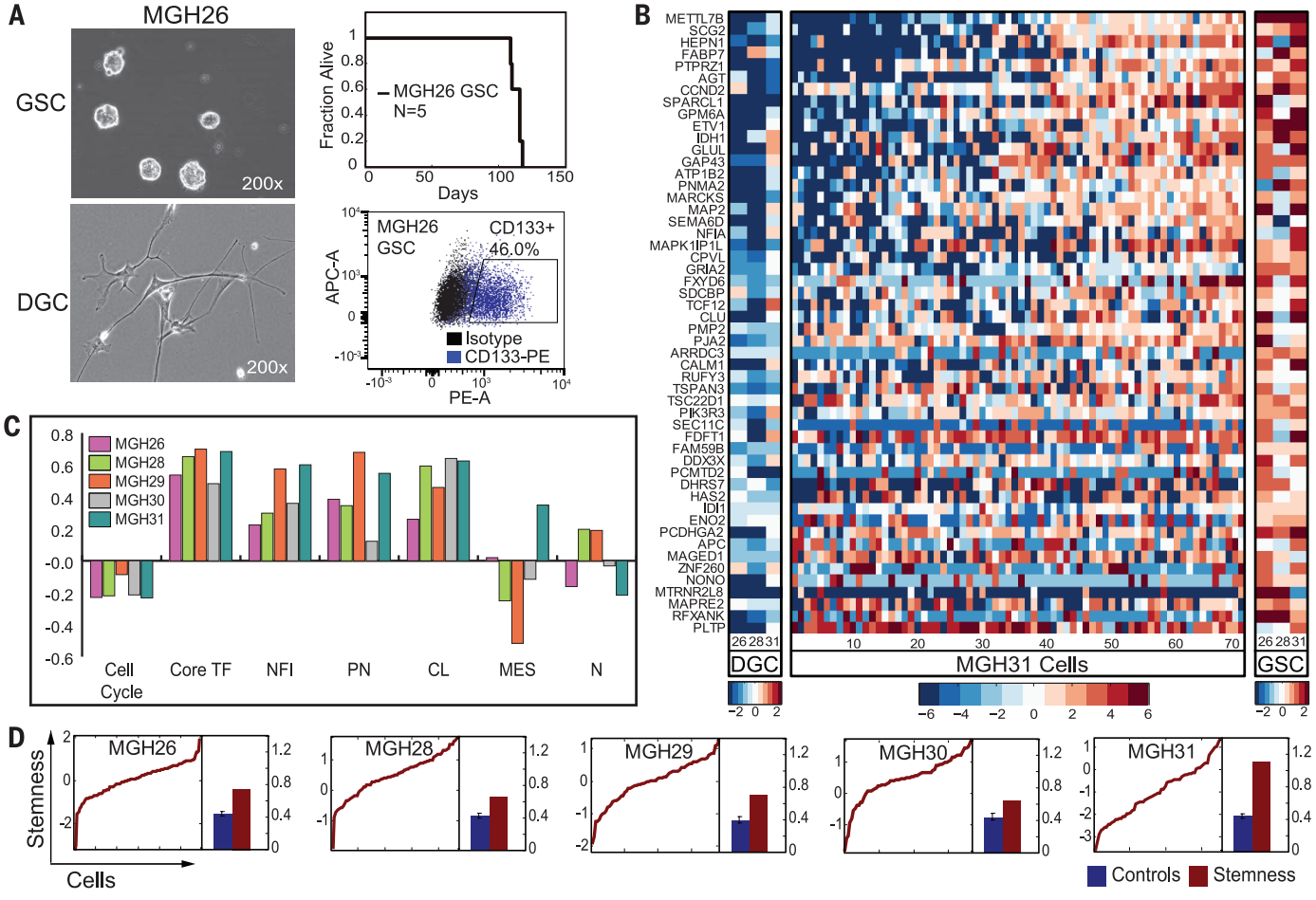

Fig. 3. Transcriptional signatures of a stemlike compartment in primary glioblastoma. (**A**) Stemlike (GSC) and differentiated (DGC) culture models were derived from patient tumor MGH26. GSCs grow as spheres (left, top), initiate tumors in xenotransplantation (right, top), and express the stem cell marker CD133 (right, bottom). (**B**) Heatmap depicts expression of genes (rows) from a stemness signature in differentiated models (DGC, left columns), stemlike models (GSC, right columns) derived from 3 tumors, and in 70 individual cells from MGH31 (middle). (**C**) Bar plot depicts the Pearson correlation coefficient (*y* axis) between the stemness signature and selected transcriptional modules in each tumor cell cycle; transcriptional targets of POU3F2, SOX2, SALL2, OLIG2 (core TF) (*42*); NFI transcriptional targets (NFI) (*41*); and the proneural (PN), classical (CL), mesenchymal (MES), and neural (N) subtypes defined by the Cancer Genome Atlas (*21*). (**D**) Plot depicts stemness score (*y* axis) computed from stemness signature gene expression in individual cells from each tumor (*x* axis) ordered by score. Bar plots depict the overall variance (*y* axis, SD) in the stemness score (red) and the average variance of simulated control gene sets (blue), confirming the significance of the gradient.

resistance to existing therapies (*16*, *18*). GSCs can be modeled in vitro as spherogenic cultures that potently initiate tumors in mice (*15*, *27*). Glioblastoma is also postulated to contain more differentiated cells (DGCs) that can be expanded as adherent monolayers in serum (*27*, *39*). We established GSC and DGC cultures from three tumors in our study (MGH26, MGH28, and MGH31). As expected, the GSCs exhibit a stemlike phenotype, express the stemness marker CD133, and propagate tumors in xenotransplantation (Fig. 3A and fig. S18). To identify in situ tumor cells with stemlike or differentiated phenotypes, we derived a stemness signature from a consensus set of genes differentially expressed between three respective GSC and DGC culture models (Fig. 3B).

Application of the stemness signature to the single-cell transcriptional profiles revealed stemness gradients in all five tumors (Fig. 3D). The stemness gradient is modestly anticorrelated to the cell cycle meta-signature (Fig. 3C), consistent with the notion that stemlike cells divide at lower overall rates (*16*). Notably, the stemness-differentiation axis was occupied continuously rather than discretely, consistent with the notion that the respective in vitro models emulate phenotypic extremes but do not capture the full spectrum of cellular states within a primary tumor.

Genes correlated to the in vivo gradient include expected classifier genes from the in vitro analysis, as well as additional candidates that may reflect aspects of stemness not evident in the culture model (fig. S19, red and blue, respectively). These include several transcription factors (TFs), such as *POU3F2*, *NFIA*, and *NFIB*, which have been implicated in tumor propagation, neural stem cell self-renewal, and quiescence (*41*, *42*). The in vivo stemness gradient also significantly correlated with the average expression of target genes for these TFs, which we predicted from chromatin immunoprecipitation (ChIP)–seq data (Fig. 3C). Thus, expression signatures and regulatory circuits derived from GSC and neural stem cell models converge to a coherent gradient of cells within primary glioblastoma and identify TFs likely to promote stemlike regulatory programs in vivo.

We next considered the classification scheme established by The Cancer Genome Atlas (TCGA) (*21*) to distinguish four glioblastoma subtypes: proneural, neural, classical, and mesenchymal. Although these original definitions were established from bulk tumor profiles, we wanted to explore whether individual cells in a tumor vary in their classification. On the basis of population-level (bulk) expression data, the tumors in our study scored as proneural (MGH26), classical (MGH30), or mesenchymal (MGH28 and MGH29) subtypes (fig. S20). To examine the distribution of subtype signatures across individual cells, we calculated subtype scores for each cell using the classifier gene sets.

All five tumors consist of heterogeneous mixtures with individual cells corresponding to different glioblastoma subtypes (Fig. 4, A and B). All tumors had some cells conforming to a proneural subtype regardless of the dominant subtype of the tumor, whereas each of the other subtypes was below detection in at least one tumor. Single-cell QPCR of 30 classifier genes in 167 additional cells from MGH26 and MGH30 (fig. S21)

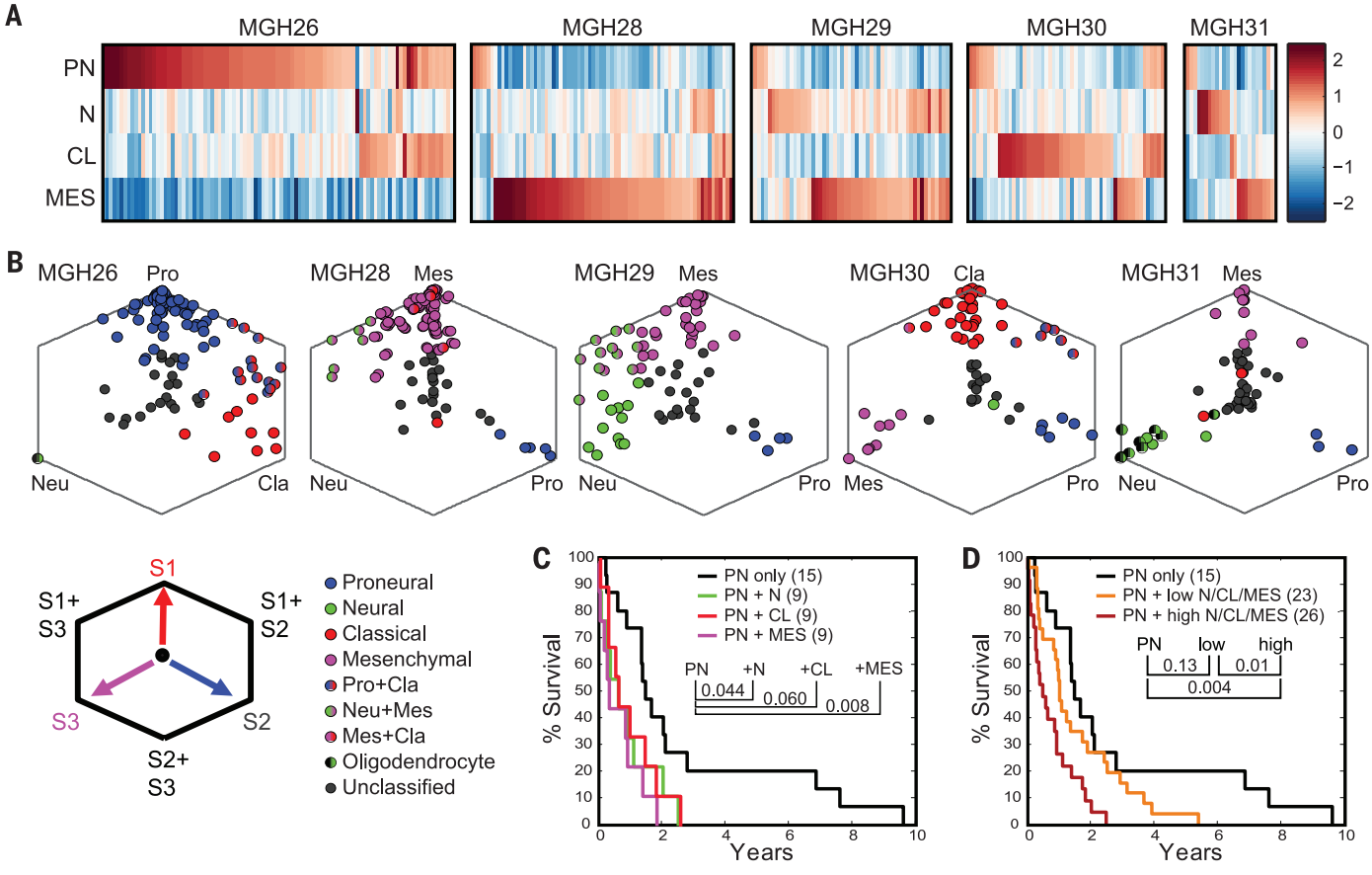

Fig. 4. Individual tumors contain a spectrum of glioblastoma subtypes and hybrid cellular states. (**A**) Heatmap depicts average expression of classifier genes for each subtype (rows) across all classifiable cells grouped by tumor (columns). PN: proneural; CL: classical; MES: mesenchymal; N: neural. Each tumor contains a dominant subtype, but also has cells that conform to alternate subtypes. (**B**) Hexagonal plots depict bootstrapped classifier scores for all cells in each tumor. Each data point corresponds to a single cell and is positioned along three axes according to its relative scores for the indicated subtypes (supplementary methods). Cells corresponding to each subtype are indicated by solid color, whereas hybrid cells are depicted by two colors. (**C**) Kaplan-Meier survival curves are shown for proneural tumors from the Cancer Genome Atlas (*21*). Intratumoral heterogeneity was estimated on the basis of detected signal for alternative subtypes and used to partition the tumors into a pure proneural group and three groups with the indicated additional subtype (group size in parentheses). Tumors with mesenchymal signal had significantly worse outcome than pure proneural tumors ($P < 0.05$). (**D**) Kaplan-Meier survival curves shown for proneural tumors partitioned on the basis of the relative strength of alternative subtype signatures in aggregate (*24*). Tumors with high signal for alternative subtypes had significantly worse outcome than pure proneural tumors ($P < 0.05$).

confirmed the presence of multiple subtypes within these tumors in proportions similar to those identified by single-cell RNA-seq. Thus, although population-level data detect the dominant transcriptional program, they do not capture the true diversity of transcriptional subtypes within a tumor.

Intratumoral subtype heterogeneity provides potentially important insights into tumor biology. The stemness signature is strongest in individual cells conforming to the proneural (r = 0.12 to 0.68, P < 0.01, Student's t test) and classical (r = 0.26 to 0.64, P < 0.01, Student's t test) subtypes, but underrepresented in cells of the mesenchymal subtype (Fig. 3C and fig. S22), which has been correlated with astrocytic differentiation (*21*). In contrast, cells of the neural subtype do not correspond to either in vitro model (Fig. 3C), but are more similar to normal oligodendrocytes (Fig. 4B). These findings highlight parallels between intratumoral cellular heterogeneity in glioblastoma and cellular diversity in the developing brain, with respective subsets of tumor cells resembling a progenitor compartment, an astrocytic lineage, or an oligodendrocytic lineage. This analysis also revealed "hybrid" states (Fig. 4B) in which a single cell scored highly for two subtypes, most commonly classical and proneural (progenitor states) or mesenchymal and neural (differentiated states). These hybrid states may reflect aberrant developmental programs and/or interconversion between phenotypic states.

Finally, we examined whether subtype heterogeneity is relevant to prognosis (*24*). We focused on tumors classified as proneural, controlling for *IDH1* status (*3*, *43*) and binning them into three groups: (i) pure proneural tumors without any transcriptional signal for other subtypes; (ii) low-heterogeneity tumors with modest signal for other subtypes (defined as average expression of the alternative subtype genes greater than the median value in the proneural group); and (iii) high-heterogeneity tumors with stronger signals for other subtypes (defined as greater than the 85th percentile in the proneural group). We also partitioned the proneural tumors according to the other detected subtype. We found that increased heterogeneity was associated with decreased survival (Fig. 4, C and D). This suggests that the clinical outcome of a proneural glioblastoma is influenced by the proportion of tumor cells of alternate subtypes and emphasizes the clinical importance of intratumoral heterogeneity.

We have leveraged single-cell transcriptomics to characterize heterogeneous gene expression programs within five glioblastoma tumors and interrelate their transcriptional, functional, and (to a limited extent) genetic diversity. These findings have fundamental implications for cancer biology and therapeutic strategies, as signaling molecules relevant to targeted therapy show cell-to-cell variability in expression and isoform selection. Moreover, in vivo tumor cells display a spectrum of stemness and differentiation states, variable proliferative capacity, and variable expression of quiescence markers, all of which may confound therapeutic strategies. Although population-level methods for glioblastoma classification have provided important prognostic insights, they do not recapitulate the diversity of transcriptional programs present in an individual tumor. Our analysis reveals that tumors contain multiple cell states with distinct transcriptional programs and provides inferential evidence for dynamic transitions. A better understanding of the spectrum and dynamics of cellular states in glioblastoma is thus critical for establishing faithful models and advancing therapeutic strategies that address the complexity of this disease.

REFERENCES AND NOTES

1. S. Yachida *et al.*, *Nature* **467**, 1114–1117 (2010).
2. K. Eppert *et al.*, *Nat. Med.* **17**, 1086–1093 (2011).
3. D. W. Parsons *et al.*, *Science* **321**, 1807–1812 (2008).
4. N. Navin *et al.*, *Nature* **472**, 90–94 (2011).
5. M. Gerlinger *et al.*, *N. Engl. J. Med.* **366**, 883–892 (2012).
6. G. Driessens, B. Beck, A. Caauwe, B. D. Simons, C. Blanpain, *Nature* **488**, 527–530 (2012).
7. A. G. Schepers *et al.*, *Science* **337**, 730–735 (2012).
8. P. L. Bedard, A. R. Hansen, M. J. Ratain, L. L. Siu, *Nature* **501**, 355–364 (2013).
9. R. Stupp *et al.*, *N. Engl. J. Med.* **352**, 987–996 (2005).
10. A. Sottoriva *et al.*, *Proc. Natl. Acad. Sci. U.S.A.* **110**, 4009–4014 (2013).
11. J. M. Stommel *et al.*, *Science* **318**, 287–290 (2007).
12. D. A. Nathanson *et al.*, *Science* **343**, 72–76 (2014).
13. M. R. Gilbert *et al.*, *N. Engl. J. Med.* **370**, 699–708 (2014).
14. C. E. Meacham, S. J. Morrison, *Nature* **501**, 328–337 (2013).
15. S. K. Singh *et al.*, *Nature* **432**, 396–401 (2004).
16. J. Chen *et al.*, *Nature* **488**, 522–526 (2012).
17. Z. Li *et al.*, *Cancer Cell* **15**, 501–513 (2009).
18. S. Bao *et al.*, *Nature* **444**, 756–760 (2006).
19. K. P. Bhat *et al.*, *Cancer Cell* **24**, 331–346 (2013).
20. C. W. Brennan *et al.*, *Cell* **155**, 462–477 (2013).
21. R. G. Verhaak *et al.*, *Cancer Cell* **17**, 98–110 (2010).
22. D. Ramsköld *et al.*, *Nat. Biotechnol.* **30**, 777–782 (2012).
23. A. K. Shalek *et al.*, *Nature* **498**, 236–240 (2013).
24. Materials and methods are available as supplementary materials on *Science* Online.
25. J. Lonsdale *et al.*, *Nat. Genet.* **45**, 580–585 (2013).
26. N. Novershtern *et al.*, *Cell* **144**, 296–309 (2011).
27. J. Lee *et al.*, *Cancer Cell* **9**, 391–403 (2006).
28. H. Wakimoto *et al.*, *Neuro-Oncol.* **14**, 132–144 (2012).
29. T. F. Cloughesy, W. K. Cavenee, P. S. Mischel, *Annu. Rev. Pathol.* **9**, 1–25 (2014).
30. M. Snuderl *et al.*, *Cancer Cell* **20**, 810–817 (2011).
31. B. D. Choi *et al.*, *Proc. Natl. Acad. Sci. U.S.A.* **110**, 270–275 (2013).
32. H. Wang *et al.*, *Neoplasia* **13**, 461–471 (2011).
33. J. Xu *et al.*, *Sci Rep* **4**, 4223 (2014).
34. M. S. Cho *et al.*, *Cell Reports* **6**, 1085–1095 (2014).
35. L. Sang, H. A. Coller, J. M. Roberts, *Science* **321**, 1095–1100 (2008).
36. K. O. Shostak *et al.*, *J. Surg. Oncol.* **82**, 57–64 (2003).
37. A. Roesch *et al.*, *Cell* **141**, 583–594 (2010).
38. L. Ricci-Vitiani *et al.*, *Nature* **468**, 824–828 (2010).
39. R. Wang *et al.*, *Nature* **468**, 829–833 (2010).
40. Y. Soda *et al.*, *Proc. Natl. Acad. Sci. U.S.A.* **108**, 4274–4280 (2011).
41. B. Martynoga *et al.*, *Genes Dev.* **27**, 1769–1786 (2013).
42. M. L. Suvà *et al.*, *Cell* **157**, 580–594 (2014).
43. H. Noushmehr *et al.*, *Cancer Cell* **17**, 510–522 (2010).

ACKNOWLEDGMENTS

We thank E. Shefler for project management, E. Rheinbay for graphical contributions, J. Kim and P. Santos for histology, and P. Bautista and Y. Yagi for slide scanning. A.P.P was supported by NIH– National Institute of Neurological Disorders and Stroke R25NS065743. I.T. was supported by a Human Frontier Science Program fellowship and a Rothschild fellowship. M.L.S was supported by a grant from Medic Foundation. This research was supported by funds from Howard Hughes Medical Institute, Burroughs Wellcome Fund, Harvard Stem Cell Institute, NIH (R01 NS032677 to R.L.M. and U24 CA180922 to A.R.), National Brain Tumor Society, and Klarman Family Foundation. A.R. is a scientific advisory board member for Syros Pharmaceuticals and a consultant for Cancer Therapeutics Innovation Group. B.E.B. is a scientific advisory board member for Syros Pharmaceuticals and a founder and scientific advisor for HiFiBio SAS. RNA-seq data are deposited in Gene Expression Omnibus with accession no. GSE57872.

SUPPLEMENTARY MATERIALS

www.sciencemag.org/content/344/6190/1396/suppl/DC1
Materials and Methods
Tables S1 to S3
Figs. S1 to S23
References (*44*–*48*)

2 April 2014; accepted 30 May 2014
Published online 12 June 2014;
10.1126/science.1254257

HIV PATHOGENESIS

HIV-1–induced AIDS in monkeys

Theodora Hatziioannou,[1]* Gregory Q. Del Prete,[2] Brandon F. Keele,[2] Jacob D. Estes,[2] Matthew W. McNatt,[1,3] Julia Bitzegeio,[1,3] Alice Raymond,[1] Anthony Rodriguez,[1] Fabian Schmidt,[1,3] C. Mac Trubey,[2] Jeremy Smedley,[4] Michael Piatak Jr.,[2] Vineet N. KewalRamani,[5]* Jeffrey D. Lifson,[2]* Paul D. Bieniasz[1,3,6]*

Primate lentiviruses exhibit narrow host tropism, reducing the occurrence of zoonoses but also impairing the development of optimal animal models of AIDS. To delineate the factors limiting cross-species HIV-1 transmission, we passaged a modified HIV-1 in pigtailed macaques that were transiently depleted of $CD8^+$ cells during acute infection. During adaptation over four passages in macaques, HIV-1 acquired the ability to antagonize the macaque restriction factor tetherin, replicated at progressively higher levels, and ultimately caused marked $CD4^+$ T cell depletion and AIDS-defining conditions. Transient treatment with an antibody to CD8 during acute HIV-1 infection caused rapid progression to AIDS, whereas untreated animals exhibited an elite controller phenotype. Thus, an adapted HIV-1 can cause AIDS in macaques, and stark differences in outcome can be determined by immunological perturbations during early infection.

In humans, HIV-1 replicates well, but like other primate lentiviruses, it encounters impediments to replication in atypical host species (*1*–*3*). This fact has limited the development of optimal animal models of AIDS (*4*, *5*). To delineate the requirements for primate lentivirus to colonize a divergent host and to aid development of better animal models of AIDS, we adapted HIV-1 to replicate efficiently and cause AIDS in a monkey species.

We inoculated pigtailed macaques (*Maccaca nemestrina*), which lack an HIV-1–restricting TRIM5 protein (*6*–*9*), with HIV-1 clones encoding SIV_{MAC} Vif (where SIV is simian immunodeficiency virus), which antagonizes several macaque APOBEC3 proteins that would otherwise restrict HIV-1 replication (*10*) (see supplementary materials and methods). The inoculum contained four clonal HIV-1_{NL4-3}–derived viruses, each encoding a gp120 envelope protein from a prototype HIV-1 strain that uses the CCR5 coreceptor (Fig. 1A and fig. S1). In two passage-1 (P1) animals, acute plasma viremia reached ~10^5 viral RNA (vRNA) copies/ml and declined thereafter (Fig. 1B). This outcome was similar to our previous findings with an HIV-1 derivative encoding an envelope protein (KB9) that primarily uses CXCR4 (*11*). One P1 animal (P1-A), in which viremia of ~10^3 vRNA copies/ml was maintained for 32 weeks (Fig. 1B), was treated with a monoclonal antibody to deplete $CD8^+$ T cells (anti-CD8) to relieve immune pressure and thereby increase the viral population size. This animal's blood was used to initiate P2 infection (Fig. 1, A and B, and fig. S2). For P2 and each passage thereafter, we treated recipient animals with anti-CD8, at the time of inoculation and 1 week later, to augment early viremia (*12*). This treatment caused transient $CD8^+$ T cell depletion in blood and lymph nodes, without major impact on $CD8^+$ T cells in gut-associated lymphoid tissue (GALT) (figs. S2 and S3). In P2-A, acute viremia reached 10^6 vRNA copies/ml, declining to ~10^4 vRNA copies/ml at 5 to 6 weeks after infection (Fig. 1B). In P1 and P2 animals, the levels of blood $CD4^+$ T cells appeared unperturbed (Fig. 2A).

We inoculated animal P3-A with blood taken from P2-A at 23 weeks postinfection, whereas animal P3-B was inoculated with blood taken 1 week later, after $CD8^+$ cell depletion of P2-A (Fig. 1, A and B). P3 recipients exhibited acute viremia at ~10^6 to 10^7 vRNA copies/ml. Blood $CD4^+$ T cell numbers and the proportion of $CD4^+$ T cells in GALT decreased after infection (Fig. 2, A and B), but these perturbations were transient or modest in magnitude. Moreover, viremia declined over the ensuing 50 to 60 weeks (Fig. 1B). We depleted $CD8^+$ cells in P3 macaques on three subsequent occasions (fig. S2). Although transient increases in plasma viremia followed antibody administration (Fig. 1B), neither animal exhibited disease.

We inoculated P4 animals with blood taken from either or both P3 macaques at 50 weeks postinfection (Fig. 1, A and B). Each developed acute viremia at ~10^6 to 10^7 vRNA copies/ml (Fig. 1B). Notably, marked and sustained $CD4^+$ T cell depletion occurred in the blood of two out of three P4 animals and in the GALT of all P4 animals (Fig. 2, A to C). Additional indications of HIV-1–induced pathogenesis included immune activation, as evidenced by more frequent Ki67 expression in GALT $CD4^+$ cells (fig. S4A), as well as fibrotic disruption and frequent Ki67 expression in T cell zones of

[1]Aaron Diamond AIDS Research Center, 455 First Avenue, New York, NY 10016, USA. [2]AIDS and Cancer Virus Program, Leidos Biomedical Research, Frederick National Laboratory, Frederick, MD 21702, USA. [3]Laboratory of Retrovirology, The Rockefeller University, 455 First Avenue, New York, NY 10016, USA. [4]Laboratory Animal Sciences Program, Leidos Biomedical Research, Frederick National Laboratory, Frederick, MD 21702, USA. [5]HIV Drug Resistance Program, National Cancer Institute, Frederick, MD 21702, USA. [6]Howard Hughes Medical Institute, 455 First Avenue, New York, NY 10016, USA.
***Corresponding author. E-mail: thatziio@adarc.org (T.H.); vineet.kewalramani@nih.gov (V.N.K.); lifsonj@mail.nih.gov (J.D.L.); pbienias@adarc.org (P.D.B.)**

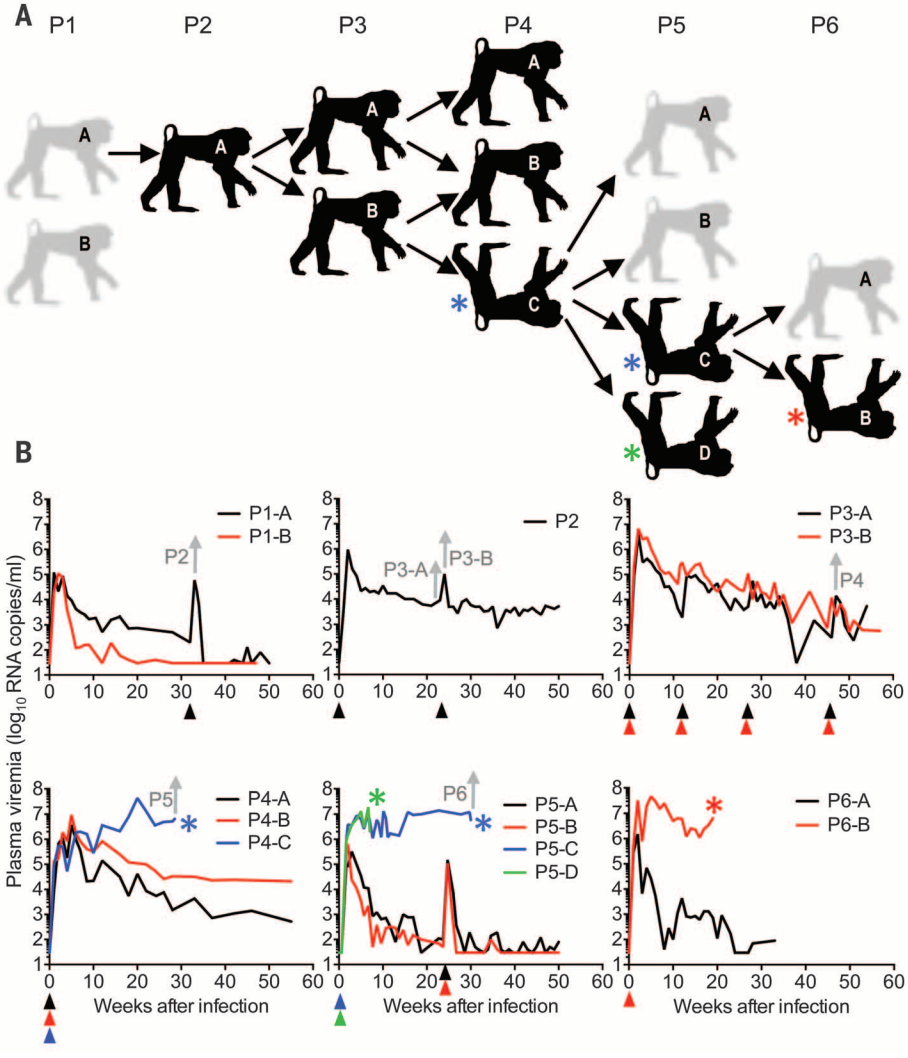

Fig. 1. Adaptation of HIV-1 to pigtail macaques. (**A**) Outline of serial animal-to-animal HIV-1 passages. Animals colored black were transiently depleted of $CD8^+$ cells at the time of inoculation. Inverted animals with colored asterisks indicate animals that were euthanized for clinical cause, including AIDS-defining conditions. (**B**) Viremia in the plasma of HIV-1–infected macaques. Color-coded arrowheads indicate anti-CD8 treatment, and asterisks indicate deaths [color code is the same for panel (A)]. Gray arrows indicate times at which blood was taken to initiate the subsequent passage.

lymph nodes (fig. S4, B to D). In P4-C, pathology was especially evident, and viremia continued to increase after the acute phase, approaching ~10^8 vRNA copies/ml (Fig. 1B). Loss of blood and GALT $CD4^+$ T cells in P4-C was virtually complete at 28 weeks (Fig. 2, A to C). At this point, P4-C succumbed to an AIDS-defining, multifocal extranodal B cell lymphoma with large retro-orbital and paraspinal tumors and extensive epicardial and renal involvement (Fig. 2D and fig. S5, A to C). Such tumors, associated with SIV-induced AIDS in macaques, have been linked to opportunistic lymphocryptoviruses or rhadinoviruses and are analogous to B cell neoplasms in humans coinfected with HIV-1 and Kaposi's sarcoma–associated herpesvirus (*13*). We also detected AIDS-defining *Pneumocystis* pneumonia in P4-C lung biopsies (Fig. 2E), but not in controls (fig. S6A).

To confirm that HIV-1 had adapted to replicate efficiently and cause AIDS in macaques, we inoculated four animals (P5-A-D) (Fig. 1A) with blood from P4-C. Two macaques that were transiently depleted of $CD8^+$ cells at inoculation (P5-C and P5-D) (Fig. 1A and fig. S2) developed persistently high viremia (~10^7 vRNAcopies/ml) with blood and GALT $CD4^+$ T cell depletion (Figs. 1B and 2A). P5-C was euthanized at week 30 after infection, with *Pneumocystis* pneumonia (fig. S6B), whereas P5-D was euthanized at week 7 after onset of severe bilateral hind limb weakness with wasting. In P5-A and P5-B, which were not CD8-depleted, acute viremia reached ~10^6 vRNA copies/ml but was controlled thereafter (Fig. 1B). Blood and GALT $CD4^+$ T cells were depleted but recovered thereafter (Fig. 2, A and B). Subsequent $CD8^+$ cell depletion in P5-A and P5-B at week 23 (fig. S2) caused transient increases (10^3-fold) in viremia and blood $CD4^+$ cell depletion in P5-A, but did not recapitulate the effect of $CD8^+$ cell depletion during acute infection (Figs. 1B and 2A). Rather, as $CD8^+$ cells recovered in P5-A and P5-B, viremia and $CD4^+$ T cells returned to predepletion levels (Figs. 1B and 2A).

This dichotomous outcome of HIV-1 infection was reproduced in animals that received blood from P5-C. Specifically, P6-A (no CD8 depletion) showed acute viremia that was subsequently controlled with modest and transient GALT $CD4^+$ T cell depletion (Figs. 1, A and B, and 2, A and B). Conversely, in P6-B (CD8 depleted at infection) (fig. S2), viremia persisted at 10^6 to 10^7 vRNA copies/ml, while blood and GALT $CD4^+$ cells were nearly completely depleted (Figs. 1B and 2, A and B). P6-B was euthanized at 9 weeks with symptoms of nephropathy or glomerulonephritis (azotemia, hyperphosphatemia, hypoproteinemia, and anemia). Necropsy revealed myocardial fibrosis, lymphoid depletion with histiocytosis, and diffuse expansion of the glomerular mesangial matrix. Although not AIDS-defining, these conditions have frequently been described in human AIDS patients (*14*) and occasionally in SIV-infected macaques (*15*).

Single viral genome amplification and sequencing (SGA) (*16*–*18*) at various points during adaptation revealed that one envelope gene in the initial inoculum (AD8) dominated the viral population in P1-A and was the only strain detected in P2 to P6 (Fig. 3A). Env sequences in P2 to P6 macaques sampled over ~3.5 years exhibited only ~2% divergence from AD8. Additionally, although T cells constituted the dominant infected cell type in lymph nodes, the propensity of AD8 to infect macrophages in GALT was preserved throughout P3 to P6 (fig. S7, A to C). In P5-C, which succumbed

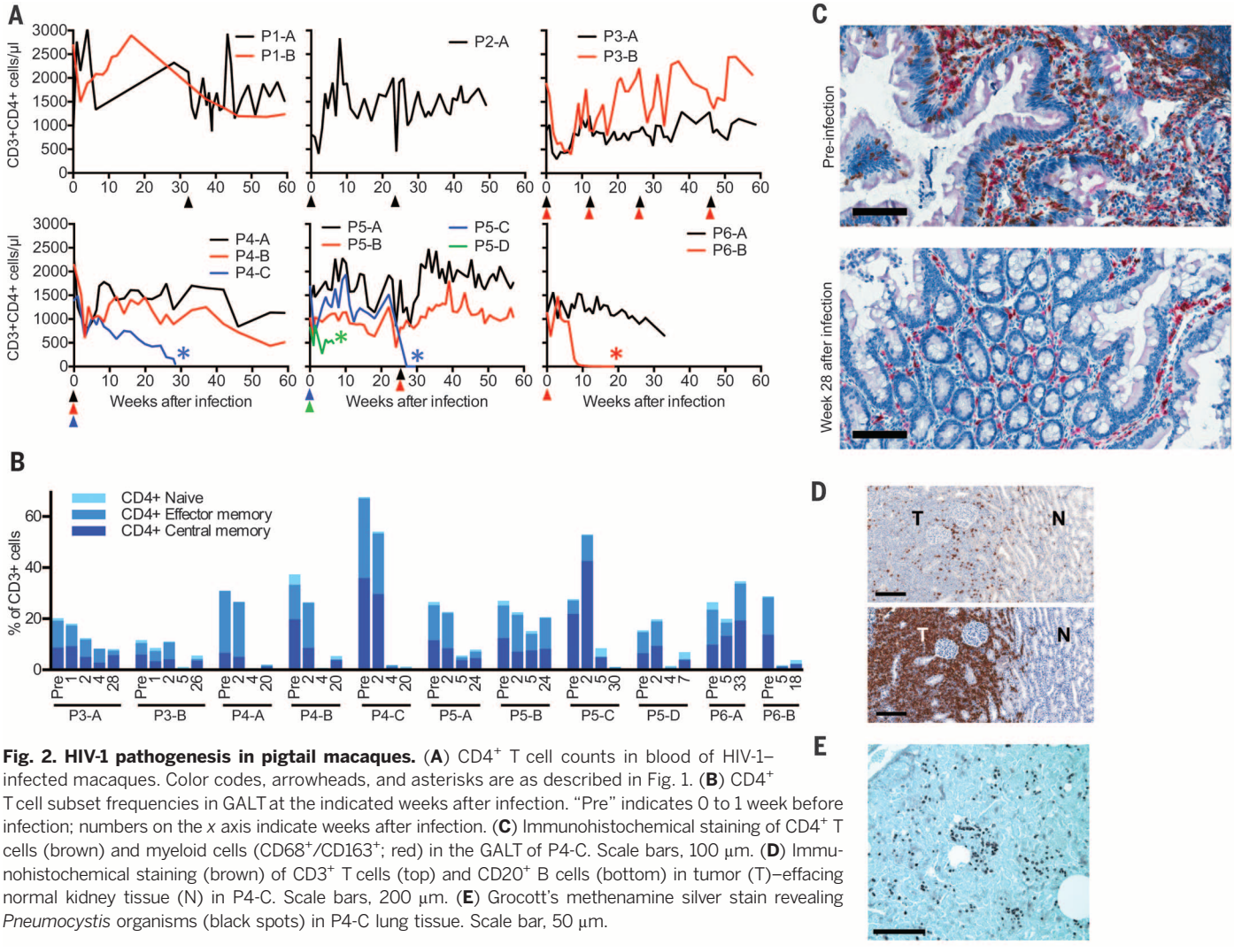

Fig. 2. HIV-1 pathogenesis in pigtail macaques. (**A**) $CD4^+$ T cell counts in blood of HIV-1–infected macaques. Color codes, arrowheads, and asterisks are as described in Fig. 1. (**B**) $CD4^+$ T cell subset frequencies in GALT at the indicated weeks after infection. "Pre" indicates 0 to 1 week before infection; numbers on the *x* axis indicate weeks after infection. (**C**) Immunohistochemical staining of $CD4^+$ T cells (brown) and myeloid cells ($CD68^+$/$CD163^+$; red) in the GALT of P4-C. Scale bars, 100 µm. (**D**) Immunohistochemical staining (brown) of $CD3^+$ T cells (top) and $CD20^+$ B cells (bottom) in tumor (T)–effacing normal kidney tissue (N) in P4-C. Scale bars, 200 µm. (**E**) Grocott's methenamine silver stain revealing *Pneumocystis* organisms (black spots) in P4-C lung tissue. Scale bar, 50 µm.

after a precipitous decline in blood CD4$^+$ T cells (Fig. 2A), about half of the envelope sequences had a four–amino acid deletion in the V3 loop (Fig. 3B), a determinant of co-receptor use (*19*). This deletion was associated with a change in co-receptor use, as evidenced by viral sensitivity to maraviroc (CCR5 antagonist) or AMD3100 (CXCR4 antagonist) (Fig. 3, C and D). Thus, HIV-1 infection in P5-C recapitulated a common feature of HIV-1 disease, namely co-receptor switching, that rarely occurs in non-human primate lentivirus infections (*20*). The V3 loop deletion associated with CXCR4 use was not detected in P6-A or P6-B, both of which received blood from P5-C.

Although the initial virus was not restricted by TRIM5α and APOBEC3, HIV-1 Vpu does not antagonize macaque tetherin, rendering the initial inoculum sensitive to this potential host-range restriction (*21*, *22*). Notably, an insertion of an amino acid at position 15 in the Vpu transmembrane (TM) domain (Fig. 4A) was detected in P1-A and was found in 100% of P2-A sequences at 52 weeks, and all sequences thereafter. Another Vpu TM mutation, V21G (Fig. 4A), was detected in P3 animals and in all sequences from P4 onward. TM domains govern Vpu-tetherin interaction (*21*), and each of the TM domain mutations contributed to

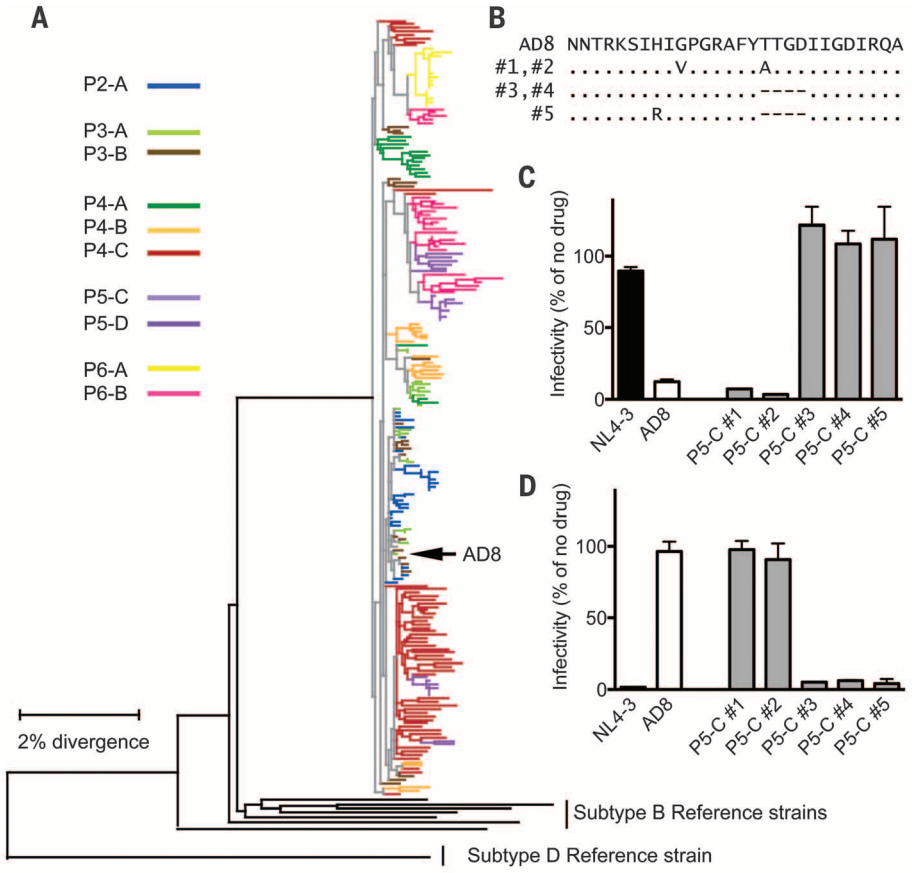

Fig. 3. Envelope evolution and co-receptor switching in HIV-1 infected macaques. (**A**) Phylogenetic analysis of Env sequences (using SGA and neighbor-joining method) found in plasma of HIV-1 infected macaques. (**B**) V3 loop amino acid sequences (*25*) from the AD8 inoculum and representative viral genomes in P5-C plasma at week 27 after infection. (**C** and **D**) Infectivity of HIV-1 ΔEnv–green fluorescent protein pseudotyped with control X4 (NL4-3), R5 (AD8), or P5-C–derived Env proteins in the presence of maraviroc (8 nM) (C) or AMD3100 (1 μM) (D) relative to no inhibitor. Values are mean ± SD (error bars) of three independent experiments.

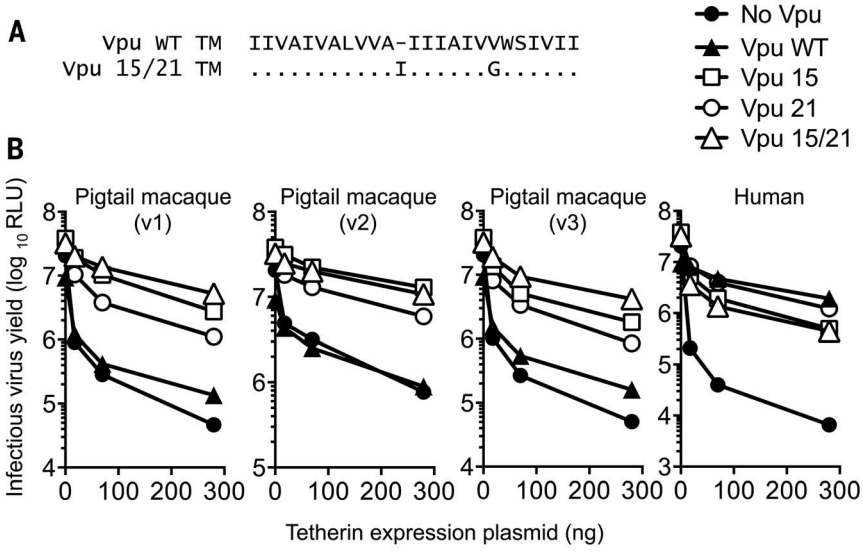

Fig. 4. Adaptation of HIV-1 Vpu to antagonize tetherin in macaques. (**A**) Amino acid alignment of the Vpu TM domain from the initial viral clone and after adaptation in pigtailed macaques. (**B**) Infectious virion yield from 293T cells transfected with HIV-1 proviral plasmids encoding the indicated Vpu proteins and plasmids expressing human or three naturally occurring variants (v1 to v3) of pigtailed macaque tetherin. RLU, relative light units.

the ability of Vpu 15/21 to antagonize pigtailed macaque tetherin (Fig. 4B). We previously showed that Vpu gained the ability to antagonize human tetherin during the emergence of HIV-1 in humans (*23*), and the passage of HIV-1 in pigtailed macaques apparently resulted in an analogous adaptation (Fig. 4B).

Beginning at week 4, antibodies to HIV-1 proteins were apparent in P4-A but were not detected until week 16 after infection in P4-B, which had higher viremia and some degree of blood $CD4^+$ T cell depletion (Figs. 1B and 2A and fig. S8). Animal P4-C, the first to succumb to AIDS, did not seroconvert (fig. S8). In fact, each macaque that progressed to AIDS after transient CD8 depletion did not seroconvert, whereas those that were not CD8 depleted and did not progress to AIDS mounted robust antibody responses (fig. S8). Previously, failure to seroconvert has been associated with rapid progression in SIV infection (*24*). HIV-1–induced loss of $CD4^+$ helper T cells in CD8-depleted animals may play a role in the failure to mount an antibody response in macaques that developed AIDS (*12*).

The approaches employed herein have enabled HIV-1 infection of macaques to recapitulate salient features of HIV-1 infection in humans. Our findings suggest that evasion or antagonism of antiretroviral proteins is key for the colonization of new hosts by primate lentiviruses. Because transient depletion of $CD8^+$ cells during acute infection determined whether macaques became rapid progressors or elite controllers, our findings suggest that the immunological insult during acute HIV-1 infection can determine the subsequent clinical course. It is also possible that adaptation to the host major histocompatibility complexes and evasion of adaptive immune responses may be required for HIV-1 pathogenesis in immunologically intact hosts. Finally, because the viral strain we used contains nearly all the targets of HIV-1 vaccines and drugs, further development of a pigtailed macaque–based model could facilitate the evaluation of new clinical HIV-1 therapies, prevention strategies, and interventions for virus eradication.

REFERENCES AND NOTES

1. D. Blanco-Melo, S. Venkatesh, P. D. Bieniasz, *Immunity* **37**, 399–411 (2012).
2. M. Stremlau *et al.*, *Nature* **427**, 848–853 (2004).
3. R. Mariani *et al.*, *Cell* **114**, 21–31 (2003).
4. Z. Ambrose, V. N. KewalRamani, P. D. Bieniasz, T. Hatziioannou, *Trends Biotechnol.* **25**, 333–337 (2007).
5. T. Hatziioannou, D. T. Evans, *Nat. Rev. Microbiol.* **10**, 852–867 (2012).
6. C. H. Liao, Y. Q. Kuang, H. L. Liu, Y. T. Zheng, B. Su, *AIDS* **21** (suppl. 8), S19–S26 (2007).
7. C. A. Virgen, Z. Kratovac, P. D. Bieniasz, T. Hatziioannou, *Proc. Natl. Acad. Sci. U.S.A.* **105**, 3563–3568 (2008).
8. G. Brennan, Y. Kozyrev, S. L. Hu, *Proc. Natl. Acad. Sci. U.S.A.* **105**, 3569–3574 (2008).
9. R. M. Newman *et al.*, *PLOS Pathog.* **4**, e1000003 (2008).
10. C. A. Virgen, T. Hatziioannou, *J. Virol.* **81**, 13932–13937 (2007).
11. T. Hatziioannou *et al.*, *Proc. Natl. Acad. Sci. U.S.A.* **106**, 4425–4429 (2009).
12. R. S. Veazey *et al.*, *J. Virol.* **82**, 5618–5630 (2008).
13. B. U. Orzechowska *et al.*, *Blood* **112**, 4227–4234 (2008).
14. T. K. Rao, *Annu. Rev. Med.* **42**, 391–401 (1991).
15. E. B. Stephens, C. Tian, Z. Li, O. Narayan, V. H. Gattone II, *J. Virol.* **72**, 8820–8832 (1998).
16. P. Simmonds, P. Balfe, C. A. Ludlam, J. O. Bishop, A. J. Brown, *J. Virol.* **64**, 5840–5850 (1990).
17. S. Palmer *et al.*, *J. Clin. Microbiol.* **43**, 406–413 (2005).
18. B. F. Keele *et al.*, *Proc. Natl. Acad. Sci. U.S.A.* **105**, 7552–7557 (2008).
19. H. Choe *et al.*, *Cell* **85**, 1135–1148 (1996).
20. S. T. Sina, W. Ren, C. Cheng-Mayer, *J. Transl. Med.* **9** (suppl. 1), S7 (2011).
21. M. W. McNatt *et al.*, *PLOS Pathog.* **5**, e1000300 (2009).
22. B. Jia *et al.*, *PLOS Pathog.* **5**, e1000429 (2009).
23. D. Sauter *et al.*, *Cell Host Microbe* **6**, 409–421 (2009).
24. V. M. Hirsch *et al.*, *J. Virol.* **78**, 275–284 (2004).
25. Single-letter abbreviations for the amino acid residues are as follows: A, Ala; C, Cys; D, Asp; E, Glu; F, Phe; G, Gly; H, His; I, Ile; K, Lys; L, Leu; M, Met; N, Asn; P, Pro; Q, Gln; R, Arg; S, Ser; T, Thr; V, Val; W, Trp; and Y, Tyr.

ACKNOWLEDGMENTS

The data presented in this paper are tabulated in the main paper and in the supplementary materials. HIV-1 Env sequences used in Fig. 3 have been deposited in GenBank (accession numbers KJ201545 through KJ201764). Sequences encompassing the full-length viral genome for P5 and P6 have also been deposited in GenBank (accession numbers KJ767573 through KJ767592). This work was supported by NIH grants R37AI64003 and R01AI50111 (to P.D.B.) and R01AI078788 (to T.H.); Deutsche Forschungsgemeinschaft fellowship BI1540/1-1 (to J.B.); the Howard Hughes Medical Institute; and in part with federal funds from the National Cancer Institute, NIH, under contract no. HHSN261200800001E. We thank V. Coalter, A. Wiles, R. Wiles, and D. Johnson for assistance with study coordination and sample processing. Histology support was provided by the Pathology/Histotechnology Laboratory core service located at the Frederick National Laboratory for Cancer Research, Leidos Biomedical Research, Frederick, MD. The content of this publication does not necessarily reflect the views or policies of the Department of Health and Human Services, nor does mention of trade names, commercial products, or organizations imply endorsement by the U.S. government.

SUPPLEMENTARY MATERIALS

www.sciencemag.org/content/344/6190/1401/suppl/DC1
Materials and Methods
Figs. S1 to S8
References (*26*–*30*)

13 January 2014; accepted 16 May 2014
10.1126/science.1250761

TOXIN MECHANISM

Molecular basis for disruption of E-cadherin adhesion by botulinum neurotoxin A complex

Kwangkook Lee,[1] Xiaofen Zhong,[2] Shenyan Gu,[1] Anna Magdalena Kruel,[3] Martin B. Dorner,[4] Kay Perry,[5] Andreas Rummel,[3] Min Dong,[2] Rongsheng Jin[1]*

How botulinum neurotoxins (BoNTs) cross the host intestinal epithelial barrier in foodborne botulism is poorly understood. Here, we present the crystal structure of a clostridial hemagglutinin (HA) complex of serotype BoNT/A bound to the cell adhesion protein E-cadherin at 2.4 angstroms. The HA complex recognizes E-cadherin with high specificity involving extensive intermolecular interactions and also binds to carbohydrates on the cell surface. Binding of the HA complex sequesters E-cadherin in the monomeric state, compromising the E-cadherin–mediated intercellular barrier and facilitating paracellular absorption of BoNT/A. We reconstituted the complete 14-subunit BoNT/A complex using recombinantly produced components and demonstrated that abolishing either E-cadherin– or carbohydrate-binding of the HA complex drastically reduces oral toxicity of BoNT/A complex in vivo. Together, these studies establish the molecular mechanism of how HAs contribute to the oral toxicity of BoNT/A.

Botulinum neurotoxin serotype A (BoNT/A) (~150 kD) is produced in *Clostridium botulinum* and, together with the nontoxic non-hemagglutinin (NTNHA) protein and three hemagglutinins (HAs) (HA70, HA33, and HA17, also known as HA3, HA1, and HA2, respectively), forms a large protein complex (*1*, *2*). NTNHA protects BoNT/A from host gastrointestinal destruction by forming a minimally functional progenitor toxin complex (M-PTC) (~290 kD) (*3*). M-PTC associates with the HAs to form the large PTC (L-PTC) (~760 kD), which exhibits up to 30-fold greater oral toxicity (*4*–*6*). Therefore, HAs are critical virulence factors that contribute to the extreme oral toxicity of BoNT/A (*7*–*10*). The HAs of BoNT/A (HA/As) assemble into a threefold symmetric hetero-dodecameric complex containing three HA70, three HA17, and six HA33 (~470 kD). The fully assembled HA complex has nine carbohydrate-binding sites, which function by enriching the L-PTC onto cell surfaces in the intestine (Fig. 1A and fig. S1A) (*9*, *11*). Additional interactions of HAs with the cell-adhesion

[1]Department of Physiology and Biophysics, University of California, Irvine, CA 92697, USA. [2]Department of Microbiology and Immunobiology, Harvard Medical School, Division of Neuroscience, New England Primate Research Center, Southborough, MA 01772, USA. [3]Institut für Toxikologie, Medizinische Hochschule Hannover, Carl-Neuberg-Strasse 1, 30625 Hannover, Germany. [4]Centre for Biological Threats and Special Pathogens–Biological Toxins (ZBS3), Robert Koch-Institut, Nordufer 20, 13353 Berlin, Germany. [5]Northeastern Collaborative Access Team (NE-CAT) and Department of Chemistry and Chemical Biology, Cornell University, Building 436E, Argonne National Laboratory, 9700 S. Cass Avenue, Argonne, IL 60439, USA.
***Corresponding author. E-mail: r.jin@uci.edu**

protein E-cadherin have been reported for the closely related HAs of BoNT serotype B (HA/Bs) (*12*), but the molecular mechanism by which HAs exploit E-cadherin and the physiological relevance of this interaction in vivo remain poorly defined.

We found that the binding of HA/As to the well-characterized human colorectal adenocarcinoma HT29 cells was greatly reduced when endogenous E-cadherin was knocked down, indicating that the cell-surface binding of HA/As requires E-cadherin (Fig. 1B and fig. S1B). To distinguish E-cadherin binding versus carbohydrate binding, we next tested two HA complexes with point mutations that abolish their ability to bind carbohydrates (HA/A$^{33\text{-}D263A/F278A}$ and HA/A$^{70\text{-}T527P/R528A}$, hereinafter referred to as HA$^{33\text{-}DAFA}$ and HA$^{70\text{-}TPRA}$) (Single-letter abbreviations for the amino acid residues are as follows: A, Ala; C, Cys; D, Asp; E, Glu; F, Phe; G, Gly; H, His; I, Ile; K, Lys; L, Leu; M, Met; N, Asn; P, Pro; Q, Gln; R, Arg; S, Ser; T, Thr; V, Val; W, Trp; and Y, Tyr. In the mutants, other amino acids were substituted at certain locations; for example, D263A indicates that aspartic acid at position 263 was replaced by alanine) (*9*). Binding of these two HA mutants to HT29 cells was similar to that of the wild-type HA complex (HA-WT), further supporting that E-cadherin is largely responsible for the observed cell-surface binding of HAs (Fig. 1C).

Binding of HAs to cells induces disruption of cell-cell adhesions. This may create a paracellular route for absorption of BoNTs across the intestinal epithelial barriers (*12*). Indeed, we observed that binding of HA-WT to HT29 cells for 24 hours severely disrupted cell-cell adhesions, shown by separation of cells (Fig. 1D). Consistent with their ability to bind HT29 cells, the two carbohydrate-binding–deficient mutant HA complexes were still capable of disrupting cell-cell junctions of HT29 cells within 24 hours. Thus, carbohydrate binding is not essential for the HA complex to disrupt cell-cell junctions under these experimental conditions. On the other hand, experiments with a much shorter incubation time (150 min) revealed that the two carbohydrate-binding–deficient HA complexes disrupted cell-cell junctions much less than HA-WT did (fig. S1, C and D), suggesting that carbohydrate binding might enhance disrupting cell-cell junctions, likely by enriching the HA complexes onto cell surfaces and increasing the overall binding avidity. Similar results on cell-surface binding of HA/As and HA-induced cell-cell dissociation were observed on Caco-2 cells, another well-established human epithelial colorectal adenocarcinoma cell line (fig. S2).

How HAs recognize E-cadherin is not known. The ectodomain of E-cadherin mediates self-assembly in adherens junctions, which are crucial intercellular structures maintaining physical association between parallel apposed cells (*13*–*15*). E-cadherin consists of five tandem extracellular cadherin (EC) domains (EC1 to EC5) (*16*), and the most amino-terminal EC1–EC2 domain binds to HA/Bs (*12*). We found that the EC1–EC2 of E-cadherin also binds to HA/As with a dissociation constant (K_d) of ~2.3 μM and 3:1 stoichiometry, indicating that each of the three arms of the HA complex likely binds one E-cadherin (fig. S3A). Consistent with this finding, a monomeric HA subcomplex (mini-HA), which represents one of the three identical arms of the HA complex comprising the D3 domain of HA70/A (HA70^{D3}, residues Pro^{378} to Asn^{626}), HA17/A, and two HA33/A (Fig. 1A), is sufficient to bind EC1–EC2 in a 1:1 ratio (fig. S3B). The binding affinity of EC1–EC2 to the mini-HA complex (K_d ~ 2.7 μM) is similar to that of the three-arm HA complex, indicating that the mini-HA complex is the minimum E-cadherin–binding unit.

To understand the molecular mechanism underlying the HA–E-cadherin interaction, we determined a 2.4 Å–resolution crystal structure of the mini-HA complex bound to EC1–EC2 of mouse E-cadherin (Fig. 2, A and B, and table S1). Two sets of nearly identical heteropentameric complexes are observed in the asymmetric unit [root mean square deviation (RMSD) ~1.01 Å over 1149 Cα pairs], in which EC1–EC2 binds to HA70^{D3}, HA17, and one of the two HA33. No conformational change is observed for the mini-HA complex upon E-cadherin binding (*9*). The EC1 and EC2 domains each adopt a seven-stranded β-barrel fold and are connected by a short linker that is maintained in a rigid conformation by the interactions with three calcium atoms (Fig. 2, A and B). Superimposing HA-bound EC1–EC2 to the structure of mouse E-cadherin EC1–EC5 (*15*) (RMSD ~1.57 Å for 206 Cα pairs) shows that the EC3–EC5 extends away from the HA complex (*9*) and thus is dispensable for HA binding.

Large conformational changes are observed in the amino-terminal region of EC1 upon HA binding (Fig. 2C). EC1 dimerizes in trans with EC1 of E-cadherin from apposing cells (*16*). Specifically, residue Trp^{2} acts as an anchor docking into a complementary Trp-binding pocket in the partner

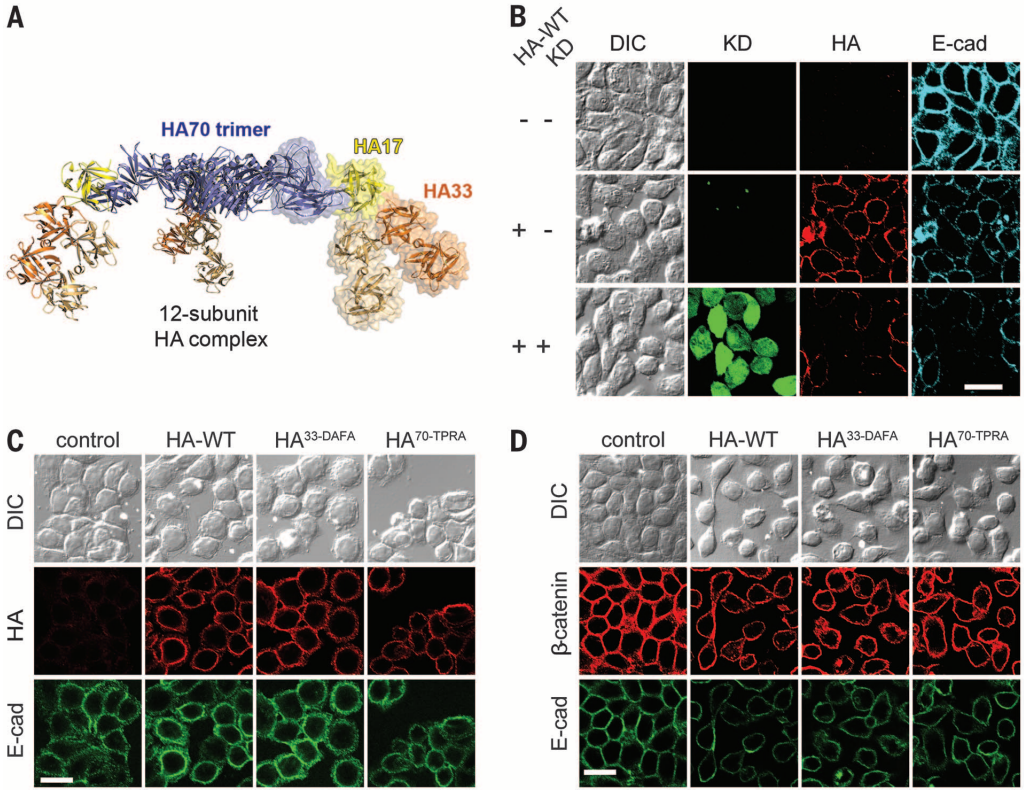

Fig. 1. The HA complex binds to E-cadherin and disrupts cell-cell adhesion. (**A**) Structural presentation of the HA complex comprising three HA70 (blue), three HA17 (yellow), and six HA33 (orange) (*9*). The moiety of the mini-HA complex is shown as a transparent surface representation. (**B**) Knocking down E-cadherin (E-cad) in HT29 cells via a lentivirus–mediated shRNA expression reduced cell binding of the HA complex (25 nM, 90 min). Lenti-shRNA–infected cells were marked with green fluorescent protein. KD, knockdown. (**C**) Binding of HA-WT, HA$^{33\text{-}DAFA}$, and HA$^{70\text{-}TPRA}$ complexes to HT29 cells (10 nM, 30 min). (**D**) HA-WT, HA$^{33\text{-}DAFA}$, and HA$^{70\text{-}TPRA}$ all disrupted cell-cell adhesion in HT29 cells (10 nM, 24 hours), marked by the separation of cells in both differential interference contrast images (top) and immunofluorescence images of E-cadherin (bottom) and β-catenin (middle). Scale bar, 20 μm.

E-cadherin molecule (*14*, *15*, *17*, *18*), leading to a three-dimensional domain swap within an E-cadherin homodimer (*19*). Using analytical ultracentrifugation, we found that EC1–EC2 forms a dimer in solution with a K_d of ~175.2 μM, which is consistent with previous reports (*15*, *20*) but is markedly weaker than its binding affinity to the HA complex.

Strand-swapping in EC1 is believed to be driven by conformational strain in its first 10 amino-terminal residues (termed the A*/A strand), which only arises in its monomeric form (*21*). Upon HA binding, the A*/A strand of E-cadherin is pushed back to its monomeric conformation through hydrogen bond interactions between Ser^{8}/$Pro^{6\text{-E-cad}}$ and Glu^{501}/$Arg^{505\text{-HA70}}$. This conformation is further stabilized by hydrophobic interactions involving Ile^{417}/Leu^{473}/$Met^{508\text{-HA70}}$ and Val^{3}/Pro^{5}/$Pro^{6\text{-E-cad}}$, whereas Pro^{5}/$Pro^{6\text{-E-cad}}$ serves as a hinge that mediates conformational changes necessary for strand swapping (Fig. 2, C and D, and fig. S4) (*14*). Therefore, the HA complex stabilizes E-cadherin in the strained monomeric conformation with Trp^{2} binding intramolecularly into its own Trp-binding pocket (Fig. 2C and fig. S4A). Meanwhile, it physically blocks the E-cadherin trans dimerization by occupying the E-cadherin dimer interface (Fig. 2E). Moreover, the HA complex also prevents E-cadherin from forming the X-dimer, which is a dimeric intermediate required for the formation of the strand-swapped trans dimer (Fig. 2F) (*14*, *22*).

Complementing the HA70–EC1 interactions, HA17 interacts with both EC1 and EC2, as well as the Ca^{2+}-binding linker (Fig. 2 and fig. S4D), and one HA33 buries a small hydrophobic interface with EC1. The HA–E-cadherin interaction was abolished when Ca^{2+} was chelated by ethylenediaminetetraacetic acid (EDTA) (fig. S3C) (*12*), suggesting that the intertwined interactions among three HAs and two EC domains rely on Ca^{2+}-coordination in the EC1–EC2 linker that fixes the relative positioning of the two EC domains. This binding mode contrasts the listerial protein internalin (InlA), which only binds to EC1 in a one-on-one manner (*23*). Because E-cadherin's adhesive function depends on Ca^{2+}-rigidified connections between successive EC domains (*14*), this is yet another example of a pathogen hijacking host cellular function.

To fine-map the HA–E-cadherin binding specificity, we examined binding of the carbohydrate-binding–deficient $HA^{33\text{-DAFA}}$ complex to wild-type or mutant mouse E-cadherin ectopically expressed in Chinese hamster ovary (CHO) or human embryonic kidney (HEK) 293 cells, which physiologically do not express E-cadherin (Fig. 3A and fig. S5). The exogenous, wild-type E-cadherin mediated robust binding of the $HA^{33\text{-DAFA}}$ complex to transfected cells, which further demonstrates their direct interaction (Fig. 3A). When key HA-binding residues on E-cadherin conserved across different species were mutated (for example, K14S and Q23A), the cell-surface binding of the $HA^{33\text{-DAFA}}$ complex was greatly diminished (Fig. 3A). Residues Lys^{19} and Asn^{20} of mouse E-cadherin contribute crucial interactions with HA70, which are likely weakened by their equivalent residues on rat (Gln^{19} and Arg^{20}) or chicken (Met^{19} and Arg^{20}) (fig. S4, B and C). We found that mutating these two residues (for example, K19M or N20R) clearly reduced binding of the $HA^{33\text{-DAFA}}$ complex onto cell surfaces (Fig. 3A). Consistently, the mini-HA-WT complex did not bind EC1–EC2 that carried these E-cadherin mutants (fig. S6A). These mutagenesis studies further confirm the physiological relevance of the HA–E-cadherin interactions observed in the crystal structure.

In contrast to carbohydrate-binding–deficient $HA^{33\text{-DAFA}}$ mutant, the HA-WT complex was still able to bind to cells that expressed E-cadherin mutants tested above (fig. S5, B and D). This suggests that the ability of HA-WT complex to bind carbohydrates enhances the overall binding

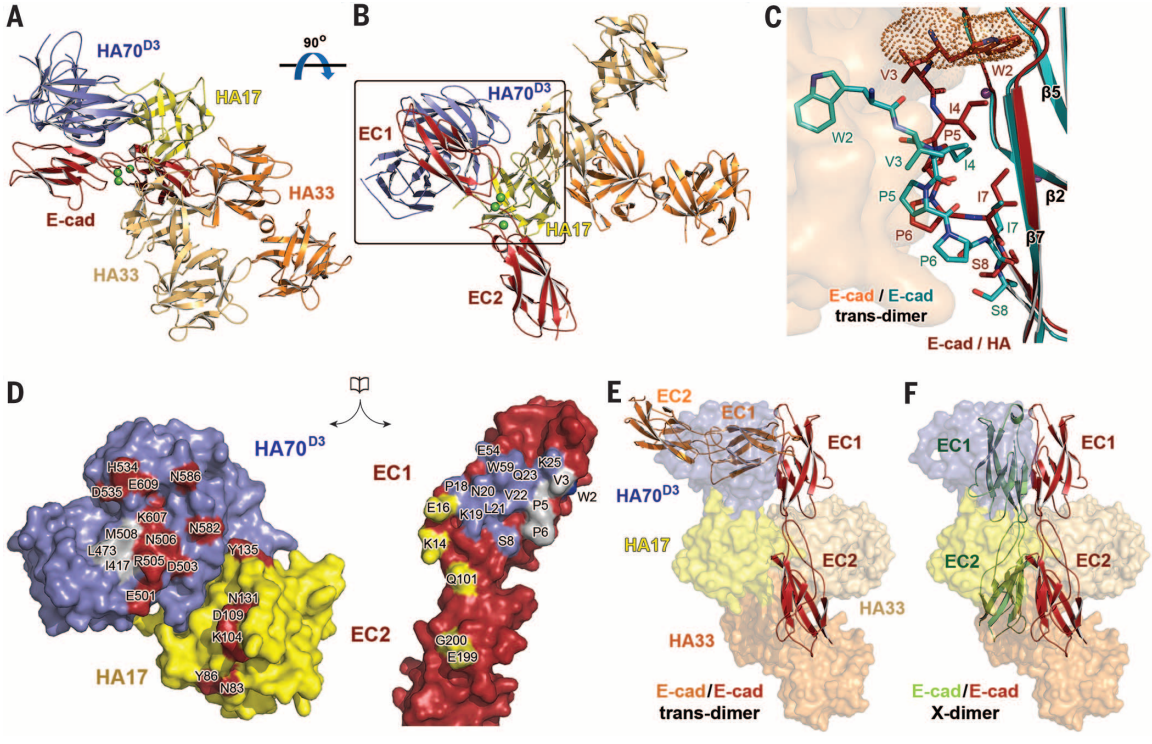

Fig. 2. Structure of the HA–E-cadherin complex. (**A**) Structure of EC1–EC2 (red) bound to the mini-HA complex. Three E-cadherin–bound calcium atoms are depicted as green balls. The view direction is similar to that shown in Fig. 1A. (**B**) A 90° rotation of the complex about a horizontal axis. (**C**) The HA-bound E-cadherin (red) is superimposed with an E-cadherin (light blue) in the context of a trans dimer (its binding partner is shown as a surface representation). Large conformational changes are observed in the amino terminus of EC1 (residues 2 to 8 are shown as sticks). The residue Trp^{2} of the HA-bound E-cadherin occupies a pocket that otherwise accommodates the swapped Trp^{2} (dots representation) of its dimeric binding partner. (**D**) An open-book view of the $HA70^{D3}$/HA17–E-cadherin interface highlighted in the box in (B). HA33 is omitted for clarity. Residues on HA70/17 that form hydrogen bonds or salt bridges with E-cadherin are red, whereas the E-cadherin residues that bind to HA70 and HA17 are blue and yellow, respectively. Residues involved in hydrophobic interaction are in gray. (**E** and **F**) The mini-HA complex is shown as a transparent surface representation. When an E-cadherin molecule is modeled to form a trans dimer [(E), orange ribbon] or an X-dimer [(F), green ribbon] with a HA-bound E-cadherin (red ribbon), it severely clashes with the HA complex.

avidity of the HA complex to cells, which compensates for the reduced binding to E-cadherin mutants. E-cadherin is known to be glycosylated, but the O-linked carbohydrates observed in the structure of mouse EC1–EC5 are distant from the carbohydrate-binding sites on HAs; the shortest distances are ~62 Å and ~69 Å to HA70 and HA33, respectively (*15*). Indeed, a low-level binding of HA-WT to untransfected CHO or HEK293 cells was mediated by carbohydrates because such binding was not detected for $HA^{33\text{-}DAFA}$ (Fig. 3A and fig. S5).

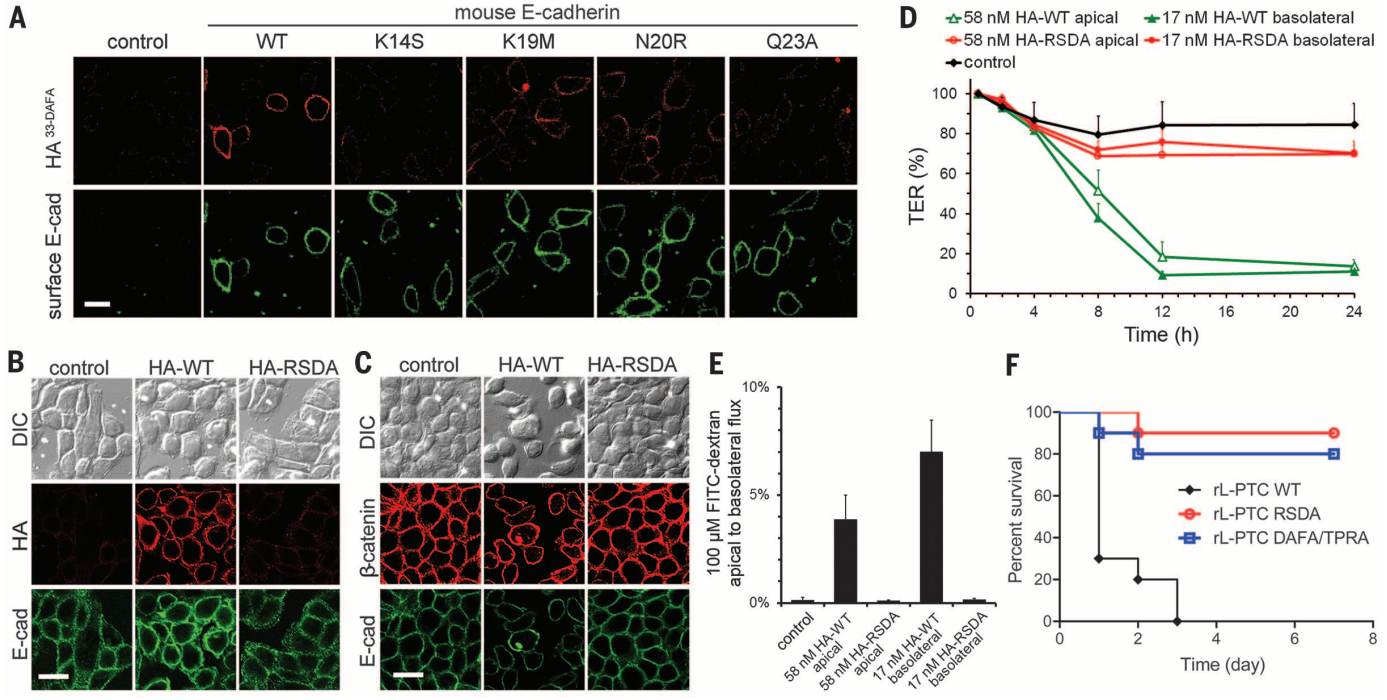

Fig. 3. The HA complex recognizes E-cadherin with high specificity to disrupt cell-cell adhesion. (**A**) Binding of the $HA^{33\text{-}DAFA}$ complex to the surface of CHO cells overexpressing WT or mutant E-cadherin as indicated. (**B**) Binding of HA-WT or HA-RSDA to HT29 cells (10 nM, 30 min). (**C**) HA-RSDA failed to disrupt cell-cell adhesions (10 nM, 24 hours). Scale bar, 20 μm. (**D**) TER of polarized Caco-2 monolayers was measured after application of HA-WT or HA-RSDA ($n \geq 3$ independent experiments + SD). (**E**) In contrast to HA-WT, HA-RSDA could not facilitate the flux of FITC-dextran from apical to basolateral compartment ($n \geq 3$ independent experiments +SD). (**F**) Survival of ten mice (combination of two experiments with five mice each) after being given by intragastric gavage the reconstituted wild-type L-PTC (rL-PTC WT), rL-PTC RSDA that contains the E-cadherin–binding deficient HAs, or rL-PTC DAFA/TPRA that contains the carbohydrate-binding deficient HAs.

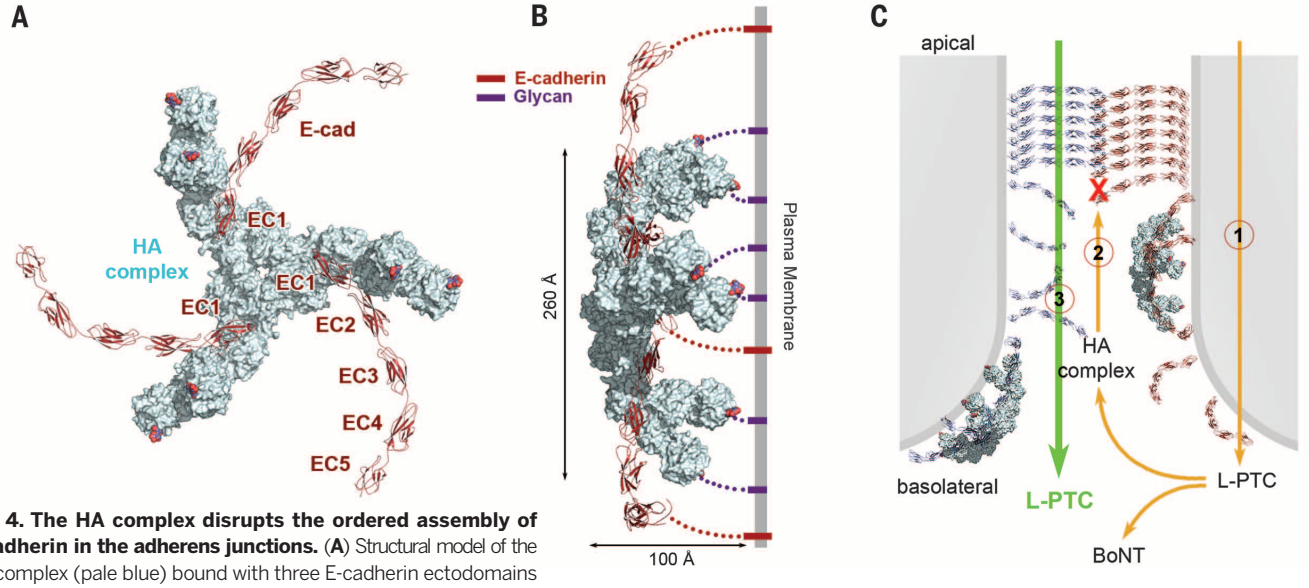

Fig. 4. The HA complex disrupts the ordered assembly of E-cadherin in the adherens junctions. (**A**) Structural model of the HA complex (pale blue) bound with three E-cadherin ectodomains (red). The lactose molecules bound to HA33 are in sphere models (*9*). (**B**) Proposed binding mode of the HA complex on the cell surface in adherens junctions, viewed along the proposed plane of the membrane. The HA complex could simultaneously bind to membrane-anchored E-cadherin and carbohydrates. (**C**) Proposed model for transepithelial delivery of the L-PTC. A small amount of L-PTC first crosses epithelial cells by means of transcytosis (1). On basolateral side, the HA complex binds to E-cadherin and carbohydrates and disrupts cell-to-cell adhesion (2). Last, more L-PTCs are absorbed via the paracellular route (3).

Sequence alignment reveals that all the E-cadherin–binding residues on HA70 and HA17 are conserved between the HAs of BoNT/A and BoNT/B that mediate foodborne botulism in humans, but few are conserved on HAs of BoNT serotypes C and D (HA/C and HA/D), which predominantly cause botulism in birds and cattle. As predicted by our structure, mutating an E-cadherin–binding residue strictly conserved across HA/A–HA/D, such as $D109A^{HA17/A}$, abolished its interaction with mouse E-cadherin because of the loss of an intermolecular salt bridge (fig. S6B). $Arg^{505\text{-}HA70/A}$, $Asn^{586\text{-}HA70/A}$, and $Lys^{104\text{-}HA17/A}$ bind to mouse E-cadherin, but the corresponding residues of HA/C and HA/D (Ser, Tyr, and Ile, respectively) are unlikely to mediate binding. Mutating residue $Arg^{505\text{-}HA70/A}$, which is crucial for binding and stabilization of the A*/A strand of E-cadherin in the monomeric form, to a serine ($R505S^{HA70/A}$) diminished the binding of the HA complex to mouse E-cadherin (fig. S6B). These data might explain why BoNT/C and BoNT/D have hardly caused human foodborne botulism. However, some E-cadherin residues (such as Ser^{8}, Glu^{54}, and Gln^{101})—which favorably bind to HA/A–HA/B–like residues, but not the HA/C–HA/D–like residues—are also conserved in chicken and bovine that are susceptible to BoNT/C and BoNT/D. Therefore, although the HA–E-cadherin binding mode is likely conserved in HA/A and HA/B, it is unclear whether or how HA/C and HA/D might act through E-cadherin.

On the basis of the structural analysis, we created a specific mutant HA complex deficient in E-cadherin binding (HA-RSDA) by combining $HA70/A^{R505S}$, $HA17/A^{D109A}$, and the wild-type HA33/A. Binding of HA-RSDA to HT29 or Caco-2 cells was greatly reduced and failed to disrupt cell-cell junctions (Fig. 3, B and C, and fig. S2). Consistently, the HA-RSDA barely decreased the transepithelial electrical resistance (TER) of the differentiated Caco-2 cell monolayers when applied to the apical or basolateral side (Fig. 3D) and did not facilitate the paracellular transport of fluorescein isothiocyanate (FITC)–dextran from apical to basolateral compartments as the HA-WT complex did (Fig. 3E). Together, these data demonstrate that the HA complex disrupts cell-cell junctions through binding to E-cadherin.

On basis of the structures of the HA complex and the full-length ectodomain of mouse E-cadherin (*9*, *15*), we built a complete structural model of the HA–E-cadherin complex, in which three molecules of E-cadherin bind the HA complex (Fig. 4A). The model shows that the carboxy-terminal EC5 of E-cadherin and the carbohydrate-binding sites on HA33 both point toward the proposed plane of the plasma membrane (Fig. 4B). Because the crescent shape of EC1–EC5 has considerable conformational flexibility to adopt different curvatures (*14*, *15*) and HA33 also displays a large structural flexibility (*9*), the HA complex is able to bind to its carbohydrate receptor and protein receptor on the same cell surface (Fig. 4B). Therefore, these two different types of receptors likely act synergistically to achieve high binding avidity and specificity on the cell surface.

The assembly of the E-cadherin network in adherens junctions (~150 to 300 Å in width) is achieved by a combination of trans-dimerization between cadherins from opposing cell surfaces and cis-dimerization between molecules from the same cell surface (fig. S7) (*14*, *15*). We propose that the condensed array of E-cadherin clustering between cells is disrupted by the bulky HA complexes (~260 Å wide and ~100 Å height) upon binding. The mini-HA complex bound to HT29 cells weakly and failed to disrupt cell-cell adhesion (fig. S8), and neither apical nor basolateral addition of the mini-HA complex disrupted the tight junctions of polarized Caco-2 cell monolayer (*9*). These results suggest that multivalent binding to carbohydrates and E-cadherin in the context of the triskelion-shape of the full HA complex is necessary to ensure its function. Furthermore, the HA complex may destabilize adherens junctions by affecting E-cadherin homeostasis because the organization of individual adherens junction is highly dynamic where E-cadherin is actively turned over (*24*).

Given the observed cellular consequences of HA–E-cadherin interactions, we determined the physiological relevance of HA–E-cadherin and HA–carbohydrate interactions to the oral toxicity of BoNT/A in vivo. This question was directly addressed by comparing the oral toxicity of BoNT/A L-PTC (L-PTC/A) containing HA-WT versus mutant HA complex. To do so, we developed a protocol to reconstitute the complete L-PTC/A, composed of a total of 14 proteins (~760 kD), using recombinant components expressed in *Escherichia coli* (fig. S9). This allowed us to compare L-PTC/As that were all constructed in the same way and contained the same active BoNT/A, with either HA-WT or mutant HA complex. The mouse oral toxicity of the reconstituted wild-type L-PTC/A (rL-PTC WT) is similar to native L-PTC/A purified from *C. botulinum* (*10*). The rL-PTC RSDA containing mutated HA/As deficient in E-cadherin binding (HA-RSDA) showed a greatly reduced oral toxicity as compared with that of the rL-PTC WT under the same assay conditions (Fig. 3F). Thus, the ability of HA complex to bind E-cadherin and disrupt cell-cell junctions is critical for the oral toxicity of BoNT/A in vivo. We also observed a drastic reduction in oral toxicity for the rL-PTC DAFA/TPRA comprising a HA complex deficient in carbohydrate binding (a combination of $HA^{33\text{-}DAFA}$ and $HA^{70\text{-}TPRA}$) (Fig. 3F) (*9*), demonstrating that binding of HA complex to carbohydrates is also important to facilitate BoNT/A absorption in vivo, likely by enriching L-PTC/A onto cell surfaces. Together, these results establish the physiological relevance of HA–E-cadherin and HA–carbohydrate interactions to the extreme oral toxicity of BoNT/A. Our study also provides a framework to investigate the oral intoxication of some HA-less BoNTs (such as BoNT/A2, BoNT/E, and BoNT/F), which instead contain several orfX proteins, whose expression and function are still unknown (*2*, *25*).

On the basis of the work described previously and presented here, we suggest the following model (Fig. 4C). The abundant carbohydrates accumulate L-PTCs on the surface of the small intestine to initiate absorption (*9*). Then, some L-PTC may cross the epithelial cells by means of transcytosis without interfering with the epithelial barrier, which could be mediated either by BoNT or HAs, although the underlying mechanism is not fully understood (Fig. 4C, step 1) (*26*–*28*). Once the HA complexes gain access to the basolateral surface, they specifically bind to E-cadherin and carbohydrates and disrupt E-cadherin–mediated cell-to-cell adhesion (Fig. 4C, step 2), opening up the paracellular route for BoNT absorption (Fig. 4C, step 3).

BoNTs are the most potent bacterial toxins known. Our findings reveal the targeting of a host protein by a component of the toxin complex to achieve efficient absorption through possibly the most challenging route of entry into the circulation of humans or other animals. Understanding this remarkable molecular machinery not only provides new targets for therapeutic intervention against oral BoNT intoxication, but also could potentially guide the development of new adherens junction modulators to enhance the permeability of the intestinal epithelium so as to facilitate drug delivery.

REFERENCES AND NOTES

1. M. D. Collins, A. K. East, *J. Appl. Microbiol.* **84**, 5–17 (1998).
2. K. K. Hill, T. J. Smith, *Curr. Top. Microbiol. Immunol.* **364**, 1–20 (2013).
3. S. Gu *et al.*, *Science* **335**, 977–981 (2012).
4. I. Ohishi, S. Sugii, G. Sakaguchi, *Infect. Immun.* **16**, 107–109 (1977).
5. I. Ohishi, *Infect. Immun.* **43**, 487–490 (1984).
6. G. Sakaguchi, *Pharmacol. Ther.* **19**, 165–194 (1982).
7. T. Matsumura *et al.*, *Cell. Microbiol.* **10**, 355–364 (2008).
8. H. Ito *et al.*, *FEMS Immunol. Med. Microbiol.* **61**, 323–331 (2011).
9. K. Lee *et al.*, *PLOS Pathog.* **9**, e1003690 (2013).
10. L. W. Cheng *et al.*, *Toxicology* **249**, 123–129 (2008).
11. S. Amatsu, Y. Sugawara, T. Matsumura, K. Kitadokoro, Y. Fujinaga, *J. Biol. Chem.* **288**, 35617–35625 (2013).
12. Y. Sugawara *et al.*, *J. Cell Biol.* **189**, 691–700 (2010).
13. W. Meng, M. Takeichi, *Cold Spring Harb. Perspect. Biol.* **1**, a002899 (2009).
14. J. Brasch, O. J. Harrison, B. Honig, L. Shapiro, *Trends Cell Biol.* **22**, 299–310 (2012).
15. O. J. Harrison *et al.*, *Structure* **19**, 244–256 (2011).
16. L. Shapiro, W. I. Weis, *Cold Spring Harb. Perspect. Biol.* **1**, a003053 (2009).
17. E. Parisini, J. M. Higgins, J. H. Liu, M. B. Brenner, J. H. Wang, *J. Mol. Biol.* **373**, 401–411 (2007).
18. T. J. Boggon *et al.*, *Science* **296**, 1308–1313 (2002).
19. Y. Liu, D. Eisenberg, *Protein Sci.* **11**, 1285–1299 (2002).
20. A. W. Koch, S. Pokutta, A. Lustig, J. Engel, *Biochemistry* **36**, 7697–7705 (1997).
21. J. Vendome *et al.*, *Nat. Struct. Mol. Biol.* **18**, 693–700 (2011).
22. O. J. Harrison *et al.*, *Nat. Struct. Mol. Biol.* **17**, 348–357 (2010).
23. W. D. Schubert *et al.*, *Cell* **111**, 825–836 (2002).
24. B. Baum, M. Georgiou, *J. Cell Biol.* **192**, 907–917 (2011).
25. G. Lin, W. H. Tepp, C. L. Pier, M. J. Jacobson, E. A. Johnson, *Appl. Environ. Microbiol.* **76**, 40–47 (2010).
26. Y. Fujinaga, Y. Sugawara, T. Matsumura, *Curr. Top. Microbiol. Immunol.* **364**, 45–59 (2013).
27. A. B. Maksymowych, L. L. Simpson, *J. Pharmacol. Exp. Ther.* **310**, 633–641 (2004).
28. A. Couesnon, Y. Pereira, M. R. Popoff, *Cell. Microbiol.* **10**, 375–387 (2008).

ACKNOWLEDGMENTS

We thank A. Bobkov for technical assistance. This work was partly supported by National Institute of Allergy and Infectious

Diseases (NIAID) grant R01AI091823 to R.J.; by the NIH grant 8P51OD011103-51 (to the New England Primate Research Center), 1R56AI097834-01, and 1R01NS080833-01 to M.D.; and by the Swiss Federal Office for Civil Protection BABS #353003325 to A.R. NE-CAT at the Advanced Photon Source (APS) is supported by a grant from the National Institute of General Medical Sciences (P41 GM103403). Use of the APS, an Office of Science User Facility operated for the U.S. Department of Energy (DOE) Office of Science by Argonne National Laboratory, was supported by the U.S. DOE under contract DE-AC02-06CH11357. The atomic coordinates and structure factors of the mini-HA–EC1–EC2 complex have been deposited in the Protein Data Bank under the accession code 4QD2. BoNT availability is subject to the restrictions that apply to Centers for Disease Control and Prevention select agents and NIAID Category A pathogens. R.J. is named as an inventor on a U.S. patent application applied for by University of California, Irvine related to oral drug delivery systems.

SUPPLEMENTARY MATERIALS

www.sciencemag.org/content/344/6190/1405/suppl/DC1
Materials and Methods
Figs. S1 to S9
Table S1
References (*29*–*42*)

24 March 2014; accepted 27 May 2014
10.1126/science.1253823

ECOLOGICAL GENOMICS

The genomic landscape underlying phenotypic integrity in the face of gene flow in crows

J. W. Poelstra,[1]* N. Vijay,[1]* C. M. Bossu,[1]* H. Lantz,[2,3] B. Ryll,[4] I. Müller,[5,6] V. Baglione,[7] P. Unneberg,[8] M. Wikelski,[5,6] M. G. Grabherr,[3] J. B. W. Wolf[1]†

The importance, extent, and mode of interspecific gene flow for the evolution of species has long been debated. Characterization of genomic differentiation in a classic example of hybridization between all-black carrion crows and gray-coated hooded crows identified genome-wide introgression extending far beyond the morphological hybrid zone. Gene expression divergence was concentrated in pigmentation genes expressed in gray versus black feather follicles. Only a small number of narrow genomic islands exhibited resistance to gene flow. One prominent genomic region (<2 megabases) harbored 81 of all 82 fixed differences (of 8.4 million single-nucleotide polymorphisms in total) linking genes involved in pigmentation and in visual perception—a genomic signal reflecting color-mediated prezygotic isolation. Thus, localized genomic selection can cause marked heterogeneity in introgression landscapes while maintaining phenotypic divergence.

Genomic studies increasingly appreciate the importance of interspecific gene flow in the context of species diversification (*1*, *2*), including that of hominids (*3*). Yet our understanding of the forces generating heterogeneity in differentiation across the genome and their relationship to phenotypic evolution is limited (*3*–*5*). The European hybrid zone between all-black carrion crows [*Corvus* (*corone*) *corone*] and gray-coated hooded crows [*C.* (*corone*) *cornix*] (*6*) provides ideal conditions for studying the evolutionary consequences of introgression in a phase of early species divergence. The geographical distribution pattern of these species suggests a population history shaped by glaciation cycles during the Pleistocene, when periods of isolation in distinct southern refugia alternated with periods of range expansion and secondary contact (*7*). The near-absence of neutral genetic differentiation across the hybrid zone (*8*) strongly contrasts with abrupt spatial segregation of plumage coloration (Fig. 1), which has remained remarkably stable over the past century despite successful backcrossing of hybrids (*6*). Evidence for color-assortative mating (*9*) and the independent recurrence of pied plumage phenotypes in the otherwise all-black genus *Corvus* has prompted the hypothesis that this color polymorphism is promoting speciation (fig. S1).

We assembled a high-quality reference genome of one hooded crow male sequenced to 152× coverage (table S1). The final assembly consisted of 1298 scaffolds with an N50 size of 16.4 Mb (*10*) and a cumulative length of 1.04 Gb, including 3.52% gaps; 95% of the assembly was contained within the 100 largest scaffolds (size range: 1 to 50 Mb), which approached chromosome size (crow karyotype: $2n$ = 80; size range of zebra finch chromosomes: 1 to 156 Mb) (fig. S2, A and B, and table S2). Evidence-based annotation of the genome with mRNA sequencing data (table S3) identified a set of 20,794 protein-coding genes.

We subsequently resequenced 60 genomes of unrelated individuals from two populations each of carrion and hooded crows (Fig. 1) to a mean sequence coverage of 12.2× (range: 7.1× to 28.6×, table S4); 8.44 million single-nucleotide polymorphisms (SNPs) segregated across all four populations, 5.27 million of which were shared between carrion and hooded crows. Several lines of evidence suggest substantial genome-wide gene flow across the hybrid zone. The major axes of genetic variation (accounting for 11.5% of the total variance) coincided with the presumed direction of spatial expansion out of Spain, yet German carrion crows clustered more closely with both hooded crow populations [Fig. 1; for pairwise fixation index (F_{ST}) estimates see Fig. 2A, fig. S3, and table S5; see fig. S4 for mitochondrial DNA divergence]. Extensive gene flow between hooded crows and the German carrion crow population was further supported by ABBA-BABA tests (fig. S5 and table S6), admixture analyses (fig. S6), and coalescence-based parameter estimates of an isolation-with-migration model (fig. S7). Consistent with a scenario of admixture upon secondary contact, all populations but Spain showed signatures of expansion and had higher nucleotide diversity than that of the presumably refugial Spanish population (table S5).

The low genome-wide differentiation across the hybrid zone was also reflected in gene expression divergence as measured by mRNA sequencing (RNA-seq) from 19 individuals and five tissues under controlled conditions. The overall proportion of differentially expressed genes between carrion and hooded crows was low, between 0.03% and 0.41% across tissues [Fig. 3B; see (*8*); false discovery rate <0.05]. The main difference in gene expression patterns corresponded to phenotypic divergence in plumage coloration. Differentially expressed genes predominated in growing feather follicles from the torso, where carrion crows produce black feathers and hooded crows gray feathers (Figs. 1 and 3A; $\chi^2_{df=4}$ = 169.34, P < 0.001), with an overrepresentation of genes in the melanogenesis pigmentation pathway (Fig. 3, B and C; n = 21, $\chi^2_{df=4}$ = 147.16, P < 0.001; see table S7 for Gene Ontology terms). Nineteen of 20 differentially expressed melanogenesis-related genes were underexpressed in the gray hooded crow torso (table S8). The pathway-wide pattern of reduced expression could not be attributed to differences in melanocyte density (Fig. 4), but rather to upstream regulatory changes inducing broad-scale down-regulation in follicles producing gray feathers (Fig. 3C).

We surveyed the landscape of genomic divergence with a window-based approach based on population genetic summary statistics derived for 22,072 nonoverlapping 50-kb windows (Fig. 2A and fig. S8) and a hypothesis-free clustering

[1]Science for Life Laboratory and Department of Evolutionary Biology, Evolutionary Biology Centre, Uppsala University, 75236 Uppsala, Sweden. [2]Bioinformatics Infrastructure for Life Sciences, Uppsala University, 75124 Uppsala, Sweden. [3]Science for Life Laboratory and Department of Medical Biochemistry and Microbiology, Uppsala University, 75123 Uppsala, Sweden. [4]Department of Organismal Biology, Evolutionary Biology Centre, Uppsala University, 75236 Uppsala, Sweden. [5]Max Planck Institute for Ornithology, 78315 Radolfzell, Germany. [6]Department of Biology, University of Konstanz, 78464 Konstanz, Germany. [7]Departamento de Ciencias Agro-Forestales, Campus La Yutera, Universidad de Valladolid, 34004 Palencia, Spain. [8]Science for Life Laboratory and Department of Biochemistry and Biophysics, Stockholm University, 171 21 Solna, Sweden.
*These authors contributed equally to this work. †Corresponding author. E-mail: jochen.wolf@ebc.uu.se

algorithm reconstructing local genomic phylogenies (so-called "cacti") (*10*) (Fig. 2C). Phylogenetic clustering segmented the genome into two major topologies (class I and class II cacti hereafter; fig. S9), with only 0.28% of the genome following a topology that clearly separated carrion and hooded crows. Both methods identified one 1.95-Mb genomic region exhibiting extreme genetic differentiation between carrion and hooded crows on scaffolds 78 and 60, which, on the basis of synteny with other birds, are located adjacently on chromosome 18 [Fig. 2, A and B, and fig. S8A; for a detailed exploration of divergence peaks, see (*10*) and fig. S8]. This region, harboring 81 of all 82 fixed sites between carrion and hooded crows, contained 40 annotated protein-coding genes, had strongly reduced levels of nucleotide diversity, and showed increased linkage disequilibrium (LD). Disrupted patterns of LD, taxon-specific dropout of paired-end read mapping (*10*) (fig. S10), and the presence of two local F_{ST} peaks connected by a saddle (*11*) suggest the possibility of an inversion in this region.

In the center of the right local F_{ST} peak (Fig. 2B), a region about 4.1 kb upstream of the *PRKCA* gene exhibited longer haplotype blocks (iES statistic) and showed evidence for recent, hooded crow–specific, positive selection: It was enriched for fixed hooded crow–specific derived variants (22 of 28) and had significantly reduced values of Fu and Li's D statistic ($P < 0.05$) in hooded crows. Furthermore, this region contains a tandem array of voltage-dependent calcium channel subunits, including those encoded by *CACNG5*, *CACNG4*, and *CACNG1*. The *CACNG* gene family codes for transmembrane regulators of AMPA receptors, which influence the microphthalmia-associated transcription factor gene *MITF*, a central regulatory element of the melanogenesis pathway (*12*) (Fig. 3C). At least 11 of the 21 melanogenesis genes underexpressed in gray hooded crow feather follicles are directly regulated by *MITF* (e.g., *TYR*, *TYRP1*, *SLC45A2*, *RAB38*, *EDNRB2*) or interact with *MITF* in feedback loops (*MC1R*, *HPGDS*) (Fig. 3C and table S8). Moreover, *RAS-GRF1*, a central mediator between calcium concentration and downstream gene expression (*13*), was significantly underexpressed in the gray feather follicles of hooded crows (Fig. 3C and table S8). This tentatively links gene expression, color phenotype, and the signature of divergent selection in the divergence peak.

Two additional strongly differentially expressed melanogenesis genes were located in divergent genomic regions: *NDP* (Norrie disease pseudoglioma) and *HPGDS* (hematopoietic prostaglandin D synthase), which also act closely upstream of *MITF* (*14*) (Fig. 3C and fig. S11). *HPGDS* was among the most strongly underexpressed genes in the hooded crow torso and also showed an extreme reduction in variance, consistent with selection (Ansari-Bradley test, $P = 0.0039$). A multigenic architecture of the color trait is consistent with the segregation pattern of different crow color phenotypes in the hybrid zone (fig. S12), indicating that a number of genes likely contribute to color divergence.

Under the left local F_{ST} peak, fixed differences enriched for carrion crow–derived variants were clustered in a narrowly defined area (Fig. 2B). An exception included a hooded-derived fixed variant in the regulatory region of the gene *RGS9* (regulator of G protein signaling 9), which affects visual perception in vertebrates (*15*), was highly expressed in eye (higher than in any other tissue by a factor of 5), and showed lower expression in hooded crows across tissues (fig. S11). Not only is *RGS9* involved in phototransduction, but different splice forms (also detected in crows; fig. S11) regulate dopamine and opioid signaling in the brain (*15*). This potential pleiotropy is of interest because the main differences between carrion and hooded crows are coloration, color-assortative mate choice (*9*), and hormone-mediated social dominance behavior (*16*). These diverse biological functions may also be explained by the *SCL24* gene family (*17*): *SLC24A2* and *SLC24A3*, involved in vision and hormonal regulation, respectively, were associated with class I cacti in crows (Fig. 2C), and *SLC24A4*, involved in pigmentation,

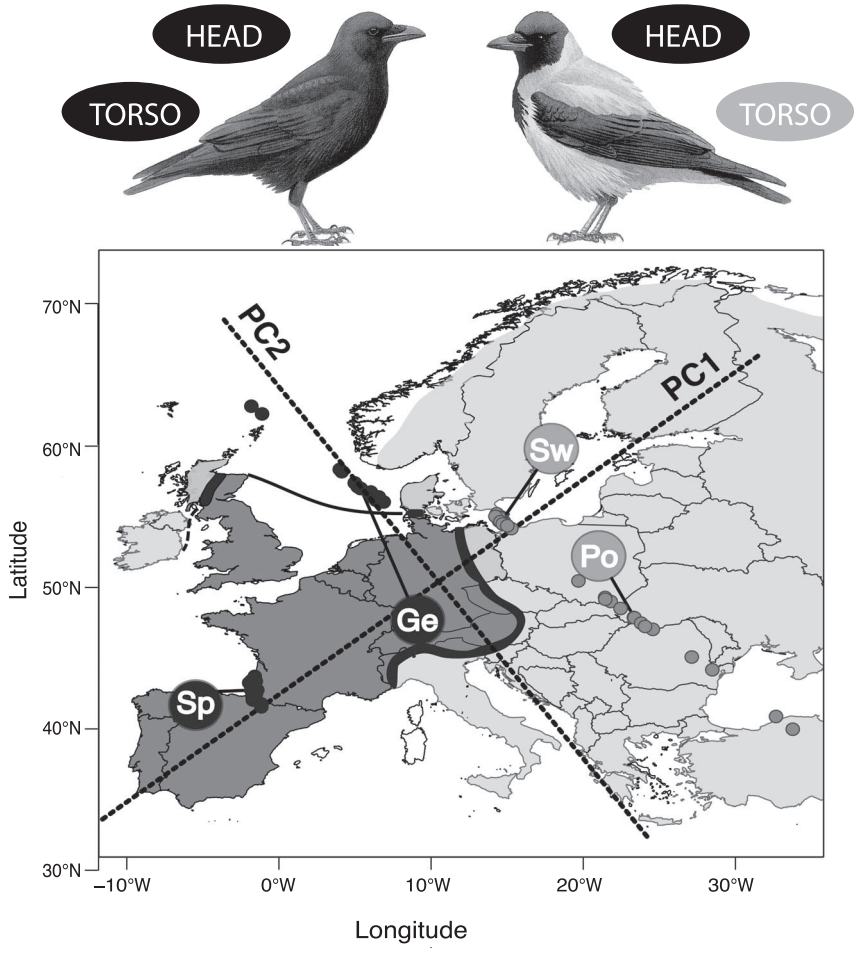

Fig. 1. The crow system. Illustrations of carrion crow (left) and hooded crow (right). We sampled gene expression data of regrowing feathers from the head and torso, which differ in coloration. The map below shows the European distribution of the carrion crow (dark gray area) and hooded crow (light gray area); the hybrid zone is shown as a black solid line. Sampling locations of this study in Spain (Sp), Germany (Ge), Poland (Po), and Sweden (Sw) are indicated by filled circles (black, carrion crow; gray, hooded crow). Superimposed on the geographical map are the major axes of genetic variation (principal components PC1 and PC2) derived from whole-genome resequencing data from the four populations (black and gray dots, respectively). [Drawings courtesy of Dan Zetterström]

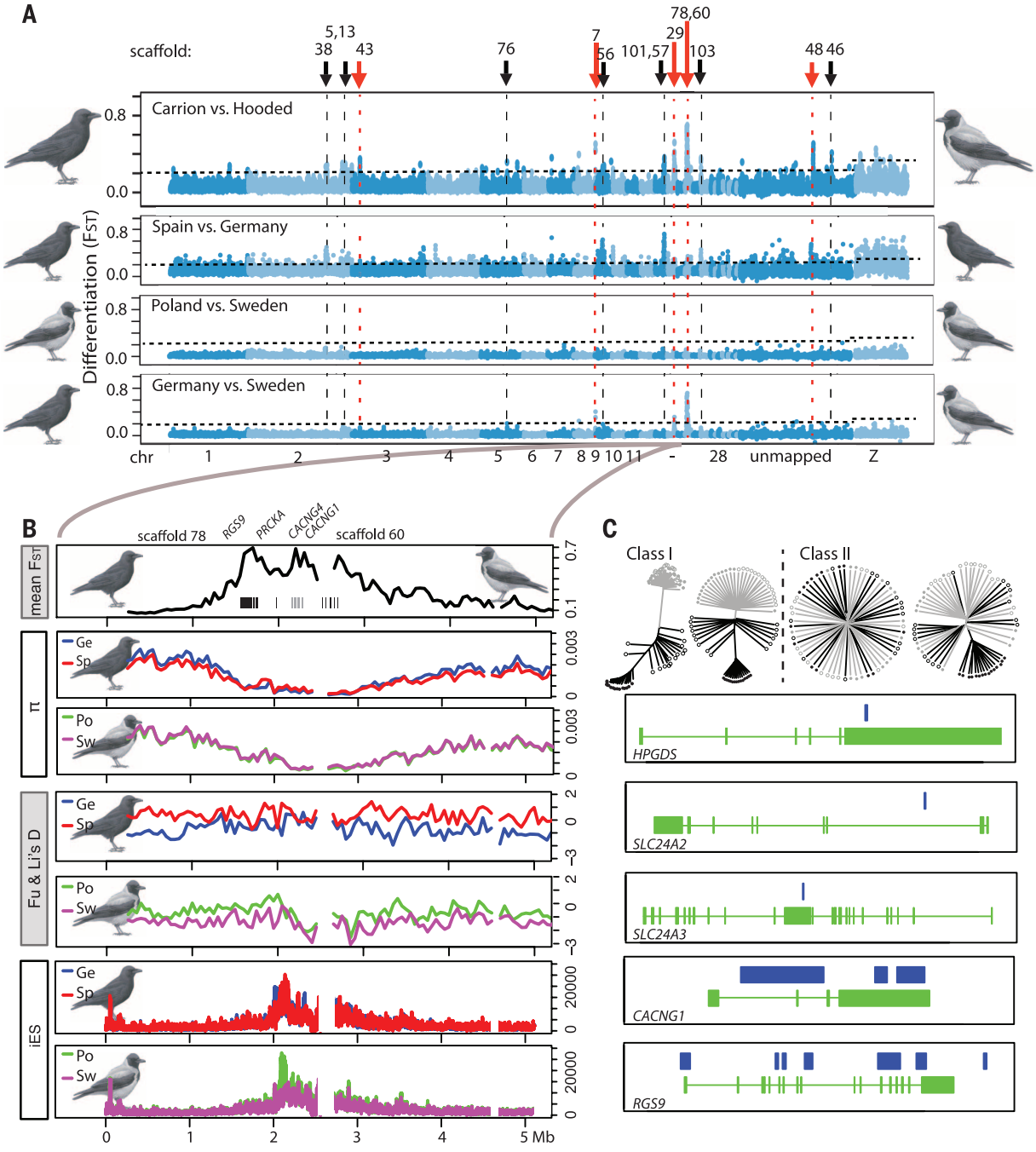

Fig. 2. The genomic landscape of divergence. (**A**) Pairwise genetic differentiation (F_{ST}) in 50-kb sliding windows across the genome between carrion crows and hooded crows (top panel), between carrion crow populations (second panel), between hooded crow populations (third panel), and between carrion crows and hooded crows from across the hybrid zone (bottom panel). Alternating colors denote the different chromosomes; and the dotted horizontal lines mark the 99th-percentile F_{ST} estimates of autosomes and the Z chromosome, respectively. Red arrows indicate taxon-specific peaks of consecutive elevated F_{ST} windows; black arrows highlight outlier peaks that are specific to comparisons with the refugial Spanish population. (**B**) The largest and most extreme F_{ST} peak was located on scaffolds 78 and 60. Plotted within the peak are 81 of 82 total fixed variants (black bars in top panel, ancestral alleles; gray bars, derived hooded crow–specific alleles). (**C**) Localized phylogenetic patterns within the genome ("cacti"). The majority of the genome exhibits neutral genetic divergence classified as class II cacti (divergent Spanish population or complete admixture). Two cacti display clear separation of carrion crows (black: Spain, solid circles; Germany, open circles) and hooded crows (gray: Sweden, solid circles, Poland, open circles) (class I cacti; fig. S9). Four exemplar gene models associated with the melanogenesis pathway and associated with visual perception are depicted (green blocks and lines represent exons and introns, respectively) along with the regions assigned to class I cacti (blue).

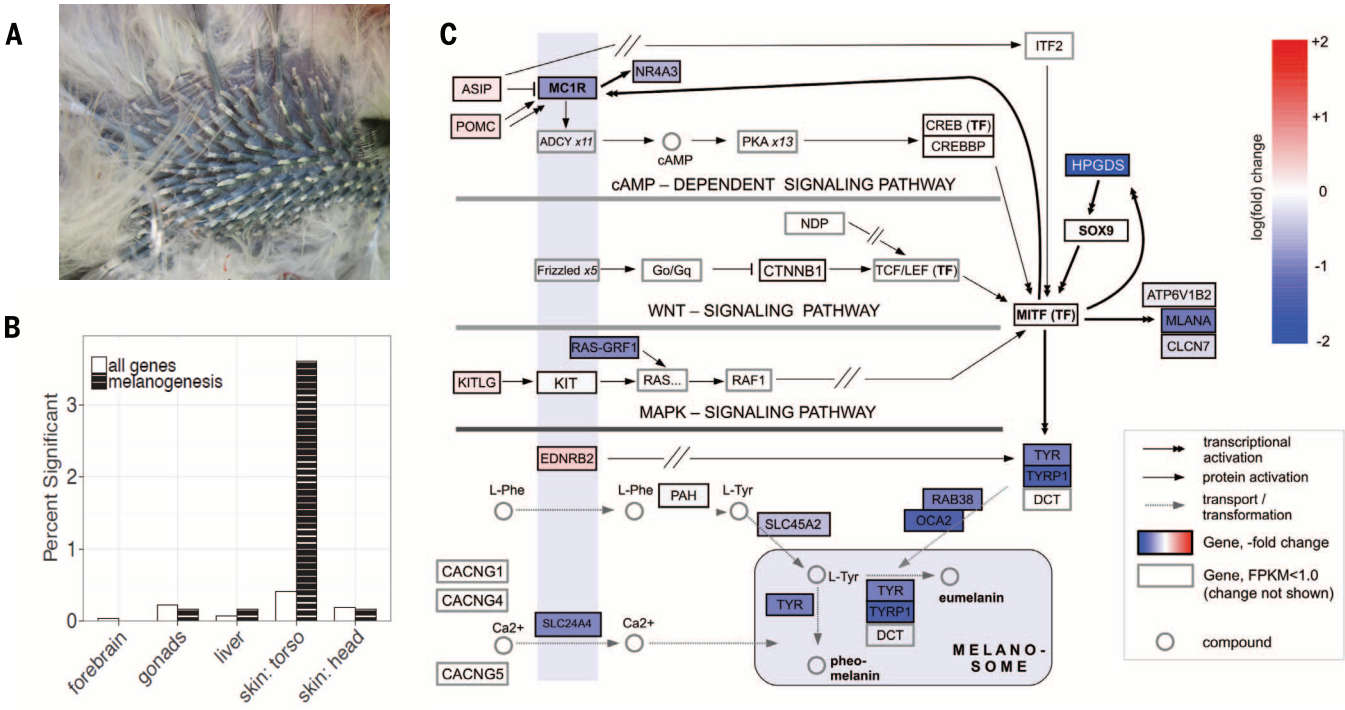

Fig. 3. The functional genomic basis of plumage color differences. (**A**) Photograph of the developmental stage of feather follicles used for gene expression quantification. (**B**) Percentage of all expressed genes (white) and melanogenesis genes (striped) inferred to be differentially expressed. (**C**) Schematic overview of the melanogenesis pathway, with genes underexpressed in skin from torso in hooded crows shown in blue, genes overexpressed shown in red (color scale indicates relative change). Genes either not supported by RNA-seq data or expressed at FPKM (fragments per kilobase of exon per million fragments mapped) levels below 1.0 in both hooded and carrion crows are shown as gray boxes. Pathway relationships are shown for transcriptional activation (black double arrows), protein activation (e.g., by phosphorylation) (black single arrows), and transport (gray single arrow, dotted line).

Fig. 4. Characterization of feather melanocytes. Immunohistochemistry on feather follicles of carrion crows (upper panel) and hooded crows (lower panel) for one of the melanogenic enzymes (a-Trp1, cyan) differentially expressed in our RNA-seq data confirms differential melanogenesis pathway activity (left column; view on to barbed ridges of whole-mount feather bulges, yellow arrows) but shows no striking differences in melanocyte density (right column; detail of sectioned feather follicle, magenta square). Matched samples from carrion crows and hooded crows were stained in parallel and imaged under identical conditions to ensure comparability. br, barbed ridge; p, pulp. Scale bar, 50 μm. [Drawing courtesy of Kristina Fraune; feather photo from Wikimedia Commons]

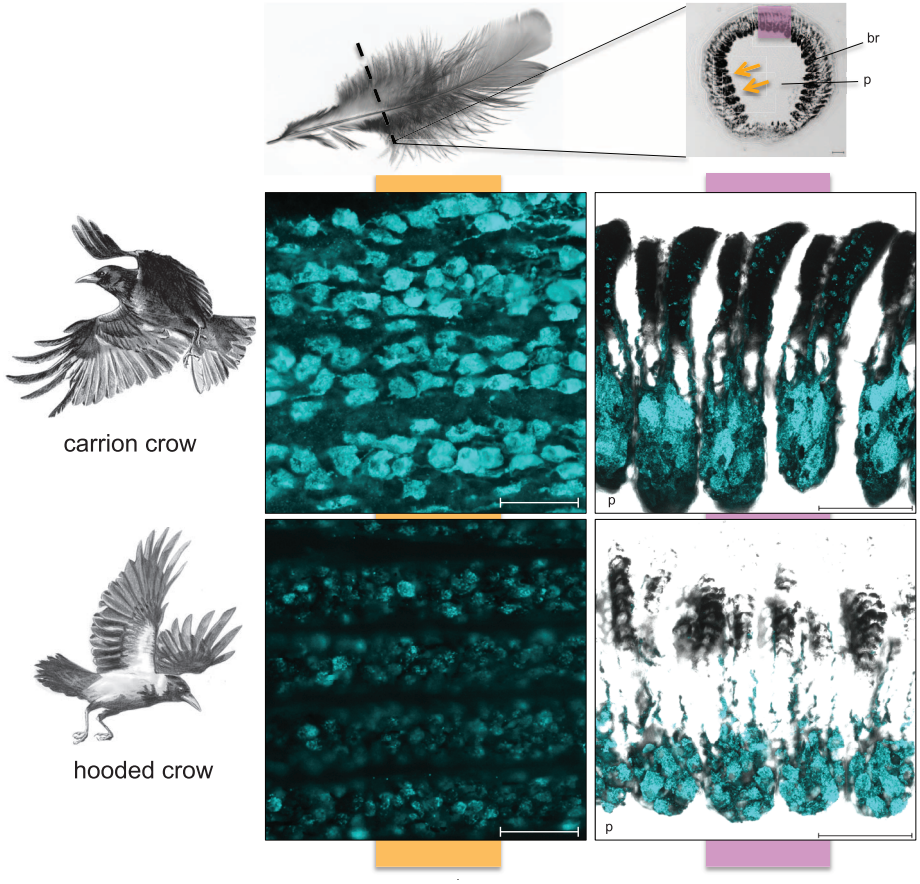

was strongly underexpressed in hooded crows (Fig. 3C).

Our results show that the pronounced phenotypic differences between hooded and carrion crows are maintained in the face of substantial gene flow by variation in less than 1% of the genome. The crow system thus constitutes an intriguing test case for the appropriate level of taxonomic delineation (*18*) and the interpretation of local peaks of divergence (often called "speciation islands") (*19*). Gene flow slightly reduced the width of the main divergence peak and eroded linkage disequilibrium at the peak margins (fig. S10B) but slightly increased the peak amplitude (*10*). Hence, divergent selection acting on small genomic regions did not appear to expand local differentiation or seed genome-wide reproductive isolation (*19*), although it did maintain phenotypic differentiation in the face of gene flow. Our findings further highlight the role of inversions in evolution (*20*, *21*), potentially linking key genes involved in a mating trait and a tentative visual preference locus. This establishes an interesting parallel to studies in which single genes (*22*), "supergenes" (*4*), or large-scale inversions (*23*) have been implicated in driving morphological change relevant to mate choice, but contrasts with studies in which many ecologically relevant loci (*21*) or structural genomic features dominated the genomic landscape of divergence (*24*). A key feature that distinguishes the crow system is the apparent lack of ecological selection on the maintenance of separate phenotypes. Instead, the data presented here are consistent with the idea that assortative mating and sexual selection can exclusively cause phenotypic and genotypic differentiation (*25*).

REFERENCES AND NOTES

1. R. Abbott *et al*., *J. Evol. Biol.* **26**, 229–246 (2013).
2. S. H. Martin *et al*., Genome-wide evidence for speciation with gene flow in *Heliconius* butterflies. *Genome Res.* **23**, 1817–1828 (2013).
3. S. Sankararaman *et al*., *Nature* **507**, 354–357 (2014).
4. Heliconius Genome Consortium, *Nature* **487**, 94–98 (2012).
5. H. Ellegren *et al*., *Nature* **491**, 756–760 (2012).
6. W. Meise, *J. Ornithol.* **76**, 1–203 (1928).
7. G. Hewitt, *Nature* **405**, 907–913 (2000).
8. J. B. W. Wolf *et al*., *Mol. Ecol.* **19** (suppl. 1), 162–175 (2010).
9. C. Randler, *Ardea* **95**, 143–149 (2007).
10. See supplementary materials on *Science* Online.
11. R. F. Guerrero, F. Rousset, M. Kirkpatrick, *Philos. Trans. R. Soc. London Ser. B* **367**, 430–438 (2012).
12. M. J. Hoogduijn *et al*., *Pigment Cell Res.* **19**, 58–67 (2006).
13. C. L. Farnsworth *et al*., *Nature* **376**, 524–527 (1995).
14. B. Moniot *et al*., *Dev. Dyn.* **240**, 2335–2343 (2011).
15. K. A. Martemyanov, V. Y. Arshavsky, *Prog. Mol. Biol. Transl. Sci.* **86**, 205–227 (2009).
16. N. Saino, L. Scatizzi, *Boll. Zool.* **58**, 255–260 (1991).
17. P. P. M. Schnetkamp, *Mol. Aspects Med.* **34**, 455–464 (2013).
18. D. T. Parkin, M. Collinson, A. J. Helbig, A. G. Knox, G. Sangster, *Br. Birds* **96**, 274–290 (2003).
19. J. L. Feder, S. P. Egan, P. Nosil, *Trends Genet.* **28**, 342–350 (2012).
20. A. A. Hoffmann, L. H. Rieseberg, *Annu. Rev. Ecol. Evol. Syst.* **39**, 21–42 (2008).
21. F. C. Jones *et al*., *Nature* **484**, 55–61 (2012).
22. K. Kunte *et al*., *Nature* **507**, 229–232 (2014).
23. H. Thorneycroft, *Evolution* **29**, 611–621 (1975).
24. S. Renaut *et al*., *Nat. Commun.* **4**, 1827 (2013).
25. C. A. McLean, D. Stuart-Fox, *Biol. Rev. Camb. Philos. Soc.* 10.1111/brv.12083 (2014).

ACKNOWLEDGMENTS

We thank W. Fiedler, K. Temnow, L. Vossen, M. Döpfner, T. Pärt, K.-H. Siebenrock, and the other staff of the Max Planck Institute for Ornithology for help with field work and animal husbandry. R. Burri assisted in population genetic analyses. Supported by VolkswagenStiftung grant I/83 496, Swedish Research Council grant 621-2010-5553, the Wallenberg Advanced Bioinformatics Infrastructure (funded by the Knut and Alice Wallenberg Foundation), Carl Tryggers foundation grant CTS11:517, CTS12:543, and European Research Council grant ERCStG-336536 (J.B.W.W.); the Max Planck Society (M.W., I.M.); and SciLifeLab Uppsala (M.G.G., H.L.). *C. brachyrhynchos* samples were provided by courtesy of the American Museum of Natural History, New York; Polish hooded crows by A. Kruszewicz and M. Gajownik, Warsaw Zoo. We thank the UPPMAX Next-Generation Sequencing Cluster and Storage (UPPNEX) project, funded by the Knut and Alice Wallenberg Foundation and the Swedish National Infrastructure for Computing, for access to computational resources. All sequencing data and the genome assembly are available in the NCBI short read archive under project PRJNA192205.

SUPPLEMENTARY MATERIALS

www.sciencemag.org/content/344/6190/1410/suppl/DC1
Supplementary Text
Figs. S1 to S13
Tables S1 to S10
References (*26*–*97*)

11 March 2014; accepted 5 May 2014
10.1126/science.1253226

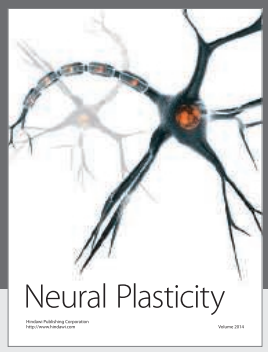

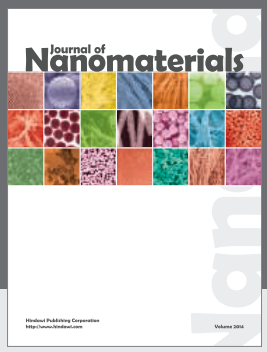

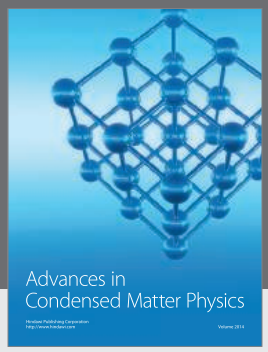

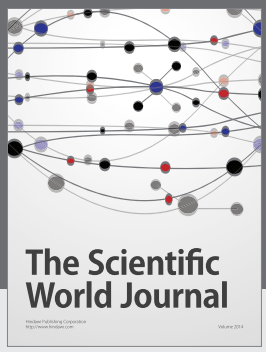

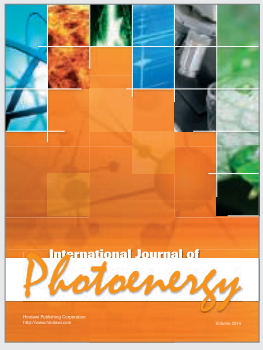

Hindawi

Submit your manuscripts at
http://www.hindawi.com

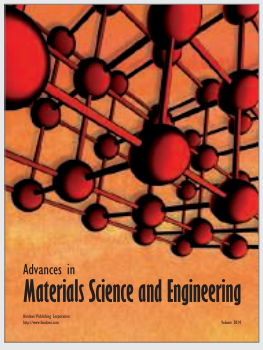

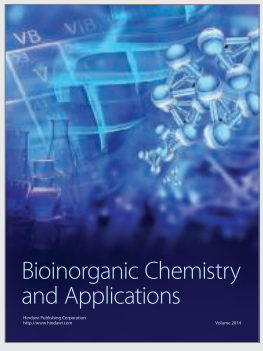

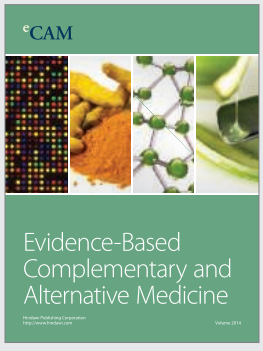

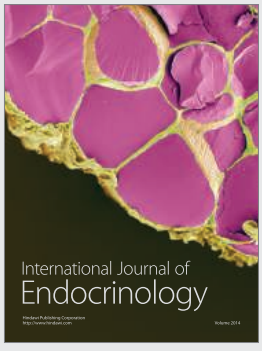

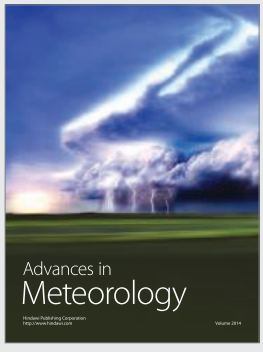

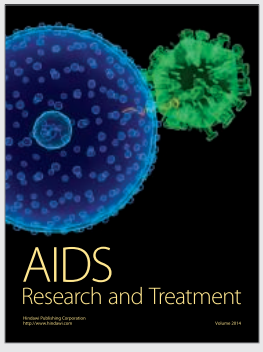

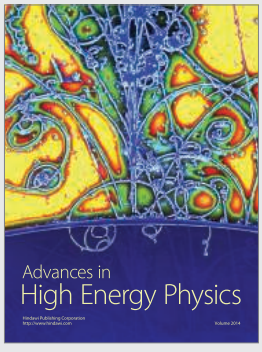

Bat man wins young scientist prize in Stockholm. Are you next?

Science & SciLifeLab PRIZE FOR YOUNG SCIENTISTS

Photo: Nancy Evelyn - UGA

The 2014 *Science* and SciLifeLab Prize is now open and we are looking for new bright ideas. Are you like Daniel Streicker? Are you a recent PhD graduate eager to win a prize? Daniel is a true "bat man" having spent many hours in dark caves studying bats, to better understand how infectious diseases emerge and establish in new host species. It is for this work that Daniel was published in the journal *Science*, December 6, 2013, as the Grand Prize winner of the 2013 *Science* & SciLifeLab Prize for Young Scientists.

The journal *Science* and SciLifeLab have come together to recognize and celebrate excellence in PhD Research. The *Science* & SciLifeLab Prize has been established to support young scientists at the start of their career.

The four categories for the 2014 prize are: Cell and Developmental Biology; Genomics and Proteomics; Environment; and Translational Medicine. The Grand Prize winner will receive 25,000USD and the other three Category Prize winners will receive 3,000USD each. The Grand Prize winning essay will be published in *Science* and the Category Prize winners will be published in *Science* online.

The deadline for submissions is August 1, 2014.
For further details and to enter, please visit: www.sciencemag.org/scilifelabprize

For over 130 years the journal Science has been the world's leading journal of original scientific research, global news and commentary.

SciLifeLab is a collaboration among four universities in Stockholm and Uppsala, Sweden, and is a national center for molecular biosciences with focus on health and environmental research.

This prize is made possible with the kind support of the Knut and Alice Wallenberg Foundation.

Science AAAS

SciLifeLab

Knut och Alice Wallenbergs Stiftelse

The Promise of the Microbiome:

Function and Dysfunction in Humans and Beyond

Tuesday, July 15, 2014

12 noon Eastern, 9 a.m. Pacific,
5 p.m. UK, 6 p.m. Central Europe

During this webinar, the speakers will:

- Provide a brief introduction to microbiomes and how they may fundamentally impact our study of the natural world
- Share their research data on human and nonhuman microbiota, including microbe-associated environmental impacts on human health
- Discuss the role of microbiomes in obesity and malnutrition
- Answer your questions live during the webinar!

REGISTER NOW!
webinar.sciencemag.org

Microbiomes—the distinct microbial populations that colonize an array of bodily and environmental niches—are rapidly gaining prominence in numerous fields of research. Increasing understanding of the composition and characteristics of these microbial communities is providing substantial insight into the function, and dysfunction, of a broad range of processes in the host organisms. Recent discoveries indicate a role of the microbiome in specific physical conditions and disease states; these discoveries suggest considerable potential for the development of microbiome-based diagnostic and therapeutic tools. While the microbiota of the human gut has drawn much attention to date, microbiome research is by no means limited to the study of the intestinal populations, or even to the study of humans. Efforts in environmental and agricultural research, for example, reflect a growing interest in the relevance of nonhuman microbiomes.

Speakers

David A. Relman, M.D.
Stanford University
Palo Alto, CA

Jack A. Gilbert, Ph.D.
Argonne National Laboratory
Lemont, IL

Rob Knight, Ph.D.
HHMI / University of Colorado
Boulder, CO

Webinar sponsored by

NEW ENGLAND BioLabs® Inc.

Brought to you by the *Science*/AAAS Custom Publishing Office

Science AAAS

@SciMagWebinars

CHN Microanalysis

An entry-level manual version of the high performance Model 440 Elemental Analyzer has been introduced for determining percentage levels of carbon, hydrogen, and nitrogen (CHN) quickly, easily and reliably across the widest range of sample types. Competitively priced, the manual Model 440 offers labs running smaller numbers of samples a no-compromise entry point into high performance CHN analysis. The manual Model 440 is based upon Exeter Analytical's proven static combustion elemental analyzer incorporating a unique horizontal furnace design. This horizontal furnace enables easy removal of sample residue (metals, inorganics) between each material analysis thereby eliminating the possibility of contamination. In addition, the gas flow characteristics of the Model 440 analyzer are superior to other elemental analyzers due to the effective elimination of troublesome residue build-up over time. Consequently the Model 440 provides longer-term calibration stability as well as enhanced accuracy and precision for measured sample data.

Exeter Analytical
For info: +44-(0)-2476-323223
www.exeteranalytical.co.uk

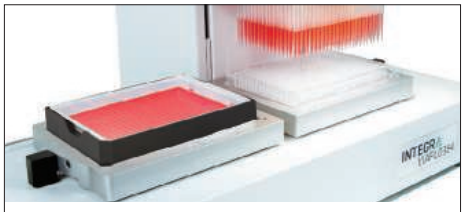

384-Well Reagent Reservoirs

Adopting a standard ANSI / SLAS footprint, Integra 384-well reagent reservoirs (100 mL) are fully compatible with all liquid handling systems including the VIAFLO 384 Handheld Multichannel Electronic Pipette. 384 individual pyramidal indentations in each reagent reservoir allow maximum liquid recovery when using a VIAFLO 384 electronic pipette as well as other platforms. VIAFLO multichannel reagent reservoirs are both economically and environmentally friendly because users can reuse the reservoir base and dispose of the reservoir inserts. These reagent reservoirs are also designed to nest within one another without sticking and come in compact, space-saving packages.

Integra Biosciences
For info: +41-(0)-81-286-9530
www.integra-biosciences.com

Direct Sample Analysis

The DART-QS Source is designed for rugged direct sample analysis using its Direct Analysis in Real-Time Mass Spectrometry technology, which can detect a range of materials from drugs of abuse to adulterated products in as little as 10 seconds per sample. Both qualitative and quantitative results can be obtained, providing rapid feedback, and alleviating backlogs. The source utilizes QuickStrip Sample Cards for automated analysis of 12 samples. They are simple to use, insure that no cross-contamination occurs, and can be loaded automatically or manually, including standards for quantitation. For critical samples, customers need an increased level of security and robustness, which is provided with the use of QuickStrip Sample Cards in the new enclosed DART-QS Source. Additionally the source can be used with nitrogen or helium, providing additional breadth of coverage, and minimizing background ions.

IonSense
For info: 781-484-1043
www.ionsense.com

FFPE Tissue Samples

CancerSeq is a new range of genetically characterized FFPE tissue samples. CancerSeq samples are prepared from genomic DNA extracted from the FFPE tumor tissues and validated by next generation sequencing using Illumina's TruSeq Amplicon-Cancer Panel (TSACP). Available as tissue slides and whole blocks, samples are delivered with the mutation and variation data for 48 cancer-related genes including BRAF, KRAS, EGFR, ALK, and TP53. CancerSeq tissue samples provide researchers with the perfect medium for applications including validation of cancer marker mutation related drug candidates; companion diagnostic assay development; cellular localization of tissue specific mRNA and protein expression; and comparison of the locations of novel genes in different tissues as well as in situ hybridization, immunohistochemistry, and in situ polymerase chain reaction experiments. In addition, AMSBIO offers custom services to characterize your specimens or selected samples from its biorepository of cancer and normal formalin-fixed, paraffin-embedded (FFPE) tissue samples.

AMS Biotechnology
For info: +44-(0)-1235-828200
www.amsbio.com

3-D Surface Profiling

The Leica DCM8 is designed for nondestructive three-dimensional surface profiling. The instrument is a combined confocal and interferometric optical profiler and therefore provides the benefits of both technologies: high-definition confocal microscopy for high lateral resolution and interferometry to reach sub-nanometer vertical resolution. Both techniques can be important for surface analysis of materials and components across numerous research and production environments. Surfaces that are made up of intricate structures with highly sloping areas demand lateral resolution of a few micrometers. In contrast to this, polished supersmooth surfaces with critical micro peaks and valleys require vertical analysis on the nanometer scale. With the Leica DCM8, users will be able to meet their specific surface metrology needs with lateral resolution up to 140 nm via confocal microscopy and vertical resolution of up to 0.1 nm with interferometry. Additionally, the user-friendly setup and operation of the microscope saves effort and delivers accurate results very quickly and conveniently.

Leica Microsystems
For info: 800-248-0123
www.leica-microsystems.com/dcm8

Electronically submit your new product description or product literature information! Go to www.sciencemag.org/products/newproducts.dtl for more information.

Newly offered instrumentation, apparatus, and laboratory materials of interest to researchers in all disciplines in academic, industrial, and governmental organizations are featured in this space. Emphasis is given to purpose, chief characteristics, and availability of products and materials. Endorsement by *Science* or AAAS of any products or materials mentioned is not implied. Additional information may be obtained from the manufacturer or supplier.

Science Translational Medicine

Integrating Science, Engineering, and Medicine

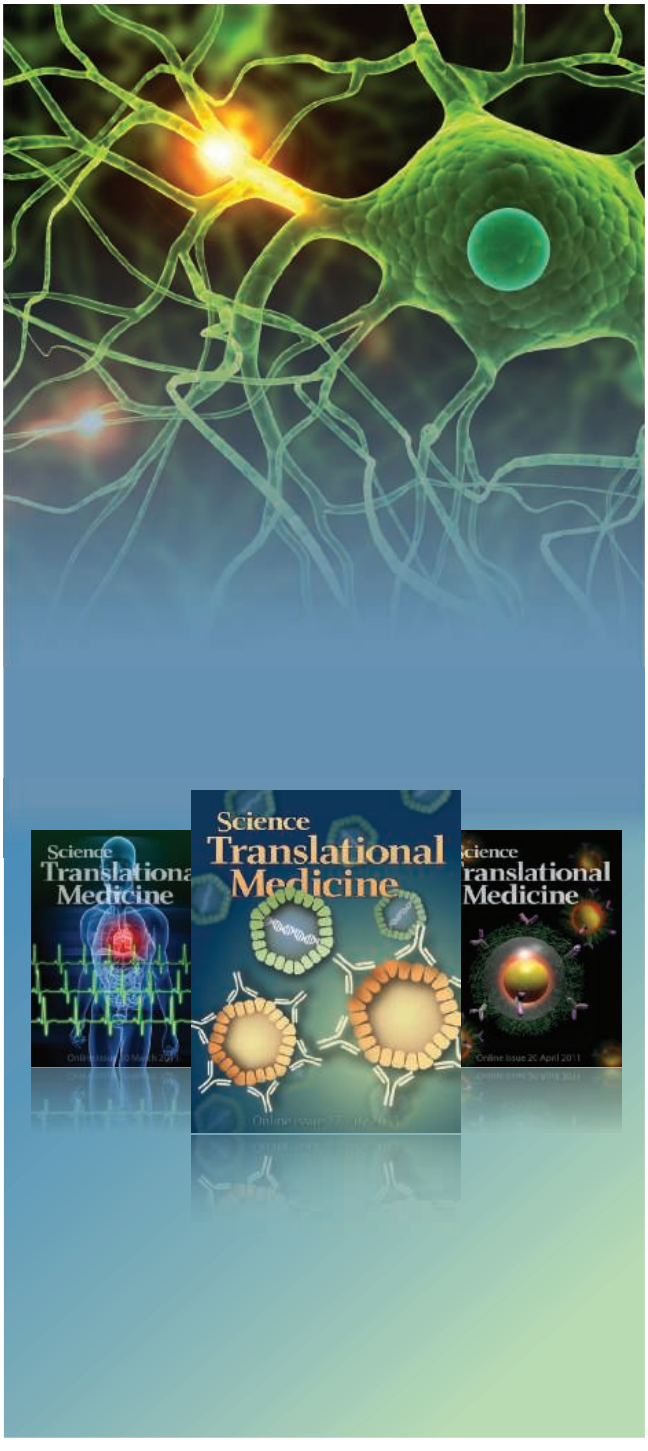

Publishing results that harness the basic sciences to advance human health in all areas of medicine

Submit your research

ScienceTranslationalMedicine.org

Recommend to your library

ScienceOnline.org/recommend

Join the ranks of high-profile papers published in *Science Translational Medicine*:

Neurology

A Theoretically Based Index of Consciousness Independent of Sensory Processing and Behavior

A. G. Casali *et al.* (M. Massimini), *Sci. Transl. Med.* **5** 198ra105 (2013)

Immunology

TGFβ Receptor Mutations Impose a Strong Predisposition for Human Allergic Disease

P.A. Frischmeyer-Guerrerio *et al.* (H. Dietz), *Sci. Transl. Med.* **5** 195ra94 (2013)

Bioengineering

A Human Disease Model of Drug Toxicity-Induced Pulmonary Edema in a Lung-on-a-Chip Microdevice

D. Huh *et al.* (D. Ingber), *Sci. Transl. Med.* **5** 159ra147 (2012)

Cancer

Genome-Wide Mutational Signatures of Aristolochic Acid and its Application as a Screening Tool

S.L. Poon *et al.* (B. T. Teh), *Sci. Transl. Med.* **5** 197ra101 (2013)

Tissue Engineering

Human Cartilage Repair with a Photoreactive Adhesive-Hydrogel Composite

B. Sharma *et al.* (J.J. Elisseeff), *Sci. Transl. Med.* **5** 167 ra6 (2013)

Chief Scientific Advisors

Elazer Edelman, M.D., Ph.D.
Massachusetts Institute of Technology

Garret FitzGerald, M.D.
University of Pennsylvania

Editor

Katrina L. Kelner, Ph.D.
AAAS, Washington, DC

Science Translational Medicine AAAS

scitranslmededitors@aaas.org

NEW ENGLAND BioLabs® Inc.
enabling technologies in the life sciences

Make ends meet.

Gibson Assembly® Cloning Kit

New England Biolabs has revolutionized your laboratory's standard cloning methodology. The Gibson Assembly Cloning Kit combines the power of the Gibson Assembly Master Mix with NEB 5-alpha Competent *E. coli*, enabling fragment assembly and transformation in just under two hours. Save time, without sacrificing efficiency.

Making ends meet is now quicker and easier than ever before, with the Gibson Assembly Cloning Kit from NEB.

NEBuilder™ for Gibson Assembly

Visit **NEBGibson.com** to view the latest tutorials and to try our primer design tool.

Gibson Assembly Cloning Kit provides robust transformation efficiencies

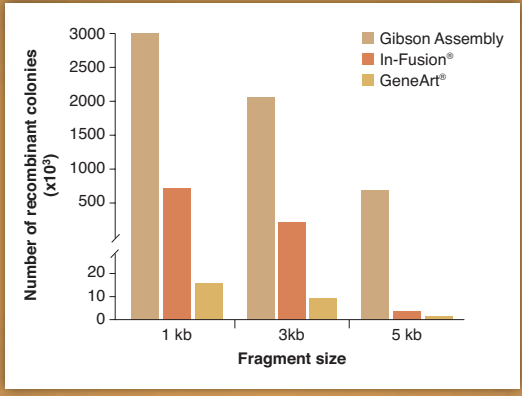

Assembly reactions containing 25 ng of linear pUC19 vector and 0.04 pmol of each fragment were performed following individual suppliers' recommended protocols and using the competent cells provided with the kit. The total number of recombinant colonies was calculated per 25 ng of linear pUC19 vector added to the assembly reaction.

IN-FUSION® is a registered trademark of Clontech Laboratories, Inc.
GENEART® is a registered trademark of Life Technologies, Inc.
GIBSON ASSEMBLY® is a registered trademark of Synthetic Genomics, Inc.

SGI-DNA

Some components of this product are manufactured by New England Biolabs, Inc. under license from Synthetic Genomics, Inc.

Science Careers Advertising

For full advertising details, go to ScienceCareers.org and click For Employers, or call one of our representatives.

Tracy Holmes
Worldwide Associate Director
Science Careers
Phone: +44 (0) 1223 326525

THE AMERICAS
E-mail: advertise@sciencecareers.org
Fax: 202-289-6742

Tina Burks
Phone: 202-326-6577

Nancy Toema
Phone: 202-326-6578

Marci Gallun
Sales Administrator
Phone: 202-326-6582

Online Job Posting Questions
Phone: 202-312-6375

EUROPE / INDIA / AUSTRALIA / NEW ZEALAND / REST OF WORLD
E-mail: ads@science-int.co.uk
Fax: +44 (0) 1223 326532

Azel Gesatzki
Phone: +44 (0)1223 326529

Sarah Lelarge
Phone: +44 (0) 1223 326527

Kelly Grace
Phone: +44 (0) 1223 326528

JAPAN
Yuri Kobayashi
Phone: +81-(0)90-9110-1719
E-mail: ykobayas@aaas.org

CHINA / KOREA / SINGAPORE / TAIWAN / THAILAND
Ruolei Wu
Phone: +86-186-0082-9345
E-mail: rwu@aaas.org

All ads submitted for publication must comply with applicable U.S. and non-U.S. laws. *Science* reserves the right to refuse any advertisement at its sole discretion for any reason, including without limitation for offensive language or inappropriate content, and all advertising is subject to publisher approval. *Science* encourages our readers to alert us to any ads that they feel may be discriminatory or offensive.

Science Careers
From the journal *Science* AAAS

ScienceCareers.org

POSITIONS OPEN

ASSISTANT, ASSOCIATE, OR FULL PROFESSOR

The UC San Diego School of Medicine is committed to academic excellence and diversity within faculty, staff, and student body.

The UC San Diego Sanford Stem Cell Clinical Center, in cooperation with the UC San Diego Health System and School of Medicine, seeks faculty applicants to join a highly interdisciplinary effort dedicated to advancing stem cell research to clinical trials. Faculty are sought to conduct strongly interdisciplinary research with clinical applicability in stem cell science and medicine. Tenure-track faculty positions are available in fall 2014 at the Assistant, Associate, or full Professor level.

The ultimate goal for the Sanford Stem Cell Clinical Center is to make a difference to patients as rapidly as possible by establishing an internationally recognized, premier stem cell clinical program, constantly fueled by research advances at the Sanford Consortium for Regenerative Medicine, its member institutions, and surrounding collaborative institutes. It will be known for advancing leading-edge stem cell medicine and science, protecting and counseling patients, and accelerating innovative stem cell research into patient diagnostics and therapy.

UC San Diego seeks candidates who will establish, or have established, independent and vigorous extramurally funded research programs in regenerative medicine, hESC/hIPSC modification & GMP processing, viral modification of cells for GMP production, or other foci in cell therapy development. Our top candidates will have innovative approaches and expertise in more than one discipline.

Candidates should have a track record of publications in internationally recognized journals, and a willingness to participate in university service, graduate and undergraduate teaching.

Applicants must possess a Ph.D. or M.D. degree or both. Successful applicants will have appointments in one or more home departments at UC San Diego.

The level of appointment will be commensurate with qualifications and experience. Successful candidates will also demonstrate strong or potential accomplishments in areas contributing to diversity, equity and inclusion, and a desire to play a leadership role in advancing UC San Diego's commitment to achieving excellence and diversity.

Salary is commensurate with qualifications and based on University of California pay scales.

Review of applications will begin on July 14, 2014 and continue until the position is filled.

Interested applicants must submit curriculum vitae, statement of research experience and interests, contact information for three references, and a separate statement summarizing past or potential contributions to diversity, see **website: http://facultyequity.ucsd.edu/Faculty-Applicant-C2D-Info.asp.** Additional information that can be submitted includes a cover letter and statement of teaching.

Applications must be submitted through the University of California San Diego's Academic Personnel RECRUIT system at **website: http://apptrkr.com/454880.**

Please direct inquiries to the Co-Chairs of the Search Committee, **Catriona Jamieson,** M.D., Ph.D., and **Lawrence S. B. Goldstein,** Ph.D., at **e-mails: cjamieson@ucsd.edu** or **lgoldstein@ucsd.edu.**

☑ More scientists agree—we are the most useful website.

Science Careers
From the journal *Science* AAAS

www.ScienceCareers.org

POSITIONS OPEN

Yale

ION CHANNEL PHARMACOLOGY AND PHYSIOLOGY
Yale Medical School

Position available for **POSTDOCTORAL RESEARCH ASSOCIATE** or **ASSOCIATE RESEARCH SCIENTIST** at Center for Neuroscience & Regeneration Research, Yale Medical School for electrophysiologist/pharmacologist with experience in patch-clamp analysis of ion channels, to join multidisciplinary research team investigating role of wild-type and mutant Na channels in hyperexcitability disorders including neuropathic pain. (See Dib-Hajj *et al.*, *Nature Reviews Neuroscience* **14:** 49-62; 2013; Faber *et al.*, *Proceedings of the National Academy of Sciences* **109:** 19444-9, 2012.) M.D., Ph.D., or MD/Ph.D. degree and publications in ion channel electrophysiology/pharmacology are essential. Experience with voltage- and current-clamp analysis of DRG or similar neurons is desirable. Superb opportunity to work collaboratively within a highly productive, interactive team setting. Send statement of interest, curriculum vitae, and three letters of reference to **Stephen G. Waxman,** M.D., Ph.D. **e-mail: stephen.waxman@yale.edu.**

RESEARCH SCIENTIST

The Center for Molecular Cardiology at Stony Brook University seeks a Research Scientist to work on funded research projects related to diseases of the cardiovascular system. Job responsibilities will include development of animal models of human cardiac arrhythmias, performing cardiac catheterizations to implant and monitor the function of electronic and biological pacemakers in the large animal model, working with gene and cell therapies to fabricate biological pacemakers, and to prevent/treat ventricular tachycardia and fibrillation induced by myocardial infarction. M.D. or Ph.D. degree or equivalent preferred. Background working in the cardiology field preferred.

Additional requirements include demonstrated ability to interpret EKGs, strong oral and written communication skills, prior experience working with small and large animal models. Interested candidates should send curriculum vitae to: **Joan Kavanaugh, Department of Physiology & Biophysics, Health Sciences Center, BST Level 6 Room 140, Stony Brook University, Stony Brook, NY 11794-8661** or **e-mail: joan.kavanaugh@stonybrook.edu.**

For a full position description, application procedures, or to apply online (preferred), visit website: **http://www.stonybrook.edu/jobs** (**Job Reference#: HS-R-9017-14-06-S**). *Affirmative Action/Equal Opportunity Employer.*

Help employers find you. Post your resume/cv.

Science Careers
From the journal *Science* AAAS

www.ScienceCareers.org

Hiring Professors at All Ranks at South University of Science and Technology (SUSTC)Shenzhen, China

The South University of Science and Technology (SUSTC) invites applications and nominations for all ranks of tenured and tenure-track faculty members in the Division of Science, Division of Engineering and Division of Management & Finance.

SUSTC, officially established in April 2012, is a public institution funded by the municipal of Shenzhen, a special economic zone city in southern China. The University is accredited by the Ministry of Education, China and is a pioneer in higher education reform in China. Set on five hundred acres of wooded landscape in the picturesque Nanshan (South Mountain) area, the new campus offers an idyllic environment suitable for learning and scholarship. SUSTC engages in basic and problem-solving research of lasting impact to benefit society and mankind.

The Division of Science, Division of Engineering, and the Division of Management & Finance wish to hire faculty members at all ranks. Key areas include but not limited to: *Neural and Cognitive Sciences, Biology and Gene Engineering, Modern Physics, Control and Modification of Materials, Nanoscience and Nanotechnology, Mathematics and Applied Mathematics, Molecular Chemistry and Catalysis, Large-Scale Computational Research, Robotics and Artificial Intelligence, Information Systems and Electronic Engineering, Modern Cities and Future Developments, Energy Sciences and Technology, Environmental Sciences, Financial Mathematics and Management Sciences.* The Divisions especially encourage research that requires a multi-disciplinary approach. Experienced researchers whose interests do not fall within the above areas are invited to suggest new areas of research. **Cluster hiring is possible, with senior members accompanied by junior members in a group.**

The teaching language at SUSTC is English or Putonghua. The choice is made by the instructor. As we expect an international faculty, the majority of teaching materials and reference books will be in English and many classes will be conducted in English. With a very high faculty-to-student ratio, SUSTC is committed to delivering a student-centered education and encourages students to develop their innovative spirits. Students at junior and senior years are expected to participate in research in the Research Centers.

The University offers competitive salaries, fringe benefits including medical insurance, retirement and housing subsidy. Leading Professors, Chair Professors and Professors will be appointed with tenure. Associate Professors and Assistant Professors will be offered tenure-track contracts.

Please visit our website to apply: http://talent.sustc.edu.cn/en/. All applications should include a CV and a detailed list of publications with Research ID. **Those interested in cluster hiring should send CVs and publication lists with Research ID as a group.** Evaluations will commence immediately and appointments will be made on a continuous basis. Additional information on SUSTC is available on the University homepage **http://www.sustc.edu.cn.**

Qualified applicants are also encouraged to apply for the Recruitment Program of Global Expert ("Thousand Talents Program") through SUSTC. Successful applicants will get extra research fund and living allowance from the government. Additional information is available through email inquiry or **http://talent.sustc.edu.cn/.**

If you have any questions, please feel free to contact us at **hiring@sustc.edu.cn.**

Science Careers online @sciencecareers.org
OPPORTUNITIES IN CHINA

Institute for Basic Science

President - The Institute for Basic Science in Daejeon, South Korea

The Institute for Basic Science (IBS) is a government-funded research institute that has been developed with the sole purpose of driving forward the development of basic science. IBS is committed to identifying, developing and advancing discoveries in basic science and groundbreaking technology through world-class basic science research. IBS is seeking candidates who have strong leadership skills and a compelling vision to lead the institute into the future as a globally-recognized frontrunner in basic science.

- **Position: IBS President**
- **Term of Position: Five years after the appointment date**
- **Qualifications**
  - Compelling vision and strategic thinking to lead IBS as a global research institute
  - Expert knowledge and significant experience in basic science and scientific policies
  - Recognized leadership skills in managing and directing a scientific research organization
  - Demonstrated ability to innovate within an organization
  - Is not subject to disqualification in accordance with Article 9 of the Articles of Incorporation of IBS
- **To Apply**

Please visit **www.ibs.re.kr/president** to submit the required documents, or mail the documents to the address below.

Planning & Budgeting Team, Institute for Basic Science
70, Yuseong-daero 1689-gil, Yuseong-gu, Daejeon, South Korea (305-811)

- **Required Documents**

Individual Candidate
- Application Form
- Curriculum Vitae (free format with a photo)
- List of All Papers Written
- Introductory Letter (less than 5 A4-Sized Pages)
- Duty Execution Plan (less than 5 A4-Sized Pages)
- Certificate of Family-Resident Registration (issued in the last one month, not required from a foreign applicant)
- Letter of Recommendation from Peers (from no more than 3 peers, optional)

Recommended by Organization or Institution*
- Letter of Recommendation from Organization or Institution
- Curriculum Vitae (free format with a photo)
- List of All Papers Written
- Introductory Letter (less than 5 A4-Sized Pages)
- Duty Execution Plan (less than 5 A4-Sized Pages)
- Certificate of Family-Resident Registration (issued in the last one month, not required from a foreign applicant)
- Letter of Recommendation from Peers (from no more than 3 peers, optional)

* List of Recognized Organizations and Institutions: The Korean Federation of Science and Technology Societies, The Korean Academy of Science Technology, The National Academy of Engineering of Korea, etc. (For the complete list, please visit **www.ibs.re.kr/president**)

- **Closing Date**

18:00 (KST) Friday, July 4, 2014
*Please submit the required documents by the closing date.

- **Others**
  - Submitted documents shall be used for application review only, and shall not be returned.
  - Incorrect information may result in the revocation of nomination for the position.
  - For more details, please visit **www.ibs.re.kr/president**, email **jungsm@ibs.re.kr** or call **+82-42-878-8159**.
  - Matters regarding evaluation criteria, procedures, appointment, contracts, etc. for foreign applicants shall comply with all Korean laws and IBS regulations.

May 26, 2014

IBS Presidential Search/Nomination Committee

THE CHINESE UNIVERSITY OF HONG KONG

Applications are invited for:-

Department of Paediatrics
Associate Professor / Assistant Professor (Non-Clinical)

(Ref. 1314/185(665)/2) (Closing date: July 18, 2014)

Applicants should have (i) a PhD degree in biomedical sciences or a closely related discipline; (ii) relevant postdoctoral training; (iii) a strong track record of research, publications and grant application; (iv) expertise in molecular, protein and cell technology; and (v) experience in supervision of postgraduate students and laboratory staff. Research experience in genetics and genomics, biomarker discovery, bioinformatics and paediatric diseases will be an advantage. Appointment will normally be made on contract basis for three years initially commencing October 2014 or as soon as possible thereafter, which, subject to mutual agreement, may lead to longer-term appointment or substantiation later.

Salary and Fringe Benefits

Salary will be highly competitive, commensurate with qualifications and experience. The University offers a comprehensive fringe benefit package, including medical care, a contract-end gratuity for an appointment of two years or longer, and housing benefits for eligible appointee. Further information about the University and the general terms of service for appointments is available at *http://www.per.cuhk.edu.hk*. The terms mentioned herein are for reference only and are subject to revision by the University.

Application Procedure

Please send full resume, together with copies of academic credentials, a publication list and/or abstracts of selected published papers, and names, addresses and fax numbers/e-mail addresses of three referees to whom the applicants' consent has been given for their providing references (unless otherwise specified), to the Personnel Office, The Chinese University of Hong Kong, Shatin, N.T., Hong Kong [fax: (852) 3943 1462] by the closing date. The Personal Information Collection Statement will be provided upon request. Please quote the reference number and mark 'Application – Confidential' on cover.

Penn Medicine

Associate/Full Professor of Radiation Oncology, Tenure-Track

Candidates with evidence of significant extramural funding and a strong publication record in any area of Tumor or Radiation Biology are encouraged to apply. We are particularly interested in individuals with research interests in normal tissue radiobiology, tumor microenvironment or tumor stem cells. The Division of Radiation Research is comprised of 14 faculty engaged in innovative, translational research with a focus on the study of the tumor microenvironment, radiation response modifiers, photodynamic therapy and proton therapy. Research in the Division is supported by multiple grants from the NIH, DoD, NASA, private foundations and industry. Faculty in the Division can have cross-appointments to other Departments and can belong to different graduate groups such as Cell and Molecular Biology and Pharmacology. The majority of the Division faculty are located in new, contiguous laboratory space in the Smilow Center for Translational Research Building (SCTR), in very close proximity to the clinic. State-of-the- art shared instrumentation includes a 3-D conformal irradiator for small animals, live cell microscopy, hypoxia chambers, multiple PDT lasers, etc. The SCTR building has its own barrier and non-barrier animal facility and small animal imaging facilities which include optical, MR and CT imaging. A competitive start-up package and laboratory space will be provided. For more information about the Department of Radiation Oncology, and the Division of Radiation Research please visit: **http://www.xrt.upenn.edu/index.shtml**

Interested candidates should send a curriculum vitae, a one page summary of their future research goals and the names of three references, preferably in a single pdf, via the online form. The deadline for applications is **July 15, 2014**.

EMBL

The European Molecular Biology Laboratory (EMBL) seeks to appoint a new

Director for the European Bioinformatics Institute (EMBL-EBI)

based in Hinxton near Cambridge, U.K.

The European Bioinformatics Institute is part of EMBL, Europe's flagship laboratory for the life sciences. EMBL operates from five sites in four European countries and is headquartered in Heidelberg, Germany. The EMBL-EBI Director collaborates closely with two Associate Directors who have specific responsibility for service delivery. All three are part of EMBL's collegial Senior Management, which is led by the EMBL Director General.

The new Director will be responsible for strategic and operational management of all aspects of EMBL-EBI, which employs 560 staff involved in research and service provision. The service portfolio includes provision of comprehensive collections of molecular life science data as part of strong international collaborations. A very strong technical software environment, with one of the largest bioinformatics computer infrastructures in the world, underpins the delivery of bioinformatics services that in total employ roughly 400 staff members.

The Director will also oversee a vibrant research community whose 16 participating groups work at the forefront of bioinformatics research. They are engaged in many aspects of research, frequently in collaboration with experimental colleagues in EMBL or beyond. Recruiting new research leaders and shaping the research portfolio is an important task.

EMBL-EBI has a thriving Industry Programme that engages with over 20 large bioscience companies and aims to help them make best use of public data. The recent Innovation and Translation Initiative has led to the establishment of a new Centre for Therapeutic Target Validation, in collaboration with the Wellcome Trust Sanger Institute and GSK, the U.K. pharmaceutical company, which aims to improve target validation using genomics and other public data. The Director will further develop both the Programme and the Initiative, seeking opportunities to work with the private sector and enable research and its translation.

EMBL-EBI played a leading role in the establishment of the distributed ELIXIR research infrastructure, and is itself an ELIXIR node. The ELIXIR Hub is housed at EMBL-EBI. The new Director will work, in collaboration with the ELIXIR Director and other nodes, to develop ELIXIR into a coordinated pan-European biological data infrastructure.

The successful individual will combine an outstanding record of relevant research achievements with proven managerial and organisational capability. The Director will have a full-time appointment and will be responsible for building on all aspects of EMBL-EBI's current role and shaping it to match the demands of the future in both service provision and research. This will involve close interaction with many other bioinformatics centres. The Directorship represents an exceptional opportunity to contribute to shaping the institute in these exciting times and to developing Europe's role in life science research and its applications in medicine, the environment and society.

APPLICATION INSTRUCTIONS

Please apply online through **www.embl.org/jobs** sending a CV and a motivation letter.

Questions concerning the role should be sent to **dg-office@embl.de** and any queries regarding the terms and conditions should be sent to **recruitment@embl.org**.

ADDITIONAL INFORMATION

EMBL is an inclusive, equal opportunity employer offering attractive conditions and benefits appropriate to an international research organisation.

Please note that this is a tenure-eligible appointment.

Commencing date: negotiable, from spring/summer 2015

Closing date: 31 July 2014

www.embl.org

Science Careers online @sciencecareers.org

CASE WESTERN RESERVE UNIVERSITY
SCHOOL OF MEDICINE

Faculty Position – Department of Genetics and Genome Sciences

Faculty positions at the assistant, associate, and full professor levels are available in the Department Genetics and Genome Sciences for outstanding scientists involved in contemporary research in genetics and genomics.

Thirty-two basic, clinical and physician scientist faculty base their research, teaching, and clinical activities in the Department of Genetics and Genome Sciences. The research programs of these investigators include human genetics and genomics, model systems (including invertebrate, mouse and induced pluripotent stem cells), translational genomics, cancer genetics/genomics, systems biology research, developmental genetics and clinical genetics. The Department includes the Center for Human Genetics, which encompasses all medical genetics activities at University Hospitals Case Medical Center, Rainbow Babies and Children's Hospital, and the Seidman Cancer Center, providing a unique bridge for translational studies. State-of-the-art research laboratories with access to core facilities in genomic sequencing, pluripotent stem cell production, imaging, transgenic/knock-out mice, bioinformatics, chemical/drug screening and animal services significantly enhance research and training within the department. The Department has active PhD and genetic counseling (MS) graduate programs, medical genetics residency programs, and faculty members engage in teaching in the medical school.

Positions are available at the level of Assistant Professor, Associate Professor, and Full Professor, (tenure and non-tenure track) rank commensurate with experience and accomplishments. Applicants at the Assistant Professor level should demonstrate promise for research and teaching excellence. Senior applicants at the Associate Professor (Professor) level should have a strong national (international) scientific reputation as well as a distinguished record of publication and research funding. Preference will be given to applications who complement ongoing programs or who bring novel experience, expertise or research perspectives. Successful applicants will have a M.D., Ph.D. or both and are expected to develop an independent research program and to teach in the Department training program. Applicants should submit a curriculum vitae, a brief statement of research and teaching interests, and arrange for at least three letters of reference. Applications and letters of reference should be submitted to:

Case Western Reserve University
Department of Genetics and Genome Sciences
Attn: Michelle Yanick
10900 Euclid Avenue
Cleveland, Ohio 44106-4955
Website: http://genetics.case.edu
Email: genetics-search@case.edu

In employment, as in education, Case Western Reserve University is committed to Equal Opportunity and Diversity. Women, veterans, members of under-represented minority groups, and individuals with disabilities are encouraged to apply.

Case Western Reserve University provides reasonable accommodations to applicants with disabilities. Applicants requiring a reasonable accommodation for any part of the application and hiring process should contact the Office of Inclusion, Diversity and Equal Opportunity at 216-368-8877 to request a reasonable accommodation. Determinations as to granting reasonable accommodations for any applicant will be made on a case-by-case basis.

CASE WESTERN RESERVE UNIVERSITY
SCHOOL OF MEDICINE

University Hospitals
Seidman Cancer Center

Hematology Investigator
Division of Hematology and Oncology

The Division of Hematology and Oncology in the Department of Medicine at Case Western Reserve University School of Medicine and the Case Comprehensive Cancer Center (Case CCC), are seeking applications for a tenure track laboratory-based investigator at the Assistant or Associate Professor level. We are seeking applicants with a research focus directly relevant to hematologic malignancies or hematopoietic stem cell transplant immunology. The section of Hematologic Malignancies and Stem Cell Transplantation within the Division, under the leadership of Dr. Marcos de Lima, is broadly focused on the development of novel therapeutics with translation of scientific concepts exploring new drugs and cell-based approaches.

The candidate is expected to develop an independently-funded research program, with close collaboration with clinical investigators. The successful applicant will have the opportunity to collaborate broadly with faculty members across the university, including the Departments of Genetics and Genome Sciences, the Center for Proteomics and Bioinformatics, and scientific programs of the Case Comprehensive Cancer Center. This individual will join a critical mass of bench-to-bedside researchers as a member in the Case Comprehensive Cancer Center Hematopoietic Disorders research program.

Candidates should hold a PhD and/or MD, postdoctoral research experience, a strong publication record, and evidence of successful extramural funding. Candidates at the Associate Professor level should have evidence of national service and recognition. A statement of research interests, curriculum vitae, and names of three references should be sent to:

Marcos de Lima, MD
Section Chief, Hematologic Malignancies and Stem Cell Transplantation
Co-Leader, Hematopoietic Disorders Research Program
University Hospitals Case Medical Center
Case Comprehensive Cancer Center
marcos.delima@case.edu

In employment and education, CWRU is committed to equal opportunity and diversity. Women, veterans, members of underrepresented minority groups, and individuals with disabilities are encouraged to apply. For information regarding reasonable accommodations, please visit: http://www.case.edu/diversity/faculty/EEO.html.

AAAS is here –
helping scientists achieve career sucess.

Every month, over 400,000 students and scientists visit ScienceCareers.org in search of the information, advice, and opportunities they need to take the next step in their careers.

A complete career resource, free to the public, *Science* Careers offers hundreds of career development articles, webinars and downloadable booklets filled with practical advice, a community forum providing answers to career questions, and thousands of job listings in academia, government, and industry. As a AAAS member, your dues help AAAS make this service available to the scientific community. If you're not a member, join us. Together we can make a difference.

To learn more, visit
aaas.org/plusyou/sciencecareers

AAAS + U = Δ

NIH National Institute of General Medical Sciences

Department of Health and Human Services
National Institutes of Health
National Institute of General Medical Sciences
Division of Training, Workforce Development, and Diversity

DIVISION DIRECTOR

The National Institute of General Medical Sciences (NIGMS), a major research component of the National Institutes of Health (NIH) and the Department of Health and Human Services (DHHS), is seeking exceptional candidates for the position of Director, Division of Training, Workforce Development, and Diversity (TWD). Information about TWD is available at **http://www.nigms.nih.gov/About/Overview/pages/twd.aspx.**

TWD funds research training, career development, diversity and capacity-building activities that foster the development of a strong and diverse biomedical research workforce. The TWD Director will be responsible for the scientific and administrative management of the Division, and coordinating the development of NIGMS goals, objectives, policies, plans and guidelines for research and research training programs. Specifically, the TWD Director is responsible for: 1) overall oversight and supervision of Division programs, including programmatic review of research grant, research training grant and fellowship applications, and priority setting in regard to payment of grants; 2) development and implementation of strategic plans to enable NIGMS to improve the effectiveness of its programs aimed at increasing participation in biomedical research; 3) coordination of Institute policies related to research and research training programs; and 4) liaison with groups at NIH, DHHS, and other federal agencies, as well as with the extramural scientific community on these matters. This individual will report to the NIGMS Director and may also coordinate activities across NIH and among other federal agencies.

Qualifications: Candidates must have an M.D., Ph.D. or equivalent degree in a field relevant to the position. The ideal candidate will have considerable research experience and will possess a broad spectrum of scientific knowledge related to the NIGMS mission. He/she will also have professional experience in the training of research scientists, as well as programs aimed at developing a diverse biomedical and behavioral research workforce. In addition, candidates should possess recognized research management and leadership abilities. This position will be filled under a Title 42(f) excepted service appointment.

Salary/Benefits: Salary is competitive and will be commensurate with the experience of the candidate. A recruitment or relocation bonus may be available, and relocation expenses may be paid. A full package of Federal Civil Service benefits is available, including: retirement, health and life insurance, long term care insurance, leave and a Thrift Savings Plan (401K equivalent). The successful candidate is subject to a background investigation and public financial disclosure requirements.

How to Apply: Applicants must submit a current curriculum vitae, bibliography, copy of degree and full contact details for three references. In addition, applicants are asked to prepare two statements: a vision statement and a statement that addresses the specific qualification requirements (please limit both statements to two pages each). NIGMS will be accepting applications from **June 1, 2014, to July 15, 2014**. Please send your application package to **NIGMSTWDDirector@mail.nih.gov**. You may contact Krystal Kelly with questions about this vacancy at **NIGMSTWDDirector@mail.nih.gov** or 301-594-3827.

DHHS, NIH and NIGMS are Equal Opportunity Employers

CAREER TRENDS Running Your Lab

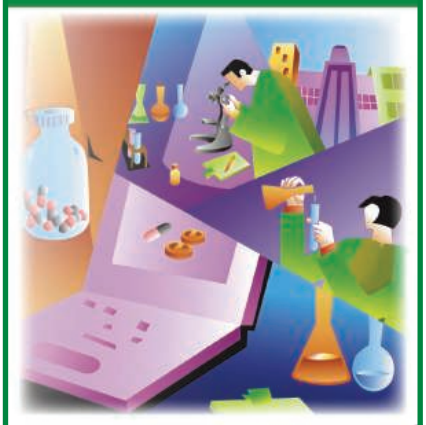

Download your free copy today at ScienceCareers.org/booklets

Science Careers
From the journal *Science* AAAS

Brought to you by the
AAAS/*Science* Business Office

C&EN ACS Publications

CHEMICAL & ENGINEERING NEWS
Editor-in-Chief

Chemical & Engineering News (C&EN) -- the official publication of the American Chemical Society (ACS) – is seeking applications for the position of Editor-in-Chief. This is an extraordinary opportunity to lead one of the largest and most talented global editorial staffs in any science publication.

C&EN is published weekly with print, web and mobile editions. It is one of the chief benefits of membership in the ACS. With a circulation of over 120,000 C&EN delivers authoritative and topical news and feature articles across all facets of chemistry – science and technology, business, government and policy. It is the leading newsmagazine in the chemistry space, and indeed is often described as the "glue that holds the ACS together." The magazine attracts strong display and classified recruitment advertising. The C&EN Media Group is also diversifying into new areas, including webinars, custom publishing and virtual symposia.

The Editor-in-Chief will set the vision and strategy for the magazine's publishing goals and develop long-range plans in support of the Society's organizational strategy. This individual will be responsible for the weekly content and direction of the publication, addressing subjects of interest across the global chemistry enterprise, in print and online. The EIC oversees a team of more than 50 reporters, editors, and web and production staff based in North America, Europe and Asia. Moreover, working closely with the Publisher, the EIC will play a key role in shaping the development of marketing and other commercial initiatives related to the publication. This position reports both to the Board of Directors of ACS as well as to the President of the Publications Division.

Qualifications: The ideal candidate will possess a B.S. or B.A. in chemistry or a chemically related field. The EIC will demonstrate a strong scientific publication record in chemistry and/or related fields with considerable experience in a journalistic environment strongly preferred. (S)he will also possess an abundance of leadership and management skills coupled with the charisma needed to lead a large editorial staff and engage in personal outreach with other constituencies. Finally, (s)he must have an intuitive understanding of the role and importance of C&EN to the American Chemical Society.

For more information and a complete job description, contact:

Lauren Aaron,
Bert Davis Executive Search,
212-838-4000, LAaron@bertdavis.com

EEO/Minority/Female/Disabled/Veteran